Determining the Origins and Impact of Hot Gas in the Milky Way

by

Matthew J. Miller

A dissertation submitted in partial fulfillment
of the requirements for the degree of
Doctor of Philosophy
(Astronomy and Astrophysics)
in the University of Michigan
2016

Doctoral Committee:

Professor Joel N. Bregman, Chair
Professor August E. Evrard
Assistant Professor Elena Gallo
Associate Professor Mateusz Ruszkowski

ACKNOWLEDGMENTS

Many people have helped me reach this point in my life. The past six years have been an incredibly special experience with many challenges that have led to my growth as a scientist and person. This could not have been possible without the support of many people that deserve recognition.

No one has affected my growth as a scientist more than my advisor, Joel Bregman. I remember the first time I met Joel when we talked about my eventual first year research project. I was immediately intrigued because the project was interesting, but also because Joel laid out a compelling story for how the project would go. It was obvious he had (and still has) a comprehensive vision for the field of astronomy, and I have learned a great deal because of that. Joel has always been an invaluable resource for any questions I have had, no matter how basic they may be, and has supported my exploration of numerous astronomy and non-astronomy projects. He has also found a remarkable balance of challenging me to find answers and learn on my own, while providing me the with right amount of guidance when needed. Because of these experiences, I have a great deal of confidence in myself and have achieved more than I thought was possible when I was first a graduate student. Thank you Joel for being my mentor over the past six years; it will always be important to me.

There are several other faculty and research science individuals that deserve special recognition. My dissertation committee members, Gus Evrard, Elena Gallo, and Mateusz Ruszkowski, have provided a great deal of insight on my research. Their advice from numerous conversations has helped make this dissertation the best work

possible. Edmund Hodges-Kluck also deserves special recognition for helping me on several projects over the course of my time as a graduate student. He has consistently helped me with many technical and everyday problems, and I am grateful for his help and support. I also want to thank Nuria Calvet and You-Hua Chu for helping me apply to UM for graduate school.

The UM Astronomy graduate students, or Astrograds, have all been important to me throughout my time here. Those deserving special recognition include: Brian Devour, Daniel Gifford, Jesse Golden-Marx, Jessica Herrington, and Rachael Roettenbacher. I would not have made it through classes, prelims, and teaching without the help of my friends. This is on top of the laughter-filled memories I now have from these wonderful friendships.

I am appreciative of all the hard work from the UM Astronomy administrative, technical, and teaching staffs. In particular, I want to thank Brian Cox for handling almost every University business-related question I have had. He always handles issues with a smile and is the reason things ran smoothly for me as a graduate student. Roy Bonser also deserves recognition for his computer and IT support, which makes our research possible. Finally, Shannon Murphy has been an invaluable reference for anything related to teaching. Instructing a class for the first time was a daunting experience, but Shannon helped ensure things ran as smoothly as possible.

I also want to acknowledge the funding sources that made this work possible. The NASA Astrophysics Data Analysis Program and Rackham Predoctoral Fellowship programs have been especially helpful in funding this work and numerous trips to discuss this work at conferences.

My family deserves more recognition than I can possibly convey here for always supporting, encouraging, and shaping me into the person I am today. Nobody has supported me more than my parents, Jim and Mary Lou Miller, and this support has always helped me achieve whatever goals I have set for myself. My sisters, Amanda,

Mallory, Marli, and Carrie, have also helped me in many ways throughout my life. The support and experiences I have shared from my parents and sisters have helped me become a better person. In addition to them, my grandparents, aunts, uncles, cousins, and extended family members have always supported my interest in astronomy. I am incredibly fortunate to have a supportive and loving family that will always be there for me.

Finally, I want to thank my fiancée, Kristin Lundine, for her support and for being my companion for so many years. You have taught me so much since we have been together, you are my inspiration every day, and your love has guided me through this journey the past six years. I am so lucky to have you in my life, and thank you for always believing in me.

TABLE OF CONTENTS

LIST OF FIGURES

Figure

LIST OF TABLES

Table

ABSTRACT

The Milky Way's circumgalactic medium (CGM) contains $\sim 10^6$ K gas that is volume-filling on $\gtrsim$10 kpc scales based on X-ray emission from the *ROSAT All-Sky Survey*, detections of O VII $K\alpha$ absorption lines at $z \sim 0$ in AGN spectra, ubiquitous detections of O VII – O VIII emission lines in ∼1000 blank-sky spectra, and the discovery of the ∼10 kpc outflow from the Galactic center known as the Fermi bubbles. Analyses on the line strengths in small sight line samples ($\lesssim$20) imply plasma densities between 10^{-5}–10^{-2} cm^{-3}, but the dominant hot gas structure is debated in the literature. This is a crucial uncertainty since different galaxy formation mechanisms predict a wide range of hot gas morphologies and masses, and the Fermi bubbles are recently discovered objects that are interacting with the ambient CGM. In this dissertation, I constrain the global hot gas density structure by comparing predictions from parametric density models with all-sky samples of O VII and O VIII line strength measurements from current X-ray telescopes. I find that a spherical profile with $n \propto r^{-3/2}$ extending to the Milky Way's virial radius reproduces how the absorption and emission line strengths vary across the sky. This extended structure accounts for $\gtrsim$90% of the observed absorption and emission, while a disk-like morphology contributes at most ∼10%. These results imply a hot gas mass between 2–5$\times 10^{10}$ $M_\odot$ within 250 kpc ($\lesssim$50% of the Galactic missing baryons), a hot gas metallicity of $Z \geq 0.3 Z_\odot$, and that most of the hot gas formed from an accretion shock during the Milky Way's formation. I also model the absorption line shapes and centroids to explore hot gas kinematic diagnostics. The observed absorption line centroids indicate that the hot gas has bulk rotation motion similar to the disk with

a rotation curve of $v_\phi = 183 \pm 41$ km s^{-1}. For the Fermi bubbles, a volume-filled bubble and shell model with a characteristic density of $\sim 10^{-3}$ cm^{-3} and temperature between $\log(T) \approx 6.60$-6.70 is consistent with the observed line intensities and ratios. These results imply a bubble expansion rate, age, and energy injection rate of 490^{+230}_{-77} km s^{-1}, $4.3^{+0.8}_{-1.4}$ Myr, and $2.3^{+5.1}_{-0.9} \times 10^{42}$ erg s^{-1}, which are consistent with the bubbles forming due to a Sgr A* accretion event. This analysis uses the most comprehensive observation samples and modeling techniques to reveal how and when $\gtrsim 10^6$ K gas formed in the Milky Way.

CHAPTER I

Introduction

1.1 Hot Gas in Galaxies

A fundamental prediction of disk galaxy formation is the existence of a hot (million-degree) galactic corona that is volume-filling, extends at least 5 kpc from the disk, and is near hydrostatic equilibrium (Spitzer, 1956). Such a corona forms if the cooling time is longer than the dynamical time and if the gas is in rough pressure equilibrium with other phases of the interstellar medium (ISM) near the disk. This is possible for gas temperatures $\gtrsim 3 \times 10^5$ K, and corresponding densities $\lesssim 10^{-3}$ cm^{-3} (Sutherland & Dopita, 1993; Gnat & Sternberg, 2007).

There are several plausible mechanisms that can heat gas to these temperatures in $L \gtrsim L^*$ galaxies (Schechter, 1976), including an accretion shock as gas falls on to the dark matter potential well, and supernova-driven outflows closer to the disk. These mechanisms operate on radically different spatial scales: an accretion shock would occur near the galactic virial radius (≈250 kpc for the Milky Way) while supernova heating dominates within ∼10 kpc of the disk. As a result, the predicted hot gas structure and mass depend on the relative importance and interplay between these processes. Thus, the $\sim 10^6$ K gas structure in $L \sim L^*$ galaxies like the Milky Way is a unique probe of galaxy formation.

1.1.1 Hydrostatic Equilibrium

Hydrostatic equilibrium occurs when pressure gradients balance the total gravitational potential well. This is represented by the following equation:

$$\nabla P = -\rho \nabla \Phi, \tag{1.1}$$

where Φ is the total gravitational potential, ρ is the density, and P is the pressure. For gas in galaxies, the pressure can include thermal, non-thermal (cosmic rays, magnetic fields, etc.), or rotational support, and the gravitational potential includes baryons and dark matter. In the case where thermal pressure dominates and the gas is isothermal (as in a galactic corona), the hydrostatic equilibrium equation is:

$$\nabla P = \frac{kT}{\mu m_p} \nabla \rho = c_T^2 \nabla \rho = -\rho \nabla \Phi, \tag{1.2}$$

where T is the gas temperature, μm_p is the average weight per particle, and $c_T^2 = kT/\mu m_p$ is approximately the sound speed. This equation can be solved to predict the hot gas density profile, which differs depending on the hot gas origins and proximity to the stellar disk.

If the hot gas is mostly within ~ 5 kpc of the disk, then the stars and H I gas in the disk dominate the gravitational potential. The gravitational acceleration due to baryons in the disk is approximately constant if the height off the Galactic plane ($|z|$) is small compared to the disk scale length. For example, the Milky Way's radial scale length is between 2–3 kpc (e.g., Gould et al., 1996; Klypin et al., 2002; Bovy & Rix, 2013), and the measured gravitational acceleration perpendicular to the disk has a characteristic value of $g_z \sim 10^{-8}$ cm s^{-2} perpendicular to the disk (e.g., Oort, 1932). Substituting $-g_z$ for $-\nabla\Phi$ produces the following solution to Equation 1.2:

$$\rho(z) \propto e^{-|z|/H}, \tag{1.3}$$

where $H = c_T^2/g_z$ is the scale height of the gas. Characteristic temperatures and gravitational accelerations for galaxies like the Milky Way predict H to be between 2–10 kpc. This is a much thicker distribution compared to the stars, neutral ISM, and warm ionized ISM in typical disk galaxies, and exceeds the disk length (e.g., Tüllmann et al., 2006; Li & Wang, 2013a). Thus, hydrostatic equilibrium predicts departures from this distribution if the gas extends beyond $|z| \gtrsim 5$ kpc.

If instead the gas extends $\gtrsim$5 kpc from the disk, then the dark matter halo dominates the gravitational potential. The dark matter density profile is assumed to be a spherically symmetric power law at large galactocentric radii (r). Using the circular rotation velocity of the galaxy disk (v_c) as an approximation for the gravitational potential gradient yields $-\nabla\Phi = GM(< r)/r^2 = v_c^2/r$. This leads to the following solution to Equation 1.2:

$$\rho(r) \propto r^{-(v_c/c_T)^2} \propto r^{-\alpha}, \tag{1.4}$$

which is a power law with a slope defined as $\alpha = (v_c/c_T)^2$. In principle, the slope can be a range of values depending on the dark matter profile, but a power law density profile is predicted if dark matter dominates the gravitational potential.

1.1.2 Formation Mechanisms

The modern picture of galaxy formation (e.g., White & Rees, 1978; White & Frenk, 1991) suggests that a galactic corona forms in massive galaxies ($L \gtrsim L^*$) at an accretion shock during the early stages of galaxy formation (Cen & Ostriker, 2006; Fukugita & Peebles, 2006; Faerman et al., 2016). As baryons from the intergalactic medium accrete onto a dark matter halo, a shock front heats the gas to the virial temperature. The virial temperature relates to the galactic circular velocity, v_c, as $T_v = 3.6 \times 10^5$ K $(v_c/100$ km s$^{-1})^2$ (Mo et al., 2010), so galaxies more massive than the Milky Way have virial temperatures $\gtrsim 2 \times 10^6$ K. At these temperatures, this hot

circumgalactic medium (CGM) is volume-filling to the galaxy's virial radius (≈250 kpc for the Milky Way) and has a density profile described approximately by a power law (Equation 1.4).

If such hot halos are ubiquitous around $L \sim L^*$ galaxies, then understanding their properties is critical to understanding galaxy formation. The theory above suggests hot halos should form around typical galaxies like the Milky Way ($L \sim L^*$), but direct detections only exist around more massive edge-on galaxies due to their low surface brightness (Anderson & Bregman, 2011; Dai et al., 2012; Bogdán et al., 2013b,a; Anderson et al., 2016). This is a crucial limitation because it is unclear when, and at what halo mass these hot halos begin to form.

Hot halos also have a significant impact on how the rest of the galaxy evolves. The inner regions of these extended halos are dense enough to cool within a Hubble time, and can supply the disk with low metallicity ($Z \lesssim 0.5 Z_\odot$) star-forming material. This process is known as hot-mode accretion, and can be the primary mechanism for how massive galaxies form their stars (e.g., Kereš et al., 2009). This also implies that a significant fraction of the remaining baryons remain hot and extended to the virial radius. This is important because most galaxies appear to be baryon depleted relative to the cosmological baryon fraction ($\Omega_b/\Omega_m = 0.171 \pm 0.006$; Dunkley et al., 2009), but hot gas masses are often not included in these estimates. If hot halos do exist around $L \gtrsim L^*$ galaxies, then they could contain most of these missing baryons. Finally, hot halos could alter the evolution of anything else within the virial radius, such as stripping H I gas in dwarf galaxies (Blitz & Robishaw, 2000; Grcevich & Putman, 2009; Gatto et al., 2013) and confining high velocity clouds in the Galaxy (e.g., Wakker & van Woerden, 1997). These considerations highlight the importance of hot gas halos, which are a recent prediction for galactic corona structure.

An alternative picture of galactic corona formation suggests that supernova activity in disk galaxies can create a hot gas atmosphere. Supernova explosions in normal

disk galaxies regulate the pressure structure and dynamics of the multiphase ISM (Cox & Smith, 1974; McKee & Ostriker, 1977). Each supernova remnant produces a shock front capable of heating the surrounding ISM to temperatures $\gtrsim 10^6$ K. Individual bubbles expand to sizes of a few hundred parsecs, but these bubbles can merge to form "tunnel" or "chimney" structures that break through the H I disk in a pressure-driven outflow (Shapiro & Field, 1976; Norman & Ikeuchi, 1989; Joung & Mac Low, 2006; Hill et al., 2012). This would produce a galactic-scale hot gas atmosphere confined within ∼10 kpc of the disk described approximately by Equation 1.3 (e.g., Bregman, 1980).

The properties of this supernova-driven distribution offer unique insights on the interaction between galactic disks and halos. This "galactic fountain" mechanism would launch enriched material ($Z \approx Z_\odot$) from the disk into the halo, where it would interact with the surrounding halo material and fall back onto the disk. This could explain features such as high velocity clouds in the Milky Way (e.g., Wakker & van Woerden, 1997) or the significant amount of dust in galactic halos (Ménard et al., 2010; Hodges-Kluck & Bregman, 2014). Additional X-ray observations of edge-on disk galaxies reveal hot coronae structures whose luminosity correlates with star formation rate (SFR) and corresponding supernovae mechanical energy input rate, indicating that supernovae indeed inject hot gas into the halo (Tüllmann et al., 2006; Li & Wang, 2013a,b). However, the amount of energy transport and metal mixing from this disk-halo interaction is still uncertain for typical $L \sim L^*$ galaxies.

Extreme energetic events, such as an active galactic nucleus (AGN) or starburst episode, can substantially alter the hot halo gas by injecting massive amounts of energy on scales $\gtrsim$10 kpc. These events operate through a combination of galactic-scale winds (AGN or starburst) or collimated jets (AGN only) inflating hot, buoyant cavities that expand at velocities $\gtrsim$1000 km s^{-1} into the surrounding halo (Veilleux et al., 2005; McNamara & Nulsen, 2007; Yuan & Narayan, 2014). The characteristic

energetics imply that these outflows can be responsible for a variety of "feedback" effects, including: shock-heating the ambient hot gas distribution, redistributing or possibly ejecting material out of the galaxy, and quenching star formation in the disk.

The theoretical formation of accretion shocks, galactic fountains, and "feedback" events indicates that understanding the hot gas structure in $L \sim L^*$ disk galaxies leads to valuable insights on how galaxies form and what processes regulate their growth. These features are fundamental predictions from galaxy formation simulations, but the expected hot gas structure is sensitive to the input physics and amount of injected feedback (Toft et al., 2002; Sommer-Larsen, 2006; Cen & Ostriker, 2006; Cen, 2012; Feldmann et al., 2013; Marinacci et al., 2014; Nuza et al., 2014; Bogdán et al., 2015; van de Voort et al., 2016). Most simulations agree that galaxies with halo masses above $\gtrsim 10^{12}$ $M_\odot$ should form massive hot halos and require some form of feedback (either stellar or AGN) to produce observed stellar masses. The main discrepancies exist for galaxies like the Milky Way, where it is unclear what drives the global hot gas structure, how much hot gas mass should exist, and which is the dominant feedback mechanism. These are important questions that can be answered by building a complete picture for hot gas in galaxies like the Milky Way.

1.2 Observations Probing Hot Gas in the Milky Way

The Milky Way is a unique laboratory for analyses on $\sim 10^6$ K gas structure due to our vantage point inside the Galaxy. The Sun's proximity from the Galactic center ($R_\odot = 8.5$ kpc) implies observational signatures of a Galactic corona should vary across the sky. The hot gas is likely in collisional ionization equilibrium since the cooling time is $\sim$10 times longer than the recombination time, and the resultant spectral energy distribution peaks at $kT \approx 0.2$ keV (e.g., Foster et al., 2012). This implies soft X-ray observations are the most direct hot gas diagnostics. Indeed, all-sky X-ray and gamma-ray intensity maps combined with X-ray spectroscopic observations over

the past ∼20 years have produced a wealth of information on the Milky Way's hot gas distribution. However, the perspective within the disk permits different interpretations for these observations, and this leads to significantly different inferences for the Milky Way's hot gas structure. I discuss the most important observations below, and summarize how different analyses lead to different conclusions.

1.2.1 X-ray Observations

The *ROSAT All-Sky Survey* provided the most complete observational evidence for a Galactic-scale hot gas distribution, as it mapped the entire sky in soft X-rays (Snowden et al., 1997). Figure 1.1 shows these maps in the three energy bands: 1/4 keV, 3/4 keV, and 1.5 keV. The anticorrelation between the 1/4 keV and 3/4 keV bands is primarily due to neutral H I absorption in the disk, where the X-ray photoabsorption cross section from hydrogen and helium rapidly changes with energy (Balucinska-Church & McCammon, 1992; Yan et al., 1998). The emission variation between these two bands provided initial evidence that multiple plasma components comprise the soft X-ray background (SXRB; Kuntz & Snowden, 2000). The emergent picture is that a "local" emission source within ≈300 pc of the Sun dominates the 1/4 keV band emission and an "extended" emission source $\gtrsim 5$ kpc from the Sun dominates the 3/4 keV band emission. The "local" emission includes contributions from a supernova remnant surrounding the Sun known as the Local Bubble (LB) and time-varying, non-thermal solar wind charge exchange reactions (SWCX; e.g., Kuntz & Snowden, 2000; Welsh & Shelton, 2009; Galeazzi et al., 2014). The "extended" plasma is difficult to interpret from the *ROSAT* maps, but the bandpass sensitivity implies the plasma temperature is $T \approx 2 \times 10^6$ K. The emission is systematically stronger across the Galactic center compared to the Galatic pole or anticenter, indicating the presence of a Galactic-scale hot gas distribution.

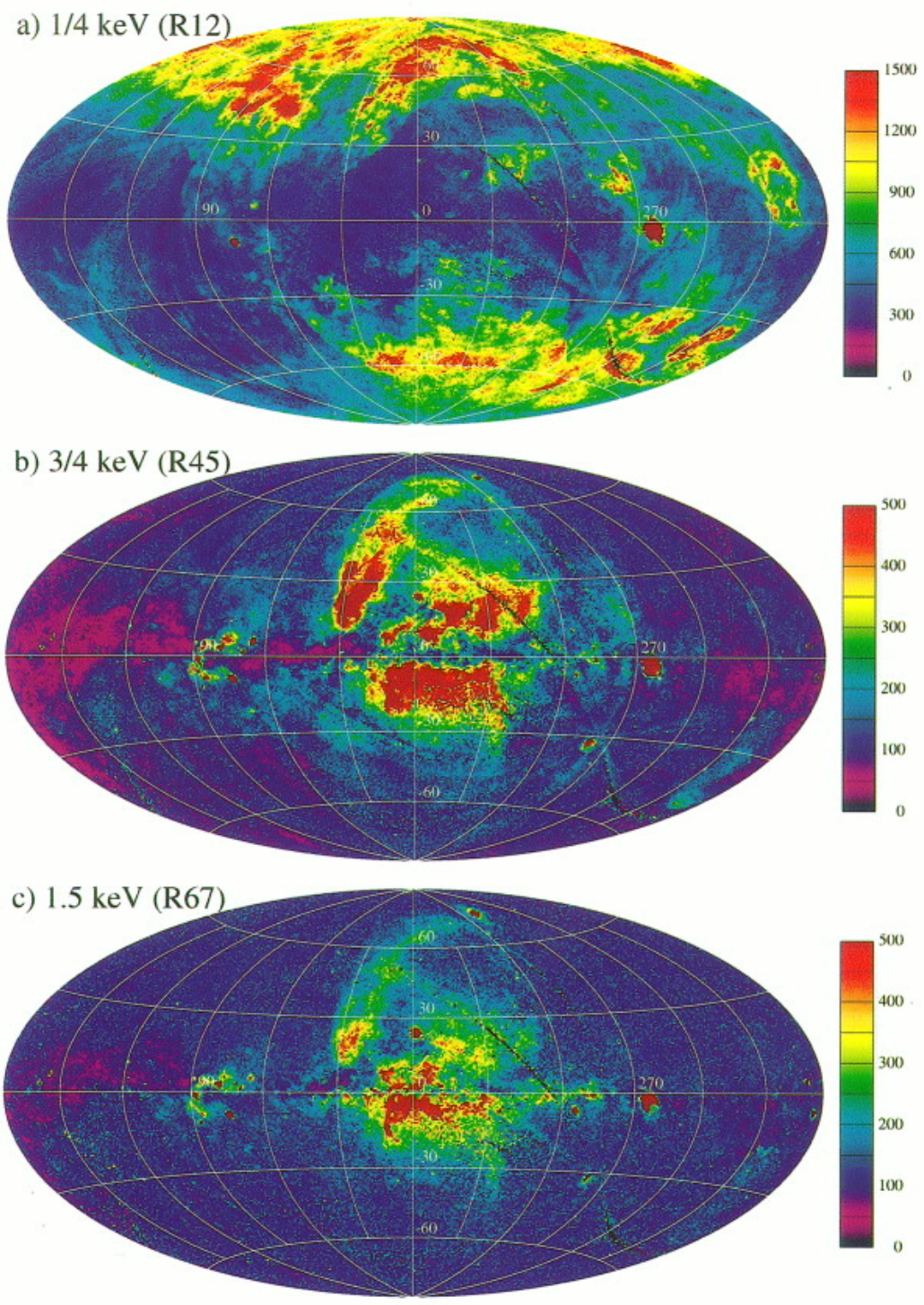

Figure 1.1: *ROSAT All-sky Survey* maps of the diffuse X-ray background (Snowden et al., 1997). From top to bottom, the maps include the 1/4 keV, 3/4 keV, and 1.5 keV bands. The 3/4 keV band map in the *middle* panel likely probes a volume-filling plasma on $\gtrsim$5 kpc scales.

More recent spectroscopic observations with *Chandra*, *XMM-Newton*, and *Suzaku* built on these constraints by measuring oxygen absorption and emission line strengths in individual sight lines. The expected lines for a $T \approx 2 \times 10^6$ K plasma are O VII at $E = 0.56$ keV ($\lambda = 21.60$ Å) and O VIII at $E = 0.65$ keV ($\lambda = 19.0$ Å), and these are observable with the CCDs or gratings on board current X-ray telescopes (Figure 1.2). One detects O VII $K\alpha$ absorption in grating spectra observations of bright AGNs or X-ray binaries (Nicastro et al., 2002; Paerels & Kahn, 2003; Rasmussen et al., 2003; Wang et al., 2005; Williams et al., 2005; Yao & Wang, 2005; Fang et al., 2006; Bregman & Lloyd-Davies, 2007; Yao & Wang, 2007; Hagihara et al., 2010; Gupta et al., 2012; Miller & Bregman, 2013; Fang & Jiang, 2014; Fang et al., 2015), while the emission lines are seen in blank-sky fields observed at CCD resolution (McCammon et al., 2002; Henley et al., 2010; Smith et al., 2007; Yoshino et al., 2009; Henley & Shelton, 2012).

These spectroscopic observations are an improvement over the *ROSAT* maps for several reasons. Resolving the separate O VII and O VIII line strengths a crucial advancement since the line strengths are a better temperature diagnostic compared to *ROSAT* bandpasses. The oxygen ion fractions and line emissivities peak at different temperatures, so the line strength ratio is sensitive to the plasma temperature between 10^6–10^7 K (Figure 1.2). The O VII absorption line detections also offer a complementary observable to previous emission-based observations, which suffer from photoabsorption in the disk. However, photoabsorption can be useful by conducting shadowing experiments toward nearby molecular clouds that are optically thick in X-rays. These observations measure the oxygen line emission for sight lines toward and adjacent to molecular clouds with known distances and confirm multiple sources contribute to the SXRB: one within ≈300 pc of the Sun and one extending beyond the Milky Way's disk (Galeazzi et al., 2007; Smith et al., 2007; Henley & Shelton, 2015).

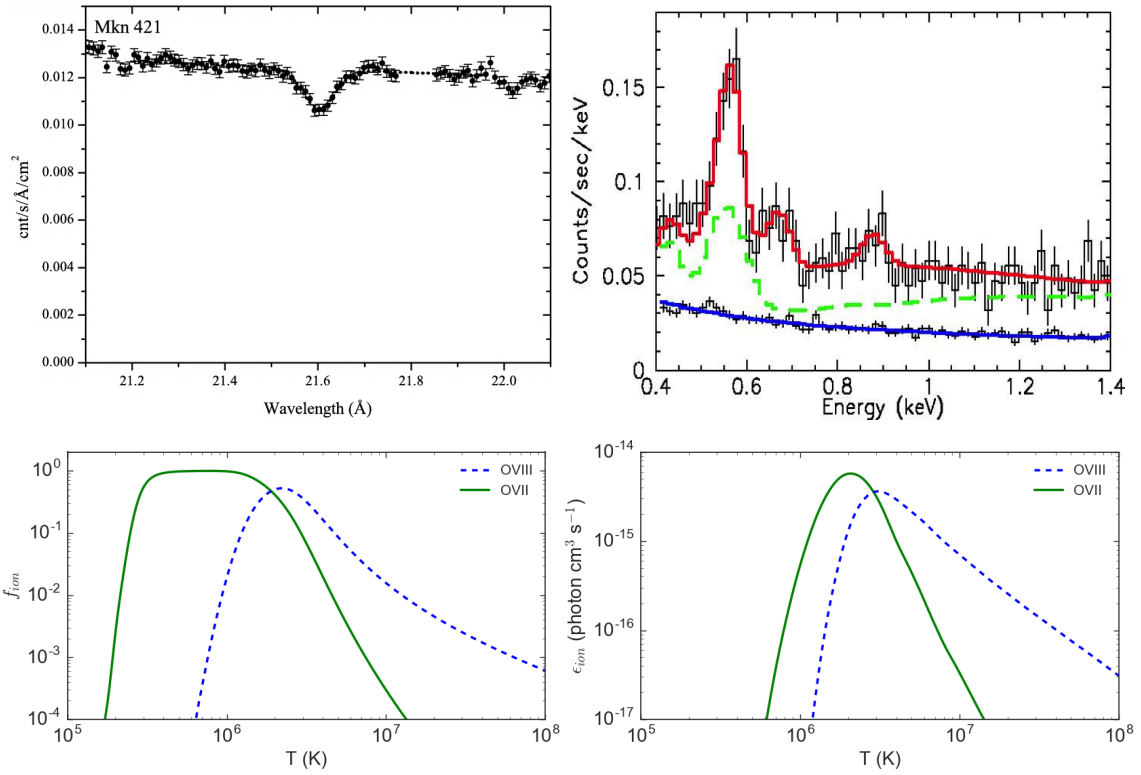

Figure 1.2: Oxygen absorption and emission line spectra with ion fractions and line emissivities. The absorption line spectrum toward Markarian 421 shows the O VII $K\alpha$ transition at λ =21.60 Å (*top left*; Bregman & Lloyd-Davies, 2007), while the blank-sky observation toward the molecular cloud MBM 12 shows the O VII and O VIII emission lines at 0.57 keV and 0.65 keV respectively (*top right*; Smith et al., 2007). The emission line spectrum includes two observations with multiple spectral components: the quiescent particle background is present in both observations (blue solid line), an on-cloud observation of MBM 12 (green dashed line), and an observation $\approx 3°$ away from MBM 12 (red solid line). The *bottom* panels show the oxygen ion fractions and volumetric line emissivities as functions of temperature, indicating these transitions trace gas at $\sim 10^6$ K (Sutherland & Dopita, 1993; Foster et al., 2012).

The measured line strengths motivate studies on the hot gas structure, but varying assumptions and small sample sizes produce significantly different interpretations for the "extended" hot plasma structure. Prior studies typically adopt the following methodology: the absorption line strength *or* emission line intensity is measured for a small sample of sight lines (1–20), a parametric hot gas density model is defined, and one finds the parameters that best reproduce the observed line strength(s). This methodology is problematic because it is not possible to rule-out significantly different models with a small number of sight lines. The observed line strengths in *individual* sight lines are reproduced by *either* an exponential disk-like morphology with scale height between 2–10 kpc and mass $\sim 10^8$ $M_\odot$ (Equation 1.3; Yao & Wang, 2007; Yao et al., 2009b; Hagihara et al., 2010), *or* a spherical profile extending to $\sim r_{vir}$ with mass between 10^{10}–10^{11} $M_\odot$ (Equation 1.4; Bregman & Lloyd-Davies, 2007; Gupta et al., 2012). These are the expected hot gas distributions to exist in the Milky Way, but small sample sizes cannot determine which structure dominates the observed absorption and emission.

The additional limiting factor is that most studies focus on either absorption *or* emission line strengths with minimal overlap between the two observables. Several analyses on ≈30 absorption line detections and $\lesssim$10 emission sight lines compare an average column density ($\propto nR_g$) to an average emission measure ($\propto n^2R_g$) to infer characteristic gas densities between 10^{-4}–10^{-3} cm^{-3} and a size scale of $R_g \gtrsim 20$ kpc (Bregman & Lloyd-Davies, 2007; Gupta et al., 2012). Alternatively, SXRB spectral fitting from ≈100 high-latitude sight lines confirms the extended plasma is nearly isothermal at $T \approx 2 \times 10^6$ K ($kT \approx 0.2$ keV), but the measured emission measures and oxygen line intensities vary on the sky by over an order of magnitude (Henley & Shelton, 2012, 2013). These measurements were not included in the absorption line-focused studies discussed above, yet the emission measure variation indicates an average emission measure may oversimplify the true emission structure. Thus, there

is not a consensus on whether any "extended" hot gas structure can reproduce *both* types of observations because no attempts have been made to self-consistently model the observed absorption *and* emission line signatures on the sky.

1.2.2 The Fermi Bubbles

The Fermi bubbles are two diffuse gamma-ray lobes extending to $|b| \sim 50^\circ$ ($|z| \sim$ 10 kpc for $R_\odot = 8.5$ kpc) away from the Galactic plane (Figure 1.3; Su et al., 2010). The gamma-rays have a flat intensity distribution on the sky, have an E^{-2} spectrum between 1–200 GeV, and coincide with diffuse microwave emission known as the *WMAP* haze (Dobler & Finkbeiner, 2008; Dobler et al., 2010; Ackermann et al., 2014). This suggests a scenario in which the bubbles are filled with cosmic rays that radiate inverse Compton emission in gamma-rays and synchrotron emission in microwaves, but the cosmic ray composition (leptonic electrons or hadronic protons) is still uncertain. Regardless, the presence of non-thermal emission combined with the bubbles' size and symmetry above and below the Galactic plane implies they formed from an energetic event in the Galactic center and are expanding into the Milky Way's ambient hot gas distribution.

Plausible bubble formation mechanisms include either an AGN event or a period of intense nuclear star formation. Nuclear star formation can drive galactic-scale winds with multiple type II supernova explosions, while black hole accretion events can inflate a hot cavity with thermal and non-thermal particles through a combination of winds or jets (e.g., Leitherer et al., 1999; Veilleux et al., 2005; McNamara & Nulsen, 2007; Yuan & Narayan, 2014). These are important events in the Milky Way's evolution, since their feedback effects on the rest of the Galaxy can be substantial (i.e., quenching star formation, heating the surrounding medium, displacing mass, etc.). The bubbles are an exciting laboratory for studying these feedback effects due to their size and location in the Galaxy. However, the bubbles' origins are still

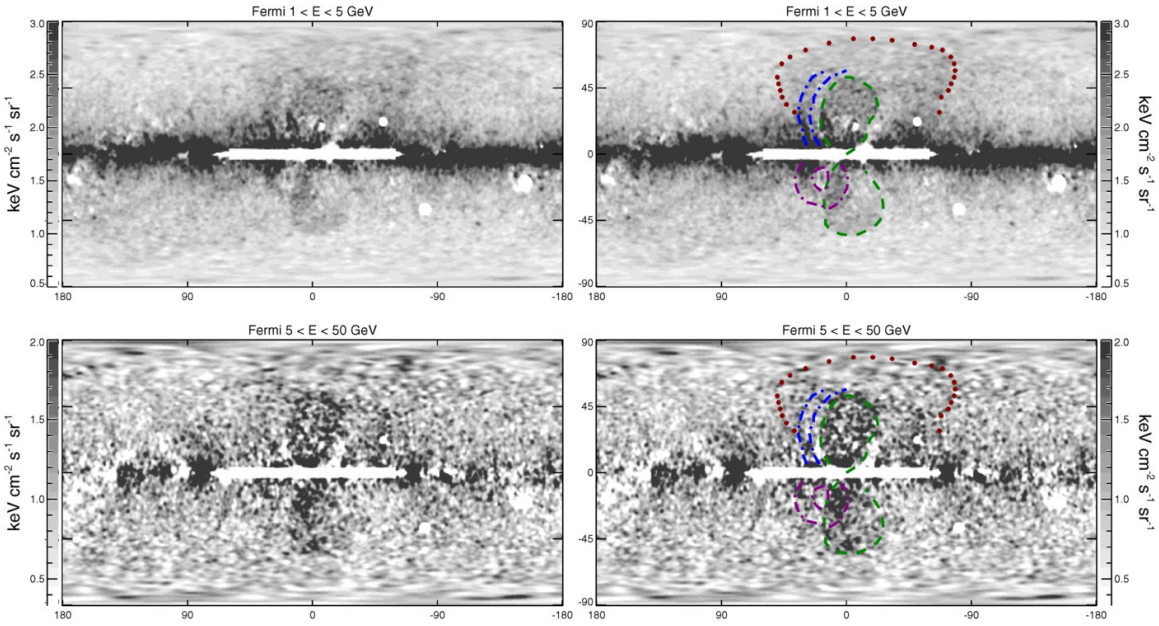

Figure 1.3: Foreground- and background-subtracted gamma-ray maps revealing the Fermi bubbles as diffuse gamma-ray lobes near the Galactic center (Su et al., 2010). The *top* panels show 1–5 GeV emission and the *bottom* panels show 5–50 GeV emission. The *right* panels outline several residual features, including the Fermi bubbles (green dashed lines), an arc feature seen in the northern hemisphere (blue dashed lines), the Loop I feature identified in radio emission (red dotted line; Haslam et al., 1982), and a spherical donut-like feature in the southern hemisphere (purple dashed lines).

uncertain since different bubble origin models with a wide range of energy injection rates and timescales can reproduce the bubbles' non-thermal properties. For example, magnetohydrodynamic (MHD) simulations of starburst- and AGN-driven outflows can reproduce the bubbles' non-thermal emission and morphology, with characteristic mechanical energy injection rates between 10^{39}–10^{44} erg s^{-1} and ages between 0.3 Myr to $\gtrsim$0.1 Gyr (Zubovas et al., 2011; Crocker, 2012; Zubovas & Nayakshin, 2012; Guo & Mathews, 2012; Guo et al., 2012; Yang et al., 2012, 2013; Crocker et al., 2014; Mou et al., 2014; Crocker et al., 2015; Mou et al., 2015; Sarkar et al., 2015). These unconstrained values complicate our interpretation of the bubbles as a source of feedback.

Measuring the bubbles' thermal gas structure and expansion speed into the surrounding medium constrains their age and energy content, since these properties directly relate to the bubbles' energy/pressure budget and kinematics. Simulations predict bubble expansion velocities greater than the ambient sound speed ($\approx$220 km s^{-1} for $T \approx 2 \times 10^6$ K), and a characteristic thermal gas morphology consisting of volume-filled and shell components. The former includes a combination of shock-heated wind material along with any entrained material in the outflow, while the latter includes shocked ambient hot gas halo material as the bubbles expand. This implies the gas temperature inside the bubbles and at the bubble-halo interface depend on the bubbles' expansion rate and energetics. Qualitatively, the *ROSAT* 1.5 keV map suggests this interaction exists as the bubbles appear to be bounded by enhanced X-ray emission (Bland-Hawthorn & Cohen, 2003; Su et al., 2010). Subsequent SXRB spectral fitting studies have attempted to improve these constraints from measurements near the bubbles' edges (Kataoka et al., 2013, 2015; Tahara et al., 2015). These studies measure systematically hotter plasma temperatures near the bubble edges compared to the surrounding medium (kT=0.3 keV compared to kT=0.2 keV), and infer a bubble expansion rate of $\approx$300 km s^{-1}. However, they do not account for

emission from the surrounding hot gas structure, and this leads to an *underestimated* bubble temperature and expansion velocity. Thus, soft X-rays constrain the bubbles' thermal gas structure and kinematics, but current results are based on incorrect assumptions.

1.3 Dissertation Overview

The goal of this dissertation is to constrain the Milky Way's hot gas structure using the most comprehensive samples of oxygen absorption and emission line strengths currently available. These line measurements are often byproducts of other science programs, so these samples primarily consist of archival data. The absorption lines are typically seen in high signal-to-noise grating spectra of bright AGN or X-ray binaries, and the number of detections has increased with growing exposure times for these objects. The emission lines are present in any CCD-resolution spectral observation, but most of these observations include point sources in the field of view that emit below 1 keV. True diffuse SXRB emission line detections require the spectral extraction regions exclude these point sources, and this is possible for a large number of archival observations. These different detection methods result in significantly different sample sizes for each observation. At the time of this work, the largest all-sky samples consist of ≈40 O VII $K\alpha$ absorption line detections (Bregman & Lloyd-Davies, 2007; Fang et al., 2015) and 1003 O VII and O VIII emission line detections with minimal SWCX emission (Henley & Shelton, 2012). These datasets are the primary observational diagnostics in this work.

The modeling methodology follows previous studies designed to constrain the Milky Way's hot gas structure, but the model constraints are a significant improvement over previous works due to several advancements. I model *all-sky* samples of oxygen absorption and emission lines in a self-consistent way. This is an improved approach because the characteristic model types (exponential disk or extended, spherical

halo) predict unique line strength variations on the sky. All-sky line strength samples are much more powerful diagnostics than individual sight lines since they encode this variation to distinguish between models. I also make the same parametric model assumptions (density, temperature, metallicity, etc.) when modeling absorption or emission line strengths, implying that the inferences gleaned from the absorption and emission lines are comparable. Finally, the models account for absorption or emission from all known sources (Local Bubble, extended hot gas distribution, Fermi bubbles), resulting in robust constraints on the *global* hot gas structure.

The results presented throughout this work address several topics related to the Milky Way's hot gas structure and formation. These include:

1. Does one hot gas model distribution reproduce the oxygen absorption *and* emission line measurements?

2. Is the Milky Way's global hot gas distribution a disk-like morphology contained within $\lesssim$5 kpc of the disk or a spherical morphology extending to $\sim r_{vir}$?

3. How much hot gas mass exists in the Milky Way, and does it account for the Milky Way's missing baryons?

4. Are there velocity flows in the Milky Way's hot gas distribution, and what are the observable signatures with current and future X-ray telescopes?

5. What is the Fermi bubbles' thermal gas density and temperature structure?

6. What is the Fermi bubbles' expansion rate, age, and energy injection rate based on the temperature structure?

7. Did the Fermi bubbles form from an AGN or starburst event?

I answer these questions using all-sky observation samples and consistent modeling techniques, which makes this dissertation the most comprehensive analysis on hot gas in the Milky Way.

The rest of the dissertation is outlined as follows. Chapter II includes a modeling analysis of 29 O VII $K\alpha$ absorption line strengths. Chapter III is a similar analysis to Chapter II, except the data include 649 O VII and O VIII emission line measurements. Chapter IV and Chapter V are complementary analyses on hot gas velocity structure and their observable signatures in absorption line measurements. Chapter VI includes an emission line modeling analysis focused on the Fermi bubbles. Finally, Chapter VII summarizes these results as an updated picture for the Milky Way's hot gas distribution.

CHAPTER II

The Structure of the Milky Way's Hot Gas Halo

2.1 Preface

This chapter is adapted from work of the same title appearing in the Astrophysical Journal, Volume 770, 118 (Miller & Bregman, 2013), and is coauthored by Joel N. Bregman. My contributions include all of the modeling and analysis, while Joel N. Bregman contributed the absorption line measurements.

2.2 Abstract

The Milky Way's million degree gaseous halo contains a considerable amount of mass that, depending on its structural properties, can be a significant mass component. In order to analyze the structure of the Galactic halo, we use *XMM-Newton* Reflection Grating Spectrometer archival data and measure O VII Kα absorption line strengths toward 26 active galactic nuclei, LMC X-3, and two Galactic sources (4U 1820-30 and X1735-444). We assume a β-model as the underlying gas density profile and find best-fit parameters of $n_\circ = 0.46\ ^{+0.74}_{-0.35}$ cm^{-3}, $r_c = 0.35\ ^{+0.29}_{-0.27}$ kpc, and $\beta = 0.71\ ^{+0.13}_{-0.14}$. These parameters result in halo masses ranging between $M(18\text{ kpc}) = 7.5\ ^{+22.0}_{-4.6} \times 10^8\ M_\odot$ and $M(200\text{ kpc}) = 3.8\ ^{+6.0}_{-0.5} \times 10^{10}\ M_\odot$ assuming a gas metallicity of $Z = 0.3\ Z_\odot$, which are consistent with current theoretical and observational

work. The maximum baryon fraction from our halo model of $f_b = 0.07\ ^{+0.03}_{-0.01}$ is significantly smaller than the universal value of $f_b = 0.171$, implying the mass contained in the Galactic halo accounts for 10%–50% of the missing baryons in the Milky Way. We also discuss our model in the context of several Milky Way observables, including ram pressure stripping in dwarf spheroidal galaxies, the observed X-ray emission measure in the 0.5–2.0 keV band, the Milky Way's star formation rate, spatial and thermal properties of cooler gas ($\sim 10^5$ K), and the observed Fermi bubbles toward the Galactic center. Although the metallicity of the halo gas is a large uncertainty in our analysis, we place a lower limit on the halo gas between the Sun and the Large Magellanic Cloud (LMC). We find that $Z \gtrsim 0.2\ Z_\odot$ based on the pulsar dispersion measure toward the LMC.

2.3 Introduction

The detection of hot gas at zero redshift by *Chandra, XMM-Newton*, and *FUSE* implies there exists a reservoir of gas that potentially contains a significant amount of baryonic mass in the Milky Way. However, there have only been detections of this hot Galactic halo with little detailed analysis of its structural properties using multiple sight lines until this point. If the density profile of this halo was constrained, the mass could be calculated and compared to the other baryon mass components of the Milky Way in an attempt to account for some or all of the "missing baryons" in the local universe.

There has been extensive work in detecting and analyzing hot gaseous halos in galaxies other than the Milky Way as probes of galaxy formation and evolution. Detailed analyses of individual galaxies have revealed that other galaxies have considerable amounts of mass in their extended gaseous halos, but there is not enough to account for their missing baryons (Bregman & Houck, 1997; Li et al., 2008; Anderson & Bregman, 2010, 2011). In addition to detailed analyses of individual galaxies, there

have been numerous studies of the global properties of diffuse X-ray emission around galaxies (Li et al., 2008; O'Sullivan et al., 2003; Strickland et al., 2004; Tüllmann et al., 2006). These properties offer a foundation for comparing the Milky Way's gaseous halo to other galaxies.

The primary tracers of the Milky Way's hot gas halo are O VII and O VIII that exist in the 10^6–10^7 K range (Paerels & Kahn, 2003). These X-ray lines have primarily been observed in absorption of active galactic nuclei (AGNs) and blazar spectra (Nicastro et al., 2002; Rasmussen et al., 2003; Wang et al., 2005; Williams et al., 2005; Fang et al., 2006; Yao & Wang, 2007; Hagihara et al., 2010) as well as Galactic X-ray binary spectra (Yao & Wang, 2005; Hagihara et al., 2011) using *Chandra* and *XMM-Newton*. The lines have also been observed in emission with the Diffuse X-Ray Spectrometer by McCammon et al. (2002). In addition to this X-ray emitting/absorbing gas, O VI , the most common ion in $\sim 10^{5.5}$ K gas, has been extensively studied with *FUSE* (Sembach et al., 2003; Wakker et al., 2003; Fox et al., 2004). While the interaction between these gas phases is an area of interest, mass estimates from this cooler gas have not helped solve the missing baryon problem.

The structural properties of the Galactic halo have not been well constrained up until this point. The combination of O VII emission and absorption has constrained the temperature of the halo to be between $\log(T) = 6.1$–6.4, however these estimates come primarily from analyses of single lines of sight toward the highest signal-to-noise (S/N) targets (Wang et al., 2005; Yao & Wang, 2007; Hagihara et al., 2010). Attempts to constrain the density profile and thus the mass of the halo have been limited by the number of extragalactic lines of sight with high enough S/N (Bregman & Lloyd-Davies, 2007; Gupta et al., 2012) or by only using Galactic sources to constrain the density profile (Yao & Wang, 2005). If the halo extends past the disk of the galaxy, the density profile could only be constrained with multiple extragalactic sight lines.

Bregman & Lloyd-Davies (2007) studied O VII absorption lines using the Reflection

Grating Spectrometer (RGS) on *XMM-Newton* with the goal to determine if these zero redshift absorption lines were from gas associated with the Milky Way's halo or from a Local Group medium. This size discrepancy between these two scenarios is critical in terms of estimating the baryon mass of gas at this temperature. Their analysis indicated the equivalent widths of O VII lines are positively correlated with angle toward the Galactic center as opposed to M31 (toward the center of mass of the Local Group). This implies these lines originate in a gas reservoir confined to the Milky Way as opposed to the Local Group.

In this chapter, we expand upon Bregman & Lloyd-Davies (2007) by adding three additional targets to our sample (one AGN and two Galactic targets) as well as provide a more detailed analysis of the structure and global properties of the hot Galactic halo, specifically the density profile. We use O VII column densities along different sight lines throughout the Milky Way to determine the density profile of the hot Galactic halo. We then estimate the mass contained in the halo as well as compare our density profile with numerous observational constraints. The outline of the chapter is as follows. In Section 2.4, we present our object selection and data analysis. In Section 2.5, we discuss our model fitting procedure as well as the different models we consider. In Section 2.6, we examine the consistency of our model with previously established constraints as well as compare our hot Galactic halo to different phases of the interstellar medium (ISM).

2.4 Object Selection

Our initial target list was identical to that of Bregman & Lloyd-Davies (2007), which was constructed from the brightest AGNs in the *XMM-Newton* RGS archival data. In addition to finding sources with suitable X-ray fluxes at 21.6 Å, the goal was also to find sources with O VII equivalent width uncertainties less than 10 mÅ (for typical equivalent widths of about 20 mÅ). This resulted in a sample of 25 AGNs

plus an additional source in the Large Magellanic Cloud (LMC).

In addition to the original sample, we added an additional AGN (ESO 141-G055) and two Galactic low-mass X-ray binaries (LMXBs; 4U 1820-30, X1735-444) to our target list (Table 2.1). These added source spectra can be seen in Figure 2.1 while the distribution of our sources on the sky can be seen in Figure 2.2. The motivation for adding these sources is their proximity to the Galactic center. Two of the parameters of interest in our model fitting are sensitive to small galactocentric radii ($r \lesssim 2$ kpc), which would not be probed by the original sample (see Figure 2.2). The inclusion of these three sources allowed us to analyze the central region of the density profile better than the previous target list would have allowed. The additional targets also have small uncertainties in the measured equivalent widths ($\lesssim 25\%$) compared to the rest of the sample.

We are unable to distinguish between O VII halo gas absorption and intrinsic absorption for our Galactic targets due to the resolution of the RGS at 21.6 Å. However, the X-ray spectra of our two Galactic sources have been previously observed with no indication of intrinsic O VII absorption. There has been evidence for a photoionized wind from an accretion disk in 4U 1820-30 (Costantini et al., 2012). However this wind has only been detected in lower ionization states of oxygen (O V and O VI) and not in the O VII absorption lines used in this study. Yao & Wang (2005) also analyzed X-ray spectra for a sample of Galactic sources, including X1735-444, to constrain the structure of the local hot ISM. They examine the possibility that some of the unresolved O VII absorption may come from photoionized winds, thus contaminating absorption from halo gas. However, they conclude this scenario is unlikely since the calculated radii where the lines would be produced are larger than the measured binary separations in six out of seven targets. We assume throughout our model fitting procedure that the O VII lines are entirely due to the halo gas and not associated with our LMXB targets.

Table 2.1. Absorption Line Measurements

Number	Name	l (°)	b (°)	EW (mÅ)	Error (mÅ)	$N_{OVII,thin}$ (10^{15} cm^{-2})	Error (10^{15} cm^{-2})	$N_{model,thin}$ (10^{15} cm^{-2})	$N_{OVII,saturated}$ (10^{15} cm^{-2})	Error (10^{15} cm^{-2})	$N_{model,saturated}$ (10^{15} cm^{-2})
1	Mrk 421	179.83	65.03	11.8	0.8	4.12	2.53	4.62	5.36	3.61	4.54
2	PKS 2155-304	17.73	-52.24	13.7	1.9	4.79	2.60	7.55	6.56	4.06	8.97
3	3C 273	289.95	64.36	24.6	3.3	8.60	2.77	5.67	18.06	9.28	5.98
4	MCG-6-30-15	313.29	27.68	32.6	6.8	11.36	3.45	7.73	42.35	27.19	9.28
5	LMC X-3	273.57	-32.08	21.0	5.0	7.34	3.07	3.91	13.00	7.37	4.39
6	1 H 1426+428	77.49	64.90	11.6	4.1	4.04	2.90	5.52	5.21	3.99	5.78
7	Ark 564	92.14	-25.34	12.3	4.6	4.29	2.98	5.25	5.63	4.23	5.38
8	NGC 4051	148.88	70.09	24.6	3.1	8.59	2.74	4.80	18.02	9.18	4.77
9	NGC 3783	287.46	22.95	24.1	7.5	8.40	3.64	6.05	17.17	10.64	6.56
10	NGC 5548	31.96	70.50	7.0	6.8	2.43	3.45	6.07	2.79	6.06	6.59
11	Ark 120	201.69	-21.13	-6.0	5.5	-2.08	3.16	4.16	-2.34	5.11	3.94
12	PKS 0558-504	257.96	-28.57	21.7	7.8	7.58	3.70	4.97	13.83	8.86	5.00
13	Mrk 766	190.68	82.27	0.1	6.8	0.05	3.45	5.06	0.07	4.27	5.12
14	NGC 4593	297.48	57.40	23.4	8.5	8.16	3.88	5.96	16.10	10.46	6.42
15	3C 390.3	111.44	27.07	27.4	7.3	9.56	3.57	4.75	23.65	14.46	4.71
16	NGC 7469	83.10	-45.47	1.6	8.9	0.57	4.01	5.51	0.59	5.57	5.75
17	Mrk 509	35.97	-29.86	25.9	7.3	9.04	3.57	8.62	20.36	12.39	10.89
18	3C 120	190.37	-27.40	13.8	9.2	4.81	4.09	4.15	6.59	5.83	3.94
19	NGC 3516	133.24	42.40	22.0	13.4	7.66	5.30	4.52	14.12	11.38	4.40
20	Ton 1388	223.36	68.21	34.5	15.7	12.04	6.03	4.83	54.68	45.38	4.82
21	1H 0414+009	191.82	-33.16	-3.1	14.8	-1.07	5.73	4.20	-1.14	10.16	4.00
22	MR 2251-178	46.20	-61.33	39.8	19.6	13.90	7.28	6.25	119.63	108.60	6.86
23	IC 4329a	317.50	30.92	33.8	19.3	11.78	7.20	7.93	49.41	43.14	9.65
24	Fairall 9	295.07	-57.83	31.1	16.4	10.84	6.27	5.89	35.30	29.08	6.31
25	MS 0737.9+7441	140.27	29.57	-13.8	20.7	-4.83	7.65	4.34	-6.65	6.57	4.18
26	3C 59	142.04	-30.54	60.9	19.2	21.24	7.15	4.33	2599.11	2463.75	4.16
27	ESO 141-G055	338.18	-26.71	21.4	5.3	7.48	3.12	10.75	13.48	7.69	15.06
28	4U 1820-30	2.79	-7.91	23.9	3.6	8.36	2.81	7.98	16.94	8.79	18.54
29	X1735-444	346.05	-6.99	24.7	9.7	8.61	4.23	5.02	18.15	12.32	9.98

Note. — Our sample consists of 26 AGN, two Galactic sources and one LMC source. The targets are listed in order of decreasing S/N with the exception of 27–29. These three targets are additions to the sample used by Bregman & Lloyd-Davies (2007). ESO 141-G055 is an AGN while 4U 1820-30 (located in the globular cluster NGC 6624) and X1735-444 are Galactic X-ray sources. All targets are used in our model fitting and analysis. The *thin* and *saturated* subscripts refer to column density conversions assuming the lines are optically thin or saturated assuming a constant Doppler width of 150 km s^{-1}. The *model* subscripts refer to the column densities along each line of sight resulting from the best-fit parameters found in Table 2.2.

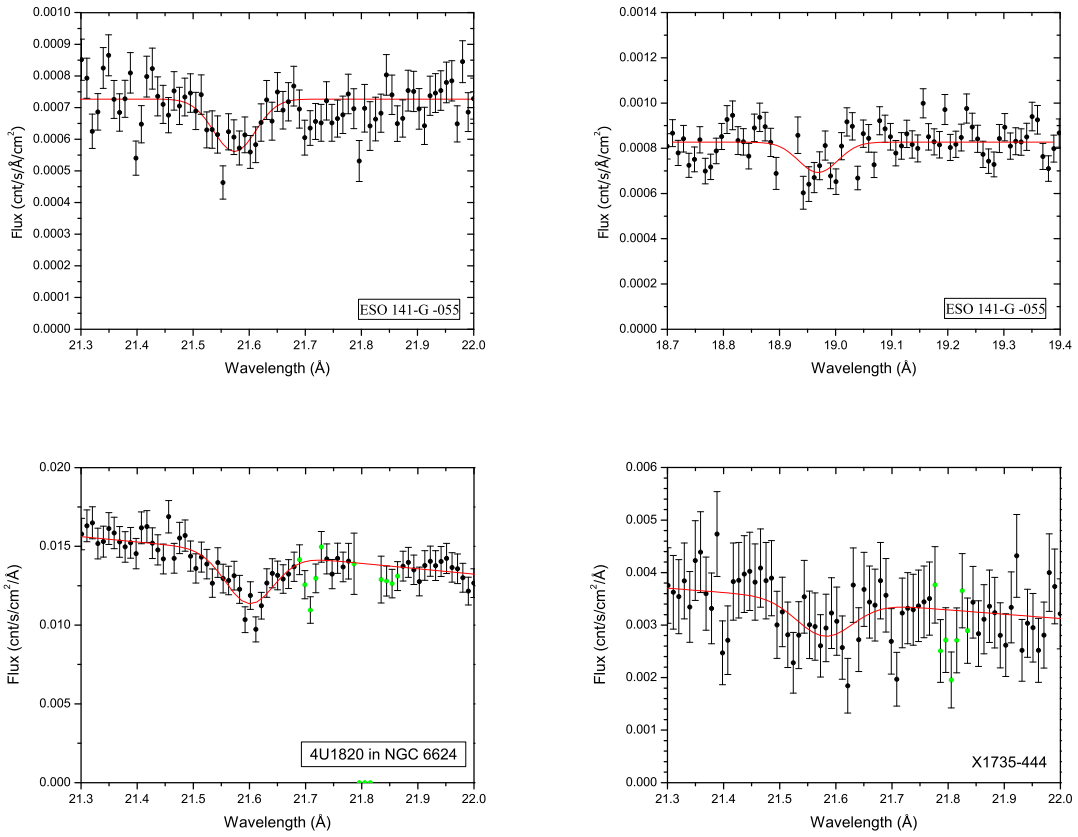

Figure 2.1: *XMM-Newton* flux of our additional targets at 21.60 Å (and 18.97 Å for ESO 141-G055) to show O VII and O VIII absorption. The continuum and line fitting procedure is the same used by Bregman & Lloyd-Davies (2007). There are instrumental features in the RGS near 21.82 Å and 18.91 Å (green points) that are not included in the continuum fitting procedure.

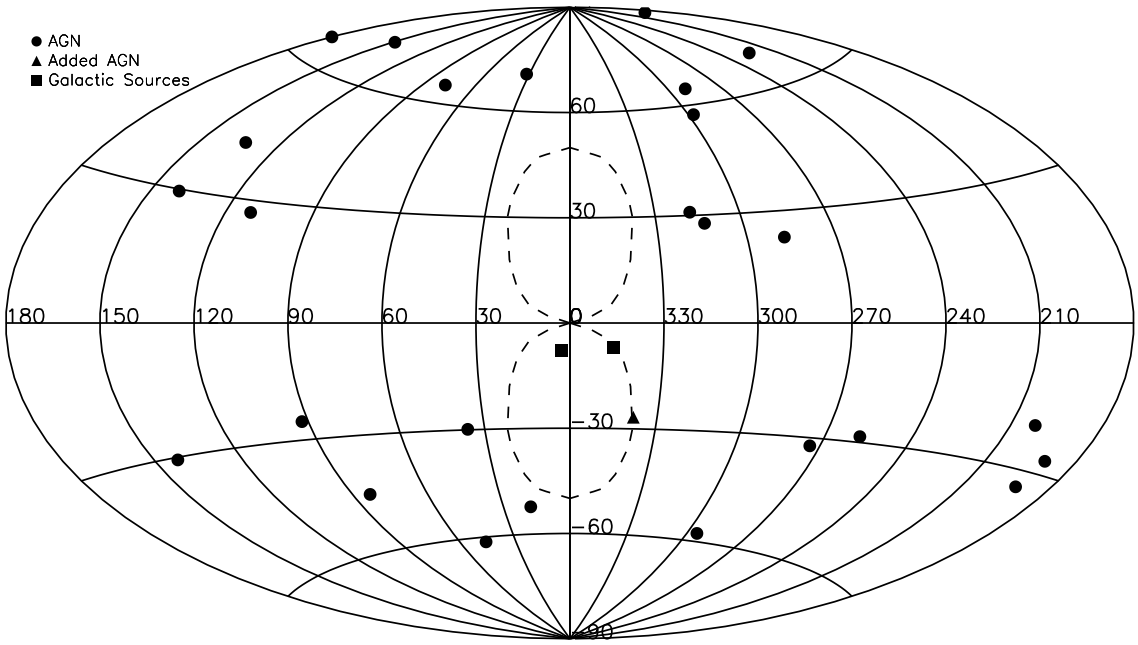

Figure 2.2: Distribution of our X-ray absorbing lines of sight on the sky. The sample from Bregman & Lloyd-Davies (2007) can be seen with solid circles while our additional targets can be seen as squares (Galactic sources) and a triangle (AGN). The dashed line represents the approximate edges of the north and south Fermi bubbles. The lines of sight of the three added targets pass through the south bubble and allow us to analyze the bubbles' density and temperature structure.

The data reduction and data analysis for our sample was identical to that of Bregman & Lloyd-Davies (2007) since this work is an extension of their results. Thus, we refer the reader to the aforementioned paper for any details concerning the data acquisition, methods of fitting the spectra, or determining equivalent widths.

2.5 Model Fitting

Our model fitting procedure focuses on the comparison between measured electron column densities of our targets and theoretical column densities calculated by our model density profile. We consider both spherical and flattened density models in

our model fitting procedure. The spherical profile is the simplest model we consider in the fitting process while the flattened profile adds one additional free parameter to account for the potential disk-like shape of the gas distribution. The coordinate transformations from a galactocentric density profile to a Sun-centered line of sight distance profile are:

$$R^2 = R_o^2 + d^2\cos(b)^2 - 2dR_o\cos(b)\cos(l), \tag{2.1}$$

$$z^2 = d^2\sin(b)^2, \tag{2.2}$$

$$r^2 = R^2 + z^2. \tag{2.3}$$

In these coordinates, d is the line of sight distance, b and l are Galactic latitude and longitude, respectively, R_o is the distance from the Sun to the Galactic center (we assume 8.5 kpc throughout our analysis), and r is the galactocentric radius. We constrain the density profile of the halo by generating model column densities for a given set of model parameters and finding the parameter set that minimizes the χ^2 calculated from our data.

2.5.1 Column Density Calculation

In order to convert from measured O VII equivalent widths to total electron column densities, we follow several assumptions presented in Bregman & Lloyd-Davies (2007). We initially convert the equivalent widths to column densities assuming the lines are optically thin. In this case, the resulting linear conversion between the measured equivalent width and O VII column density is $N(\mathrm{O\,VII}) = 3.48 \times 10^{14}$ EW, where EW is the O VII equivalent width in mÅ and the column density has units of cm^{-2}. However, recent work has shown the lines are likely mildly saturated based on

the observed Kβ to Kα ratio for the O VII ion (Williams et al., 2005; Gupta et al., 2012). To analyze the saturation effects in our lines, we make assumptions on the Doppler widths of the lines since the lines are not resolved by the RGS. We expect the gas to be turbulent from supernovae mixing and subject to turbulent mixing layers between the hotter and cooler phases of halo gas (Begelman & Fabian, 1990; Kwak & Shelton, 2010). Thus, we assume the gas is turbulent at the sound speed of hydrogen, which is consistent with simulations of halo gas (Fukugita & Peebles, 2006; Cen, 2012). This results in an assumed Doppler width of $b \approx 150$ km s^{-1}. For a typical equivalent width in our sample (≈ 20 mÅ) the optical depth at line center is of order unity, implying minor saturation corrections for our lines. To account for this, we initially calculate column densities linearly from our measured equivalent widths and determine correction factors using the curve of growth and assuming a Doppler width associated with turbulent motions discussed above. We use both sets of column densities to calculate best-fit parameters for our halo model due to the uncertainty in the Doppler widths of the lines and to examine how our best-fit parameters change after accounting for line saturation (see Section 2.6.4). However, we use the model fitting results from the saturated column densities in our analysis since the lines are expected to be minorly saturated. Both sets of column densities can be found in Table 2.1.

We make several assumptions while converting between O VII and total electron column densities. We assume that the abundance of oxygen is similar to the solar value and thus adopt a value of $\log(A_O) = 8.74$ (Holweger, 2001). This results in a total electron column of:

$$N_e = 4.4 \times 10^{19} \left(\frac{N_{\rm O\ VII}}{10^{16}\ {\rm cm}^{-2}}\right) \left(\frac{f}{0.5}\right)^{-1} \left(\frac{Z}{Z_\odot}\right)^{-1}\ {\rm cm}^{-2}, \tag{2.4}$$

where f is the ion fraction of O VII and Z is the metallicity of the gas. We assume an ion fraction of 0.5 for O VII , which is constrained by the temperature of the gas. We

note that while we do assume a solar gas metallicity initially, the metallicity of the halo gas is a significant uncertainty in our analysis. We expect a portion of the halo to be enriched due to feedback from the Milky Way disk, but the true metallicity is likely less than the solar value. We discuss the implications of this assumption throughout our analysis.

2.5.2 Spherical Model

The simplest model we consider in our analysis is the β-model. We choose this model as opposed to a simpler model (such as a uniform density sphere) because it reproduces the observed X-ray surface brightness profiles of other galaxies (Li et al., 2008; O'Sullivan et al., 2003). The β-model consists of three parameters and is defined as:

$$n(r) = n_o(1 + (r/r_c)^2)^{-3\beta/2}. \tag{2.5}$$

In this model, $n_\circ$ is the core density, r_c is the core radius, and β is the slope of the profile at large radii. The parameters $n_\circ$ and r_c describe the density near the center of the profile since $n_\circ$ is the density at $r = 0$ and typical values for r_c are $\lesssim 1$ kpc. These parameters are of little importance for the mass estimates of the halo gas since majority of the mass comes from material at large radii. On the other hand, β defines the behavior of the density profile at $r > r_c$ and is thus the primary parameter of interest.

Our best-fit parameters can be seen in Table 2.2 while the O VII column densities resulting from our best-fit models can be seen in Table 2.1. We also show how our observed saturated column densities compare with our best-fit model column densities in Figure 2.3. Initially, the best-fit model results in a χ^2 that is unacceptably large in both the optically thin and saturated column density conversions (χ^2_{thin}(dof) = 85.2 (26), $\chi^2_{saturated}$(dof) = 56.3 (26)), which is possible if the variation due to

Table 2.2. Absorption Line Model Fitting Results

Model	n_o (cm^{-3})	r_c / R_c, z_c (kpc)	β	$n_o r_c^{3\beta}$ (cm^{-3} $\mathrm{kpc}^{3\beta}$)	χ^2 (dof)
Spherical—optically thin [a]	$0.09^{+0.14}_{-0.06}$	$0.33^{+0.25}_{-0.23}$	$0.56^{+0.10}_{-0.12}$	$0.013^{+0.016}_{-0.010}$	31.0 (26)
Spherical—saturated [b]	$0.46^{+0.74}_{-0.35}$	$0.35^{+0.29}_{-0.27}$	$0.71^{+0.13}_{-0.14}$	$0.049^{+0.341}_{-0.047}$	26.0 (26)
Approximated [c]	–	–	$0.71^{+0.17}_{-0.20}$	$0.048^{+0.085}_{-0.037}$	26.0 (27)
Flattened [d]	$0.46^{+0.74}_{-0.35}$	$0.42^{+0.16}_{-0.10}, 0.26^{+0.13}_{-0.09}$	$0.71^{+0.13}_{-0.14}$	–	29.4 (25)
Truncated sample [e]	$0.48^{+0.71}_{-0.43}$	$0.33^{+0.25}_{-0.23}$	$0.70^{+0.14}_{-0.14}$	$0.046^{+0.255}_{-0.045}$	26.0 (26)
S/N cut sample [f]	$0.51^{+0.72}_{-0.46}$	$0.20^{+0.18}_{-0.17}$	$0.60^{+0.12}_{-0.13}$	$0.028^{+0.124}_{-0.027}$	20.0 (20)

[a]Results assuming the absorption lines are optically thin and a spherical density profile described by Equation 2.5.

[b]Results assuming the absorption lines are saturated with a Doppler width of 150 km s^{-1} and a spherical density profile described by Equation 2.5.

[c]Results assuming an approximated spherical density profile described by Equation 2.6.

[d]Results assuming a flattened density profile described by Equation 2.7.

[e]Same model as the spherical—saturated case, but with negative equivalent width measurements truncated at 0.

[f]Same model as the spherical—saturated case, but while only analyzing observations in our sample with S/N greater than 1.1.

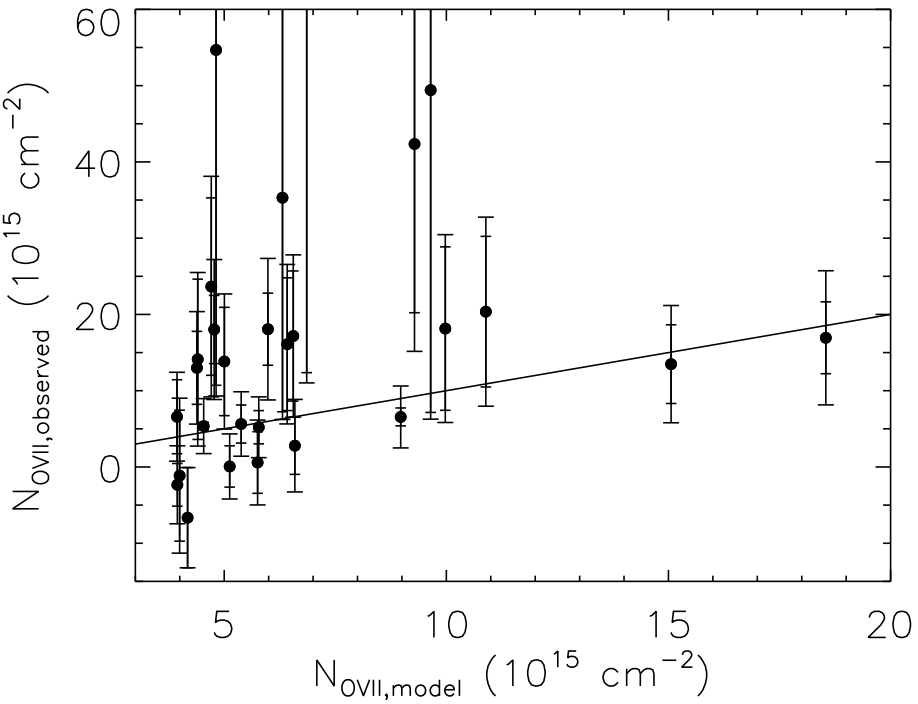

Figure 2.3: Comparison between our observed O VII column densities and best-fit model column densities in the saturated line case. The solid line indicates where the observed column density equals the model column density. The larger errors with larger tick marks for each point represent the initial error with the additional 7.2 mÅ added to each target in order to obtain an acceptable χ^2. For clarity, the targets MR 2251-178 and 3C 59 are not visible on the plot due to their large observed equivalent widths. However these lines of sight also have very large uncertainties and are both within 2σ of their model column densities.

substructure of the absorbing medium is larger than the statistical uncertainty of the equivalent widths. In order to account for this intrinsic variation, we add an additional uncertainty to all the equivalent widths of 7.5 mÅ for the optically thin column density conversion and 7.2 mÅ in the saturated case ($\sim$30% of the average equivalent width). We also examine the variation in our calculated χ^2 to place a constraint on the halo size. Initially, we assume a halo size of 200 kpc when determining our best-fit parameters. By changing the size of the halo after we find our best-fit parameters,

we can determine how the halo size changes the minimum χ^2 until our fit becomes unacceptable. We find a halo size 32 kpc at the 95% confidence level and 18 kpc at the 99% confidence level for both column density calculations.

The quality of the constraints on the halo parameters depends on both the quality of the data used as well as the location of our sources on the sky. The parameters $n_\circ$ and r_c are the least constrained primarily due to only three of our targets passing near the Galactic center. In particular, the two Galactic targets that come closest to the Galactic center are less than 8.5 kpc away and thus do not probe the full inner region of the halo. Note that this would not be the case if r_c were larger, implying a more extended profile. The fact that these two parameters are not well constrained results from a degeneracy between them which is most apparent in Figure 2.4. To account for this, we note that for $r_c \ll r$ Equation 2.5 can be approximated by the power law:

$$n(r) \approx \frac{n_o r_c^{3\beta}}{r^{3\beta}}. \tag{2.6}$$

This reduces the dimensionality of the problem by making the free parameters a constant ($n_o r_c^{3\beta}$) and β. We expect the constraints on these parameters to be more reliable than the three parameter model due to the few lines of sight near the Galactic center. The 1σ, 2σ, and 3σ contours for all of our parameter spaces can be seen in Figure 2.4, considering the three and two parameter spherical models and using saturated column densities. We note little difference in the quality of our constraints between the three and two parameter spherical models. Fortunately, the parameter β is relatively well constrained for both models due to the majority of our sample being extragalactic targets.

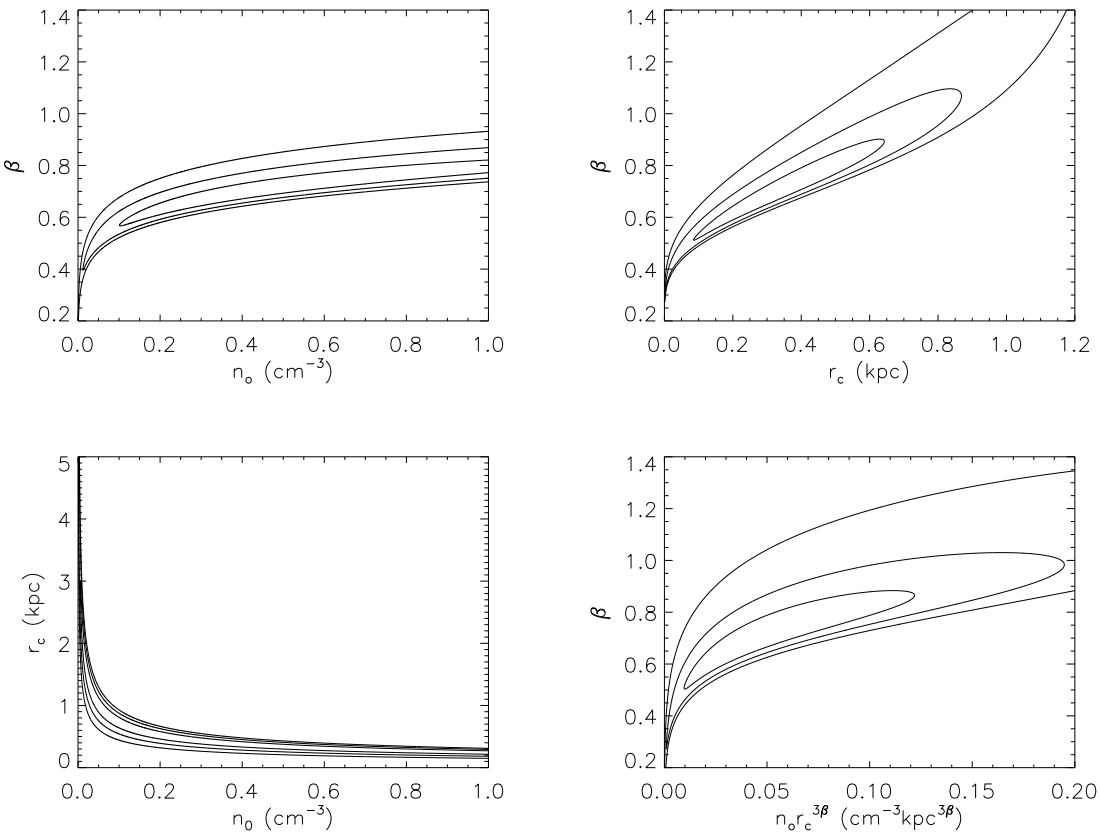

Figure 2.4: 1σ, 2σ, and 3σ contours for r_c, n_o, β, and $n_o r_c^{3\beta}$ for our spherical model and using saturated column densities assuming $b = 150$ km s^{-1}. The elongation of the contours in the r_c–n_o plane illustrates the degeneracy discussed in Section 2.5.2. The contours constraining $n_o r_c^{3\beta}$ are based on the parameters in Equation 2.6.

2.5.3 Flattened Model

We also consider a flattened model in our fitting process by modifying the spherical β-model. The motivation behind considering a flattened density profile is based on the angular momentum associated with the Milky Way. The rotation of dark matter and baryons in the Milky Way could potentially alter a spherical gas profile into a flattened profile. We modify the traditional β-model in the following way:

$$n(r) = n_o(1 + (R/R_c)^2 + (z/z_c)^2)^{-3\beta/2}. \tag{2.7}$$

In this flattened model, R is the radius in the plane of the disk and z is the height off of the Galactic plane with R_c and z_c representing the effective core radii for each coordinate. The parameters R_c and z_c are thus measures of density profile flattening. For this portion of our model fitting procedure, we fix the central density and slope of the density profile to their best-fit values associated with the spherical model and saturated column densities. Thus, we consider a flattened model only to see how the core radii associated with the orthogonal coordinates R and z change from a single, spherical core radius.

The best-fit parameters for our flattened model can be seen in Table 2.2. The flattened model initially has the same issue as the spherical model in that the best-fit parameters result in a χ^2 that is unacceptably large. Thus, we adopt the same procedure applied to the spherical model and add an additional uncertainty to the equivalent widths along each line of sight. We find that we must add the same additional uncertainty as the spherical case, 7.2 mÅ, to the equivalent widths to obtain an acceptable χ^2. After accounting for this additional uncertainty, the best-fit parameters still result in core radii of less than 1 kpc and an axial ratio of $\sim$3/2. The 1σ, 2σ, and 3σ contours for the core radii parameters can be seen in Figure 2.5 and indicate that profile is preferentially elongated in the R direction. However, the χ^2 change is small between the spherical and flattened models. This implies that the flattened and spherical models are equivalent in describing the density profile of the halo. Thus, we assume the density profile is spherical for the rest of our analysis for simplicity.

2.5.4 Negative Column Densities

Our sample contains three negative equivalent width measurements with corresponding negative column density conversions (see Table 2.1), which are possible if the S/N (the ratio between the measured equivalent width and corresponding uncer-

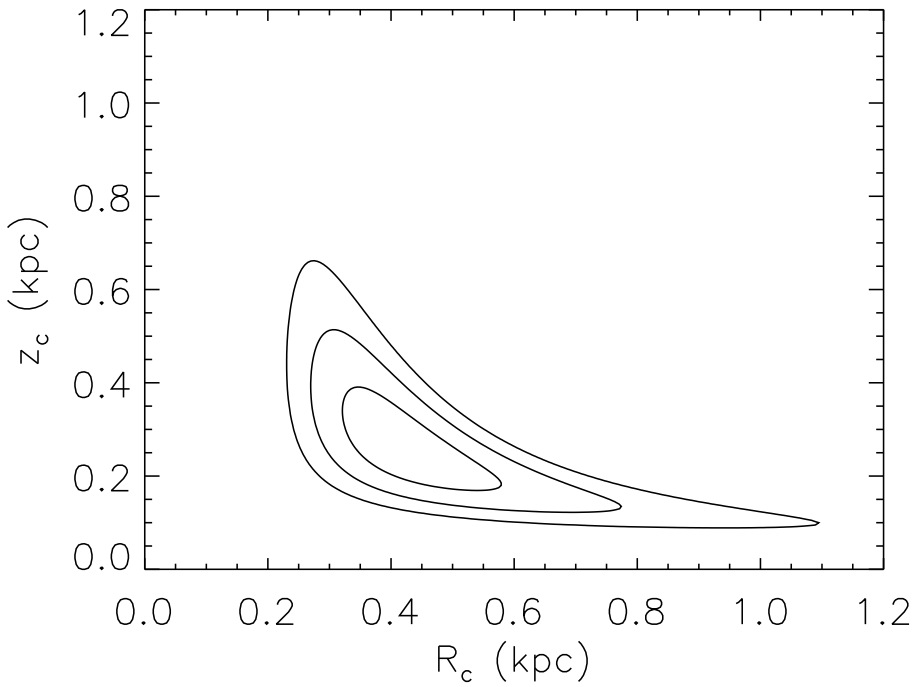

Figure 2.5: 1σ, 2σ, and 3σ contours for R_c and z_c for our flattened model. R_c corresponds to the core radius in the disk of the Milky Way and z_c corresponds to the core radius out of the plane of the Milky Way. The shape of the contours indicates that the halo is preferentially aligned with the disk of the Milky Way.

tainty) is not sufficiently high for the observations. Although negative columns are not physical, we emphasize our measurements are all consistent with positive values based on their 1σ uncertainties and our model fitting procedure is sensitive to the difference between the measured and model column densities and the uncertainties associated with our measurements. Furthermore, the negative equivalent width measurements are not heavily weighted in our model fitting procedure due to their large uncertainties. We explore the effects of negative equivalent width measurements on our model fitting procedure by truncating the negative measurements at zero and refitting the data assuming the same spherical model and saturation effects discussed above. The best-fit parameters for our sample with these truncated values are nearly

identical to our results from our original sample. Alternatively, we apply a S/N cut to our sample to remove the negative equivalent width measurements from our model fitting procedure and determine how our results change. We choose a S/N threshold of 1.1, which removes the three negative equivalent width measurements as well as three positive measurements. The model fitting results from these two altered samples can be seen in Table 2.2. The best-fit parameters from these samples are consistent with our initial model fitting results based on their 1σ uncertainties. In particular, the parameter β is nearly identical between our initial and truncated sample results and shows a 16% variation between the initial and S/N cut sample results. It should be noted that both of these alterations to our sample impose a slight bias to our results toward the higher S/N observations, which may be due to strong absorption features or simply low noise measurements. However, our model fitting results are not strongly dependent to these changes due to the weak weighting of the low S/N measurements in our initial model fitting procedure. We therefore use the negative equivalent width measurements with uncertainties in our analysis, as opposed to truncating the values to zero or limiting our sample based on S/N, to retain the most information from the data.

We examine the validity of this model fitting approach by running Monte Carlo simulations to determine if we could recover our best-fit model parameters with the inclusion of negative column densities in our sample. For each line of sight, we assume the column density is normally distributed around its best-fit model value with σ defined by the measured uncertainty. Assuming these underlying normal distributions, we deviate the column densities from their best-fit model values and find new best-fit parameters for the deviated data. Figure 2.6 shows histograms of best-fit parameters β and $n_o r_c^{3\beta}$ from Equation 2.6 and the number of negative column densities in each simulation for 20,000 Monte Carlo simulations. Due to the large uncertainties for several of our column density measurements, our simulations

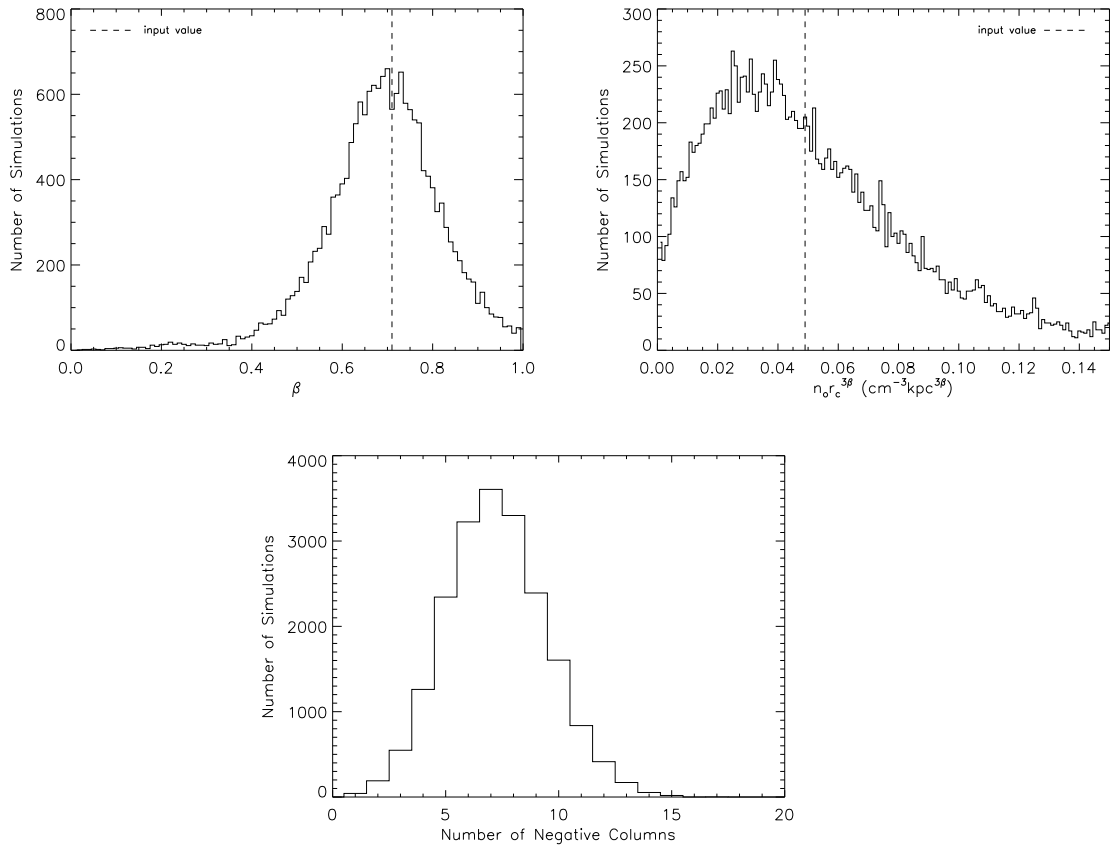

Figure 2.6: Histograms of best-fit parameters β and $n_o r_c^{3\beta}$ in addition to the number of negative column densities for 20,000 Monte Carlo simulations. Our input values for each parameter were our best-fit parameters from Table 2.2. We found median values of 0.71 for β and 0.050 cm^{-3} kpc$^{3\beta}$ for $n_o r_c^{3\beta}$, which are consistent with the measured values of 0.71 and 0.048 cm^{-3} kpc$^{3\beta}$ (dashed lines). The distributions and medians for β, $n_o r_c^{3\beta}$, and other model parameters are consistent with our measured best-fit parameters and their 1σ uncertainties, implying we recover our best-fit model with negative column densities in our sample.

consistently deviate column densities to negative values (median value of 7). The median values of β and $n_o r_c^{3\beta}$ are 0.71 and 0.050 cm^{-3} kpc$^{3\beta}$, which are both consistent with our input values of 0.71 and 0.048 cm^{-3} kpc$^{3\beta}$ for β and $n_o r_c^{3\beta}$, respectively. Furthermore, the distributions of β and $n_o r_c^{3\beta}$ are consistent with the 1σ boundaries of their best-fit values (see Table 2.2). This implies we reproduce our model fitting results with negative column densities in our sample and thus motivates the inclusion of the negative column density measurements in our sample.

2.6 Summary and Discussion

2.6.1 Spatial Distribution of the Gas

There has been recent work on the structure of the Milky Way's hot gas halo utilizing the combination of emission ($\approx n_e^2 L$) and absorption ($\approx n_e L$) to constrain the density and size of the halo gas. While our model is more sophisticated than a uniform density halo, these results serve as a foundation for comparing our density profile results. Bregman & Lloyd-Davies (2007) initially used the same $XMM-Newton$ dataset as this paper without targets 27–29 (see Table 2.1) and found $n_e = 9 \times 10^{-4}$ cm^{-3}, $L = 19$ kpc. Alternatively, Gupta et al. (2012) conducted a similar analysis with eight *Chandra* targets and found $n_e = 2 \times 10^{-4}$ cm^{-3}, $L = 72$ kpc. Both of these results are more simplistic than our β-model and do not extend to the virial radius of the Milky Way. For comparison, we calculate the χ^2 for these models with our expanded dataset, while also including an additional uncertainty of 7.2 mÅ, and find $\chi^2(\mathrm{dof}) = 39.5\ (27)$ and $44.7\ (27)$. Both of these are larger than the χ^2 we find for our best-fit model, $\chi^2 = 26.0\ (26)$. Although the halo size is not a parameter in our model, our best-fit model is a statistical improvement over the uniform density models that have previously characterized the halo gas.

The best-fit parameters for our density model are also comparable to observations

of hot gas halos around other galaxies where structural analysis has been possible. When comparing the Milky Way's hot halo to that of other galaxies, the core radius and β parameters are the most applicable. The core density acts as a normalization of the overall profile and is physically not as significant as the other two parameters. Li et al. (2008); O'Sullivan et al. (2003) conducted a study of early-type galaxies and extrapolated hot gas density profiles from the observed X-ray surface brightness profiles. Their model fitting procedure resulted in β values between 0.4–0.8 and core radii of less than 1 kpc for majority of their sample, both consistent with our best-fit parameters. There has also been more detailed work on the individual early-type galaxy NGC 1600. Sivakoff et al. (2004) analyzed the diffuse gas around NGC 1600 and found a two-component model to fit the surface brightness profile with $r_{c,in} = 4.2$ kpc, $\beta_{in} = 1.18$, $r_{c,out} = 7.3$ kpc, $\beta_{out} = 0.36$. The fitting results of NGC 1600 are odd in that a double β profile is not typically required to fit the X-ray surface brightness profiles around galaxies, particularly with β values that are inconsistent with analyses of other galaxies. This may be attributed to NGC 1600 residing in a group environment rather than in isolation. Detailed structure analysis of hot gas halos around late-type galaxies has been limited to only the most massive spirals. Anderson & Bregman (2011) analyzed the hot gas halo around NGC 1961 ($M_{vir} = 2.1 \times 10^{13}\ M_{\odot}$) and found $\beta = 0.47$ and $r_c = 1.00$ kpc. Similarly, Dai et al. (2012) have analyzed the hot gas halo of UGC 12591 ($M_{vir} = 3.5 \times 10^{13}\ M_{\odot}$) and found $\beta = 0.48$ and $r_c = 3.04$ kpc. Our measured β of 0.71 is steeper than observations of these massive spirals and the measured core radii for the most massive spirals are larger than the core radius determined for the Milky Way. The discrepancy between these parameters may be explained by the larger stellar disks and dark matter halos associated with NGC 1961 and UGC 12591 compared to the Milky Way. The comparison between the core radii and β parameters is also limited due to the weak constraint we have on the Milky Way's core radius and the degeneracy

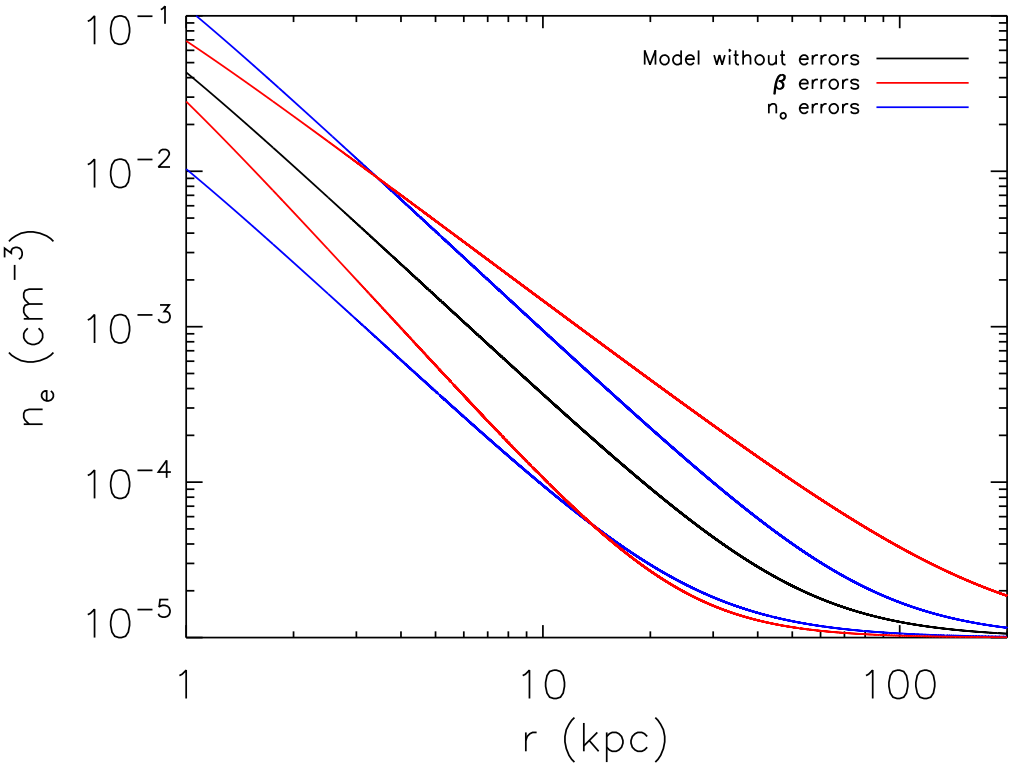

Figure 2.7: Density profile given our best-fit parameters (black line) with 1σ errors on β (red line) and n_o (blue line). The profile also includes an additional ambient medium of $n_e = 1{\times}10^{-5}$ cm^{-3} to account for observed ram-pressure stripping of dwarf spheroidal galaxies.

between the core radius and core density.

The best-fit parameters from our model fitting procedure result in a density profile that is consistent with previously established constraints. The density model with best-fit parameters can be seen in Figure 2.7. Based on analyzing the pulsar dispersion measure toward the LMC, the average electron density between the Sun and the LMC must be $\langle n_e \rangle \leq 5 \times 10^{-4}$ cm^{-3} (Anderson & Bregman, 2010). For our density profile, the best-fit parameters result in an average electron density of $\langle n_e \rangle = 1.2 \times 10^{-4}$ cm^{-3} between the Sun and the LMC assuming a solar metallicity. This is well below the upper limit established by the pulsar dispersion measure. The combination of

having an upper limit to the average electron density between the Sun and the LMC and the fact that the total electron column density scales with metallicity as $\propto Z^{-1}$ (Equation 2.4) allows us to place a lower limit on the metallicity of the gas toward the LMC. We find a minimum metallicity of $Z \gtrsim 0.2\ Z_{\odot}$ in order to satisfy the pulsar dispersion measure toward the LMC. This lower limit is consistent with the metallicities of some high velocity clouds (HVCs), particularly Complex C, and the Magellanic Stream (Gibson et al., 2000; van Woerden & Wakker, 2004; Fox et al., 2005), implying the halo gas metallicity may be predominantly sub-solar.

We also examine the possibility of this hot gas extending out to the Milky Way's virial radius, which would affect satellites of the Milky Way. There have been numerous studies investigating ram-pressure stripping of dwarf spheroidal galaxies orbiting the Milky Way, which implies the presence of a hot corona associated with the Milky Way out to ∼200 kpc (Blitz & Robishaw, 2000; Grcevich & Putman, 2009). Blitz & Robishaw (2000) found that dwarf spheroidal galaxies orbiting the Milky Way will effectively lose their cold gas due to ram-pressure stripping for an ambient halo with density of $n \geq 2.4 \times 10^{-5}$ cm^{-3} out to the virial radius of the Milky Way. Grcevich & Putman (2009) found a considerably larger value, 2.5×10^{-4} cm^{-3}, out to similar distances. Our best-fit model results in densities that are too low to satisfy either of these constraints. In order to account for this we add an ambient density to our model of $n = 1 \times 10^{-5}$ cm^{-3} out to 200 kpc. We choose a medium consistent with Blitz & Robishaw (2000) as opposed to Grcevich & Putman (2009) because an additional ambient medium as large as 2.5×10^{-4} cm^{-3} violates the observational constraint of the emission measure out of the Galactic plane, which will be discussed in greater detail in Section 2.6.2. We note that the addition of this density component does not change the best-fit parameters derived in our model fitting because the low ambient density does not contribute a significant fraction to the observed column densities. Thus, we can add this ambient medium to our density profile without jeopardizing

Table 2.3. Scale Heights

		R (kpc)				
		0	1	5	8.5	20
	1	0.5	1.0	12.2	34.4	187.8
	2	1.0	1.2	6.8	17.9	94.6
z (kpc)	3	1.4	1.6	5.3	12.7	63.8
	4	1.9	2.0	4.8	10.3	48.7
	5	2.3	2.4	4.7	9.1	39.8

the validity of our best-fit parameters.

We compare the scale height of our density model to the scale heights of different ions that represent different temperature phases of the ISM. The scale height is defined as:

$$h = \left| \frac{n}{dn/dz} \right| = \frac{r_c^2}{3\beta z} \left(1 + \frac{R^2 + z^2}{r_c^2} \right). \tag{2.8}$$

When evaluating the scale height for our density model, we note that the function for the scale height is dependent on both R and z for our spherical model. We calculate the scale height for our profile at several different R and z distances (Table 2.3). The applicable comparison is for $R = 8.5$ kpc values since previous studies of other ions are inherently observed at the solar circle. The Li-like ions with peak abundances at temperatures 3, 2 and 1 $\times$ 10^5 K are O VI , N V and C IV (Sutherland & Dopita, 1993). The scale heights of these ions have been measured to be h(O VI , $b > 0$) = 4.6, h(O VI , $b <0$) = 3.2, h(N V) = 3.9, and h(C IV) = 4.4 kpc (Savage et al., 1997; Bowen et al., 2008). The scale height(s) we determine for O VII gas at $T \sim 10^6$ K are larger than these cooler ions by about an order of magnitude. This is expected due to the difference in temperature between the ions being approximately an order of magnitude. Thus, the distribution of our density model is more extended than the 10^5 K gas, indicating they are not cospatial (Williams et al., 2005).

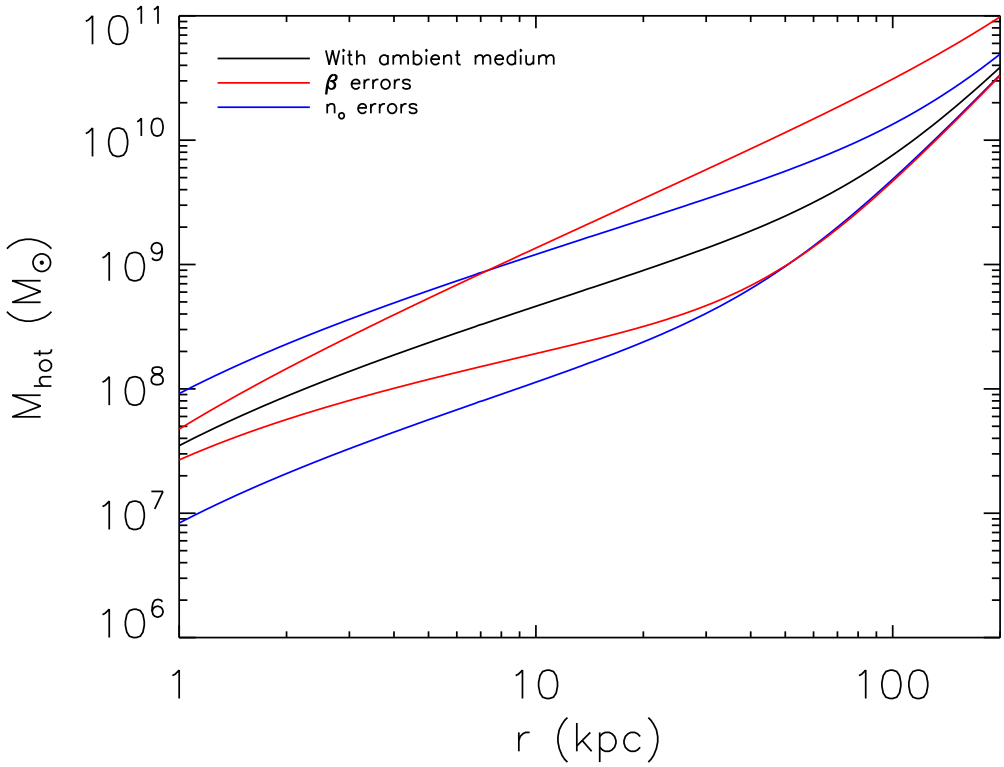

Figure 2.8: Enclosed mass as a function of radius with the same uncertainties as Figure 2.7. The enclosed mass of the halo is much smaller than the virial mass of the Milky Way and is only comparable to the stellar + cold gas mass of the Milky Way if the size is comparable to the virial radius of the Milky Way. The mass profile here is for solar metallicity gas.

2.6.2 Density and Mass Considerations

The primary goal for determining the density profile of the Milky Way's hot gas halo is to determine the amount of mass it contains. The best-fit parameters and size of the halo determine whether there is enough mass contained in this temperature gas to account for some or all of the missing baryons in the Milky Way. The mass profile corresponding to the best-fit density profile can be seen in Figure 2.8 assuming the gas has a solar metallicity. We consider the mass contained within 18 kpc and 200 kpc as limits on the minimum and maximum mass of the halo. The minimum halo size

is based on statistical arguments presented in Section 2.5.2 while we assume the halo extends to the Milky Way's virial radius for a maximum halo size. Given our best-fit parameters, we find $M(18\text{ kpc}) = 2.2\ ^{+6.7}_{-1.3} \times 10^8\ M_\odot$ and $M(200\text{ kpc}) = 1.2\ ^{+1.7}_{-0.2} \times 10^{10}\ M_\odot$. The mass contribution from the additional ambient medium discussed in Section 2.6.1 is substantial at 200 kpc ($\approx 7 \times 10^9\ M_\odot$), but generally consistent with the error bars on our mass estimates. The known baryonic mass in the Milky Way (stars + cold gas) is approximately $5 \times 10^{10}\ M_\odot$ (Binney & Tremaine, 2008). This implies stellar + cold gas to hot gas mass fractions of 230 (18 kpc) and 4 (200 kpc). We then compare the hot gas mass to the virial mass of the Milky Way ($\sim 2 \times 10^{12}\ M_\odot$) and define the baryon fraction as $f_b = M_b/M_{tot}$. The resulting baryon fractions are $f_b\ (18\text{ kpc}) = 0.02\ ^{+0.01}_{-0.01}$ and $f_b\ (200\text{ kpc}) = 0.03\ ^{+0.01}_{-0.01}$, both of which are much smaller than the value obtained from the *Wilkinson Microwave Anisotropy Probe* five-year data $f_b = 0.171 \pm 0.006$ (Dunkley et al., 2009).

There are several uncertainties in our analysis that can significantly change our mass estimate and corresponding baryon fraction. The virial mass of the Milky Way has been estimated to be between 1.0–2.4 $\times 10^{12}\ M_\odot$ (Boylan-Kolchin et al., 2013). If we consider the virial mass of the Milky Way to be $1 \times 10^{12}\ M_\odot$ as opposed to $2 \times 10^{12}\ M_\odot$, the missing baryon mass is $1.5 \times 10^{11}\ M_\odot$ as opposed to $3.6 \times 10^{11}\ M_\odot$. This also changes the virial radius of the Milky Way by about a factor of $\sim$0.8 ($r_{vir} \propto M_{vir}^{1/3}$). For a virial mass of $1 \times 10^{12}\ M_\odot$ and virial radius of 160 kpc, our best-fit model halo results in a hot gas mass and baryon fraction of $M(160\text{ kpc}) = 6.5\ ^{+13.2}_{-1.3} \times 10^9\ M_\odot$ and $f_b\ (160\text{ kpc}) = 0.05\ ^{+0.02}_{-0.00}$. In this case, the halo gas bound to the Milky Way accounts for 5%–15% of the missing baryons.

One possibility that increases the baryon fraction is halo gas extending beyond the Milky Way's virial radius, implying the gas is not bound to the Milky Way. Given our best-fit parameters and the range of virial masses discussed above, the halo would need to be between 400–600 kpc ($\sim 3r_{vir}$) to account for the missing baryons. We are

unable to rule out a halo this large since our results are insensitive to the low density gas that potentially exists at this radius. Other studies have explored the possibility of non-local O VII absorption by examining galaxies who have impact parameters within 2–3 virial radii of a given AGN line of sight (Fang et al., 2006; Anderson & Bregman, 2010). These nondetections of halo gas result in upper limits on the column densities of halo gas beyond the virial radii of other galaxies.

The metallicity of the halo gas also can potentially increase our mass estimates. We initially assumed a solar gas metallicity in our conversion from O VII to electron column density. However, we note $N_e \propto Z^{-1}$ (see Equation 2.4), implying all of our inferred electron columns will increase if the metallicity is sub-solar. This effectively changes the normalization of our profile and results in $M \propto Z^{-1}$ for a given halo size. If we consider a halo gas metallicity of $Z = 0.3\ Z_\odot$ (within the lower limit established by the pulsar dispersion measure toward the LMC), $M_{vir} = 1 \times 10^{12}\ M_\odot$ and a halo extending to the virial radius, our mass estimate and baryon fraction become $M(160$ kpc$) = 2.2\ ^{+4.4}_{-0.5} \times 10^{10}\ M_\odot$ and f_b (160 kpc) $= 0.07\ ^{+0.03}_{-0.01}$. The upper 1σ limit on this mass estimate adds a considerable amount of mass to the Milky Way, but only accounts for $\sim$50% of the missing baryons.

Our mass estimates are comparable to observations of the Milky Way's hot gas halo and simulations of the circumgalactic medium (CGM) around galaxies similar to the Milky Way. Although previous observations of the Milky Way's hot gas halo have relied upon uniform density approximations (see Section 2.6.1), the derived masses are consistent with our model parameters with assumptions regarding the gas metallicity. The model found by Bregman & Lloyd-Davies (2007) resulted in a halo gas mass of $4 \times 10^8\ M_\odot$ for a halo size of 20 kpc, which is consistent with our 1σ uncertainties for the enclosed mass at that radius. Alternatively, Gupta et al. (2012) found a lower limit on the halo gas mass of $> 6.1 \times 10^{10}\ M_\odot$ for $L > 139$ kpc assuming the gas metallicity is $0.3\ Z_\odot$. Our halo model predicts a mass between 1.2–

5.2×10^{10} $M_\odot$ for that same radius and metallicity. Our mass estimates are also in agreement with simulations of the CGM around Milky Way-sized galaxies if we assume a gas metallicity of $\sim$0.3 $Z_\odot$. Hydrodynamical simulations by Feldmann et al. (2013) predict CGM densities of $\sim 10^{-4}$ cm^{-3} out to $\sim$100 kpc, resulting in mass estimates of [0.2, 1.0, 3.5] $\times 10^{10}$ $M_\odot$ at r = [50, 100, 200] kpc. These estimates are within our 1σ uncertainties at each radius for a gas metallicity of $\sim$0.3 $Z_\odot$, indicating the halo gas mass is likely comparable to the observed stellar + cold gas mass previously observed for the Milky Way.

The enclosed hot gas mass near the disk of the Milky Way is comparable to the observed mass in ionized HVCs. The total mass of ionized HVCs within 5–15 kpc of the Sun is $M \approx 1.1 \times 10^8 (d/12 \text{ kpc})^2 (f_c/0.5)(Z/0.2Z_\odot)^{-1}$ $M_\odot$, where f_c is the covering fraction (Lehner et al., 2012). For typical ionized HVC parameters, this mass estimate is approximately equal to the suggested hot gas mass enclosed within 10 kpc of the Galactic center (see Figure 2.8). One possibility to explain the similarity between these masses is that the ionized HVCs could have cooled out of the hot halo and are accreting on the disk of the Milky Way. However, the origin of HVCs is still poorly understood and likely a combination of several sources. The consistency between the mass estimates offers one possible formation mechanism.

The Milky Way's hot gas halo has been observed in X-ray emission by several groups and our density profile must be consistent with these observational constraints. We note that because the density profile of the gas falls off faster than $n \propto r^{-1}$ the column density is dominated by gas closest to the Galactic center. This effect is more drastic when we examine the X-ray emission of the halo due to the emission measure scaling as n^2. We define the emission measure as:

$$EM = \int_0^d n_e n_p ds, \tag{2.9}$$

where we note that to be consistent with Equations (1)–(3), d is the line of sight

distance and n_e and n_p are functions of both b and l.

One constraint we must address is the X-ray emission measure toward the Galactic center determined by Snowden et al. (1997) using the *ROSAT* all-sky survey. The observed count rate toward the Galactic center is $\sim$150 $\times$ 10^{-6} counts s^{-1} arcmin^{-2}, which includes extinction in the Galactic plane. However, by assuming an absorbing column of 4.4 $\times$ 10^{21} H I cm^{-2}, they extrapolate a peak count rate of $\sim$900 $\times$ 10^{-6} counts s^{-1} arcmin^{-2} for the 3/4 keV band. Using their conversion between count rate and emission measure, which is sensitive to temperature, we determine that the extrapolated count rate corresponds to an emission measure of 0.45 cm^{-6} pc. In order to reproduce this emission measure, we need to consider an inner radius where the density is constant for $0 \leqslant r \leqslant r_{in}$. We find that our density model must be constant at $n_{in} = 8.8 \times 10^{-3}$ cm^{-3} out to an inner radius of $r_{in} = 2.2$ kpc to reproduce the observed emission measure toward the Galactic center. We note that this inner radius does not affect the other parts of our analysis. In particular, the mass estimate is not affected by this due to the small volume associated with this region. Also, we note that this inner radius is larger than the core radius of our profile. This is not a major concern since r_c is not well constrained and we still constrain the extended regions of the profile reasonably well.

The other emission measure constraint of interest is the emission measure out of the Galactic plane. McCammon et al. (2002) analyzed a 1 sr region of sky centered on $l = 90°$, $b = +60°$ using a quantum calorimeter sounding rocket. Their sensitivity and spectral resolution allowed them to model the soft X-ray diffuse background into an absorbed thermal component with EM = 0.0037 cm^{-6} pc and an unabsorbed thermal component with EM = 0.0088 cm^{-6} pc. Given our best-fit halo model, the predicted absorbed emission measure is 0.0017 $(Z/Z_\odot)$ cm^{-6} pc for $r_{halo} = 18$ kpc and 0.0018$(Z/Z_\odot)$ cm^{-6} pc for $r_{halo} = 200$ kpc. This implies that the emission is dominated by the gas within $\approx$ 20 kpc of the Galactic center. The emission measure

produced by our best-fit halo model underproduces the observed emission measure near $l = 90°$, $b = +60°$ regardless of the halo size we consider and for solar metallicity. However, the 1σ upper limit on our emission measure along this line of sight is 0.0122 $(Z/Z_{\odot})$ cm^{-6} pc, implying our emission measure estimate is consistent with the observed value at the 1σ level. We also do not consider a separate temperature source in our calculation that could add another component to the observed emission measure, which would also explain the initial discrepancy.

The addition of the AGN ESO 141-G055 to our target list allows us to discuss our halo model in the context of recent observations by the *Fermi Gamma-ray Space Telescope*, which revealed two large gamma-ray emitting bubbles above and below the galactic plane (Su et al., 2010). These Fermi bubbles are aligned with features seen in the *ROSAT* soft X-ray maps and are believed to be interacting with the Galactic halo gas as they expand away from the Galactic plane. Although these Fermi bubbles are considerably hotter than the Galactic halo gas, they will still contribute free electrons to lines of sight toward the Galactic center. For this comparison, we can use the dispersion measure toward the Galactic center, which is sensitive to the total electron density along a given line of sight. Taylor & Cordes (1993) showed that the dispersion measure toward the Galactic center is 650–800 cm^{-3} pc, which is thought to be primarily due to free electrons from gas in the 10^3–10^4 K range (the warm ionized medium) (Gaensler et al., 2008). The contribution from our Galactic halo model toward the galactic center is only DM = 72 cm^{-3} pc, which is negligible compared to the model expectations. The contribution from these Fermi bubbles also appears to be negligible and even less than that of our Galactic halo model. Guo & Mathews (2012) and Yang et al. (2012) modeled the Fermi bubbles, assuming an ambient medium similar to our determined halo model, to recreate the bubbles' observed structure and found an average density in the plane of $\sim 10^{-3}$ cm^{-3}. This results in a dispersion measure toward the galactic center of DM = 24 cm^{-3} pc. Thus,

both the *Fermi* bubbles and Galactic halo contribute a small fraction (∼10%) of the total electrons near the Galactic plane.

The sight line toward ESO 141-G055 has a peculiarity in the ion column densities that are detected which is directly related to the presence of the Fermi bubbles. Most of our present sample shows little or no O VIII absorption, which allows us to constrain the temperature of the Galactic halo gas. However, the line of sight toward ESO 141-G055 suggests an enhancement of O VIII , with a column density ratio of $N(\text{O VIII})/N(\text{O VII}) = 1.4 \pm 0.5$. Yang et al. (2012) are able to produce the observed O VIII/O VII ratio and find that the shocked region of the bubbles is $\sim 10^8$ K while the interior is 10^7–10^8 K. This implies little contribution from O VII or O VIII to the total electron column along the line of sight. While the ion fractions of both ions are small inside the bubbles ($f \ll 0.1$), the O VIII ion fraction is at least an order of magnitude higher than the O VII fraction everywhere inside the bubbles. This results in the enhancement of O VIII relative to O VII for any line of sight that passes through the Fermi bubbles. However, these results do not explain the infrequent detection of O VIII along most of our other sight lines. A more detailed analysis of the density and temperature structure of the bubbles is beyond the scope of this work and will be the topic of a future project.

2.6.3 Thermal Considerations

The thermal properties of the hot gas halo (mainly the cooling time and radius) can be used as a measure of how large the halo could be if it were stable. We first adopt an expression for the cooling time (Fukugita & Peebles, 2006):

$$\tau(r) = \frac{1.5nkT}{\Lambda(T,Z)n_e(n-n_e)} \approx \frac{1.5kT \times 1.92}{\Lambda(T,Z)n_e \times 0.92}, \tag{2.10}$$

which assumes a primeval helium abundance. The cooling time as a function of radius can be seen in Figure 2.9 for different metallicities.

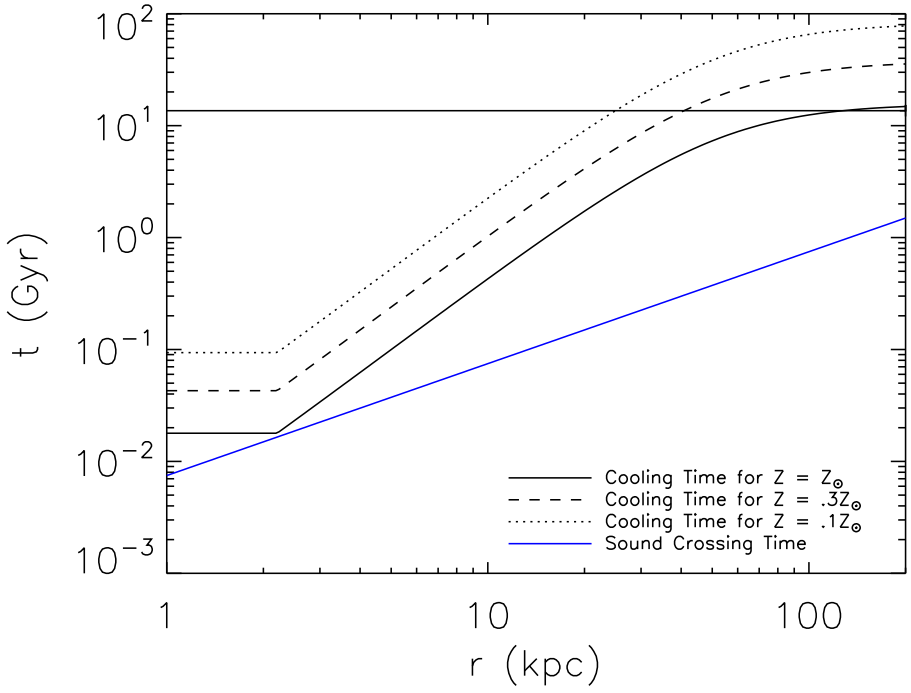

Figure 2.9: Cooling time as a function of radius given our best-fit parameters and assuming the halo is isothermal at $\log(T) = 6.1$. The cooling time is sensitive to the assumed metallicity of the halo and is comparable to a Hubble time at the Milky Way's virial radius for solar metallicity gas. This implies that the halo either has a sub-solar metallicity or is subject to a continuous heating source. We also plot the sound crossing time as a function of galactocentric radius. This shows that the cooling time is greater than the sound crossing time at all radii, implying the halo is in hydrostatic equilibrium.

One result to note is that the cooling time is less than a Hubble time for a solar metallicity halo out to near the virial radius, implying a need for a continuous heating source if the halo were stable. This can be explained if the primary source of the halo gas is feedback from the disk in the form of supernovae or AGN, which would enrich and heat the halo. This allows the cooling time of the halo to be less than the Hubble time since the halo would receive an input of energy, making it stable throughout the Milky Way's lifetime. Alternatively, if the halo gas is primarily accreted material by the Milky Way, the gas metallicity would be sub-solar. This implies a cooling radius

between 30–40 kpc for a $\sim$0.3 $Z_{\odot}$ halo, so the halo at $r > r_{cool}$ could not have cooled since the formation of the Milky Way.

We compare the cooling time as function of radius to the sound crossing time as a function of radius to determine if the Milky Way's hot gas halo is in hydrostatic equilibrium. We assume that the halo is isothermal at a temperature of $\log(T) = 6.1$, which results in a sound speed of $c_s \sim 130$ km s^{-1}. Figure 2.9 shows that the sound crossing time is smaller than the cooling for $r \gtrsim 1$ kpc, implying the halo is in hydrostatic equilibrium.

The cooling time discussed above also has implications for the cooling and accretion rates of the Galactic halo gas on the disk of the Milky Way. The accretion rate is determined by integrating the mass within a radial shell divided by the cooling time at a given radius and can be seen in Figure 2.10. The sensitivity of the result on metallicity has various implications. For a solar metallicity halo, the accretion rate is similar to modeled accretion rates of similar mass spiral galaxies (Fraternali & Binney, 2008). Figure 2.10 also indicates that the accretion rate is broadly consistent with the current observed star formation rate (SFR) in the Milky Way of 0.68–1.45 $M_{\odot}$ yr^{-1} (Robitaille & Whitney, 2010). This implies that the cooling of the Galactic halo may be a significant source of cold gas that fuels star formation in the disk of the Milky Way. However, there is also evidence indicating the observed Milky Way SFR can be balanced by stellar mass loss alone. Leitner & Kravtsov (2011) modeled mass loss rates for single-age stellar populations and determined star formation histories for several galaxies using the relationship between SFR and stellar mass in star-forming galaxies. Their results indicate that in most of their sample, including the Milky Way, mass loss from later stages of stellar evolution can more than compensate for the current observed SFRs. This indicates that the sub-solar metallicity accretion rate of 0.1–0.5 $M_{\odot}$ yr^{-1} from the halo is more likely than a solar metallicity accretion rate if the mass supply rate is to be less than the observed SFR. If the halo has a

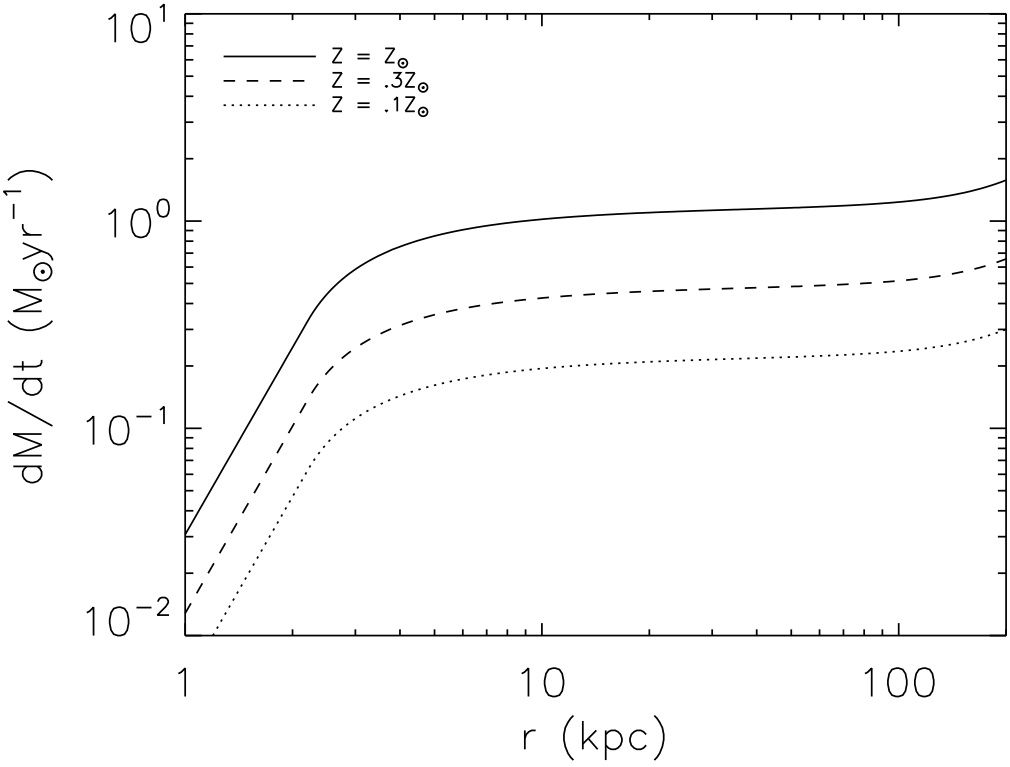

Figure 2.10: Cooling rate (or accretion rate) as a function of radius for our best-fit parameters. The solar metallicity gas results in an accretion rate that is roughly consistent with the SFR observed in the Milky Way, but sub-solar metallicity gas is more consistent with what has been observed in other spiral galaxies.

solar metallicity ($\sim$1.0 $M_\odot$ yr^{-1}) and stellar mass loss contributes $\sim$1.5 $M_\odot$ yr^{-1} back to the Milky Way disk, then the Milky Way's SFR should increase with time. This opposes the observed cosmic SFR, indicating that the halo is likely not entirely at a solar metallicity (Borch et al., 2006). Another possibility that prevents the halo cooling rate from overproducing the observed Milky Way SFR is a heating agent for the halo gas, such as supernovae. The addition of a heating source increases the cooling time of the halo gas, particularly near the stellar disk, and can significantly reduce the amount of gas cooling out of the halo.

The luminosity of the Galactic halo can be determined from the measured cooling rate discussed above. The conversion between the 0.5–2.0 keV luminosity and cooling rate is:

$$L_X(r) = 0.362 \times \dot{M} \frac{1.5kT}{\mu m_p}, \tag{2.11}$$

where $\dot{M}$ is the cooling rate and 0.362 is the conversion between the bolometric luminosity and the 0.5–2.0 keV band luminosity. For typical cooling rates seen in Figure 2.10 and a solar gas metallicity, the corresponding 0.5–2.0 keV band luminosity is $\sim 7 \times 10^{39}$ erg s^{-1}. This is larger than what has been determined from *ROSAT* measurements of the diffuse X-ray background (Snowden et al., 1997), which imply $L_X \sim 2 \times 10^{39}$ erg s^{-1}. The difference is likely due to the uncertainty in the gas metallicity. A solar metallicity halo should be considered as an upper limit to $\dot{M}$ since only part of the halo is expected to be enriched. In order to match the luminosity determined by *ROSAT*, the metallicity would need to be $\sim$0.3 $Z_\odot$. Thus, our luminosity is broadly consistent with previous estimates of the Milky Way's diffuse X-ray luminosity if the average metallicity is less than solar.

If we assume that this hot halo is volume filling we can compare the pressure of this hot halo with other phases of the ISM. In particular, we compare our model pressure to pressures associated with HVCs measured by Fox et al. (2005), which are at temperatures ranging from $10^4 \sim 10^5$ K. In their analysis, they average six HVC models to find thermal pressures of $P/k = [530, 140, 50]$ cm^{-3} K at distances of [10, 50, 100] kpc. If we assume a temperature of $\log(T) = 6.1$, our model results in a range of pressures of $P/k = [694, 41, 24]$ cm^{-3} K for $r = [10, 50, 100]$ kpc respectively. This indicates that our hot gas is close to pressure equilibrium with these observed HVCs. However, it should be noted that the distances toward these HVCs are not well constrained and the results here are strongly dependent on both the density and temperature of the gas. We also do not consider the addition of a hotter gas phase

Table 2.4. Saturation Effects

	Optically Thin	Saturated
Added uncertainty to EW (mÅ)	7.5	7.2
M(18 kpc) ($M_\odot$)	$3.1\ ^{+6.8}_{-1.9} \times 10^8$	$2.2\ ^{+6.7}_{-1.3} \times 10^8$
M(200 kpc) ($M_\odot$)	$2.4\ ^{+4.9}_{-0.5} \times 10^{10}$	$1.2\ ^{+1.7}_{-0.2} \times 10^{10}$
Z_{LMC} ($Z_\odot$) [a]	0.4	0.2
$EM_{GalacticPole}(Z/Z_\odot)$ cm^{-6} pc [b]	0.0038	0.0018

[a]Lower limit placed on the gas metallicity based on the pulsar dispersion measure toward the LMC.

[b]Model emission measures toward $l = 90°$, $b = +60°$.

in our analysis which would add an additional pressure component.

2.6.4 Final Comments

The goal of this study was to constrain the density profile of the Milky Way's hot gas halo better than previous studies, which have primarily relied upon simple models of the halo structure. We use *XMM-Newton* RGS archival data of 29 sight lines to analyze O VII absorption from the halo. One limitation of our analysis is the inability of the RGS to resolve the observed absorption lines. This prohibits us from analyzing the true saturation effects in the lines. From Table 2.2, accounting for line saturation with a Doppler width of 150 km s^{-1} increases $n_\circ$ of our density model but steepens the best-fit β compared to the optically thin fitting results. The parameter $n_\circ$ increases since all of the inferred column densities increase if we assume any line saturation. The parameter β also increases since the lines that have the largest equivalent widths, and thus the largest inferred column densities, also have large uncertainties in the curve of growth analysis. Table 2.4 shows the most important results of our analysis assuming both optically thin and saturated best-fit parameters from Table 2.2. By using saturated column densities, the steeper β parameter is

more important than the increased normalization relative to the optically thin results in terms of the overall mass estimate. However, the inferred masses assuming the lower metallicity limits established by the pulsar dispersion measure toward the LMC result in comparable masses for each case. The emission measure estimates toward $l = 90°$, $b = +60°$ differ by a factor of $\sim$2, which is also due to the steeper β in the saturated parameter case. Neither of these estimates overproduce the observed emission measure for a solar metallicity, implying an additional component to the observed emission measure. By comparing our best-fit results for optically thin and saturated column densities, we find the best-fit parameters change, but the inferred masses from the best-fit profiles are similar.

The metallicity of the halo gas has not been thoroughly analyzed for the Milky Way's halo and is crucial for understanding various properties of the halo gas. Although we initially assumed a solar metallicity halo in our analysis, we recognize that the metallicity of the gas is a large uncertainty in our analysis and is likely sub-solar. We are able to place a constraint on the metallicity of the gas between the Sun and the LMC based on the observed pulsar dispersion measure (Anderson & Bregman, 2010). The metallicity of the gas must be $Z \gtrsim 0.2\ Z_{\odot}$ to satisfy the pulsar dispersion measure constraint. This lower limit applies to the average metallicity of the gas between the Sun and the LMC ($r \approx 55$ kpc) and does not necessarily apply to halo gas beyond the LMC. Our results for the mass accretion rate and X-ray luminosity of the halo suggest that a halo metallicity of $Z = 0.3\ Z_{\odot}$ is more appropriate. This metallicity is consistent with cosmological simulations (Toft et al., 2002; Cen & Ostriker, 2006) and observations of both spiral galaxies (Rasmussen et al., 2009; Meiring et al., 2013) and some HVCs (Gibson et al., 2000; van Woerden & Wakker, 2004; Fox et al., 2005). We also ignore a metallicity gradient in our analysis, which is possible from the mixing of ejected gas from the disk of the Milky Way and cooling primordial gas from the formation of the Milky Way. Both mechanisms are likely contributing

to the halo gas, but the metallicity gradient of the halo gas is not well understood. An analysis of the halo gas metallicity and on the extent there exists a metallicity gradient will be critical in determining several halo gas properties.

With the density profile of the halo constrained, we are able to analyze useful properties of the halo and determine how the halo relates to the baryon content of the Milky Way. We find the mass contained in the halo for our best-fit parameters is between $M(18\text{ kpc}) = 7.3\ ^{+22.3}_{-4.3} \times 10^8\ M_\odot$ and $M(200\text{ kpc}) = 4.0\ ^{+5.7}_{-0.7} \times 10^{10}\ M_\odot$ for an assumed metallicity $Z = 0.3\ Z_\odot$. If we assume a lower estimate of the virial mass of the Milky Way ($1 \times 10^{12}\ M_\odot$) and the gas extending to the virial radius of the Milky Way for a halo that size, the largest baryon fraction we obtain is f_b (160 kpc) $= 0.07\ ^{+0.03}_{-0.01}$. This accounts for 10%–50% of the missing baryons required to match the universal baryon fraction of $f_b = 0.171$.

The constraints we place on the Milky Way's hot gas halo are close to the best we are able to accomplish with *Chandra* and *XMM-Newton*. Improvements can be made on eliminating the degeneracy between the parameters $n_\circ$ and r_c with additional Galactic targets near the Galactic center, however this does not affect the global properties of the halo. There is also work to be done exploring the interaction between the hot gas halo and the Fermi bubbles. The combination of O VII and O VIII emission will reveal the temperature structure just outside and inside the bubbles, which will help probe the contribution of thermal and non-thermal electrons inside the bubbles.

CHAPTER III

Constraining the Milky Way's Hot Gas Halo with O VII and O VIII Emission Lines

3.1 Preface

This chapter is adapted from work of the same title appearing in the Astrophysical Journal, Volume 800, 14 (Miller & Bregman, 2015), and is coauthored by Joel N. Bregman. The initial emission line sample is from the publicly available Henley & Shelton (2012) dataset. My contributions include the additional observation screening, data modeling, and data analysis.

3.2 Abstract

The Milky Way hosts a hot ($\approx 2 \times 10^6$ K), diffuse, gaseous halo based on detections of $z = 0$ O VII and O VIII absorption lines in quasar spectra and emission lines in blank-sky spectra. Here we improve constraints on the structure of the hot gas halo by fitting a radial model to a much larger sample of O VII and O VIII emission line measurements from *XMM-Newton*/EPIC-MOS spectra compared to previous studies (≈650 sight lines). We assume a modified β-model for the halo density distribution and a constant-density Local Bubble from which we calculate emission to compare with the observations. We find an acceptable fit to the O VIII emission line observa-

tions with χ^2_{red} (dof) = 1.08 (644) for best-fit parameters of $n_o r_c^{3\beta} = 1.35 \pm 0.24 \times 10^{-2}$ cm^{-3} kpc$^{3\beta}$ and $\beta = 0.50 \pm 0.03$ for the hot gas halo and negligible Local Bubble contribution. The O VII observations yield an unacceptable χ^2_{red} (dof) = 4.69 (645) for similar best-fit parameters, which is likely due to temperature or density variations in the Local Bubble. The O VIII fitting results imply hot gas masses of $M(< 50$ kpc) $= 3.8^{+0.3}_{-0.3} \times 10^9 M_\odot$ and $M(< 250$ kpc) $= 4.3^{+0.9}_{-0.8} \times 10^{10} M_\odot$, accounting for $\lesssim$50% of the Milky Way's missing baryons. We also explore our results in the context of optical depth effects in the halo gas, the halo gas cooling properties, temperature and entropy gradients in the halo gas, and the gas metallicity distribution. The combination of absorption and emission line analyses implies a sub-solar gas metallicity that decreases with radius, but that also must be $\geq 0.3 Z_\odot$ to be consistent with the pulsar dispersion measure toward the Large Magellanic Cloud.

3.3 Introduction

The detection of X-ray-emitting and -absorbing gas at zero redshift implies the existence of a diffuse volume-filling plasma associated with the Milky Way's interstellar medium (ISM) and circumgalactic medium (CGM). Detections of these absorption and emission lines along individual lines of sight imply plasma densities between 10^{-5} and 10^{-3} cm^{-3} and plasma temperatures of $\sim 10^6$ K. These observations constrain the detailed properties of the gas along individual sight lines, but there has not been a comprehensive analysis on the global properties of the absorption and emission lines. Analyzing the global properties of the observations is necessary to constrain the overall structure and extent of the gas. Constraints on the structure of the gas, specifically the density profile, are necessary to estimate the hot gas mass within the Milky Way's virial radius. The contribution of the hot gas to the Milky Way's baryon budget may account for a significant fraction of the Milky Way's "missing baryons".

The tracers of the Milky Way's hot halo gas are O VII and O VIII absorption and

emission lines characteristic of gas in the 10^6–10^7 K range (Paerels & Kahn, 2003). The emission lines are thought to be a significant contributor to the 0.5–2.0 keV portion of the Milky Way's diffuse soft X-ray background (SXRB; Snowden et al., 1997; McCammon et al., 2002; Henley & Shelton, 2012) and are typically seen in otherwise empty fields of view in the sky (∼1000 sight lines; Yoshino et al., 2009; Henley & Shelton, 2010, 2012). On the other hand, the absorption lines are only seen in ∼30 bright active galactic nucleus (AGN) and blazar spectra (Nicastro et al., 2002; Rasmussen et al., 2003; Wang et al., 2005; Williams et al., 2005; Fang et al., 2006; Bregman & Lloyd-Davies, 2007; Yao & Wang, 2007; Hagihara et al., 2010; Gupta et al., 2012; Yao et al., 2012; Miller & Bregman, 2013; Fang & Jiang, 2014) or X-ray binaries (Yao & Wang, 2005; Hagihara et al., 2010). The sensitivity of current X-ray telescopes in the soft X-ray band is the limiting factor on the number of absorption line detections, but still results in the nearly ubiquitous detection of the emission lines.

The SXRB, with some contribution from O VII and O VIII emission lines, has been observed in broadband images from the *ROSAT All-Sky Survey* (RASS; Snowden et al., 1997), in blank-sky spectra from current X-ray telescopes (Yoshino et al., 2009; Henley & Shelton, 2010, 2012), and with the Diffuse X-ray Spectrometer sounding rocket (McCammon et al., 2002). A combination of results from analyses comparing the RASS 1/4 keV and 3/4 keV bands (Snowden et al., 1997; Kuntz & Snowden, 2000) and shadowing experiments toward nearby molecular clouds (Galeazzi et al., 2007; Smith et al., 2007) imply that multiple plasma components comprise the 0.5–2.0 keV component of the SXRB.

The "local" emission component of the SXRB is believed to come from a combination of the Local Bubble (LB) and solar wind charge exchange (SWCX) processes. The LB is thought to be a supernova (SN) remnant that the Sun is currently inside (Snowden et al., 1990, 1993), although its physical and corresponding emission prop-

erties are debated in the literature. Arguments exist either for the LB being filled with X-ray-emitting gas at $\sim 10^6$ K (Smith et al., 2007) or that the emission comes more from a wall of material at the edges of the bubble (100–300 pc away; e.g., Welsh & Shelton, 2009). On the other hand, SWCX emission is a known soft X-ray emission source where neutral hydrogen and helium atoms undergo charge exchange reactions with solar wind ions in and around our solar system (Cravens et al., 2001; Snowden et al., 2004; Wargelin et al., 2004; Carter & Sembay, 2008; Koutroumpa et al., 2007; Kuntz & Snowden, 2008; Carter et al., 2011; Ezoe et al., 2010; Koutroumpa et al., 2011). These reactions are difficult to predict or quantify, but are known to produce time-variable line emission at energies $\lesssim$1 keV. While the details of both emission sources are still unclear, a combination of both SWCX and LB emission models are necessary to reproduce the *ROSAT* 1/4 keV band emission (Galeazzi et al., 2014; Smith et al., 2014a). The picture at high energies, specifically for the O VII and O VIII emission lines, has uncertainties as well. Shadowing experiments toward nearby molecular clouds show that local O VII emission is common, but O VIII emission is not always detected (Smith et al., 2007; Koutroumpa et al., 2011). It is clear the LB and/or SWCX *can* produce O VII and O VIII emission, but their global oxygen line emission properties are still unclear.

The "non-local" plasma component of the SXRB is believed to come from a more extended, diffuse plasma at a slightly hotter temperature than the LB (Yoshino et al., 2009; Henley & Shelton, 2013), although the source and exact spatial extent of the plasma is unclear. One potential source would be a plane-parallel, exponential distribution of $\sim 10^6$ K due to SN-driven outflows from the Milky Way's disk (Norman & Ikeuchi, 1989; Joung & Mac Low, 2006; Hill et al., 2012). Indeed, this type of density distribution is suggested by Hagihara et al. (2010) based on O VII and O VIII absorption line measurements along the PKS 2155-304 sight line. They fit their absorption line observations with an exponential disk density model with a scale height of $2.8^{+6.4}_{-1.0}$

kpc, implying a much more confined medium compared to the diffuse, volume-filled halo picture. However, this type of distribution results in inconsistencies with additional "non-local" plasma observables, including the emission measure distribution across the sky of the "non-local" plasma (Henley et al., 2010; Henley & Shelton, 2013) and the Milky Way's diffuse X-ray surface brightness (Fang et al., 2013). This implies that the "non-local" plasma contribution to the SXRB, and thus the O VII and O VIII emission lines, is likely from an extended distribution of gas in the Milky Way's halo.

Analyses of the O VII and O VIII absorption lines typically assume that the lines arise from a large (scales $\gtrsim$20 kpc), diffuse, volume-filled halo consistent with shock heated gas at the Milky Way's virial temperature in quasi-static equilibrium (White & Frenk, 1991). Detailed work on the absorption strengths between O VII and O VIII (when detected) along individual sight lines suggests a plasma temperature between $\log(T) = 6.1$–6.4, but do not provide constraints on the large-scale properties of the plasma. Recent work by Bregman & Lloyd-Davies (2007) and Gupta et al. (2012) analyzed larger samples of the absorption lines using *XMM-Newton* Reflection Grating Spectrometer and *Chandra* High and Low Energy Transmission Grating data. Bregman & Lloyd-Davies (2007) compared their column densities to a single line of sight emission measurement (McCammon et al., 2002) while Gupta et al. (2012) compared their column densities to an average emission measure from $\sim$20 lines of sight (Yoshino et al., 2009; Henley et al., 2010) to estimate a characteristic density and path length of the absorbing material. There are several discrepancies between these works, but both find characteristic densities between 10^{-4} and 10^{-3} cm^{-3} and path lengths >20 kpc.

Miller & Bregman (2013) provided an improvement on these works by modeling the local O VII absorption lines in 29 AGN and X-ray binary spectra with a more physical hot halo density model (as opposed to a constant-density sphere). They found the absorption lines could be modeled with a modified spherical β-model (ef-

fectively a power law) with β ranging between 0.56 and 0.71, depending on the effects of absorption line saturation ($\beta = 0.5$ corresponds to $n \propto r^{-3/2}$). These density model constraints resulted in hot gas mass estimates of 3.3–9.8 $\times 10^{10} M_{\odot}$ within 200 kpc.

Until now, there has been no comprehensive comparison between the O VII and O VIII emission and absorption line observations thought to be due to a Galactic hot gas halo. This is partially due to the difficulty in disentangling the LB and hot halo contributions to the emission lines across the entire sky. The characteristic densities and size scales (L) for each component imply the LB contributes more to the emission lines ($\propto n^2 L$) than the absorption lines ($\propto nL$). (e.g., Gupta et al., 2014) Additionally, the differences in sample sizes between the two observables have prevented a large-scale analysis between the two. The number of O VII absorption line measurements with current X-ray telescopes ($\sim$30) is at its maximum due to the sensitivity of current detectors, while many published O VII and O VIII emission line measurements are focused on individual sight lines or are limited to a certain region of the sky. This is important since the absorption and emission properties of the hot gas halo vary across the sky, meaning comparisons between absorption lines in one area of the sky with emission lines in a different area may yield incorrect results about the hot halo plasma.

Henley & Shelton (2012) have offered a resolution to the latter issue by presenting an all-sky catalog of O VII and O VIII emission line measurements of the SXRB using *XMM-Newton*/EPIC-MOS data. Their sample is an incredibly useful tool for probing the Milky Way's hot gas halo since there are many targets (1868 in their whole sample) and their sample covers the entire sky. The combination of these two effects should provide improved constraints on the Milky Way's hot gas halo compared to the absorption line data sets, even with the known LB emission.

In this work, we unify the procedure outlined in Miller & Bregman (2013) with this O VII and O VIII emission line data set to constrain the density properties of the

Milky Way's hot gas halo. We develop a parametric model for the Milky Way's hot gas halo density profile and LB, calculate model line intensities along each line of sight and for a given parameter set, and find the model parameters that are most consistent with the data. In this way, we constrain the density properties of the hot gas halo and place more precise estimates on important quantities such as its mass and metallicity.

There are several advantages to this work on the O VII and O VIII emission lines. The most critical benefit of this work is that we are analyzing the emission lines in the same way Miller & Bregman (2013) analyzed O VII absorption lines. This is crucial since we expect the Milky Way's hot halo to contribute to both sets of observables, so any similarities or differences between the two results can tell us about the physical properties of the gas. The other main benefit is that the quality of our constraints using this emission line sample should be much improved compared to the absorption line constraints. This is largely due to the increase in sample size by a factor of $\approx$20.

The outline for the rest of the chapter is as follows. In Section 3.4, we describe the observation selection, data reduction, and line measurement procedure of the O VII and O VIII emission lines from Henley & Shelton (2012). In Section 3.5, we describe our model fitting procedure. This includes a discussion of our parametric model and emission line calculation. In Section 3.6, we discuss our model fitting results and constraints on our density model. In Section 3.7, we discuss the implications of our results and compare them with other studies on the Milky Way's hot gas halo. Finally in Section 3.8, we summarize our results.

3.4 Data Reduction

Our emission line sample is a subset of the comprehensive O VII and O VIII emission line sample from Henley & Shelton (2012). The authors compiled their sample from all public *XMM-Newton* observations prior to 2010 August 4 that contained any EPIC-

MOS exposure time (5698 observations). The goal of creating this sample was to analyze the various sources of the Milky Way's SXRB, including SWCX, the LB, and the Milky Way's hot gas halo. Our data set is a subset of the Henley & Shelton (2012) full sample that maximizes our sensitivity to the Milky Way's hot halo emission.

This work focuses on the analysis and modeling of our subset of the emission lines presented in Henley & Shelton (2012), not the line measurements or sample compilation itself. Here we provide an overview of their procedure and refer the reader to the full sample references for a more detailed description of the sample (Henley & Shelton, 2010, 2012). We describe their data selection and reduction procedure in Section 3.4.1, their emission line measurement procedure in Section 3.4.2, and our additional screening procedure to create our sample in Section 3.4.3.

3.4.1 Data Filtering

The 5698 archival *XMM-Newton* observations were processed with the standard *XMM-Newton* Science Analysis System [1] version 11.0.1, including the *XMM-Newton* Extended Source Analysis Software [2] (*XMM*-ESAS; Kuntz & Snowden, 2008; Snowden & Kuntz, 2011). The *XMM*-ESAS script `mos-filter` was used to remove any observing time affected by soft-proton flaring. This contamination is identified by an excess or deficit in the 2.5–12 keV count rate. After this filtering, the authors kept observations with $\geqslant$5 ks of good observing time and with at least one good exposure with the MOS1 and MOS2 cameras each. This resulted in a sample of 2611 observations out of the original 5698.

Bright X-ray sources were removed from the observations using both visual inspection and automated source removal procedures. These screening methods are necessary to isolate SXRB emission in the extracted spectra. The authors used data from

[1] `http://xmm.esac.esa.int/sas/`
[2] `http://heasarc.gsfc.nasa.gov/docs/xmm/xmmhp_xmmesas.html`

the Second *XMM-Newton* Serendipitous Source Catalog [3] (2XMM; Watson et al., 2009) for automated X-ray point source removal. For each observation, any 2XMM source with 0.5–2.0 keV flux $F_X^{0.5-2.0} \geqslant 5 \times 10^{-14}$ erg cm^{-2} s^{-1} inside the field of view was removed using a 50″ circular region. These regions typically enclose ≈90% of the sources' fluxes. The authors also employed a visual inspection of the observations to remove any bright or extended sources that were not included in the automated point source removal. The exclusion regions for these sources typically ranged between 1′ and 4′ (Henley & Shelton, 2010).

SWCX reactions are a known source of O VII and O VIII line emission that must be accounted for in the emission line measurements. These reactions occur between solar wind ions and neutral hydrogen atoms in the Earth's atmosphere (geocoronal SWCX) or neutral hydrogen and helium atoms in the heliosphere (heliospheric SWCX). Geocoronal SWCX emission is strongest in the magnetosheath (Robertson & Cravens, 2003b) and often occurs at times when the solar wind proton flux is high (Carter & Sembay, 2008; Kuntz & Snowden, 2008). Heliospheric SWCX tends to be stronger near the ecliptic plane (Robertson & Cravens, 2003a; Koutroumpa et al., 2006) and varies with the overall solar cycle (11 yr). Fortunately, techniques to reduce SWCX emission to O VII and O VIII emission line measurements exist (Carter & Sembay, 2008; Carter et al., 2011).

Henley & Shelton (2012) address several SWCX filtering techniques in detail, but their primary approach utilizes solar wind proton flux data from OMNIWeb [4]. This database includes solar wind proton flux data from numerous satellites, including the *Advanced Composition Explorer* and *Wind*. They reduce SWCX contamination to the emission lines by removing portions of the *XMM-Newton* data taken when the solar wind proton flux was greater than 2×10^8 cm^{-2} s^{-1}. This filtering procedure caused the number of usable observations to fall from 2611 to 1435 due to some of

[3] `http://xmmssc-www.star.le.ac.uk/Catalogue/2XMMi-DR3/`
[4] `http://omniweb.gsfc.nasa.gov/`

the observations falling below the 5 ks observing time threshold mentioned above. The authors presented both their full sample of emission lines and this "flux-filtered" sample of emission lines that are less contaminated by SWCX emission. Figure 3.1 shows the distribution of the flux-filtered sample on the sky and the corresponding emission line strengths.

3.4.2 Emission Line Measurements

In this section, we outline the emission line measurement procedure from Henley & Shelton (2012). This includes fitting for all emission sources in a typical SXRB spectrum, including the emission lines of interest, the continuum of the LB and hot halo, the extragalactic background (EPL), the instrumental lines in the 0.4–10.0 keV range, and any residual soft proton contamination present after filtering out the quiescent particle background (QPB). This entire measurement procedure used XSPEC [5] version 12.7.0.

The authors fitted each observation in the 0.4–10.0 keV range with a multicomponent spectral model discussed above. The O VII and O VIII emission line model consisted of two δ-functions (or Gaussians with widths fixed to zero) with the O VII energy centroid left as a free parameter and the O VIII energy centroid fixed at 0.6536 keV (from APEC; Smith et al., 2001). Note that this line measurement method includes the total line emission from all sources in the extracted spectrum (hot halo, LB, and any residual contamination). The Galactic continuum included an absorbed APEC thermal plasma model (Smith et al., 2001) with the oxygen Kα emission disabled (Lei et al., 2009). The EPL was modeled as an absorbed power law with a photon index of 1.46 (Chen et al., 1997). Both the APEC and EPL components included attenuation by absorbing H I columns from the LAB survey (Kalberla et al., 2005) using the XSPEC `phabs` model (Balucinska-Church & McCammon, 1992; Yan

[5] `http://heasarc.gsfc.nasa.gov/docs/xanadu/xspec/`

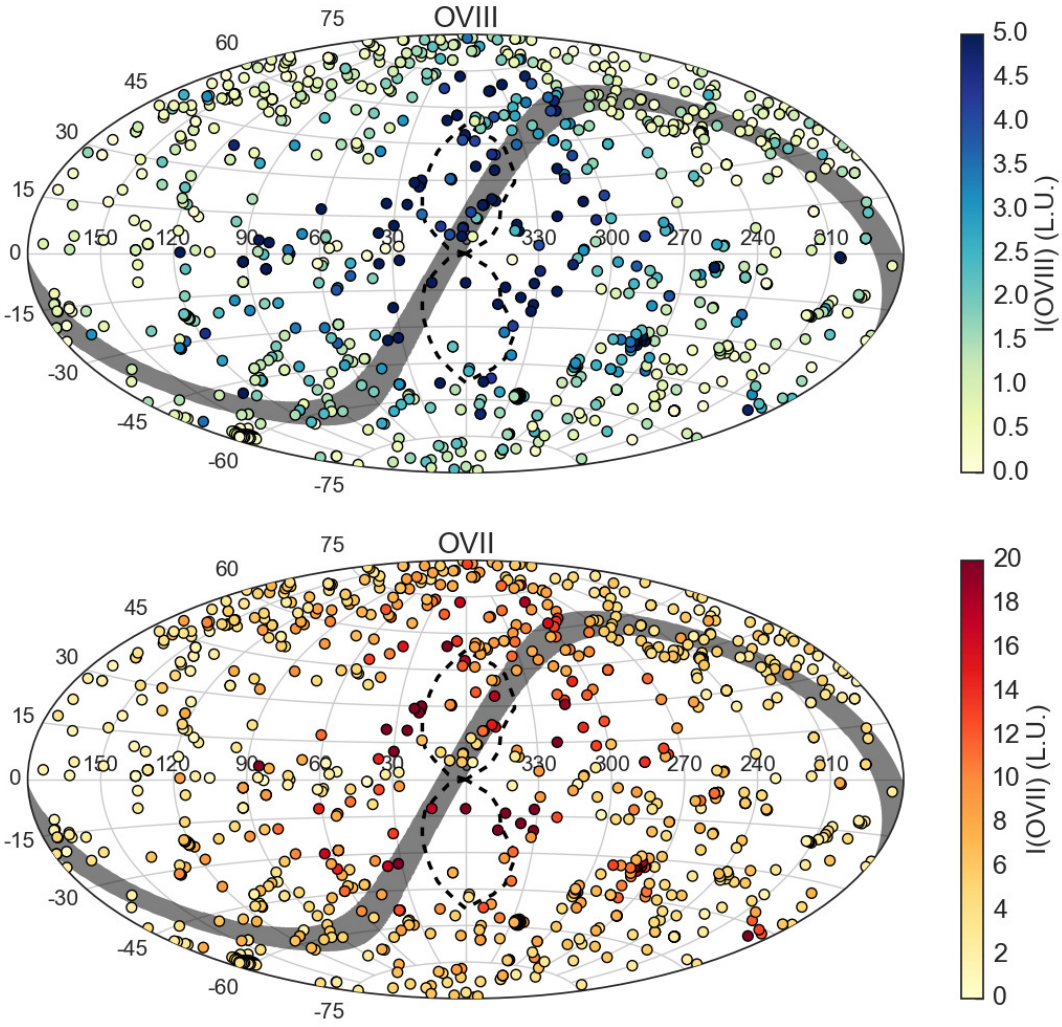

Figure 3.1: Flux-filtered sample of O VIII (top) and O VII (bottom) emission line strengths across the sky from Henley & Shelton (2012). The dashed line represents the observed gamma-ray emission from the Fermi bubbles (Su et al., 2010) and the shaded gray strip represents 5° above and below the ecliptic plane.

et al., 1998). The APEC and `phabs` components assumed Anders & Grevesse (1989) abundances. The model included two Gaussians for the Al-K and Si-K instrumental lines in this energy range (Kuntz & Snowden, 2008). The final model component included a power law (not folded through the instrumental response) to account for residual soft proton contamination from the QPB (Snowden & Kuntz, 2011).

Henley & Shelton (2012) provide a detailed discussion of the assumptions made in the above model and how these assumptions relate to the uncertainties presented in their results. Here we highlight those that affect the uncertainties of the emission line measurements. The statistical errors of the emission line measurements come from the standard XSPEC `error` command. The authors also provide a systematic uncertainty estimate based on the type of thermal plasma model used and variation in the EPL normalization parameter. The former compares the original line intensity measurements assuming an APEC thermal plasma model with measurements assuming a MEKAL (Mewe et al., 1995) or Raymond & Smith (1977) model (see Equation 1 in Henley & Shelton, 2012). The latter accounts for sightline-to-sightline variation in the EPL normalization parameter due to variable soft proton contamination and/or unresolved sources with $F_X^{0.5-2.0} < 5 \times 10^{-14}$ erg cm^{-2} s^{-1} (Moretti et al., 2003). The total systematic error for each observation is the combination of these two estimates in quadrature.

The final filtering procedure discussed in Henley & Shelton (2012) applies a more restrictive constraint on residual soft proton contamination to the emission line measurements. The authors introduced the ratio between the total 2–5 keV band flux (F_{total}^{2-5}) and the EPL flux in the same energy band (F_{exgal}^{2-5}) as a quantitative measure of residual soft proton contamination to the count rates (Henley & Shelton, 2010). Any observations where this ratio was greater than 2.7 were rejected from the sample. This decreased the number of useful observations from 2611 to 1868 for their full sample and from 1435 to 1003 for their flux-filtered sample.

3.4.3 Additional Observation Screening

We apply additional screening methods to the data in order to produce a sample that is most sensitive to the Milky Way's hot halo emission. These are spatial screening methods where we discard observations that are located near possible contaminates to the O VII and O VIII emission lines. These include bright X-ray sources in the sky and any Galactic features that show evidence for enhanced soft X-ray emission (see Table 3.1 for a summary). Although Henley & Shelton (2012) account for a range of point source removal methods in their data reduction procedure (see Section 3.4.1), this additional screening is designed to provide a cleaner sample of Milky Way hot halo emission.

Our automated screening discards any observations within 0.5° (or within the *XMM-Newton* field of view) of sources that could produce soft X-rays, thus complicating the O VII or O VIII emission line measurement. We utilize several all-sky catalogs that cover a range of astrophysical objects to generate a potential contaminating source list. The final contaminating source list is a subset of the objects in these catalogs based on either direct or inferred X-ray brightness cuts. For example, for *ROSAT* Bright Source Catalog objects we include sources with fluxes > 1 counts s^{-1}, but for Principal Galaxy Catalog objects, which do not have observed X-ray fluxes, we include sources with sizes $> 10'$. This does not create a completely uniform list of different types of X-ray-emitting objects and their fluxes, but it does provide a general list of objects that could contaminate the O VII or O VIII emission line measurement.

We also discard observations by hand that are known Galactic X-ray features and that are not discarded by our automated screening procedure outlined above. We remove any observations within $\leq 10°$ of the Galactic plane to reduce emission from SNe in the Milky Way's disk (Norman & Ikeuchi, 1989; Joung & Mac Low, 2006; Hill et al., 2012). This region also contains the largest H I columns that attenuate

Table 3.1. Automated Screening Criteria

Catalog	Types of Sources	Screening Criteria [a]
ROSAT-BSC [b]	Any bright X-ray source	> 1 counts s^{-1}
ROSAT-RLQ [c]	Radio loud quasars	$F_{0.1-2.4}$ [d] $> 10^{-11}$ erg cm^{-2} s^{-1}
ROSAT-RQQ [e]	Radio quiet quasars	$F_{0.1-2.4} > 10^{-11}$ erg cm^{-2} s^{-1}
PGC 2003 [f]	Galaxies	Apparent diameter $> 10'$
MCXC [g]	Galaxy clusters	$z < .1$

[a]Objects satisfying these criteria in their respective catalogs compose our potential contaminant source list. All observations from the Henley & Shelton (2012) Flux-filtered sample within 0.5° of these objects are removed in our model fitting procedure.

[b]ROSAT All-Sky Survey Bright Source Catalog (`http://www.xray.mpe.mpg.de/rosat/survey/rass-bsc/`; Voges et al., 1999).

[c]ROSAT Radio Loud Quasar Catalog (`http://heasarc.gsfc.nasa.gov/W3Browse/rosat/rosatrlq.html`; Brinkmann et al., 1997).

[d]0.1–2.4 keV flux.

[e]ROSAT Radio Quiet Quasar Catalog (`http://heasarc.gsfc.nasa.gov/W3Browse/rosat/rosatrqq.html`; Yuan et al., 1998).

[f]Principal Galaxy Catalog (`http://leda.univ-lyon1.fr/`; Paturel et al., 2003).

[g]Meta-Catalog of X-ray Detected Clusters of Galaxies (`http://heasarc.gsfc.nasa.gov/W3Browse/rosat/mcxc.html`; Piffaretti et al., 2011).

hot halo line emission, thus making the de-absorbed emission line intensities more uncertain. We also remove observations within $|l| \leq 22^\circ$ and $|b| \leq 55^\circ$, or near the Fermi Bubbles (e.g., Su et al., 2010). It is unclear how the bubbles have impacted the Milky Way's hot gas halo, but there are signatures of the bubbles in X-ray spectra (Bland-Hawthorn & Cohen, 2003; Kataoka et al., 2013). The observations that pass through these regions will be part of a separate study. Finally, we remove a cluster of observations near the Large Magellanic Cloud and Small Magellanic Cloud.

After our additional screening criteria discussed above, we are left with 649 of the 1003 observations from the flux-filtered sample. Figure 3.2 shows the distribution of our screened sample on the sky with the corresponding O VII and O VIII emission line strengths. Other than the Galactic plane and Fermi Bubble regions, our screened sample has similar sky coverage compared to the original all-sky samples. This sub-sample of observations should contain minimal emission from sources other than the LB and Milky Way hot halo and serves as our working sample of observations in our model fitting procedure.

3.5 Model Fitting

Here we describe how we compare the emission line observations from Henley & Shelton (2012) with simulated line intensities from a parametric density model for the Milky Way's hot gas halo. The goal of this work is to explore our model parameter space and find the set of parameters that is most consistent with the observations. This way we constrain the density profile of the Milky Way's hot gas halo with the same approach as previous studies on O VII absorption lines (Miller & Bregman, 2013).

3.5.1 Halo Density Model

We consider various forms of a spherical β-model to represent the Milky Way's hot gas halo density profile. We choose this model because of its success in fitting

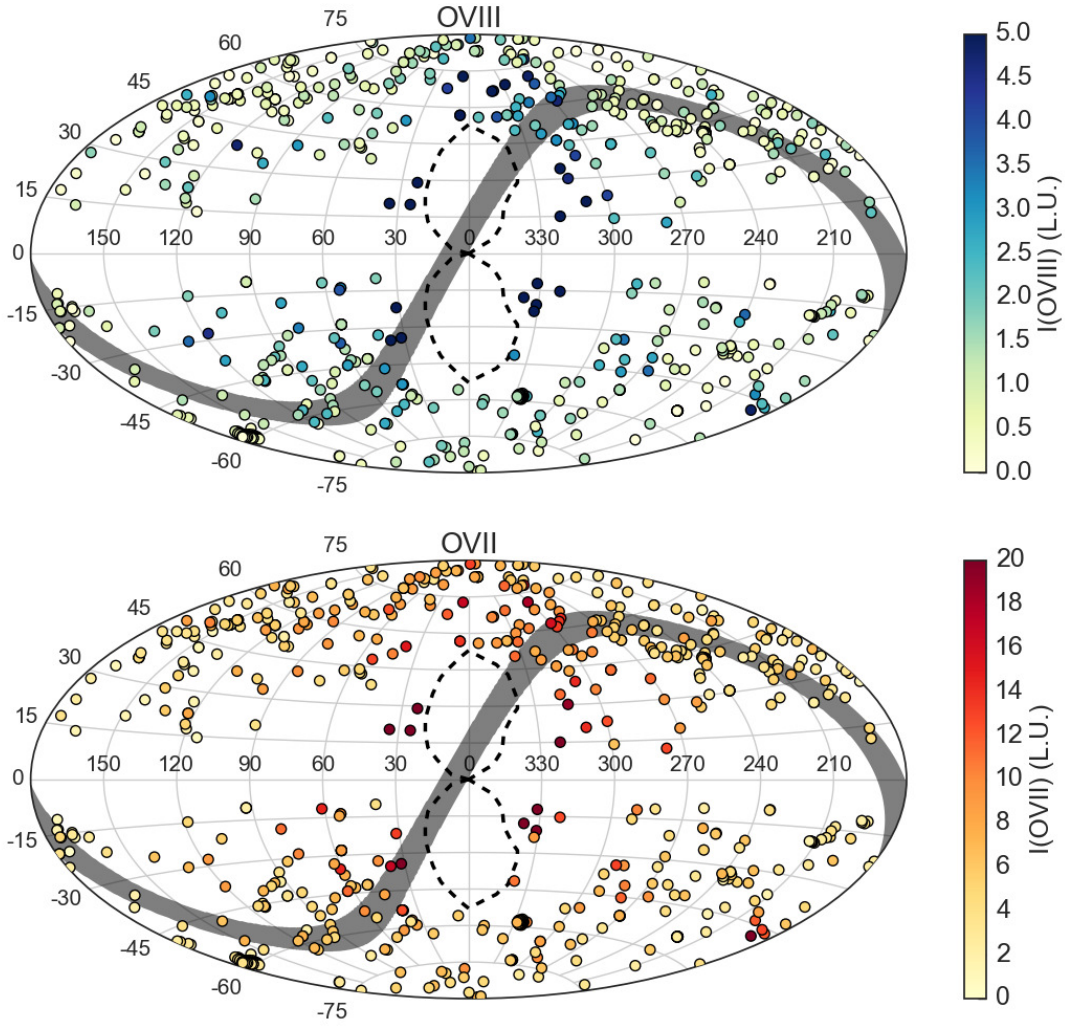

Figure 3.2: Same as Figure 3.1 but with our additional screening criteria applied to the observations (see Section 3.4.3). Note the emission line strengths tend to increase from Galactic anticenter toward the Galactic center. These observations serve as our sample in our model fitting procedure.

X-ray surface brightness profiles around early- (Forman et al., 1985; O'Sullivan et al., 2003) and late-type (Anderson & Bregman, 2011; Dai et al., 2012) galaxies and to be consistent with previous work on the Milky Way's hot halo (Miller & Bregman, 2013). The β-model is defined as:

$$n(r) = n_o(1 + (r/r_c)^2)^{-3\beta/2}, \tag{3.1}$$

where $n_\circ$ is the central density, r_c is the core radius, and β defines the slope of the profile at large radii. Typical values for β range between 0.4 and 1.0 while typical core radii are $\lesssim 5$ kpc.

The typical observed values for the core radii parameter combined with our removal of observations near the Galactic center limit our ability to simultaneously constrain all three parameters of the β-model. Out of the 649 pointings in our sample discussed above, only 4 pass within 5 kpc of the Galactic center. Following the work of Miller & Bregman (2013), we adopt a modified β-model in the limit where $r \gg r_c$:

$$n(r) \approx \frac{n_o r_c^{3\beta}}{r^{3\beta}}. \tag{3.2}$$

This modified density profile is essentially a power law with a normalization of $n_\circ r_c^{3\beta}$ and slope of -3β. We use this two-dimensional hot gas halo density profile for the majority of our analysis.

We also consider a flattened hot gas halo density profile in our analysis by modifying the spherical β-model. One expects a flattened hot gas distribution if the dark matter (DM) profile is flattened due to rotation or its merger history (e.g., Bailin & Steinmetz, 2005), or if the hot gas acquires net angular momentum (Stewart et al., 2013). The flattened β-model becomes:

$$n(R,z) = n_o(1 + (R/R_c)^2 + (z/z_c)^2)^{-3\beta/2}, \tag{3.3}$$

where R and z are the radius in the plane of the Milky Way's disk and height off the Galactic plane, respectively, and R_c and z_c are the core radii in those directions. We infer a flattening of the density profile based on the ratio between R_c and z_c.

3.5.2 LB/SWCX Model

We have to model all other known sources of O VII and O VIII line emission (e.g., the LB and residual SWCX) simultaneously with our hot halo density model. This is because the observed emission lines contain the total emission from all these sources and because the sources may produce emission line strengths comparable to one another. However, we emphasize that the goal of this work is to understand properties of the Milky Way's hot gas halo, not the LB or SWCX. We thus develop a parametric model for the LB (similar to the hot gas halo), but we do not claim this parametrization to be the correct physical interpretation for the LB. This still parameterizes the *emission* properties of the LB, which is necessary for correctly interpreting the hot gas halo emission.

We model any emission not due to the Milky Way's hot halo as a volume-filled, constant-density LB. The density and temperature along every sight line is assumed to be the same while the path length of the LB ranges between ≈100–300 pc depending on the direction of the observation. These path lengths come from Na I absorption line measurements of 1005 nearby ($\lesssim$350 pc) stars (Lallement et al., 2003). Figures 4–6 in Lallement et al. (2003) show contours separating local ionized and neutral gas, or equivalently defining an LB edge. The contours show a variety of substructure associated with the LB, although there is a general shape defining the ionized gas region. In our analysis, we parameterize the LB edges with a geometrical model to approximately match the contours discussed above. This implies that the LB

emission varies by a factor of ∼3, depending on the observed direction. We note this parametrization may not accurately represent the physical properties of the LB, specifically the constant-density and volume-filled assumptions. There are reports indicating that the LB is better described as a "cavity" where the emission comes from a wall of material with little emission from diffuse, volume-filling material (e.g., Welsh & Shelton, 2009). However, other works have modeled the LB X-ray emission properties assuming that the bubble is filled with a diffuse plasma along the line of sight (Smith et al., 2007). Differentiating between these scenarios is beyond the scope of this work since this simple parametrization still characterizes the X-ray emission of the LB with some physical motivation.

3.5.3 Temperature Assumptions

All O VII and O VIII line emissivities come from AtomDB version 2.0.2 (Foster et al., 2012). The line emissivities assume an APEC thermal plasma in collisional ionization equilibrium (CIE) at a given temperature (Smith et al., 2001). We initially assume that the halo and LB plasmas are isothermal with temperatures of $\log(T_{halo})$ = 6.3 and $\log(T_{LB})$ = 6.1, resulting in O VII and O VIII line emissivities (in units of photons cm^3 s^{-1}) of $\epsilon_{\mathrm{O\,VII}}$ (halo) = 6.05×10^{-15}, $\epsilon_{\mathrm{O\,VIII}}$ (halo) = 1.45×10^{-15}, $\epsilon_{\mathrm{O\,VII}}$ (LB) = 1.94×10^{-15}, and $\epsilon_{\mathrm{O\,VIII}}$ (LB) = 2.67×10^{-17}. Note that the O VII line emissivities quoted here include the resonance, forbidden, and intercombination lines since the observed emission lines are unresolved.

We assume that the hot gas halo is a constant-temperature plasma in CIE with fixed $\log(T_{halo})$ = 6.3. The strongest observational evidence for the hot gas halo being isothermal comes from modeling the 0.5–2.0 keV spectra of the SXRB for a large number of sight lines. Henley & Shelton (2013) analyzed 110 observations of the SXRB based on a subset of the observations from Henley & Shelton (2012). Their spectral fitting routine was similar to the line measurement procedure above, except

they fit the spectra with thermal plasma models for the hot gas halo instead of measuring the individual O VII and O VIII line intensities. This resulted in hot gas halo emission measures and temperatures for a subsample of the Henley & Shelton (2012) observations. The primary benefit of this approach is the ability to fit for the hot gas halo emission measure and temperature separately from the LB, as opposed to the emission lines that include all emission sources. The drawback to this spectral fitting technique is that one requires more counts to constrain the plasma properties as opposed to just the emission line surface brightnesses, thus requiring more exposure time per observation. We note that Henley & Shelton (2013) discuss an in-preparation study indicating the emission measure and line intensity observations are generally consistent with each other. Furthermore, the sample analyzed in Henley & Shelton (2013) is subjected to stronger temporal and spatial screening criteria than the Henley & Shelton (2012) sample that limit the sample's sky coverage. Thus, the significant increase in sample size and sky coverage of the emission line measurements compared to the emission measure/temperature measurements imply the former are better suited for this study. This study still found that the hot halo temperature showed little variation with a median of 2.22×10^6 K with an interquartile range of 0.63×10^6 K (we discuss their emission measure results in Section 3.7.2). This is also consistent with previous temperature estimates of the hot gas halo from its emission properties (McCammon et al., 2002; Yoshino et al., 2009), thus validating this assumption.

As discussed above, we also assume that the LB is a constant-temperature plasma in CIE with fixed $\log(T_{LB}) = 6.1$. Similar to our constant-density parametrization, this assumption is also debated in the literature. Smith et al. (2007) conducted a shadowing experiment toward the nearby molecular cloud MBM12 to constrain the O VII and O VIII line emission due the LB. They found that the ratio of the emission line strengths implied an LB plasma temperature of 1.2×10^6 K. However, recent

work also implies that the LB may not be in CIE and that non-equilibrium ionization effects can change the interpretation of LB observations (de Avillez et al., 2013). Although departures from CIE are crucial for understanding the physical properties of the LB, the work by Smith et al. (2007) motivates our temperature assumption given our model parametrization.

3.5.4 Optical Depth Considerations

There has been growing evidence for optical depth effects associated with the Milky Way's hot halo plasma. This has been a difficult effect to quantify since both the emission and absorption lines are unresolved, making direct measurements of the line widths impossible. The best evidence for optical depth effects in the plasma comes from weak detections of O VII $K\beta$ absorption lines in several QSO spectra (Bregman & Lloyd-Davies, 2007; Williams et al., 2005; Gupta et al., 2012). These works imply optical depths ranging between $\approx$ 0.1–2.0 depending on the Doppler width assumed for the lines, whether one is observing O VII or O VIII , and which direction one observes (Gupta et al., 2012; Miller & Bregman, 2013).

These optical depth estimates mean assuming that the plasma is optically thin (which is often an implicit assumption) may be incorrect. To estimate the optical depth corrections, we calculate line intensities both in the optically thin limit and assuming a Doppler width of $b = 150$ km s^{-1}. This Doppler width is characteristic of the hydrogen sound speed at this temperature and is consistent with simulations of halo gas (Fukugita & Peebles, 2006; Cen, 2012). The Doppler width is necessary for calculating the absorption cross section of the line transitions (see below). Since these effects are difficult to quantify, we present results both by calculating emission lines in the optically thin limit and by accounting for optical depth corrections.

3.5.5 Line Intensity Calculation

The model line intensity along each line of sight involves a unique calculation given the geometry of the halo, the LB, and our proximity to the Galactic center. For every (l, b) coordinate, there is a unique coordinate transformation between that line of sight distance and galactocentric radius. This coordinate transformation is summarized by the following equations:

$$R^2 = R_o^2 + s^2 \cos(b)^2 - 2sR_o \cos(b) \cos(l), \tag{3.4}$$

$$z^2 = s^2 \sin(b)^2, \tag{3.5}$$

$$r^2 = R^2 + z^2. \tag{3.6}$$

In these equations, R and z are respectively the distance from the Galactic center in the plane of the Milky Way's disk and height off the Galactic plane, r is the galactocentric radius, R_o is the distance between the Sun and the Galactic center (we assume $R_o = 8.5$ kpc), and s is the line of sight distance. These are the equations we use to evaluate the halo emission contribution along every line of sight.

The simplest line intensity calculation we make assumes an optically thin hot halo plasma. The transfer equation under this assumption is:

$$\frac{dI_{thin}}{ds} = j(s) = \frac{n_{halo}(s)^2 \epsilon(T_{halo})}{4\pi}, \tag{3.7}$$

where $n_{halo}(s)$ is the halo density profile along a given line of sight and $\epsilon(T_{halo})$ is the halo line emissivity discussed in Section 3.5.3. This leads to the integral form of our optically thin emission line calculation:

$$I_{thin}(l, b) = \frac{1}{4\pi} \int n_{halo}(s)^2 \epsilon(T_{halo}) ds, \tag{3.8}$$

where we integrate the halo density profile out to the Milky Way's virial radius (≈250

kpc).

We also calculate line intensities while estimating optical depth corrections in the plasma (see Section 3.5.4). This calculation is different than the optically thin calculation by accounting for self absorption/scattering of photons by the plasma and scattering of photons into the line of sight. This changes the transfer equation in the following way:

$$\frac{dI_\tau}{ds} = j(s) - \kappa(s)I(s) + \kappa(s)J(s), \tag{3.9}$$

where $j(s)$ is the same as in Equation 3.7. The absorption coefficient ($\kappa(s)$) quantifies the interaction between photons and ions and is defined as:

$$\kappa(s) = n_{halo}(s)A_O X_{ion} \times \sigma = n_{halo}(s)A_O X_{ion} \times .015 f \lambda b^{-1}, \tag{3.10}$$

where A_O is the oxygen abundance relative to hydrogen, X_{ion} is the ion fraction of the absorbers, σ is the absorption cross section, .015 is a constant with units of cm^2 s^{-1}, f is the oscillator strength of the transition, λ is the transition wavelength in centimeters, and b is the Doppler width of the lines in cm s^{-1}.

Anders & Grevesse (1989) abundances are the most commonly cited solar abundance values, but more current estimates advocate a solar oxygen abundance between 35% and 50% lower than the Anders & Grevesse (1989) value (Holweger, 2001; Asplund et al., 2005). Here, we adopt the Anders & Grevesse (1989) oxygen abundance ($\log(N_O)$=8.93) to be consistent with previous work and with APEC metal abundances. We also assume X_{ion} of 0.5 for both O VII and O VIII (Sutherland & Dopita, 1993) and a Doppler width of 150 km s^{-1}.

The positive scattering term in Equation 3.9 accounts for single-scattered photons into the line of sight and depends on the mean intensity at every point along the line of sight ($J(s)$). The mean intensity follows the formal definition:

$$J(r) = \frac{1}{4\pi} \int_{4\pi} I(r, \Omega) d\Omega. \tag{3.11}$$

We introduce the standard definition of optical depth here, $d\tau = \kappa(s)ds$, to represent Equation 3.9 in a simpler way:

$$\frac{dI_\tau}{d\tau} = \frac{j(s)}{\kappa(s)} - I(s) + J(s) = S(s) - I(s), \tag{3.12}$$

where $S(s)$ is the source function along the line of sight, defined as $j(s)/\kappa(s) + J(s)$. This differential equation can be solved to represent our line intensity calculation accounting for optical depth effects:

$$I_{halo,\tau}(l, b) = \int e^{-(\tau_\circ - \tau)} S(s) d\tau, \tag{3.13}$$

where $\tau_\circ = \int \kappa(s)ds$ is the total optical depth for that line of sight.

These optical depth corrections are an approximation in the single-scattered photon case. The expression for $J(r)$ assumes we know the true mean intensity (or photon density) at every location in the halo for a given set of model parameters. Thus, for each model parameter set, we calculate $J(r)$ once to estimate the scattering contribution to the emission lines. This is only an approximation because $J(r)$ depends on I from all directions, which inherently depends on $J(r)$. We discuss this approximation in more detail in Section 3.6.3.

The LB line intensity calculation is more straightforward than our halo calculation due to our constant density and temperature assumptions. We treat the LB as an optically thin plasma, thus making the line intensity calculation the limiting case of Equation 3.8 for a constant-density plasma. The calculation simplifies to:

$$I_{LB}(l, b) = \frac{n_{LB}^2 L(l, b) \epsilon(T_{LB})}{4\pi}, \tag{3.14}$$

where n_{LB} is our LB density parameter, $L(l,b)$ is the LB path length inferred from Lallement et al. (2003), and $\epsilon(T_{LB})$ is the LB line emissivity discussed in Section 3.5.3.

We finally add our halo and line intensities together to make a total model line calculation defined as:

$$I_{total}(l,b) = I_{LB}(l,b) + I_{halo}(l,b)e^{-\tau_{HI}}, \tag{3.15}$$

where the $e^{-\tau_{HI}}$ term accounts for H I absorption in the Galactic disk. Here we define $\tau_{HI} = \sigma_{HI} N_{HI}$ where σ_{HI} is the H I absorption cross section (Balucinska-Church & McCammon, 1992; Yan et al., 1998) and N_{HI} is the column density for a given line of sight from the LAB survey (Kalberla et al., 2005). This is a necessary step since the observed line intensity measurements account for the total line emission due to all emission sources along the line of sight. Note we assume the LB is the only plasma component between the Sun and $L(l,b)$, and the halo line intensity integration goes from $L(l,b)$ to R_{vir} along a given line of sight. We still attenuate all our model halo emission with the observed H I column densities since starting our halo integration at $\sim$100–300 pc compared with distances securely beyond the Milky Way's H I disk ($\sim$1 kpc) results in $\lesssim$5% differences in the halo line emission. In this way, we calculate a model line intensity along any location in the sky given a set of halo and LB density parameters.

3.5.6 Fitting Procedure

The purpose of our model fitting procedure is to find the parameters for our emission model that best reproduce the observed line intensities. Quantitatively, our goal is to minimize the χ^2, or maximize the likelihood $\mathcal{L} \propto \exp(-0.5\chi^2)$ in our case, between our model and the observations. We utilize the Markov Chain Monte Marlo (MCMC) package `emcee` (Foreman-Mackey et al., 2013) to explore our model parameter space (note we assume uniform prior distributions for all MCMC runs

unless otherwise noted). This package is a Python implementation of Goodman & Weare's Affine Invariant MCMC Ensemble sampler designed for parameter estimation (Goodman & Weare, 2010). We define the input $\ln(\mathcal{L})$ as $-0.5\chi^2$, generate a random set of starting points for our parameters, and allow the code to explore the parameter space to maximize the likelihood.

We examine the marginalized posterior probability distributions of our model parameters to determine the parameter set that best reproduces our observed line intensities. The `emcee` package conveniently outputs these distributions for each sampler run on a set of line observations and for a given plasma type (optically thin or with optical depth corrections). The binned distributions are then fit with Gaussian functions with the centroid being the optimal parameter and the σ parameter being the uncertainty of the optimal parameter. In this way, we constrain the model parameter set that is most consistent with the observations.

3.6 Results

Here we present our results based on our model fitting procedure discussed above. We spend most of our analysis fitting the O VII and O VIII emission line observations separately rather than both measurements simultaneously. This is the better approach since the typical signal-to-noise ratio (S/N) of the O VII measurements (mean = 4.9) are larger than the O VIII measurements (mean = 1.3) in our sample. We also present results with and without optical depth effects present in the line intensity calculation. A summary of our results can be found in Table 3.2. Note that throughout the rest of the chapter, our quoted χ^2 and χ^2_{red} values are from the best-fit values in Table 3.2. We use these metrics to quantify the consistency between our models and the observations.

Table 3.2. Emission Line Model Fitting Results

Lines Fitted	Plasma Type [a]	$n_o r_c^{3\beta}$ (10^{-2} cm^{-3} kpc$^{3\beta}$)	β	n_{LB} (10^{-3} cm^{-3})	σ_{add} [b] L.U.	χ^2_{red} (dof)	$M(<50$ kpc) [c] ($10^9 M_\odot$)	$M(<250$ kpc) [c] ($10^{10} M_\odot$)
O VIII	Optically thin	1.35 ± 0.24	0.50 ± 0.03	0.77 ± 4.10	None	1.08 (644)	$3.8^{+0.3}_{-0.3}$	$4.3^{+0.9}_{-0.8}$
O VIII	τ corrections	1.50 ± 0.24	0.54 ± 0.03	1.13 ± 4.69	None	1.08 (644)	$2.9^{+0.3}_{-0.4}$	$2.7^{+0.7}_{-0.6}$
O VII	Optically thin	0.89 ± 0.06	0.43 ± 0.01	3.86 ± 0.26	None	4.69 (645)	$5.1^{+0.2}_{-0.2}$	$7.9^{+0.8}_{-0.8}$
O VII	Optically thin with σ_{add}	0.76 ± 0.11	0.41 ± 0.03	3.83 ± 0.63	2.1	1.03 (645)	$5.3^{+0.5}_{-0.6}$	$9.1^{+2.2}_{-1.9}$
O VII	τ corrections	0.91 ± 0.06	0.47 ± 0.01	4.02 ± 0.25	None	4.67 (645)	$3.5^{+0.2}_{-0.2}$	$4.5^{+0.5}_{-0.5}$
O VII	τ corrections with σ_{add}	0.79 ± 0.10	0.45 ± 0.03	3.98 ± 0.62	2.1	1.03 (645)	$3.7^{+0.4}_{-0.4}$	$5.2^{+1.4}_{-1.2}$

Note. — Best-fit model parameters and corresponding 1σ uncertainties from our MCMC analysis described in Section 3.5.6.

[a]We calculate model line intensities assuming the plasma is optically thin or with optical depth corrections.

[b]Added uncertainty to the observations required to find an acceptable χ^2_{red}.

[c]Hot gas masses assuming a gas metallicity of 0.3 $Z_\odot$.

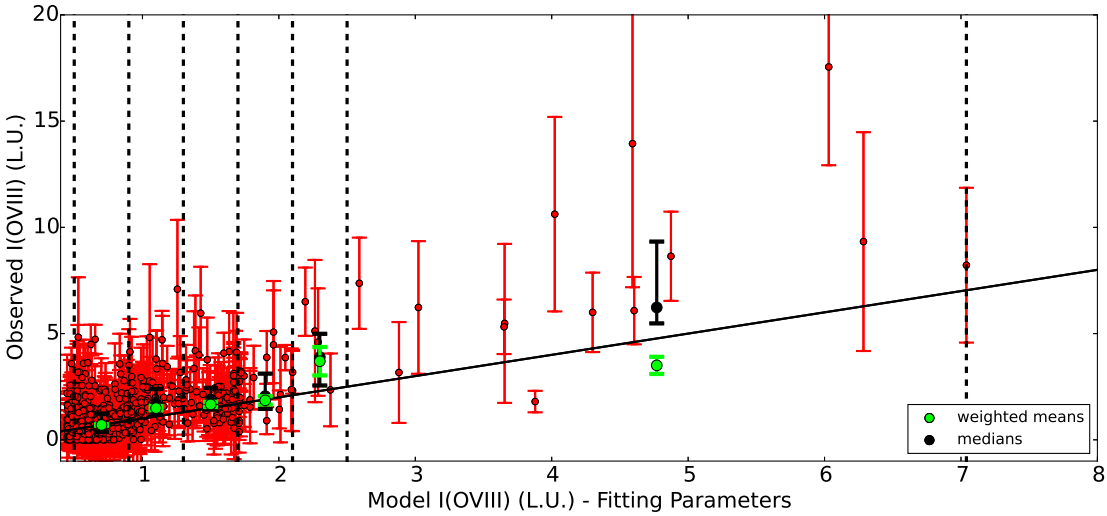

Figure 3.3: Observed O VIII emission line values compared with our best-fit model values assuming an optically thin plasma. The error bars on the observations are the addition of statistical and systematic uncertainties in quadrature. We bin the data and show the medians with first through third quartile regions (black points) along with the weighted means (green points). The vertical black dotted lines are the bin edges used while the black solid line represents the one-to-one line. The binned data indicate our best-fit model reproduces the data.

3.6.1 Analyzing O VIII Line Emission

The O VIII emission line observations are fit very well with our parametric model (χ^2_{red} (dof) = 1.08 (644)) regardless if we assume the plasma is optically thin or apply our optical depth corrections. The β parameter ranges between 0.50 and 0.54 depending on the type of plasma we assume, corresponding to a $\sim r^{-3/2}$ density profile. Figure 3.3 shows the relationship between the observed O VIII and our best-fit model intensities, assuming that the plasma is optically thin. This includes weighted means and medians (with interquartile regions) for several model intensity bins to show that our best-fit model reproduces the O VIII observations. Note that we use smaller bin sizes for $I \lesssim 2$ L.U. (where the unit L.U. = photons cm^{-2} s^{-1} sr^{-1}) to show that we reproduce the general properties of the O VIII observations with our

best-fit model.

The quality of our fit to the O VIII observations significantly improves with the exclusion of one outlier observation (*XMM-Newton* Observation ID 0200730201, (l, b) = 327.59°, +68.92°). This observation has an abnormally large line strength and S/N (I_{obs} = 8.69 L.U., S/N with total uncertainty = 10.84) compared to the expected model value in this direction (I_{mod} = 1.18 L.U.), making it a $\approx 9\sigma$ outlier. We ran our model fitting procedure on our O VIII emission line sample with and without this observation included and found that the best-fit parameters did not change, but the χ^2_{red} (dof) dropped significantly from 1.21 (645) to 1.08 (644). This observation was subjected to the standard flux-filtering procedure discussed above, so we do not expect SWCX contamination to be the cause of this peculiarity. It is, however, located at the tip of the north polar spur, a known region of enhanced X-ray emission thought to be caused by a nearby SN remnant (Miller et al., 2008). We intend to examine this region in more detail in the future, but the quality of our fit results and density model constraints with its removal from the sample indicates that the O VIII observations are well described by our model.

We allow the hot gas halo size to vary as a free parameter to estimate the minimum size halo necessary to still be consistent with the O VIII observations. Initially, we calculate line intensities assuming a halo size of 250 kpc, but our line intensity calculation becomes less sensitive at larger galactocentric radii due to the decrease in density. In other words, our model line intensity values do not change much once we integrate past a line of sight distance of ≈50 kpc. When we allow the halo size to vary, we find nearly identical posterior probability distributions for the original model parameters. The distribution for the halo size is not a well-defined Gaussian like the other parameters, but instead is a flat distribution between 15 and 250 kpc. Thus, we find a minimum halo size of ≈15 kpc. This size scale is consistent with a large, extended gas distribution, rather than a compact disk morphology. Miller &

Bregman (2013) also found similar minimum halo sizes of 32 kpc and 18 kpc at the 95% and 99% confidence levels from a similar analysis of O VII absorption lines.

Similar to the work by Miller & Bregman (2013), we had trouble fitting a flattened density model to the observations. This is likely due to the inferred vales for r_c, R_c, and z_c ($\lesssim$1 kpc) and our lack of observations near the Galactic center. The only way we can constrain R_c and z_c for the flattened model is by limiting the explored parameter space of the other free parameters in our model. We employ boundaries of 0.01–0.50 cm^{-3} for n_o, 0.3–0.8 for β, and 0.0–0.1 for n_{LB} in our MCMC analysis while R_c and z_c are left to explore their full parameter space. When we set these boundaries and assume an optically thin plasma, we find a best-fit model with $R_c = 0.23 \pm 0.09$ kpc and $z_c = 0.27 \pm 0.10$ kpc (χ^2_{red} (dof) = 1.08 (644)). The orthogonal core radii are consistent with each other based on their 1σ uncertainties, indicating that a flattened density profile is not an improvement over our spherical density model.

The hot gas halo density parameters have much tighter constraints than the LB density parameter when we fit the O VIII emission lines. Furthermore, the LB density parameter is consistent with zero, implying that there is little O VIII emission due to the LB. This is seen in our marginalized posterior probability distributions (Figure 3.4) and joint probability distributions (Figure 3.5) for fitting the O VIII lines with an optically thin hot halo plasma. This is a somewhat self-imposed constraint based on our temperature assumption for the LB. The O VIII line emissivity for the LB is $\approx$50 times weaker than the halo line emissivity. However, the LB density parameter would be much larger if there was a global contribution to the O VIII emission lines from the LB. The fact that the LB density parameter does not compensate for the relatively small line emissivity implies that the LB has little contribution to the O VIII . This means the O VIII emission lines are effectively fit with just our hot halo model, making them a good tracer of halo gas.

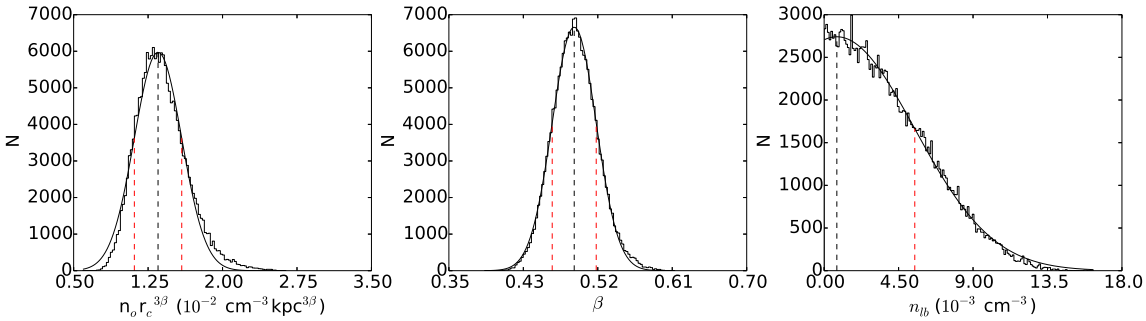

Figure 3.4: Marginalized posterior probability distributions of our model parameters while fitting the O VIII observations with an optically thin plasma. The smooth black curve is a fitted Gaussian function to the distributions while the dashed lines represent the Gaussian centroid (black) and 1σ (red) parameters. These dashed lines in each plot represent the best-fit parameter values and uncertainties quoted in Table 3.2.

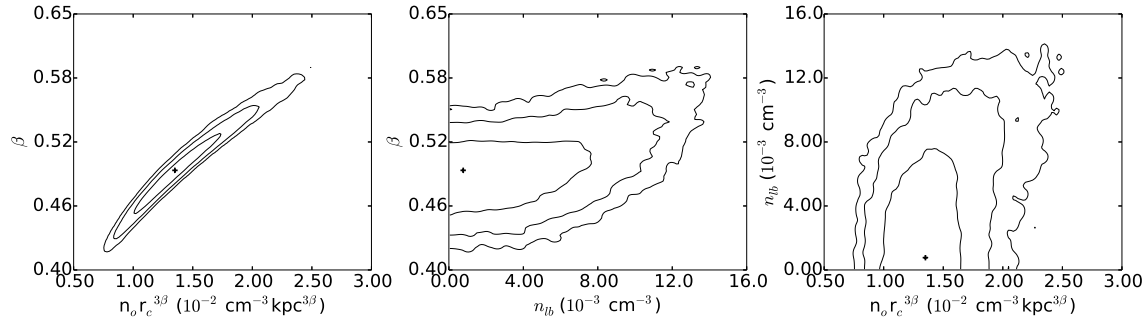

Figure 3.5: Joint posterior probability distributions for our model parameters while fitting the O VIII observations with an optically thin plasma. The lines represent the 1σ, 2σ, and 3σ confidence regions. We trace the 1σ boundary on the left plot (between $n_o r_c^{3\beta}$ and β) to estimate the uncertainties on halo density, mass, etc., with radius. The black crosses represent the best-fit parameter values from the first row of Table 3.2.

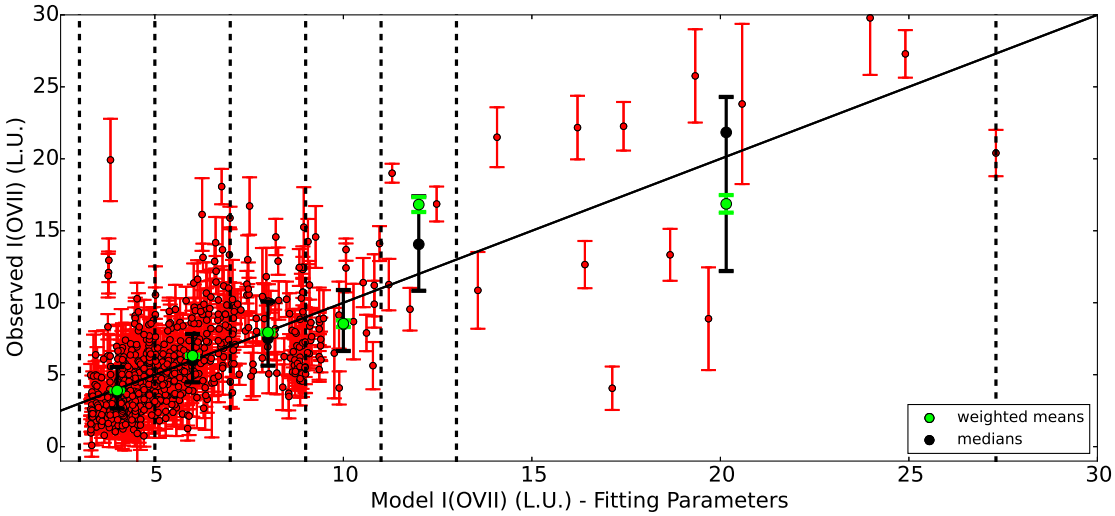

Figure 3.6: Same as Figure 3.3 but for our O VII fit results.

3.6.2 Analyzing O VII Line Emission

The O VII emission line observations show very different fitting results compared to the O VIII observations. Our fitting procedure does find optimal parameters to reproduce the data, but our best-fit model finds a χ^2_{red} (dof) = 4.69 (645) for the O VII observations compared to 1.08 (644) for the O VIII observations. Figure 3.6 shows an analog of Figure 3.3, but for our best-fit O VII optically thin plasma model compared to the O VII observations. While the constraints on the fitted parameters are comparable to the O VIII fitting results (even significantly better for n_{LB}), the quality of our fit implies that the O VII observations are not well described by our parametric model.

Following the approach of Miller & Bregman (2013) on O VII absorption lines, we fit the O VII emission line observations with the inclusion of an additional uncertainty to the observations (σ_{add}). The purpose of this approach is to add the smallest uncertainty to the measurements (σ_{add} is added in quadrature with the statistical and systematic uncertainties) while also finding an acceptable model fit to the data. In this

way, σ_{add} is a crude estimate of the sightline-to-sightline variation or a way to quantify the deviation of the observations from our ideal density model. We find for both an optically thin and optical depth corrected plasma, including $\sigma_{add} = 2.1$ L.U. ($\approx$40% of the median O VII line intensity and $\approx$1.7 times the median O VII uncertainty) results in a χ^2_{red} (dof) = 1.03 (645). Fitting the O VII observations with and without this added uncertainty causes a small change in the best-fit parameters (within 1σ of each other, see Table 3.2). The source of this variation and its relation to the differences between our O VII and O VIII fitting results are discussed in Section 3.7.4.

3.6.3 Optical Depth Effects

Optical depth corrections in our line intensity calculation have a subtle, yet important imprint on our model fitting results. Regardless of whether or not we analyze O VII and O VIII , applying optical depth corrections to our intensity calculation increases both our fitted halo normalization parameter and β. This is likely due to the absorption term dominating the scattering term in Equation 3.9. For a given model parameter set, the absorption term causes the calculated line intensity along a given line of sight to be smaller than the optically thin calculation (i.e., some photons are absorbed along the line of sight). This explains the increase in the halo normalization parameter since more photons must be created everywhere in the halo to account for these absorbed photons and still reproduce the observations. But the absorption term $\kappa \propto n$, implying that denser gas regions are more susceptible to this effect. This explains the increase (or steepening) of the fitted β parameter since regions closer to the Galactic center need to generate more photons compared to the outer regions of the halo to reproduce the observations. This qualitative argument explains the behavior we see in our fit results, but we need to quantify this effect to constrain the true halo gas density profile.

We evaluate these optical depth corrections quantitatively by comparing the true

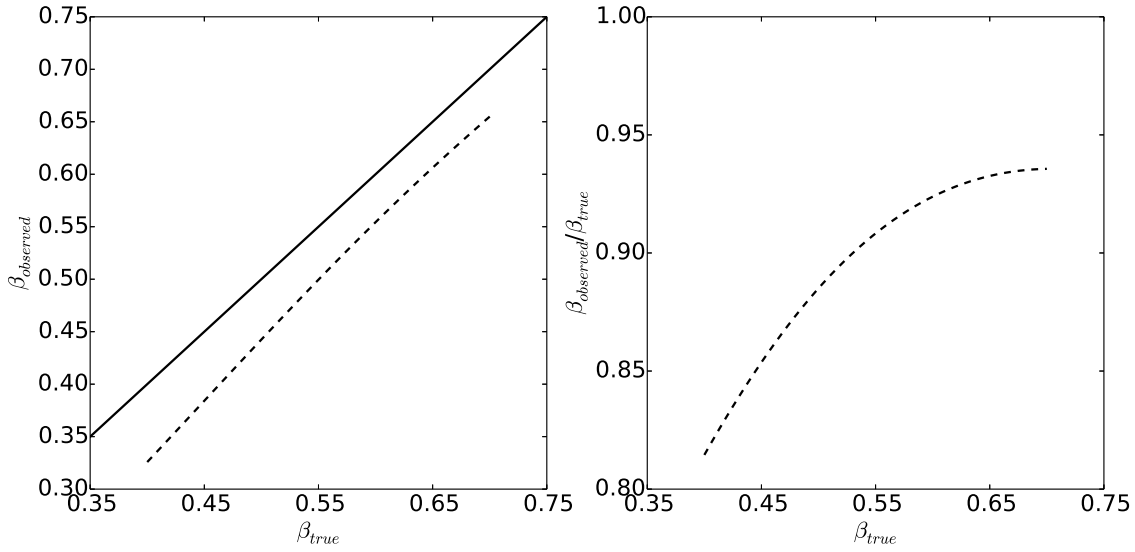

Figure 3.7: Plots illustrating the optical depth effects we model in our fitting procedure. We fit optical depth-corrected observations from a halo density profile with β_{true} assuming the plasma is optically thin. The "observed" or "fitted" $\beta_{observed}$ values compared to the β_{true} values are seen on the left while the right shows the ratio between the two (dashed lines). One sees $\beta_{observed}$ ranges between 80% and 95% of β_{true} for a range of true halo profiles.

and fitted β parameters if the true plasma accounts for optical depth corrections, but we assume that the plasma is optically thin. Given a true model parameter set, $(n_o r_c^{3\beta})_{true}$ and β_{true}, we simulate 160 O VIII emission line observations randomly distributed across the sky accounting for optical depth effects. We then fit the simulated observations assuming the plasma is optically thin. This gives us an estimate of how much the optical depth corrections actually effect our fit parameters. Figure 3.7 shows the results of this procedure for a true halo normalization of 1.3×10^{-2} cm^{-3} kpc$^{3\beta}$ and a range of β_{true}. One sees if we assume the plasma is optically thin, our inferred β would be smaller (shallower) than β_{true}. The strength of this effect depends on β_{true}, but the observed β ranges between 80% and 95% of β_{true}. This is consistent with the differences we see in our own fit results.

At this point it is difficult to assess the accuracy of these optical depth corrections, even with the estimation procedure above. This is because finding solutions to the transfer equation is inherently an iterative process. We assumed in the above calculations that our single calculation of the mean intensity for a given halo parametrization is an accurate representation of the true radiation field everywhere in the halo. This is not necessarily the case when accounting for multiple photon scatterings, assumptions on the turbulence of the medium, etc. Future work will involve developing a Monte Carlo radiative transfer code designed for this system so we can more accurately estimate these effects. However, our calculation above is consistent with our expected scenario where optical depth corrections are largest toward denser regions of the halo (near the Galactic center). Furthermore, the O VIII best-fit parameters are consistent with each other at the 1σ level with and without optical depth corrections. This enhances our argument that we can indeed constrain the true density profile of the Milky Way's hot gas halo.

3.7 Discussion

Here we discuss the implications of our model fitting results for both O VII and O VIII observations. Our constraints on the Milky Way's hot gas halo density profile provide additional constraints on other Milky Way properties, such as its total baryonic mass, mass accretion rates, etc. We will also discuss how our model constraints compare with previous analyses on the Milky Way's SXRB, local O VII absorption lines believed to be caused by the same hot gas halo plasma, and theoretical work on galactic hot halos.

3.7.1 Implications for the Milky Way

The primary quantity we estimate with our halo model constraints is the total hot gas mass within the Milky Way's virial radius (R_{vir}). Estimates of the Milky Way's

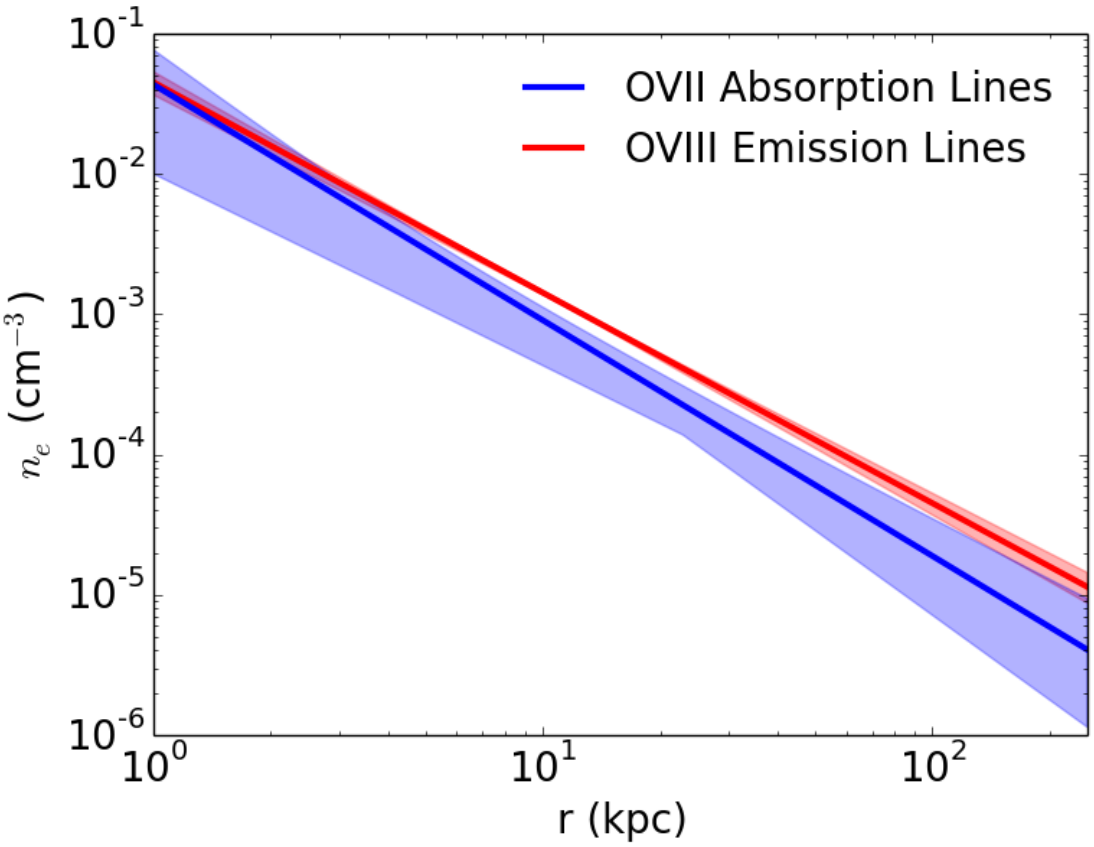

Figure 3.8: Our best-fit density profile as a function of galactocentric radius from fitting the O VIII observations with an optically thin plasma and assuming a gas metallicity of 0.3 $Z_{\odot}$ (red). The blue curve shows the best-fit density profile from Miller & Bregman (2013), who analyzed O VII absorption lines with a similar procedure to this work. The shaded regions represent the 1σ boundaries on these values.

R_{vir} range between 207 kpc (Loeb et al., 2005) and 277 kpc (Shattow & Loeb, 2009) with additional estimates in between (Klypin et al., 2002). Here we adopt a R_{vir} = 250 kpc. Figures 3.8 and 3.9 show our density and integrated mass profiles for our O VIII optically thin plasma results assuming a gas metallicity of 0.3 $Z_{\odot}$ (red curves). The shaded regions indicate the 1σ mass boundaries by tracing the 1σ contour in $n_o r_c^{3\beta}$–β space (see Figure 3.5). Table 3.2 also shows the integrated hot gas mass out to 50 and 250 kpc for every observation/plasma combination we examine. Our model fitting results imply hot gas masses between 2.9–5.3$\times 10^9 M_{\odot}$ within 50 kpc

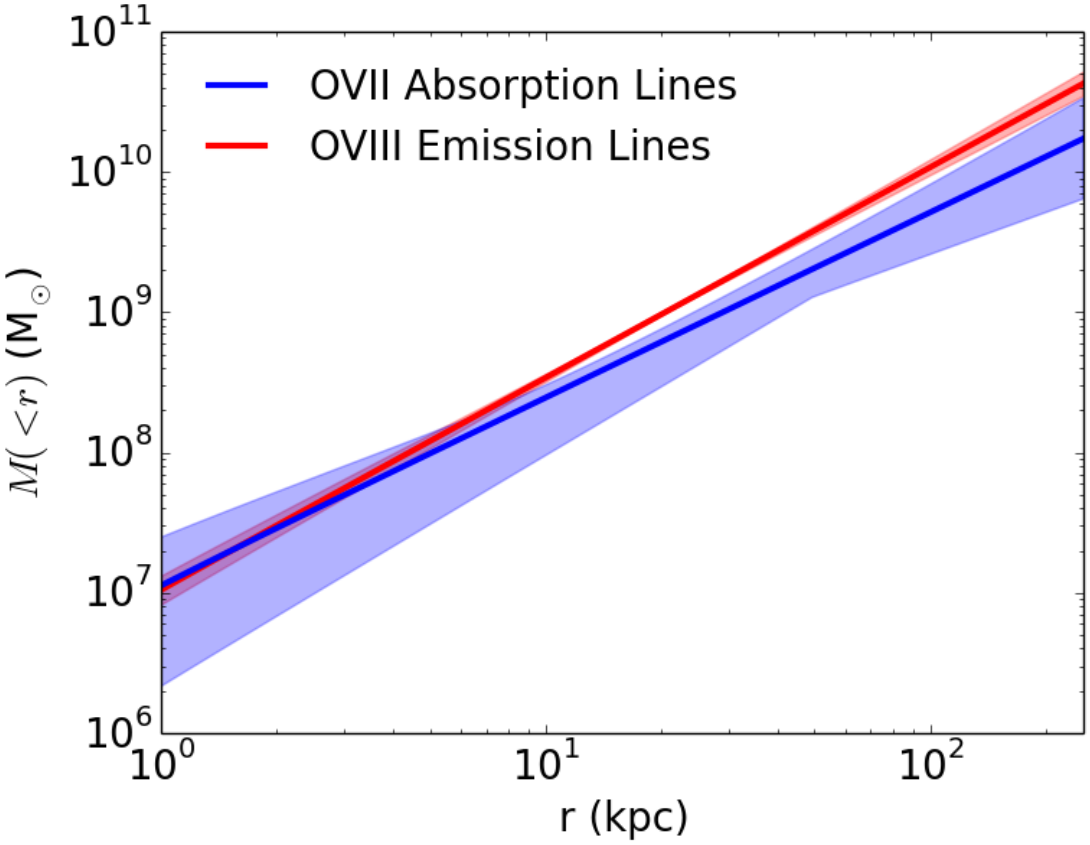

Figure 3.9: Enclosed mass as a function of galactocentric radius for the same density profiles in Figure 3.8. We find characteristic masses of the hot gas halo to be 2.9–5.3×$10^9 M_\odot$ within 50 kpc and 2.7–9.1×$10^{10} M_\odot$ within R_{vir} when we examine all of our fitting procedures.

and 2.7–9.1×$10^{10} M_\odot$ within R_{vir}. These estimates are more tightly constrained if we only consider our O VIII fitting results, which reproduce the data much better than our O VII fitting results. The characteristic masses have a range of 2.9–3.8×$10^9 M_\odot$ within 50 kpc and 2.7–4.7×$10^{10} M_\odot$ within 250 kpc in this case.

We compare these hot gas mass estimates to the known baryonic and total mass of the Milky Way. The known baryonic mass in the Milky Way (stars + cold gas + dust) is between 6–7×$10^{10} M_\odot$ (Binney & Tremaine, 2008). If our hot gas density profile extends out to R_{vir}, the hot gas and known baryonic masses are comparable. We can extend these mass constraints to estimate the Milky Way's total baryon fraction,

defined here as $f_b \equiv M_b/M_{tot}$, where M_b is the total baryon mass and M_{tot} is the total baryon plus DM mass . Current estimates for the Milky Way's virial mass have a range of 1.0–2.4$\times 10^{12} M_\odot$ (Boylan-Kolchin et al., 2013). If we account for this range of virial masses, our range of hot gas masses from our O VIII observations (with 1σ uncertainties), we estimate the Milky Way's total baryon fraction to be between 0.03 and 0.11. Even the upper limit of this range (which makes numerous assumptions on the various mass estimates involved) falls well below the cosmological baryon fraction of $f_b = 0.171 \pm 0.006$ measured by the *Wilkinson Microwave Anisotropy Probe* (Dunkley et al., 2009). This implies that if our best-fit hot halo density profile extends to the R_{vir}, it contains a significant amount of mass compared to the other baryons in the Milky Way but does not account for all of the Milky Way's "missing baryons".

It is possible our hot gas density profile extends past R_{vir}, thus increasing our mass estimates. In particular, we estimate how far our density profile would need to extend to account for all the Milky Way's missing baryons. The Milky Way's virial mass, the other known baryonic mass components (excluding the hot gas mass), and the cosmological baryon fraction discussed above imply a missing baryon mass of $\sim 2 \times 10^{11} M_\odot$. Given the range of assumptions made above for our hot gas mass estimates above (gas metallicity, mass uncertainties, etc.), our halo would need to extend between 3 and 5 R_{vir} to account for all of the Milky Way's missing baryons (Bregman et al., 2015).

The hot mass estimates quoted in Table 3.2 all assume a gas metallicity of 0.3 $Z_\odot$ based on pulsar dispersion measurements toward the LMC. This is a powerful constraint in our analysis since it probes the gas properties out to the fixed distance of the LMC, ≈50 kpc. Here we define the dispersion measure as:

$$DM = \int_0^d n_e(s) ds, \tag{3.16}$$

where d is the distance to the source and $n_e(s)$ is the density profile along the line of sight. Anderson & Bregman (2010) examined numerous DM measurements for sources associated with the LMC. After accounting for DM contributions from the Milky Way's disk and from the LMC itself, they estimated a DM for the Milky Way's hot halo of 23 cm^{-3} pc (Fang et al. (2013) conducted a similar analysis and found similar results). Integrating our O VIII optically thin halo gas model in the LMC direction (l, b = 273.57°, -32.08°) yields a DM of 8.2 cm^{-3} pc. However, the calculated DM $\propto Z^{-1}$ and the line emissivity values used in our analysis assumed Anders & Grevesse (1989) solar abundances, or equivalently a solar metallicity. This means that we match the hot halo DM estimate from Anderson & Bregman (2010) if we assume a halo gas metallicity of $Z = 0.3\ Z_{\odot}$. This estimate assumes that our hot gas halo density profile accounts for all of the residual DM, which may not be the case if there are other unknown electron sources along our line of sight. We thus present this estimate as a lower limit to the hot halo characteristic gas metallicity, $Z \geq 0.3\ Z_{\odot}$.

We also examine the thermal properties of the halo gas given our range of best-fit models. Quantities such as the cooling time and corresponding cooling radius for the halo gas offer insight on whether or not our hot gas model is stable at this moment in the Milky Way's evolution. We adopt the expression for the cooling time from Fukugita & Peebles (2006):

$$t_{cool}(r) = \frac{1.5nkT}{\Lambda(T,Z)n_e(n-n_e)} \approx \frac{1.5kT \times 1.92}{\Lambda(T,Z)n_e \times 0.92}, \tag{3.17}$$

where $\Lambda(T, Z)$ is the bolometric cooling rate as a function of temperature and metallicity (Sutherland & Dopita, 1993). Figure 3.10 shows the cooling time as a function of radius for our best-fit O VIII optically thin plasma model. The colors represent cooling times for different metallicities and the shaded boundaries are calculated in the same way as the mass boundaries in Figure 3.9.

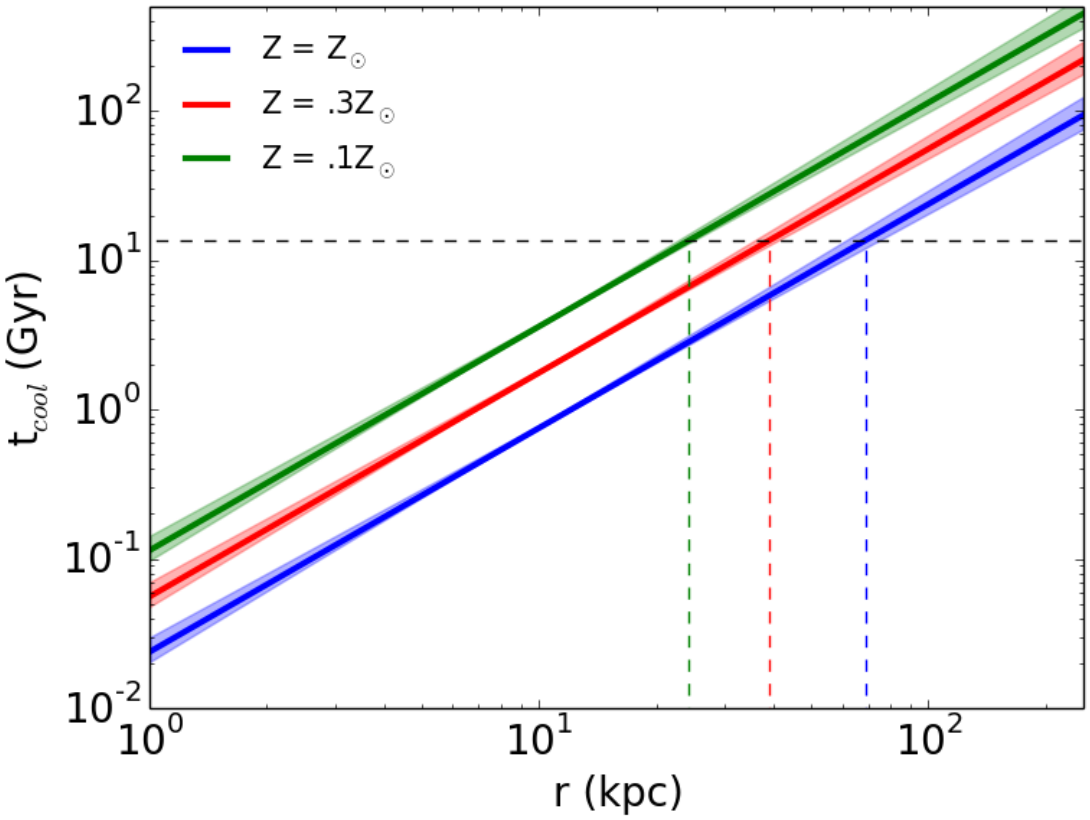

Figure 3.10: Cooling time as a function of radius calculated using Equation 3.17 for the density profile in Figure 3.8. The different colors represent different gas metallicities with more metals resulting in shorter cooling times. The black horizontal line represents the age of the universe (13.6 Gyr) and the colored dashed lines represent the cooling radii for different metallicities (between 25 and 70 kpc).

One useful quantity we estimate from these cooling times is the hot gas halo cooling radius, or where $t_{cool} = 13.6$ Gyr. The cooling radius is a potential constraint on the inner radius to our halo profile since $t_{cool} < 13.6$ Gyr for $r < r_{cool}$, implying that the halo gas would be in a cooler phase at this point in the Milky Way's evolution in the absence of additional heating sources. The dashed lines in Figure 3.10 show the instantaneous r_{cool} for metallicities ranging between 0.1 and 1.0 $Z_{\odot}$, assuming no extra thermal energy has been added to the gas. The range of metallicities result

in r_{cool} between 25 and 70 kpc, with 40 kpc being the cooling radius if $Z = 0.3\ Z_{\odot}$. We emphasize these cooling radius estimates should not be taken as literal estimates for an inner gas halo radius since they completely ignore energy input that is likely present in the form of SNe (Mac Low et al., 1989; de Avillez & Mac Low, 2001) or possibly AGNs (Su et al., 2010) in the Milky Way. These estimates do characterize the physical state of the gas as it currently exists and are important for estimating other quantities related to the cooling time of the gas.

The hot gas cooling time is directly related to the cooling rate and corresponding hot gas halo mass accretion rate. These estimates offer constraints on the halo gas as it cools into a cooler phase gas and eventually falls back on to the Milky Way's disk to eventually form stars. We calculate the current integrated mass accretion rate by integrating the mass within spherical shells divided by the cooling time at the shells' radii. This is represented by the following equation:

$$\dot{M}(r) = \int_0^r \frac{\mu m_p n_{halo}(r')}{t_{cool}(r')} 4\pi r'^2 dr', \tag{3.18}$$

where $\mu = 0.59$ is the mean mass per particle and m_p is the proton. Figure 3.11 shows our integrated mass accretion rate profiles for the same density and cooling time profiles discussed above. Like Figure 3.10, the dashed lines here also represent the cooling radii for each metallicity curve we show. Note the curves flatten for $r > r_{cool}$ because we calculate the *current* mass accretion rate. In this case, regions where $t_{cool} > 13.6$ Gyr have not had time to cool at this point. These results imply that the hot gas halo loses between 0.08 and 0.50 $M_{\odot}$ yr^{-1} in the inner regions of the halo as the gas cools. The upper limits of these accretion rates are similar to simulated accretion rates of halo gas around Milky Way analogs (Fraternali & Binney, 2008). The upper limits here also imply accretion of halo gas may be an important contributor to the Milky Way's current star formation rate (SFR), observed to be between 0.68 and 1.45 $M_{\odot}$ yr^{-1} (Robitaille & Whitney, 2010). Alternatively,

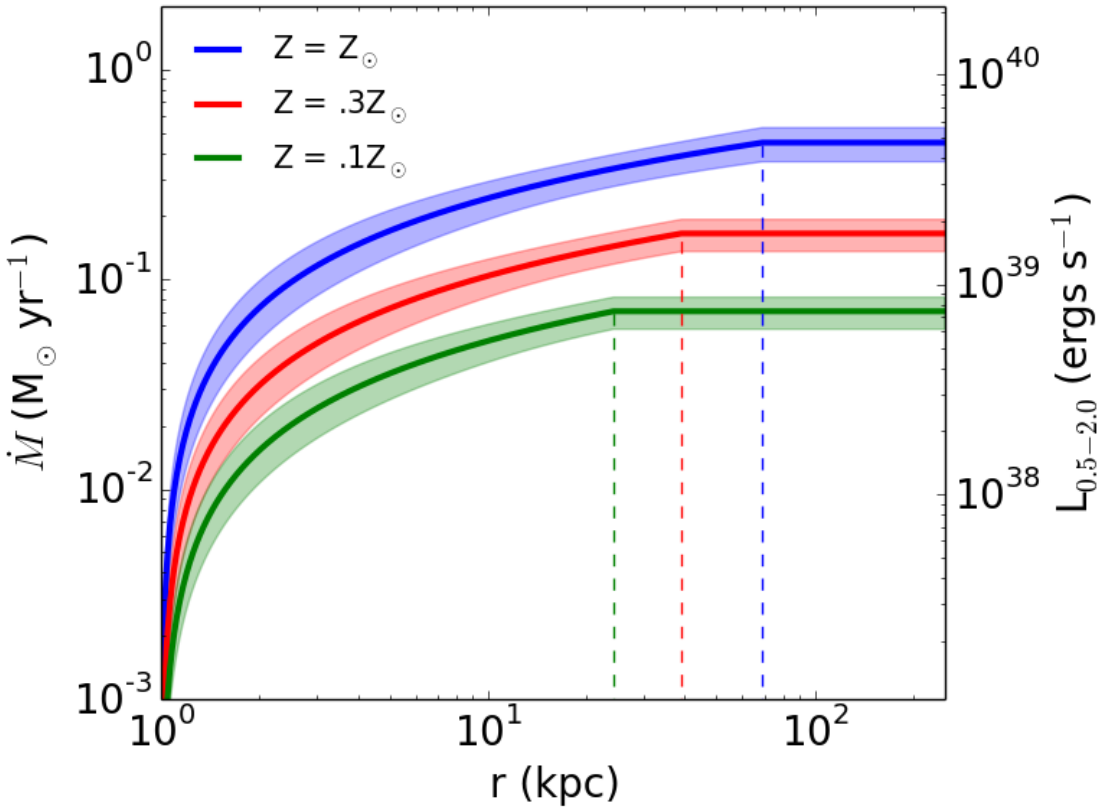

Figure 3.11: Integrated mass accretion rate calculated using Equation 3.18 for the density profile and cooling times in Figures 3.8 and 3.10. The colors and dashed lines are also the same as in Figure 3.10. We find mass accretion rates $\lesssim 0.5\ M_\odot\ \mathrm{yr}^{-1}$, less than the Milky Way's SFR. The right axis of the plot also shows the conversion between $\dot{M}$ and L_X in the 0.5–2.0 keV band (Equation 3.19).

Leitner & Kravtsov (2011) modeled the mass-loss rates and star formation histories for a sample of galaxies (including the Milky Way) to examine if recycled gas from stellar mass loss could sustain observed levels of star formation in the galaxies. They concluded that mass loss from later stages of stellar evolution could provide most of the fuel required to produce the observed Milky Way SFR. This favors a sub-solar halo gas metallicity such that the combination of stellar mass loss and our estimates for accretion from the CGM do not overproduce the observed Milky Way's SFR.

The final quantity we calculate related to the thermal properties of the halo gas is the halo X-ray luminosity (L_X). Specifically, we estimate the 0.5–2.0 keV band luminosity to compare with results from the RASS (Snowden et al., 1997). The 0.5–2.0 keV band luminosity is related to the cooling rate (or mass accretion rate) by the following conversion:

$$L_X(r) = 0.412 \times \dot{M}(r) \frac{1.5kT}{\mu m_p}, \tag{3.19}$$

where $\dot{M}(r)$ is the accretion rate from Equation 3.18 and the constant 0.412 is the conversion between bolometric to 0.5–2.0 keV flux using WEBPIMMS [6]. Figure 3.11 shows this conversion, represented by the scaling on the right side of the figure. Our calculated 0.5–2.0 keV band luminosity has a range of 0.8–5.0$\times 10^{39}$ erg s^{-1}. Previous works have modeled the *ROSAT* 3/4 keV background with non-spherical geometrical models and arrived at similar luminosities. Snowden et al. (1997) modeled the X-ray bulge emission as a cylinder with a radius of 5.6 kpc and density scale height of 1.9 kpc to find a bulge 0.5–2.0 keV luminosity of $\sim 2 \times 10^{39}$ erg s^{-1}. Similarly, Wang (1998) modeled the all-sky *ROSAT* emission with a axisymmetric, disk-like geometry and found a 0.5–2.0 keV luminosity of $\sim 3 \times 10^{39}$ erg s^{-1}. Our calculated 0.5–2.0 keV luminosity is consistent with these estimates of 2–3$\times 10^{39}$ erg s^{-1} for an assumed metallicity of 0.3 $Z_\odot$. This is another indication that the halo gas metallicity is sub-solar, with $Z = 0.3\ Z_\odot$ being a limit that satisfies numerous observational constraints.

3.7.2 Comparing with Previous Observational Work

Our primary comparison with previous work on the Milky Way's hot gas halo follows the work by Miller & Bregman (2013) on O VII absorption lines in QSO spectra. Other works on different observations with different analyses will be addressed, but we focus on this work since the procedure for fitting and analyzing the absorption lines

[6] `http://heasarc.gsfc.nasa.gov/cgi-bin/Tools/w3pimms/w3pimms.pl`

in Miller & Bregman (2013) is identical to our work. Both of these works model the observations with a hot gas halo model defined by a modified β-model (Equation 3.2). The obvious difference between these works is the type of observation analyzed, O VII column densities/equivalent widths ($\propto nL$) in Miller & Bregman (2013) compared to O VII – O VIII emission line intensities ($\propto n^2L$) here. The physical differences between the absorption and emission line density scalings imply that the similarities or differences between the results tell us about the structure of the hot gas halo.

The model fitting results from Miller & Bregman (2013) yielded hot gas halo structural parameters of $n_o r_c^{3\beta} = 1.3^{+1.6}_{-1.0} \times 10^{-2}$ cm^{-3} kpc$^{3\beta}$, $\beta = 0.56^{+0.10}_{-0.12}$, χ^2 (dof) = 31.0 (26) assuming an optically thin plasma and $n_o r_c^{3\beta} = 4.8^{+8.5}_{-3.7} \times 10^{-2}$ cm^{-3} kpc$^{3\beta}$, $\beta = 0.71^{+0.17}_{-0.20}$, χ^2 (dof) = 26.0 (27) accounting for saturation of the absorption lines. Both of these results include added uncertainties to the equivalent width observations of 7.5 and 7.2 mÅ for the optically thin and optical depth correction cases to find acceptable χ^2 values. There are several important comparisons to make between these absorption line results and our fit results from the emission lines in Table 3.2.

We point out that the uncertainties on the absorption line fit parameters are much larger than any of our emission line fitting results. This is likely due to the sample size for the emission lines being ≈20 times larger than the absorption line sample. Even with the relatively small uncertainties on the emission line fit results, the fit parameters are consistent with each other based on their 1σ uncertainties. This consistency applies when comparing the optically thin results separately from the optical depth corrected results. The only exception is the O VII emission line result with optical depth corrections, where we report a shallower β (0.47±0.01) than the absorption line results. This discrepancy is likely due to a combination of our treatment of optical depth corrections (for both the absorption and emission lines) and the overall variation we see in the O VII emission lines. The fact that the model fitting results are consistent with each other allows us to compare additional quantities

based on our halo models.

We provide an additional estimate of the halo gas metallicity (or oxygen abundance) independent from the LMC pulsar dispersion measure constraint. This estimate utilizes the ratio between the absorption and emission line density profile results. The O VII absorption lines/column densities probe $n_{OVII}(r) = X_{OVII} n_{ox}(r)$, where $X_{OVII} = 0.5$ is the O VII ion fraction and $n_{ox}(r)$ is the oxygen density profile. On the other hand, the emission lines are sensitive to $n_e(r)^2$ or $n_H(r)^2$ since $I \propto \int n_e n_{ion} ds \propto \int n_e^2 X_{ion} Z ds$ (see Equation 3.8). Thus, the ratio between the absorption and emission line density profiles is a direct estimate of the gas metallicity distribution, $n_{ox}(r)/n_H(r)$. Here, we take the optically thin electron density distribution from Miller & Bregman (2013) and convert it to an oxygen density distribution using a solar oxygen abundance of $\log(N_O) = 8.74$ from Holweger (2001). For the hydrogen density profile, we use our O VIII optically thin model fitting results in Table 3.2 and assume $n_H = 0.8 n_e$ (note the results in Table 3.2 are for electron densities). When we divide these two density profiles, we find a weak halo gas metallicity gradient of approximately $Z \propto r^{-0.2}$ with a metallicity of $Z = 0.26 \pm 0.10\ Z_\odot$ (1σ) at 10 kpc for Holweger (2001) solar abundances. These results are also consistent with the pulsar dispersion measure gas metallicity constraint of $Z \geq 0.3\ Z_\odot$ discussed in Section 3.7.1.

The most important quantity we compare between this work and the Miller & Bregman (2013) results is the hot gas mass profile. In addition to the best-fit model results in this chapter, Figures 3.8 and 3.9 show the density and mass curves from Miller & Bregman (2013) assuming an optically thin plasma (red shaded area). Like the best-fit parameters, the total mass estimates within R_{vir} are consistent with each other based on the 1σ uncertainties. This implies characteristic hot gas halo masses of $\approx$2–5$\times 10^{10}\ M_\odot$ within R_{vir} regardless if one analyzes the emission or absorption lines.

We compare these mass estimates and underlying density profiles with other independent absorption line studies on the Milky Way's hot gas halo. The comparisons here are limited since previous work on the X-ray absorption lines has either been confined to individual sight lines (e.g., Rasmussen et al., 2003) or compared an ensemble of absorption lines with individual or small samples of emission line measurements (Bregman & Lloyd-Davies, 2007; Gupta et al., 2012). The latter implies that results on the aggregate absorber properties may not be consistent with the aggregate emission properties while the former results are only valid for individual lines of sight.

Examples of detailed analyses of local X-ray O VII and O VIII absorption include Yao et al. (2009b), who analyzed the LMC X-3 sight line, and Hagihara et al. (2010), who analyzed the PKS 2155-304 sightline. Both studies assume the absorbers are due to a local Galactic disk density model and fit their observations with scale heights of $\approx$2 kpc. These result in mass estimates of $\sim 10^8 M_\odot$, significantly lower than our expected values. However, these exponential disk models tend to overproduce the Milky Way's X-ray surface brightness profile (Fang et al., 2013), whereas our results are consistent with this constraint.

Alternatively, the analyses by Bregman & Lloyd-Davies (2007) and Gupta et al. (2012) assume that the absorption lines come from a more extended hot gas halo medium. Bregman & Lloyd-Davies (2007) compared the aggregate column densities of 26 high S/N local O VII absorbers with a single emission measure estimate for the Milky Way's hot halo (McCammon et al., 2002). Gupta et al. (2012) took a similar approach, but they used a smaller sample of absorption lines (8 targets) and an average hot halo emission measure from multiple SXRB observations distributed across the sky (14 measurements from Yoshino et al. (2009) and 26 measurements from Henley et al. (2010)). Both works characterize the Milky Way's hot gas halo as a constant density sphere of size L by comparing an average column density ($\propto nL$) with an average emission measure ($\propto n^2 L$). The two studies disagree, though,

where Bregman & Lloyd-Davies (2007) find $n_e = 9 \times 10^{-4}$ cm^{-3}, $L = 20$ kpc, $M(< L) = 4 \times 10^8 M_\odot$ and Gupta et al. (2012) find $n_e = 2.0 \times 10^{-4}$ cm^{-3}, $L > 139$ kpc, $M > 6.1 \times 10^{10} M_\odot$. The differences come from a number of effects, including the measurement procedure of the equivalent widths and the conversion between equivalent widths and column densities. Regardless of these differences, the constant density sphere models used in these works are not physically motivated. One expects the gas density to decrease with distance away from the Milky Way's center if it is approximately in hydrostatic equilibrium with the Milky Way's DM distribution. We emphasize the benefit of our procedure since we analyze the X-ray emission and absorption lines assuming the same type of density distribution that decreases with galactocentric radius.

Similar to absorption line studies on the Milky Way's hot gas halo, we also compare our results to studies focusing exclusively on the hot gas halo emission properties. These works also range from detailed analyses of the SXRB on individual sight lines (e.g., McCammon et al., 2002; Smith et al., 2007) to analyses on the global emission properties of the SXRB (e.g., Yoshino et al., 2009; Henley & Shelton, 2013). Our work offers an improvement over these previous works since we are using the largest data set to date to characterize the line emission properties of the hot gas halo with a physical model. We nonetheless compare our results as a consistency check with previous work.

As simple consistency checks, we compare our best-fit model line intensities and emission measures to measured values along individual sight lines. McCammon et al. (2002) analyzed a $\sim$1 sr region of the sky at $l, b = 90°, 60°$ using a quantum calorimeter sounding rocket. The sensitivity and spectral resolution of their detectors allowed them to produce precise measurements of the SXRB, including an absorbed component emission measure (EM) of 3.7×10^{-3} cm^{-6} pc. We compute our best-fit O VIII optically thin model EM in this region and find a range of values covering the 1 sr field

of view of 1.6–3.8 $\times 10^{-3}$ cm^{-6} pc with a solid angle-weighted value of $2.6 \pm 0.2 \times 10^{-3}$ cm^{-6} pc. This implies that our computed model EM broadly comports with the observed value and does not overproduce the non-local emission in this region of the sky. While this is only one individual line of sight observation against which we compare our model, our work is designed to characterize the global properties of the hot halo component of the SXRB.

There have been limited studies on the emission properties of the Milky Way's hot gas halo using a large sample of sight lines. These works typically follow a similar fitting procedure to that outlined in Section 3.4.2, except one fits the spectrum with two APEC models for the LB and hot gas halo emission components. Yoshino et al. (2009) analyzed SXRB spectra in nine fields of view with *Suzaku*, but limited their sky coverage to $65^\circ < l < 295^\circ$. Although this sample presents limited sky coverage, they report a range of hot halo EM values between $\approx$0.5–5$\times 10^{-3}$ cm^{-6} pc. Henley & Shelton (2013) presented a similar analysis on 110 *XMM-Newton* observations, but also limited their observation selection to $|b| > 30^\circ$ (among other selection criteria). They report a similar range in EM from $\approx$0.4–7$\times 10^{-3}$ cm^{-6} pc with a median detection of 1.9×10^{-3} cm^{-6} pc. We calculate our best-fit O VIII optically thin EM for the same set of sight lines as Henley & Shelton (2013) and find a range of $\approx$1–7$\times 10^{-3}$ cm^{-6} pc with a median of 2.2×10^{-3} cm^{-6} pc. These model values are also consistent with the work from both Yoshino et al. (2009) and Henley & Shelton (2013).

We have shown in the above discussion our model fitting results are generally consistent with previous observational results on the local X-ray absorption and emission line observations. The methods in previous works range from detailed studies on individual sight lines to analyzing the global properties of either the emission or absorption lines in question. The physical interpretation of the emission and absorption lines also ranges from a compact exponential disk of hot gas material to more extended distributions. We have attempted to unify this picture by analyzing both

a large sample of emission and absorption line observations independently, but with the same model fitting procedure. With these comparisons, we have shown that our modified β-model for an extended hot gas halo density profile can describe both the emission and absorption line observations, but is also broadly consistent with previous independent projects on the various types of observations.

3.7.3 Comparing with Simulations

We compare our hot gas density model results with simulations of isolated Milky-Way-sized halos. Specifically, we focus on simulations designed to analyze hot diffuse halo gas in the galaxies. There are many details to compare between our parametric model results and these simulations, but here we compare the most basic properties of the halo gas: the density estimates at different radii, the mass contained in hot gas, and the gas metallicity.

Our best-fit halo density model is consistent with recent simulations on the Local Group system. Nuza et al. (2014) analyzed the distribution of all gas phases in a suite of simulations of the Local Group as part of the Constrained Local Universe Simulations project. Figure 3.12 shows our best-fit halo density profile compared to their hot gas ($T \geq 10^5$ K) density profile for the Milky Way analog. Even though their simulations show some variation (the gray shaded region represents density profile estimates from random viewing angles of their simulated galaxy), the two density profiles are remarkably similar for $r \gtrsim 50$ kpc. The discrepancy within $\approx$50 kpc is likely due to feedback mechanisms within the galactic disk and contributions from gas $< 10^6$ K. This recent result indicates that the structure of our model hot gas halo is qualitatively similar to current simulations.

We compare our best-fit halo mass estimates within R_{vir} to hot gas halo simulations. These simulations are all designed to analyze different aspects of their host galaxies, but typically estimate hot gas masses with a range of 10^{10}–10^{11} $M_{\odot}$. For

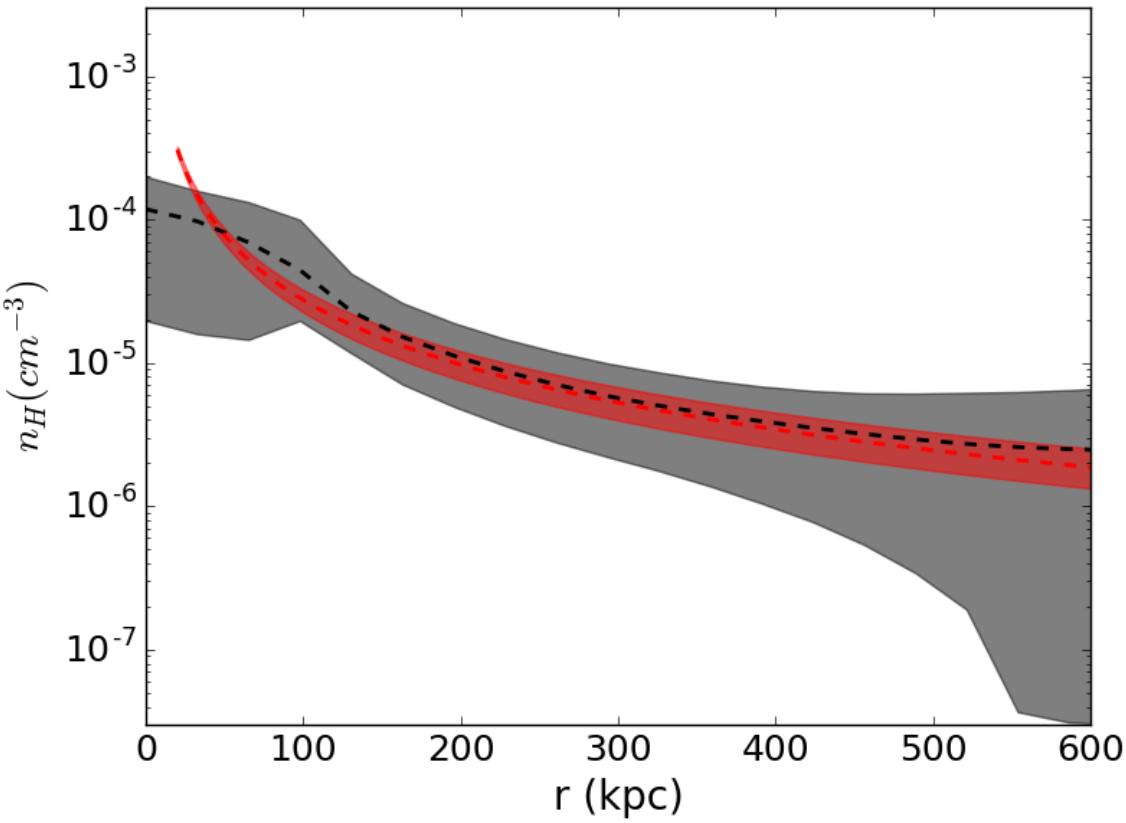

Figure 3.12: Our best-fit model density profile (red) compared to a recent suite of simulations from Nuza et al. (2014). They calculate the hot gas density profile for many random projections with the black dashed line and shaded region representing the mean and standard deviation of their calculations. We find excellent agreement with these simulations for $r \gtrsim 50$ kpc.

example, the Nuza et al. (2014) simulations discussed above were designed to analyze gas properties in the Local Group medium and report hot gas masses between 4 and $5 \times 10^{10} M_{\odot}$ within R_{vir} of their Milky Way analog. Another example by Marinacci et al. (2014) utilized the moving-mesh code `AREPO` to analyze the relationship between stellar feedback processes and diffuse gas in galaxies. They report a wider range of warm plus hot gas masses between 10^{10}–10^{11} $M_{\odot}$. N-body simulations from Sommer-Larsen (2006) focused specifically on the hot gas mass contained within R_{vir}

of Milky-Way-type galaxies and found hot gas masses comparable to the stellar masses of the host galaxies ($\approx 2.3 \times 10^{10} M_{\odot}$). This result is qualitatively similar with our hot gas mass estimates compared to the Milky Way's stellar mass. In an entirely different approach, Feldmann et al. (2013) used hydrodynamical simulations to analyze cosmic rays scattering off the Milky Way's hot gas halo and their observational signatures in the diffuse gamma-ray background (Keshet et al., 2004). They report H II gas masses of [0.2, 1.0, 3.5] $\times 10^{10} M_{\odot}$ for r = [50, 100, 200] kpc. These results indicate that our best-fit model hot gas mass estimates between 2.7 and $4.7 \times 10^{10} M_{\odot}$ within 250 kpc are consistent with current simulations of galaxy formation.

Our lower limit on the halo gas metallicity of $\geq$0.3 $Z_{\odot}$ is consistent with simulations as well. The halo gas metallicity tends to have more variation in the literature depending on the simulation and the investigated galaxy evolution properties (typically feedback mechanisms). For example, hydrodynamical simulations analyzing hot gas halos as shock-heated material accreted on the DM potential wells of their galaxies favor sub-solar halo gas metallicities of $\lesssim$0.5 $Z_{\odot}$ (Toft et al., 2002; Cen & Ostriker, 2006; Cen, 2012). On the other hand, the Marinacci et al. (2014) simulations discussed above were designed to analyze stellar feedback properties on the hot gas. These results predict a metallicity gradient in the halo gas starting $\sim$1 $Z_{\odot}$ near the galaxy disk and dropping below $\sim$0.3 $Z_{\odot}$ for $r \gtrsim 20$ kpc. The lower limit we place on the Milky Way's halo gas metallicity of $\geq$0.3 $Z_{\odot}$ implies a minimal level of enrichment from the Milky Way's disk.

3.7.4 O VIII – O VII Discrepancy

The O VII and O VIII observations yield 2–3σ discrepancies for our best-fit model parameters (see Table 3.2). For example, the difference between our O VII and O VIII fitted β with optical depth corrections and with an added uncertainty to the O VII observations is 0.09, a 2.6σ discrepancy. Not only are these differences statistically

significant, but the O VII fitting results yield systematically smaller halo gas normalization and β parameters compared to the O VIII fitting results. Moreover, our best-fit models for the O VII observations consistently yield unacceptable χ^2_{red} values (χ^2_{red} (dof) = 4.7 (645)), whereas the O VIII observations are well described by our parametric model (χ^2_{red} (dof) = 1.1 (644)). Although these discrepancies do not significantly affect our mass estimates, they contain additional information on the physical properties of the hot halo or LB.

The difference in the fitting parameters may be evidence for a radial temperature gradient in the Milky Way's hot gas halo. The O VII and O VIII volumetric line emissivities peak at similar temperatures of $\log(T) = 6.3$ and 6.5 respectively (Sutherland & Dopita, 1993; Foster et al., 2012), implying the halo gas O VII and O VIII emission lines arise from a single plasma with the same density and temperature profile. To address this constraint, we note our model line intensities depend both on density and temperature ($dI \propto n^2\epsilon(T)$ for every location along each line of sight). Thus, changes to our flat temperature distribution would change our best-fit density profiles to produce the same model line emission. We represent these changes by the following equation:

$$n^2_{ion,flat}(r)\epsilon_{ion}(T_{flat}) = n^2_{ion,grad}(r)\epsilon_{ion}(T_{grad}(r)), \tag{3.20}$$

where the *flat* subscripts refer to our isothermal halo model fitting results and the *grad* subscripts refer to the corrected density profile with a new temperature gradient.

We estimate temperature and corrected density profiles of the halo gas using the ratio between our best-fit optically thin models for the O VIII and O VII observations separately. We utilize Equation 3.20 for our O VIII and O VII model fitting results to estimate a temperature gradient as:

$$\frac{n^2_{OVIII,flat}(r)\epsilon_{OVIII}(T_{flat})}{n^2_{OVII,flat}(r)\epsilon_{OVII}(T_{flat})} = \frac{n^2_{OVIII,grad}(r)\epsilon_{OVIII}(T_{grad}(r))}{n^2_{OVII,grad}(r)\epsilon_{OVII}(T_{grad}(r))} = \frac{\epsilon_{OVIII}(T_{grad}(r))}{\epsilon_{OVII}(T_{grad}(r))}, \tag{3.21}$$

where $n_{OVIII,flat}$ and $n_{OVII,flat}$ are the best-fit models presented in Table 3.2 for an optically thin plasma. The $n_{OVIII,grad}$ and $n_{OVII,grad}$ terms cancel out because we assume the O VIII and O VII observations come from the same plasma (i.e., the plasmas are cospatial). Thus, we take the ratio on the left side of Equation 3.21 and map it into a temperature gradient $T_{grad}(r)$. Figure 3.13 shows these temperature corrections create a relatively small change in temperature with T decreasing from 2.4–1.5$\times10^6$ K from 1–250 kpc (the $T \propto r^{-0.08}$ line is only included for illustrative purposes). This new temperature gradient changes our best-fit density profiles to make the O VII and O VIII fits consistent with each other based on Equation 3.20. The corresponding density profile is consistent with the initial O VII and O VIII fit results within $\approx$ 10 kpc and remains consistent with the O VII fit results beyond $\approx$ 10 kpc (see shaded regions in Figure 3.13). This implies the corrected density profile predicts similar masses, cooling times, cooling rates, etc. as our O VII flat temperature profile fit results (5–9$\times10^{10}M_{\odot}$ within 250 kpc). We also note these corrected density and temperature profiles are significantly different from adiabatic profiles in hydrostatic equilibrium with the Milky Way's DM distribution used by Maller & Bullock (2004) and Fang et al. (2013) to analyze the structure of the Milky Way's hot gas halo (maroon curves in Figure 3.13). This inconsistency indicates there has been heating or cooling occurring in the halo gas.

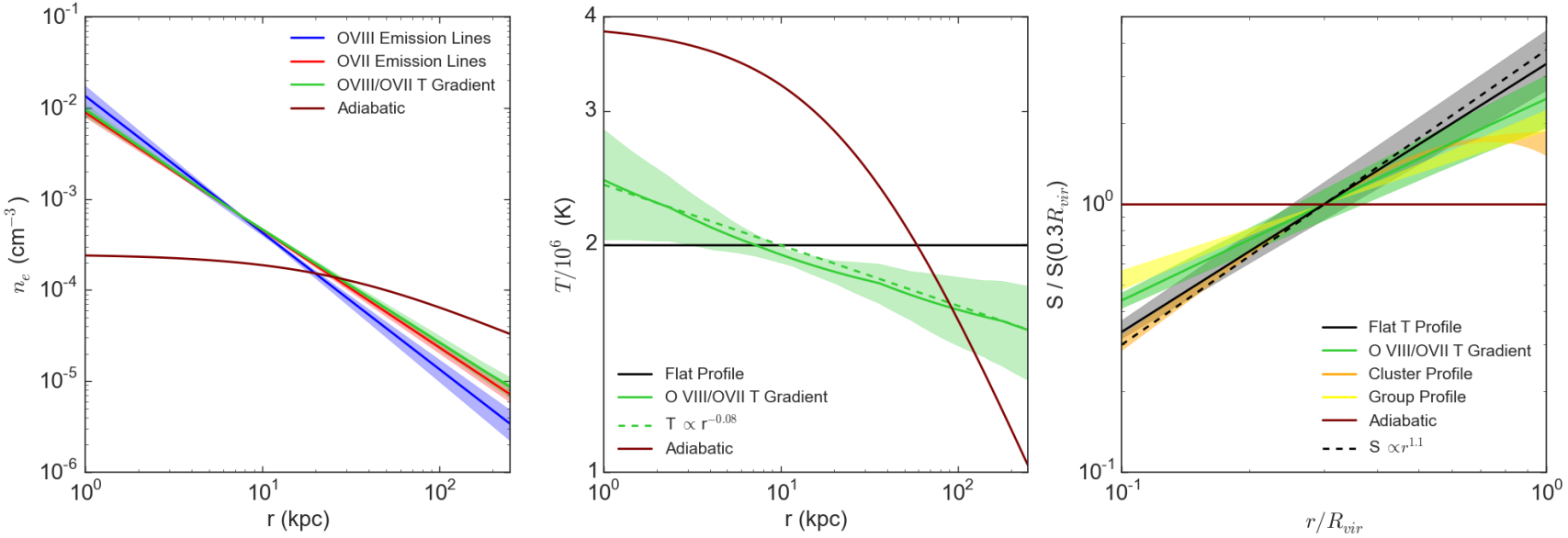

Figure 3.13: Left: density profiles from fitting the O VII (red) and O VIII (blue) emission observations with an optically thin plasma. The green line is the corrected density profile using the inferred temperature gradient from the red and blue density profiles. The maroon line is the adiabatic halo density profile used by Maller & Bullock (2004) and Fang et al. (2013). Center: initial isothermal temperature profile (black line) compared to the corrected halo temperature profile using the O VII and O VIII model fitting results (green solid line). The green dashed line represents a $T \propto r^{-0.08}$ slope for reference. The maroon line again represents the adiabatic halo gas temperature profile. Right: entropy profiles scaled by $S(0.3R_{vir})$ for our initial flat temperature fitting results (black solid line), corrected temperature and density model (green line), galaxy groups (yellow shaded region), and galaxy clusters (orange shaded region). The black dashed line represents an $S \propto r^{1.1}$ slope (see text for details) while the maroon line is a flat, or adiabatic entropy profile.

Given a new temperature and density profile for the halo gas, we calculate the entropy profile for the Milky Way's halo gas and compare it to the observed entropy profiles of galaxy groups and clusters. Figure 3.13 shows our model entropy profiles (defined as $S = kT/n_e^{2/3}$) scaled by the entropy at 0.3 R_{vir}. The black and green shaded regions show the 1σ boundary regions for the flat temperature and corrected temperature profiles respectively. The orange shaded region represents the "universal" entropy profile for galaxy clusters determined from measuring the intracluster medium density and temperature profiles of approximately 15 galaxy clusters (Walker et al., 2012; Okabe et al., 2014). This profile closely follows an $S \propto r^{1.1}$ slope (black dashed line) within 0.3 R_{vir}. This slope is the characteristic entropy profile for gas accreting onto virialized objects in the absence of radiative cooling or additional heating due to feedback (Tozzi & Norman, 2001; Voit et al., 2005). The yellow shaded region represents results from similar studies on samples of galaxy groups, with slopes ranging between $S \propto r^{0.5-0.7}$ (Finoguenov et al., 2007; Panagoulia et al., 2014). Our corrected halo gas entropy profile is bounded by the scaled group and cluster profiles, and the profile uncertainties indicate that they are consistent with both profile shapes. We also note the inconsistency between our profiles and the group/cluster profiles compared to the adiabatic profile from Maller & Bullock (2004) and Fang et al. (2013). Our entropy profiles are consistent with the observed "universal" profiles around more massive virialized objects.

The exercise discussed above is a simple estimate that yields a relatively minor temperature gradient compared to the observed halo gas temperature of $\approx 2 \times 10^6$ K (assuming the halo gas is isothermal). We remind the reader that it is unclear if the O VII fit results are a valid description of the halo gas profile given the fits are still unacceptable at this point. This caveat implies that we are missing some emission contribution in our model that has a much stronger effect in O VII line emission compared to O VIII emission.

We examine if SWCX emission contributes to the O VII – O VIII χ^2_{red} discrepancy, although we conclude it is not the primary driver of the unacceptable O VII fits. This is a possible source for this discrepancy since the typical SWCX O VII emission is larger than the typical O VIII line emission (Koutroumpa et al., 2007). The relative strengths of the typical O VII versus O VIII line emission due to SWCX reactions may cause many of the O VII observations to deviate from our smooth model predictions more than the O VIII observations. However, the sample we are analyzing was already subjected to a reasonable SWCX screening procedure outlined in Henley & Shelton (2012) (their flux-filtered sample). This screening likely removed most of the geocoronal SWCX emission, which should correlate with the solar wind proton flux (Robertson & Cravens, 2003a,b; Robertson et al., 2006). We also analyze a subset of observations near the ecliptic plane (see gray strip in Figure 3.2) to probe heliospheric SWCX contamination. This contamination is expected to be stronger near the ecliptic plane, although with longer temporal variation compared to geocoronal SWCX emission (Robertson & Cravens, 2003a; Koutroumpa et al., 2006). We find no noticeable excess in the emission line strengths, the strengths of the observed minus model residual emission, or the outlier strength (defined as the absolute value of the difference between the model and observed value divided by the measurement uncertainty) for sight lines near the ecliptic plane compared to sight lines in an equivalent gray strip rotated by 180° in Galactic longitude. For example, the χ^2_{red} (dof) for the optically thin O VII observations is 5.35 (64) for the ecliptic plane strip and 5.39 (50) for the rotated ecliptic plane strip. These lines of evidence imply that the *global* properties of the emission line observations are not affected by SWCX emission, even for the O VII observations. There is likely a different source for our O VII versus O VIII fit quality discrepancy.

The more likely explanation to our O VII – O VIII fit discrepancy is variation in the physical properties of the X-ray-emitting gas creating these emission lines.

Specifically, variation in the density/temperature structure associated with the LB or inner regions of the hot gas halo can cause the observations to deviate from a smooth density profile. Variation in the LB plasma is a likely scenario here because the "local" emission source (SWCX or LB) contributes more O VII than O VIII emission (if any) compared to the "non-local" emission source. This evidence comes from a range of shadowing experiments (e.g., Kuntz & Snowden, 2000; Smith et al., 2007; Koutroumpa et al., 2011) and from additional analyses on the *ROSAT* R12 band maps (e.g., Galeazzi et al., 2014). These results indicate that regardless of the physical properties of the "local" X-ray-emitting gas, the emission is patchy across the sky. On the other hand, the O VII absorption line analysis by Miller & Bregman (2013) showed they could only find an acceptable fit to the observations with the inclusion of an additional uncertainty of 7.5 mÅ to the measured equivalent widths (≈30% of the average equivalent width). This variation is comparable to what we see with the O VII emission lines, where we must add an additional 2.1 L.U. uncertainty to the measurements (≈40% of the median O VII line intensity) to find an acceptable χ^2_{red}. Given these two types of analyses, we cannot definitively say which plasma causes the O VII absorption/emission line variation. Understanding the source of the variation is beyond the scope of this work, but will involve detailed analysis on physical models of the local ISM (de Avillez et al., 2013).

3.8 Summary

We have presented an in-depth analysis of the Milky Way's SXRB using the largest sample of O VII and O VIII emission lines to date. Our sample is a subset of the work by (Henley & Shelton, 2010, 2012), who presented O VII and O VIII emission line measurements of the SXRB from *XMM-Newton* archival data. We applied additional observation screening methods to their sample to maximize our sensitivity to emission from the Milky Way's hot gas halo. These screening methods left us with 649 out of

1003 observations from the Henley & Shelton (2012) flux-filtered sample covering all regions of the sky outside the Galactic center and Galactic plane. The combination of the size and sky coverage of this sample allows us to constrain the physical properties of the Milky Way's hot gas halo much better than previous works.

The advantage of this work over previous studies on the SXRB is that our model fitting procedure to the emission lines is identical to the work by Miller & Bregman (2013) on O VII absorption lines. This is critical since the both types of observations are likely due to the same plasma sources in the Milky Way (although the different sources are expected to have different strengths in absorption and emission). Thus, this work is a positive step toward unifying the absorption and emission line observations associated with the Milky Way's ISM/CGM.

We find an acceptable fit to the O VIII observations with a diffuse volume-filled hot gas halo model described as a modified β-model (a power law). Our best-fit fitting results depend on whether we account for optical depth effects in the plasma, but we constrain β to be between 0.50 and 0.54 without and with these corrections. We also include a simple parametrization for LB emission in our model, but its contribution to the O VIII emission lines is negligible ($\lesssim$0.02 L.U.) and it is unconstrained by the observations.

The O VII observations show considerably different behavior than the O VIII observations, both in the quality of our best-fit models and in the best-fit parameters themselves. The best-fit β parameter is consistently smaller (shallower) when we analyze the O VII observations compared to the O VIII observations. This is possibly due to departures from an isothermal halo profile assumed in the analysis. This interpretation is speculative however, since our best-fit parameters to the O VII observations yield unacceptable χ^2_{red} (dof) = 4.7 (645). This implies there is significant sightline-to-sightline variation in the O VII observations that deviate the observations from our smooth hot halo + LB emission model.

The implications of our model-fitting results are discussed in detail in Section 3.7. We reiterate the most important results here.

1. The O VIII model fitting results are consistent with previous work on O VII absorption lines utilizing the same model fitting procedure (Miller & Bregman, 2013). The fact that these results are consistent with each other implies we are starting to develop a cohesive picture of the Milky Way's hot gas halo structure. Specifically, this result is a positive step toward unifying the emission and absorption line observations that are due to the Milky Way's hot gas halo.

2. The inferred mass from our O VIII best-fit hot gas halo parameters ranges between 2.7–4.7$\times10^{10} M_{\odot}$ within 250 kpc. This mass is considerable when compared to the known baryon mass in the Milky Way (6–7$\times10^{10} M_{\odot}$), but is 6–10 times smaller than the missing baryon mass in the Milky Way.

3. Several computed quantities from our best-fit model results suggest a gas metallicity of 0.3 $Z_{\odot}$. The halo gas metallicity must be $\geq$0.3 $Z_{\odot}$ to not overproduce the residual pulsar DM toward the LMC due to a hot gas halo component. We also are consistent with the previously observed 0.5–2.0 X-ray luminosity for the Milky Way ($\sim 2 \times 10^{39}$ erg s^{-1}; Snowden et al., 1997) if we assume a gas metallicity of 0.3 $Z_{\odot}$. An independent estimate of the halo gas metallicity using absorption line profile results from Miller & Bregman (2013) and these current emission line results also suggests a gas metallicity of $\approx$0.3 $Z_{\odot}$. This metallicity is also consistent with simulations of galactic coronae (Toft et al., 2002; Cen & Ostriker, 2006; Cen, 2012).

4. The discrepancy between our O VIII and O VII fit results is likely due to variation in the emission properties of the LB rather than residual SWCX emission. This patchiness in the emission has been analyzed in the ROSAT R12 band (1/4 keV; Kuntz & Snowden, 2000; Galeazzi et al., 2014), which would have

a stronger effect on the O VII emission lines compared to the O VIII emission lines. We attempt to quantify this patchiness in the emission lines by adding an uncertainty to the O VII observations. We find we must add an uncertainty of 2.1 L.U. to the emission lines (≈40% the median line strength) to find an acceptable χ^2_{red}.

5. Optical depth corrections are likely necessary in our model emission line calculation since evidence suggests the hot halo plasma has optical depths of order unity (Williams et al., 2005; Gupta et al., 2012; Miller & Bregman, 2013). We attempt to quantify these effects and find optical depth corrections to the emission line calculations increase (steepen) our fitted β by about 10%.

Future work will involve rectifying the final two topics discussed above. We aim to reproduce the sightline-to-sightline variability in the O VII observations with a physical model plasma model including our smooth hot gas halo profile with a presumably more clumpy or variable LB model. This will involve detailed observational and theoretical work on the local ISM/CGM.

We also intend to utilize more detailed radiative transfer codes to quantify the optical depth effects present in the plasma. Our simple parametrization of the optical depth corrections indicates these effects may be minor, but they will provide even tighter constraints on the Milky Way's hot gas density profile. This will lead to improved estimates on quantities such as the mass and metallicity of the halo gas.

Even with the above limitations, we emphasize the significant improvement these results are compared to previous work on the Milky Way's hot gas halo. Not only have we dramatically reduced the density and resultant mass uncertainties for the Milky Way's hot gas halo, but have done so while utilizing emission lines rather than absorption lines. This supports the power of these new large samples of emission lines (several hundred sight lines) compared with the much smaller absorption line samples

(≈30 sight lines). We intend to use these emission line observations and modeling techniques for future work on other Galactic-scale features observed in X-rays.

CHAPTER IV

The Milky Way's Hot Gas Kinematics: Signatures in Current and Future O VII Absorption Line Observations

4.1 Preface

This chapter is adapted from work of the same title appearing in the Astrophysical Journal, Volume 818, 112 (Miller et al., 2016), and is coauthored by Edmund J. Hodges-Kluck and Joel N. Bregman. My contributions include all absorption line modeling and subsequent analysis. The models presented here complement the observations discussed in Chapter V and the corresponding companion paper (Hodges-Kluck et al., 2016).

4.2 Abstract

Detections of $z \approx 0$ oxygen absorption and emission lines indicate the Milky Way hosts a hot ($\sim 10^6$ K), low-density plasma extending $\gtrsim$50 kpc into the Milky Way's halo. Current X-ray telescopes cannot resolve the line profiles, but the variation of their strengths on the sky constrains the radial gas distribution. Interpreting the O VII Kα absorption line strengths has several complications, including optical depth and

line of sight velocity effects. Here, we present model absorption line profiles accounting for both of these effects to show the lines can exhibit asymmetric structures and be broader than the intrinsic Doppler width. The line profiles encode the hot gas rotation curve, the net inflow or outflow of hot gas, and the hot gas angular momentum profile. We show how line of sight velocity effects impact the conversion between equivalent width and the column density, and provide modified curves of growth accounting for these effects. As an example, we analyze the LMC sight line pulsar dispersion measure and O VII equivalent width to show the average gas metallicity is $\gtrsim 0.6 Z_{\odot}$ and $b \gtrsim 100$ km s^{-1}. Determining these properties offers valuable insights into the dynamical state of the Milky Way's hot gas, and improves the line strength interpretation. We discuss future strategies to observe these effects with an X-ray instrument that has a spectral resolution of about 3000, a goal that is technically possible today.

4.3 Introduction

The observed dynamics of stars and gas in galaxies have played vital roles in interpreting the content, structure, and formation of galaxies. Baryons respond to the total galactic gravitational field, implying the observed velocity structure probes the underlying dark matter distribution. Measurements of the H I rotation curves of late-type galaxies (e.g., Kent, 1987; de Blok et al., 2008), the stellar velocity dispersions of early type galaxies (e.g., Bernardi et al., 2005; Matković & Guzmán, 2005), and the orbits of satellite galaxies (e.g., Boylan-Kolchin et al., 2013) have all been crucial in understanding how and why galaxies form the way they do. Additionally, kinematic observations and simulations show inflows and outflows of multiphase gas are prevalent in the galaxy evolution process (e.g., Kaufmann et al., 2006; Coil et al., 2011; Kacprzak et al., 2012). The latter probe galactic feedback mechanisms while the former probe the accretion of gas onto galaxies that can generate future star formation activity. All of these methods provide a unique view of the galaxy formation

and evolution process, and help shape the view of the Milky Way.

There has been extensive work on the Milky Way's neutral and warm ionized gas kinematics, providing valuable information on the Milky Way's total H I content and interplay between the Galactic disk and halo. In the Galactic disk, all-sky maps of 21 cm emission line radiation reveal emission across a range of velocities as a function of Galactic longitude (e.g., Westerhout, 1957). Decoding the emission strength as a function of l and v implies the existence of a H I disk corotating with the stellar disk and with $\sim$10% its mass along with numerous spiral arm structures (see review by Burton, 1976). Ultraviolet absorption line surveys probing gas at $T \sim 10^5$ K have also revealed absorbers at a wide range of Local Standard of Rest (LSR) velocities. Absorbers observed at $|v_{LSR}| \lesssim 100$ km s^{-1} are typically associated with a warm-ionized atmosphere corotating with the disk (e.g., Savage et al., 2003; Bowen et al., 2008), while absorbers at $|v_{LSR}| \geqslant 100$ km s^{-1} are interpreted as discrete clouds or complexes of material, commonly referred to as high velocity clouds (e.g., Wakker & van Woerden, 1997; Sembach et al., 2003). The clouds' origins are still debated, with the leading theories including galactic fountain processes in the Galactic disk, material stripped from orbiting satellite galaxies, or material condensed out of a hotter phase of halo gas (see review by Putman et al., 2012). Regardless of their origins, the clouds' characteristic velocities imply they can supply a substantial amount of neutral gas to the H I disk and that the clouds interact with the surrounding hot gas material.

The Milky Way and Milky Way-like galaxies also host hot gas distributions between 10^6–10^7 K (Spitzer, 1956), which formed either from supernova explosions in the disk (e.g., Joung & Mac Low, 2006; Hill et al., 2012) or from gas that was shock-heated to the Milky Way's virial temperature as it accreted onto the dark matter halo (e.g., White & Frenk, 1991; Cen & Ostriker, 2006; Fukugita & Peebles, 2006). Like the cooler gas, the hot gas responds to the Milky Way's gravitational field, im-

plying any kinematic structure is connected with its formation and evolution. These motions include global rotation from residual or injected angular momentum, turbulence, bulk flows, and net inflow (accretion) or outflow (wind), all of which relate to how the galaxy has formed and evolved. However, the large spatial extent of the hot gas ($\gtrsim$10 kpc from the Sun) combined with current observational capabilities limit constraints on hot gas dynamics. This is important since the gas velocity structure can impact hot gas observables and the inferred structure, similar to the H I analyses discussed above.

The Milky Way's hot gas distribution is volume-filling on $\gtrsim$10 kpc scales, has density estimates ranging between 10^{-5}–10^{-3} cm^{-3}, and a temperature characteristic of the Milky Way's virial temperature, $\approx 2\times10^{6}$ K. A collisionally ionized plasma at this temperature emits in the soft X-ray band, 0.5–2.0 keV, making it the dominant source of the *ROSAT* 3/4 keV background (Snowden et al., 1997). All-sky maps from the *ROSAT* All-sky Survey constrained the characteristic densities and temperature of the plasma, but higher resolution spectroscopic observations with current X-ray telescopes provide additional constraints on the gas structure and origin.

Recent work on hot gas in the Milky Way has relied on O VII and O VIII emission and absorption line observations characteristic of a 10^{6}–10^{7} K plasma (Paerels & Kahn, 2003). The emission lines are observed in $\sim$ 1000 blank fields of view using either sounding rocket experiments (McCammon et al., 2002), or the CCDs on board current X-ray telescopes (e.g., Yoshino et al., 2009; Henley & Shelton, 2012). The number of bright X-ray point sources in the soft X-ray band limits the number of absorption line measurements, but they are detected in about 40 active galactic nuclei (e.g., Nicastro et al., 2002; Rasmussen et al., 2003; Wang et al., 2005; Bregman & Lloyd-Davies, 2007; Yao & Wang, 2007; Gupta et al., 2012; Miller & Bregman, 2013; Fang et al., 2015) and X-ray binary (Yao & Wang, 2005; Hagihara et al., 2010) spectra. Interpreting the line strengths has several difficulties: (1) weak detections of O VII Kβ

absorption lines suggest some of the lines may not be optically thin ($\tau_o \lesssim 2$; Williams et al., 2005; Gupta et al., 2012; Fang et al., 2015), (2) the Sun exists within the Local Hot Bubble, which is 100-300 pc in size and has signatures in the soft X-ray band (e.g., Snowden et al., 1990, 1993; Kuntz & Snowden, 2000; Lallement et al., 2003; Smith et al., 2007; Welsh & Shelton, 2009; Smith et al., 2014a), (3) solar wind charge exchange emission can add significant time-varying emission to individual emission line observations (e.g., Snowden et al., 2004; Koutroumpa et al., 2007; Carter & Sembay, 2008; Carter et al., 2011; Galeazzi et al., 2014; Henley & Shelton, 2015). Analyses of the line strengths that account for these issues suggest the gas structure is an extended, spherical corona as opposed to a flattened disk-like morphology (Fang et al., 2013; Miller & Bregman, 2013, 2015).

The above studies focused primarily on the line strengths since the lines are unresolved with current X-ray telescopes, however recent data reduction techniques and improved calibration allow the line centroids to be measured with high precision as well. The emission lines are significantly blended at CCD resolution (EPIC-MOS FWHM $\sim$50 eV $\sim$25,000 km s^{-1} at 0.6 keV; Sembay et al., 2004), implying they do not encode hot gas kinematic information. The absorption lines are also unresolved at current grating resolutions (Reflection Grating Spectrometer FWHM $\sim$2 eV$\sim$1000 km s^{-1} at 0.6 keV; den Herder et al., 2003), but the higher resolution compared to the CCDs yields accurate equivalent width and line centroid measurements in high signal-to-noise ratio targets. In particular, Hodges-Kluck et al. (2016) utilized the improved calibration for sun angle and heliocentric motion in *XMM-Newton* RGS observations to significantly improve the precision for line centroid measurements. This updated calibration resulted in a sample of 37 O VII absorption line centroids from archival *XMM-Newton* RGS data with uncertainties ranging from $\approx$25-400 km s^{-1}. The measured values are inconsistent with a stationary hot gas halo, and suggest the hot gas rotates in the same direction as the disk. This analysis highlights that high

resolution absorption line observations are useful probes of the Milky Way's hot gas kinematics.

Here, we present model absorption line profiles for different hot gas velocity structures and analyze their effects on current and future high resolution absorption line observations. The modeling is analogous to the long-established work on the Milky Way's H I structure and kinematics discussed above, however the hot gas system we consider is extended and spherical out to the Milky Way's virial radius. For velocity profiles, we explore the effects of gas rotation in the same direction as the disk and global inflows/outflows of gas. We show that the absorption lines can exhibit significant asymmetries, broadening beyond the Doppler width, and different line centers depending on the underlying velocity structure. These model line centroids complement the work discussed above, but observing the profile shapes requires a higher resolution X-ray spectrograph. We discuss the instrument requirements to observe such effects and how future observations will provide additional constraints on the Milky Way's hot gas kinematics and baryon content (see discussion by Bregman et al., 2015).

In addition to the line profile calculations, we show how optical depth and kinematic effects impact ongoing work on the Milky Way's hot gas structure. Accounting for velocity flows in the halo can broaden the total absorption line profile in velocity space, which impacts the conversion between observed equivalent widths and the inferred column densities. We present curves of growth that account for these velocity effects along with the plasma optical depth, providing more accurate inferences for the gas density structure.

The rest of the chapter is structured as follows. In Section 4.4, we describe our line profile calculation, including a discussion on the inferred hot gas density and velocity structures. This also includes the altered conversions between equivalent widths and column densities. Section 4.5 includes a discussion and summary of our results, with

additional implications for future X-ray missions.

4.4 Calculations of Line Shapes and Equivalent Widths

The calculation and interpretation of absorption line shapes is analogous to the Galactic H I distribution. In these studies, resolved H I 21 cm emission line measurements in velocity space constrain the neutral hydrogen distribution and kinematics in the Galactic disk (e.g., Kalberla et al., 2007). These methods involve analyzing the amount of emission received at different velocities and different Galactic longitudes. Here, we make similar predictions for the hot gas absorption line profiles, but assuming different underlying hot gas density and velocity profiles compared to the neutral hydrogen distribution. The primary difference here is the assumption that the hot gas is a volume-filled distribution of material extending to the Milky Way's virial radius as opposed to only being confined to the Galactic disk. Similarly, we explore different large-scale velocity profiles for the hot gas that deviate from simple corotating motion with the disk. These factors imply that different density and velocity profiles produce unique line shapes and line center shifts for different l, b coordinates. We explore these effects and estimate their impact on current and future absorption line measurements.

4.4.1 Model Assumptions

We make several assumptions for the hot gas density, temperature, and metallicity distribution based on previous observational and theoretical analyses. Most of these assumptions are based on the results from Miller & Bregman (2013, 2015), and we refer the reader to these studies for a more detailed description. Here, we outline the most important assumptions and any caveats in terms of how they could affect our absorption line profile calculations.

We assume the hot gas density distribution follows a modified spherical β-model

extending to the Milky Way's virial radius. The β-model has the following functional form:

$$n(r) = n_o(1 + (r/r_c)^2)^{-3\beta/2}, \tag{4.1}$$

where n_o is the core density, r_c is the core radius, and β controls the slope at $r \gg r_c$. The Milky Way's expected r_c is ($\lesssim$5 kpc), a region that is not well sampled by absorption or emission line observations. To account for this, Miller & Bregman (2013) defined a modified β-model in the limit where $r \gg r_c$:

$$n(r) \approx \frac{n_o r_c^{3\beta}}{r^{3\beta}}, \tag{4.2}$$

where $n_o r_c^{3\beta}$ is the density normalization and -3β is the slope. This density profile is effectively a power law describing the Milky Way's hot gas distribution. Unless otherwise stated, we assume density parameters of $n_o r_c^{3\beta} = 1.3 \times 10^{-2}$ cm^{-3} kpc$^{3\beta}$ and $\beta = 0.5$ based on results from Miller & Bregman (2015).

This model, although simple, is not arbitrarily chosen, and has successfully reproduced several Milky Way hot gas observables. Most recent studies on the Milky Way's hot gas structure follow a general methodology. One assumes one of two types of underlying density distributions: an exponential disk with scale height of 5-10 kpc, or a lower-density, spherical model extending to the virial radius. Given a model choice, one compares model observations to measured observations and determines if the model is consistent with the data. The primary observables of the Milky Way's hot gas are O VII and O VIII absorption and emission line strengths (e.g., Paerels & Kahn, 2003; Rasmussen et al., 2003). Several analyses argue that an exponential disk-like morphology can reproduce the line strengths for *individual* sight lines (Yao & Wang, 2007; Hagihara et al., 2010). However, independent analyses on all-sky samples of absorption and emission line strengths suggest a density model like Equation 4.2

reproduces the global line strength trends better than a disk-like morphology (Miller & Bregman, 2013, 2015; Hodges-Kluck et al., 2016). Additional work by Fang et al. (2013) explored more sophisticated spherical, extended density models (an adiabatic profile and a cuspy NFW profile) and an exponential disk model to compare with other observed constraints, such as the residual pulsar dispersion measure toward the Large Magellanic Cloud (LMC) (Anderson & Bregman, 2010) and ram-pressure stripping of dwarf spheroidal galaxies (e.g., Grcevich & Putman, 2009). They found the spherical, extended models were consistent with these constraints, while the exponential disk model was not. Therefore, an extended, spherical density morphology appears to be consistent with several observed hot gas properties, and a simple power law can reproduce how the observed line strengths vary across the sky.

The β-model is also used for fitting the observed X-ray surface brightness profiles around nearby galaxies. This has historically been done for $\approx$50 early-type galaxies, with fitted β values ranging between 0.4–1.0 for a typical early-type galaxy (Forman et al., 1985; O'Sullivan et al., 2003). More recently, there have been detections of diffuse X-ray halos around massive ($\sim$10 times larger than the Milky Way) late-type galaxies within $\sim$70 kpc (Anderson & Bregman, 2011; Dai et al., 2012; Bogdán et al., 2013a,b; Anderson et al., 2016). Although there are only four late-type galaxies where these coronae are detected, their fitted β values are also comparable to the results from early-type galaxy surveys. This further motivates our initial choice to use a β model as our underlying Milky Way hot gas density profile.

We also assume that the hot gas temperature, oxygen abundance, and metallicity are constant with radius. Observationally, the Milky Way's hot gas temperature is inferred from a combination of fitting soft X-ray background (SXRB) spectra with thermal plasma models, or comparing the O VII to O VIII absorption line ratio in individual sight lines where both lines are detected. Both methods indicate that the hot gas temperature is $\approx 2 \times 10^6$ K, with the latter method providing the most current

observational constraints. Henley & Shelton (2013) fit the 0.5–2.0 keV band of 110 SXRB spectra with multiple thermal APEC plasma models to measure the Milky Way's hot halo emission measure and temperature distribution. The found the halo gas temperature shows little variation across the sky with a median value of 2.22×10^6 K and interquartile region of 0.63×10^6 K. The fact that this value is consistent across the sky implies the gas is close to isothermal. Therefore, we assume a constant halo gas temperature of 2×10^6 K, resulting in an O VII ion fraction of 0.5 (Sutherland & Dopita, 1993).

There is less certainty when considering the hot gas metallicity and oxygen abundance since there are no direct observational constraints on these values. The reported solar oxygen abundance relative to hydrogen has varied in the literature, but we assume a value of 5.49×10^{-4} Holweger (2001). Galaxy evolution simulations suggest halo gas metallicities can range between $\approx$0.05–2 $Z_\odot$ depending on the stellar feedback prescription, with a typical value of $\approx 0.3 Z_\odot$ (Toft et al., 2002; Cen & Ostriker, 2006; Marinacci et al., 2014). This is consistent with the model-dependent constraint Miller & Bregman (2015) placed on the hot gas metallicity in order to not overproduce the pulsar dispersion measure in the LMC direction, $Z \geq 0.3 Z_\odot$. Miller & Bregman (2015) also estimated a model-dependent hot gas metallicity profile by comparing their emission line fitting results (sensitive to $n_e n_{ion}$) with absorption line results (sensitive to n_{ion}) from Miller & Bregman (2013). They found evidence for a shallow metallicity gradient of $Z \propto r^{-0.2}$ with $Z = 0.26 Z_\odot$ at $r = 10$ kpc, although the uncertainty in the relation was consistent with a constant gas metallicity. Thus, we assume a constant metallicity value of $0.3 Z_\odot$, which still results in $\gtrsim$50% of the absorption coming from $\gtrsim$5 kpc of the Sun and $\gtrsim$90% coming from $\lesssim$50 kpc (Hodges-Kluck et al., 2016).

It is worth noting that these hot gas distribution assumptions are all broadly consistent with the theoretical prediction that the hot gas formed via an accretion

shock and is in hydrostatic equilibrium with the Milky Way's dark matter potential well. Our density parametrization of a power law is the simplest functional form that can remain in hydrostatic equilibrium with the dark matter potential well at large radii, with $\beta = 0.5$ implying the gas should be close to hydrostatic equilibrium. Given this type of distribution and formation mechanism, one expects the gas temperature to be close to the Galactic virial temperature of 2×10^6 K. This prediction is consistent with the observed, and therefore assumed hot gas temperature. The global hot gas distribution adopted here has a reasonable theoretical basis, and is also consistent with multiple types of observations.

Finally, our calculations depend on several Milky Way parameters that have been measured from different techniques. For the Milky Way's size and geometry, we assume a solar distance to the Galactic center of $R_\odot = 8.34$ kpc, a solar rotation velocity around the Galactic center of $v_\odot = 240$ km s^{-1} (Reid et al., 2014), and an average virial radius of $r_v = 250$ kpc (Klypin et al., 2002; Loeb et al., 2005; Shattow & Loeb, 2009). The former do not affect our overall line shapes, but act as a net shift in wavelength/velocity space for the line profiles. We extrapolate our model profiles and calculations to r_v, however gas within ≈50 kpc of the Sun dominates our column densities and equivalent widths (Miller & Bregman, 2013; Hodges-Kluck et al., 2016). This implies that our choice for r_v has a negligible impact on our results, and that our model profiles are explicitly valid within ≈50 kpc.

4.4.2 Velocity Profile and Line Profile Calculation

We consider bulk rotation motion, radial inflow/outflow, and flows perpendicular to the Galactic disk for our velocity profiles. A net rotational flow (denoted as the $\hat{\phi}$ direction henceforth) is expected if the gas has residual angular momentum from the Milky Way's formation. The radial and perpendicular flows ($\hat{r}$ and $\hat{z}$ directions) are considered as a net accretion of material onto the Galactic disk or a net ejection

of material from the Galactic disk. We assume constant flow velocities as a function of R, z, or r, depending on the flow type, where R is the distance from the rotation axis, z is the distance perpendicular to the Galactic plane, and r is the galactocentric radial distance. These are represented by the following equations:

$$v_\phi(R) = v_\phi \hat{\phi} = constant, \tag{4.3}$$

$$v_r(r) = v_r \hat{r} = constant, \tag{4.4}$$

$$v_z(z) = v_z \hat{z} = constant, \tag{4.5}$$

where v_ϕ follows a flat rotation curve similar to the disk, and v_r/v_z are net flows in the $\hat{r}/\hat{z}$ directions respectively. Therefore, positive v_r/v_z values assume flows away from the Galactic center (v_r) or Galactic plane (v_z). We also consider models with a constant mass inflow/outflow rate by allowing $v_r(r)$ to not be a constant. The mass flux depends on the density and radial velocity, and is represented by the following equation:

$$\dot{M}_r(r) = 4\pi r^2 \rho(r) v_r(r) \hat{r} = constant, \tag{4.6}$$

where $\rho(r)$ is the mass density as a function of radius. If $\rho(r) \propto n(r) \propto r^{-3\beta}$, this implies $v_r(r) \propto r^{3\beta-2}$ in order for $\dot{M}_r$ to be constant.

Optical depth effects and the assumed absorption line Doppler width play an important role when inferring column densities from measured equivalent widths. The observed absorption lines are never broader than the instrumental line widths of current X-ray spectrographs (the Chandra Low-energy Transmission Grating has a FWHM of $\approx$0.05 Å). This sets an upper limit on the Doppler width of $\lesssim$550 km s^{-1}.

Given these spectral resolutions, it becomes difficult to quantify deviations from an optically thin plasma. There have been several detections of the O VII Kβ transition along with the O VII Kα line, suggesting Doppler widths ranging from the thermal width ($\approx$45 km s^{-1} at 2×10^6 K) to $\approx$150 km s^{-1} (Williams et al., 2005; Gupta et al., 2012; Fang et al., 2015). Galaxy formation and evolution simulations predict a similar range of b values with a characteristic value of 85 km s^{-1} (Cen, 2012). The additional turbulent velocity can arise from a variety of sources, including turbulent mixing layers, satellite galaxy orbits, bulk flows of material in and out of the disk, etc. (e.g., Kwak & Shelton, 2010; Cen, 2012; Hill et al., 2012). We adopt a b value of 85 km s^{-1} for our initial line profile calculations, but explore how the Doppler width compares with different velocity flows.

Given a density profile, velocity profile, and Doppler width for the absorbing medium, we calculate model absorption line profiles for different sight lines in the Galaxy. For a given l, b coordinate, we divide the line of sight into cells with densities and Galactic standard of rest (GSR) velocities dependent on the cells' locations in the Galaxy. The coordinate transformations between the line of sight position, s, and Galactic coordinates is:

$$R^2 = R_\odot^2 + s^2 \cos(b)^2 - 2sR_\odot \cos(b) \cos(l) \tag{4.7}$$

$$z^2 = s^2 \sin(b)^2 \tag{4.8}$$

$$r^2 = R^2 + z^2 \tag{4.9}$$

The density in each cell comes from the cells' r positions and using Equation (4.2). The conversions between GSR and LSR velocities for our velocity models are repre-

sented by the following equations:

$$v_{s,\phi}(s) = \left(\frac{v_\phi}{R(s)} - \frac{v_\odot}{R_\odot}\right) R_\odot \sin(l)\cos(b), \tag{4.10}$$

$$v_{s,r}(s) = \frac{v_r}{r(s)}[\sin(|b|)z(s) + (s\cos(b) - R_\odot\cos(l))\cos(b)], \tag{4.11}$$

$$v_{s,z}(s) = v_z \sin(|b|), \tag{4.12}$$

where $R(s)$, $z(s)$, and $r(s)$ are the Galactic coordinates along the sight line s, $v_{\phi/r/z}$ are the GSR flow velocities, and $v_{s,\phi/r/z}$ are the LSR velocities for each cell. We generate a Voigt profile for each cell that is shifted to the cell's LSR velocity and weighted by the density, or optical depth, in the cell. The cell line center optical depth is defined as:

$$\tau_o = 0.015 \times n(s) f \lambda b^{-1} ds, \tag{4.13}$$

where $n(s)$ is the number density of absorbers in the cell, f is the transition oscillator strength ($f = .6945$ for the O VII Kα transition), λ is the transition wavelength in centimeters, b is the Doppler width of the plasma in cm s^{-1}, .015 is a constant with units cm^2 s^{-1}, and ds is the cell path length in centimeters. The total model line optical depth, τ_v or τ_λ, is the sum of each cell's line profile out to the Milky Way's virial radius with the resultant absorption line profile following the usual definition:

$$\frac{F_{v/\lambda}}{F_{v/\lambda,c}} = e^{-\tau_{v/\lambda}}, \tag{4.14}$$

where $F_{v/\lambda}$ is the source flux in velocity or wavelength space and $F_{v/\lambda,c}$ is the continuum flux.

The resultant model line profiles include asymmetric line shapes, widths broader

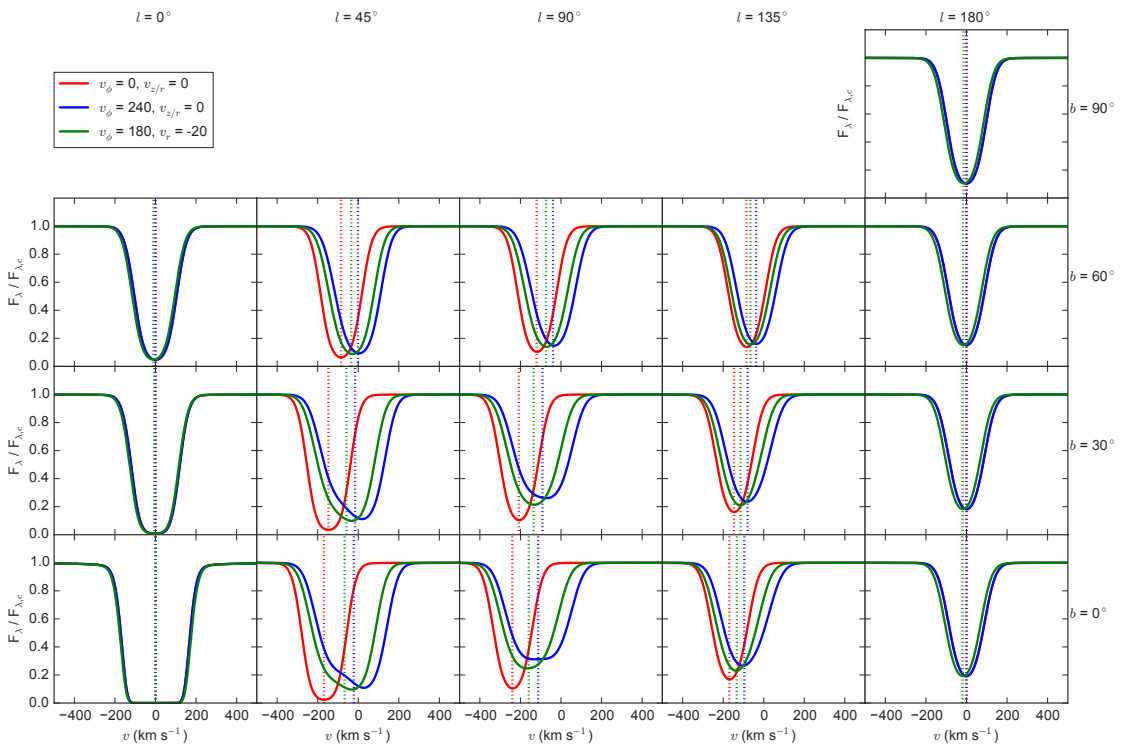

Figure 4.1: Model absorption line profiles, normalized to the continuum, for different positions on the sky and velocity profiles. Each model spectrum assumes the gas density follows a modified β-model (Equation 4.2 with $\beta = 0.5$) and that the gas is either stationary (red), corotating with the disk (blue), or lagging behind the disk with a modest radial inflow velocity (green). The model profiles exhibit asymmetric shapes and varying line centroids (vertical dotted lines) depending on the observed position and underlying velocity profile.

than the plasma Doppler width, and significant line center shifts. Figure 4.1 shows our absorption line calculations for a grid of $0° \leq l \leq 180°$ and $0° \leq b \leq 90°$ coordinates. The velocity profiles include a stationary hot gas model ($v_\phi = v_{r/z} = 0$ km s^{-1}), a hot gas distribution corotating with the disk ($v_\phi = 240$ km s^{-1}, $v_{r/z} = 0$ km s^{-1}), and a profile similar to the best-fit model from Hodges-Kluck et al. (2016) that best reproduces a sample of observed line centroids ($v_\phi = 180$ km s^{-1}, $v_r =$ -20 km s^{-1}). One immediately sees the line profiles can be highly asymmetric or broadened beyond the assumed 85 km s^{-1} for observations near $l \approx 90°$ and for $b \lesssim 30°$. Figure 4.2

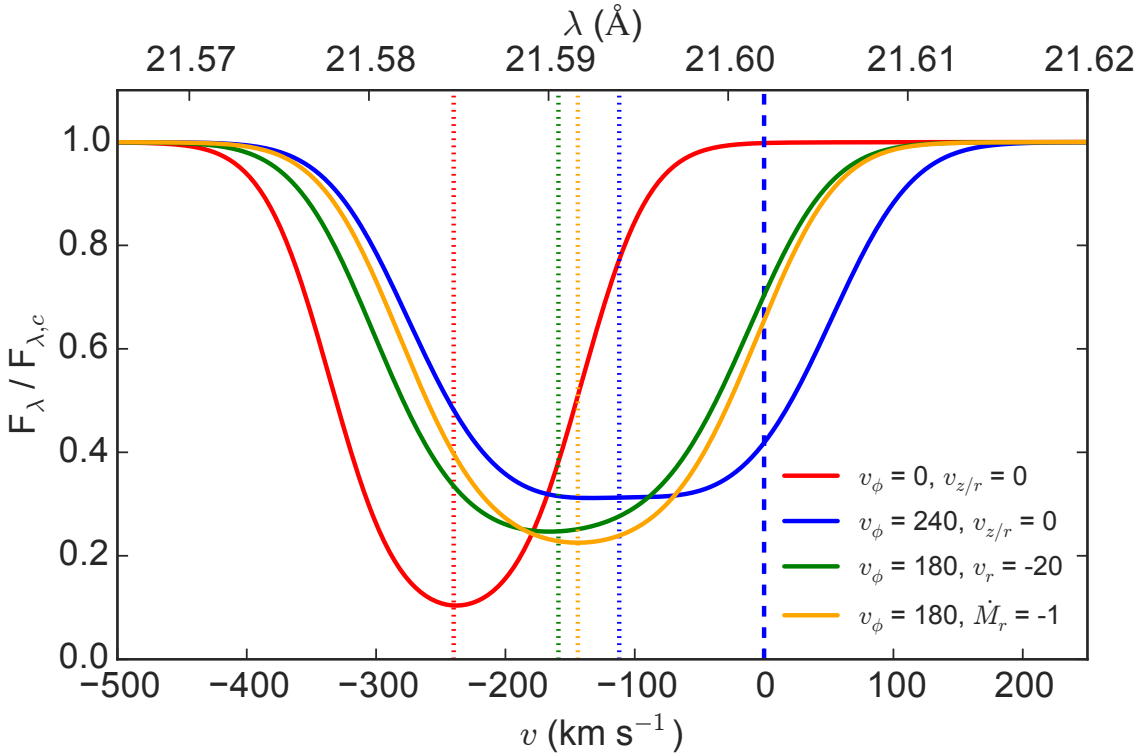

Figure 4.2: Same model spectra as Figure 4.1, except focusing on an $l, b = 90°, 0°$ sight line. The velocity effects are apparent, where the corotating line profile (blue) is much broader than the stationary line profile (red). The additional orange line is for a constant radial mass flux model with $\dot{M}_r$ = -1 $M_\odot$ yr^{-1}, which has minor differences from the constant v_r model. The dashed vertical blue line represents the tangent point velocity for this sight line (0 km s^{-1}), although there is still absorption at $v > 0$ km s^{-1} due to the inferred b value of 85 km s^{-1}.

shows a detailed plot of the model profiles toward the $l, b = 90°, 0°$ direction, where the velocity effects will be strongest. This figure includes a constant $\dot{M}_r$ model line profile with $v_\phi = 180$ km s^{-1}, $\dot{M}_r$ = -1 $M_\odot$ yr^{-1}. There are minor differences between the line shapes and centroids ($\approx$15 km s^{-1}) for this model and the v_r = -20 km s^{-1} model, so we only consider the constant v_r model for the rest of the analysis.

There are several apparent trends seen in these figures. If the halo gas is stationary, all of the absorption occurs at the reflex motion of the Sun's orbit around the Galactic center, $v_s = -v_\odot \sin(l) \cos(b)$. If instead the hot gas corotates with the disk,

the absorption can be spread out between $\pm v_{\odot}$ depending on the direction observed (Figure 4.3). The resultant density-weighted LSR velocities create the asymmetric line profiles and significantly broader lines compared to the stationary plasma results. For example, the corotating model line width (defined as the full width at half the line depth) for the $l, b = 90°$, $0°$ direction in Figure 4.2 is 326 km s^{-1} compared to 200 km s^{-1} for the stationary model, a 63 % increase. Furthermore, the absorption line centroids depend on the underlying velocity profile (vertical dotted lines in Figures 4.1 and 4.2). The stationary plasma halo produces the strongest deviations from the rest wavelength, or 0 km s^{-1}, since all of the absorption is at the same velocity. If the gas is corotating with the disk, one expects weaker line shifts since dense gas near the Galactic disk produces $v_s \approx 0$ km s^{-1} absorption, while gas futher in the halo produces absorption at $|v_s| \gtrsim 100$ km s^{-1}. Flows in the r or z directions produce similar net velocity shifts, although flows in these directions have stronger effects near the Galactic center, anti-center, and poles. These effects imply that the hot gas kinematics produce observable signatures on the absorption line centroids, and alter the inferred conversion between measured equivalent width and column density.

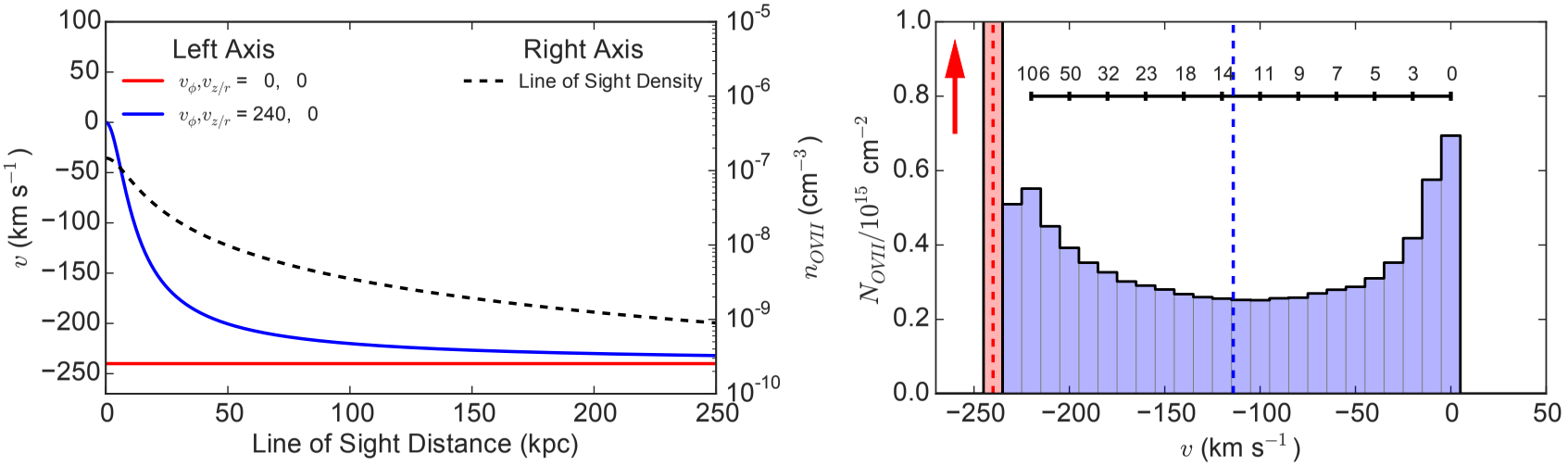

Figure 4.3: The $l, b = 90°, 0°$ line of sight density (dashed line) and velocity (solid lines) profiles (*left*) and O VII column density in 10 km s^{-1} bins along the line of sight (*right*). In the stationary case (red), all of the gas is at the reflex velocity of the Sun around the Galactic center, -240 km s^{-1} (the column density bin goes above the plot limits to a value of 8.4 in order to emphasize the corotating velocity effects). In the corotating case (blue), the column density is spread out in velocity space, with the black horizontal scale indicating the median line of sight distance in kpc for every other velocity bin. Material near the Sun produces ≈0 km s^{-1} absorption while material further in the halo produces ≈-200 km s^{-1} absorption.

4.4.3 Model Line Strengths

These line of sight velocity effects have important consequences when analyzing the absorption line strengths. Specifically, these effects impact observable quantities (equivalent widths, resolved line profiles, etc.) and how we infer the gas column density. This is not a new concept in the broad field of absorption line analysis, but these large scale velocity flows have never been considered when analyzing the Milky Way's O VII absorbers. Here, we discuss how these effects impact current line strength interpretations when the lines are unresolved and potential future analyses if the lines can be partially resolved.

Modeling the line of sight velocity flows and corresponding line profiles leads to a more accurate conversion between measured absorption line equivalent widths and the inferred column densities. The measured equivalent widths are currently the best way to measure the absorption line strengths since the lines are unresolved by current X-ray spectrographs. The inferred column densities are usually determined from a curve of growth analysis with various assumptions for the plasma optical depth. Velocity flows alter this conversion by spreading out the absorption in velocity space, producing larger equivalent widths for a given column density. To quantify the strongest velocity corrections, we generate model line spectra in the $l, b = 90°, 0°$ direction, for a range of column densities and Doppler b values, and for a corotating halo. We vary the column density by changing the halo normalization parameter in Equation 4.2, thus keeping the gas distribution the same with $\beta = 0.5$. We create curves of growth with velocity effects by calculating equivalent widths for each line profile/column density. Figure 4.4 shows these new growth curves, where the solid lines represent traditional curve of growth calculations with no velocity effects and the opposite edges of the shaded regions represent our curves of growth with rotational velocity effects. Therefore, the shaded regions represent the range of possible velocity corrections, depending on the true halo velocity structure.

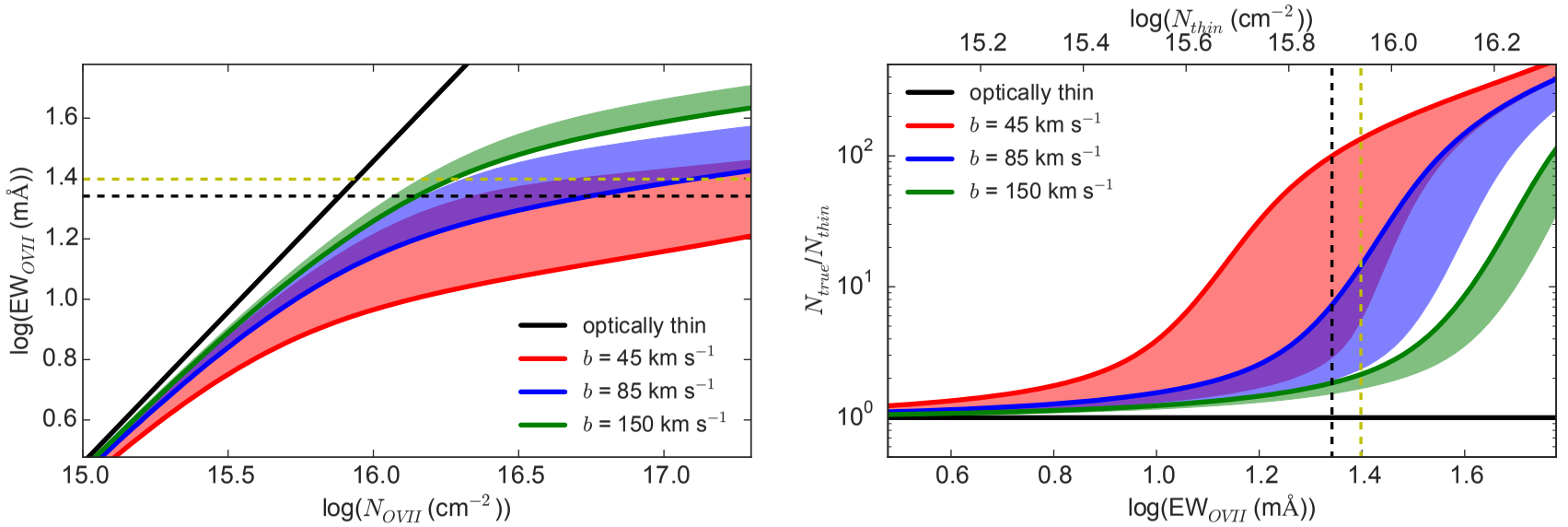

Figure 4.4: Conversions between the observed equivalent widths and column densities for different Doppler values and with velocity effects along an $l, b = 90°, 0°$ line of sight. The *left* panel shows curves of growth, where the colored solid lines represent normal growth curves for different b values (or equivalently a stationary halo), and the upper boundaries of the shaded regions represent the growth curves assuming a corotating velocity profile. The *right* panel is the same as the *left* panel, but with the column densities normalized to the optically thin values. The dashed lines represent the median equivalent widths from the Miller & Bregman (2013) (black) and Fang et al. (2015) (yellow) samples, indicating the optical depth and velocity effects can be substantial.

These velocity effects have a significant impact on the inferred column densities, with potentially large deviations from optically thin values. Here, we examine corrections to the inferred optically thin column densities with and without considering velocity effects and for different b values. The right hand panel of Figure 4.4 rescales the curves of growth in the left hand panel into the ratio between the true and optically thin column density for a given equivalent width. The Doppler b value plays a critical role when inferring the correct column density for a given measured equivalent width, where corrections without velocity effects range between $\approx$50% to over an order of magnitude for b between 45 and 150 km s^{-1} and a typical equivalent width measurement of 20 mÅ . The velocity effects discussed above mitigate these differences, but still cause significant deviations from optically thin values. For example, the ratio between the true and optically thin column ranges from a factor of $\approx$2 if the halo gas is corotating to a factor of $\approx$5 without velocity effects for $b = 85$ km s^{-1} and a 20 mÅ equivalent width. This implies that velocity effects result in *smaller* column densities than would be inferred from a traditional curve of growth conversion. These results are useful in the current limit where the lines are unresolved, but there are alternative approaches if the lines are partially resolved.

A useful approach for future analyses on these absorption lines will be the apparent optical depth method (Savage & Sembach, 1991). In this method, one decomposes the observed line profile into an apparent optical depth function $\tau_a(v)$ and converts this into an apparent column density function $N_a(v)$, which can be integrated to determine a total column density. This method makes no assumption for the underlying line of sight density or line of sight velocity profile, but it would be useful to reconstruct a column density distribution similar to our Figure 4.3. The reason this method is not used in current analyses on the O VII absorbers is because: 1) the lines need to be at least partially resolved (FWHM(instrument) $\lesssim$ 2FWHM(line)) and 2) it requires multiple lines of the same species with different $f\lambda$ products to estimate

saturation effects. The lines are completely unresolved with current X-ray telescopes and detecting the O VII Kβ transition at 18.63 Å is difficult because it is intrinsically weaker than the Kα transition and there is an RGS instrumental feature near the transition[1]. Thus, this method will be useful if we obtain absorption line observations with a higher resolution spectrograph (see Section 4.5.2).

4.5 Discussion and Conclusions

We have shown that the Milky Way's hot gas kinematics produce signatures in the intrinsic absorption line shapes and centroids. Bulk velocity flows in the disk rotation direction along with a net inflow or outflow of gas can produce strong asymmetrical line shapes and significant line centroid deviations from the the absorption line rest wavelength. These results alter the conversion between equivalent widths and column densities, producing significant deviations from both optically thin and zero velocity assumptions, but also imply the line shapes (not currently observable) and observed centroids encode information on the Milky Way's hot gas kinematics. The new velocity considerations presented here motivate future analyses on the Milky Way's hot gas structure and kinematics.

4.5.1 Implications for the Milky Way

The model line calculations presented in this chapter form the basis for the Hodges-Kluck et al. (2016) analysis on the Milky Way's hot gas kinematics. Their non-parametric statistical tests concluded that the observed line centroid measurements were inconsistent with a stationary hot gas profile (a result not requiring additional modeling or assumptions for the gas distribution), whereas corotating model centroids from calculations in Section 4.4.2 were more consistent with the data. Figure 4.5

[1] http://xmm.esac.esa.int/external/xmm_user_support/documentation/uhb/rgsmultipoint.html

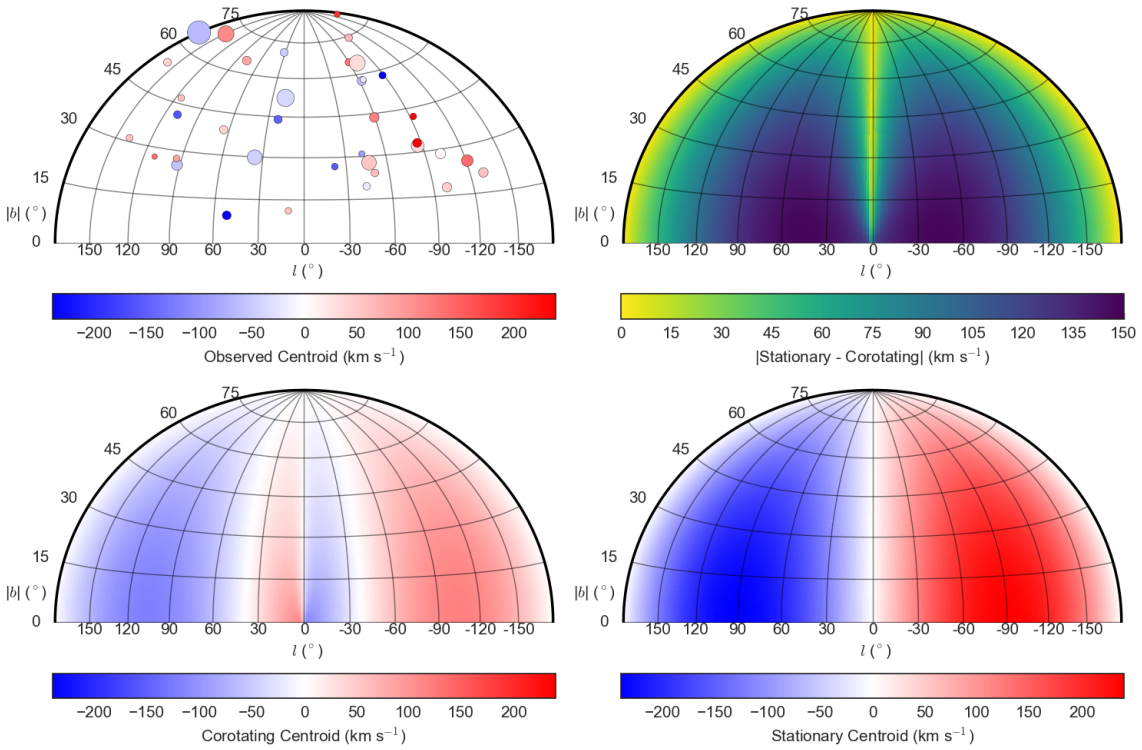

Figure 4.5: Absorption line centroids in single-hemisphere Aitoff projections. The upper-left panel shows the observed line centroid distribution from Hodges-Kluck et al. (2016) where the point sizes are inversely proportional to their measurement errors. The bottom panels represent model centroid calculations for a cororating (left) and stationary (right) halo gas distribution. The upper-right panel shows the absolute difference between the stationary and corotating model, indicating where on the sky one has the greatest leverage to differentiate between models.

shows their observed centroid distribution on the sky with maps of the model line centroid distributions for the stationary and corotating profiles to illustrate how the models compare with the data. They also used parametric modeling techniques with v_ϕ as a free parameter to show that a velocity profile lagging behind the disk with v_ϕ = 183 ± 41 km s^{-1} is most consistent with the observed line centroid distribution. The v_z and v_r flow parameters were also included, but the constraints were within 1σ of 0 km s^{-1}. These results are the first constraints on the Milky Way's $T \sim 10^6$ K gas kinematics, and they depend on the absorption line profile calculations presented here.

The inferred velocities also have implications for other inferred hot gas properties, such as the density distribution and metallicity.

Significant hot gas rotation velocities can change the net potential well affecting the hot gas, resulting in a flattened or "bow-tie" morphology. The prediction of hot, extended coronae around late-type galaxies is based on the assumption that the shock-heated gas exists in hydrostatic equilibrium with the dark matter potential well. If the dark matter distribution is approximately spherical on large galactic scales and the gas is isothermal, hydrostatic equilibrium implies a spherical power law distribution for the hot gas:

$$n \propto \exp\left(-\frac{\Phi}{c_T^2}\right), \tag{4.15}$$

where Φ is the potential ($\Phi \propto ln(r)$ for an isothermal sphere) and $c_T^2 = 2kT/\mu m_p$. Rotation modifies the potential in the following way:

$$\Phi_{\text{eff}} = \Phi - \int_{R_o}^{R} \Omega^2(R') R' dR', \tag{4.16}$$

where R_o is an arbitrary radius for normalization, $\Omega(R)$ is the angular rotation profile, and Φ_{eff} is the effective potential (see Equation 8 in Barnabè et al., 2006). Inserting the effective potential into Equation 4.15 for flat rotation curves can alter the initial spherical profile into a flattened morphology.

To visualize this effect, we calculate an effective potential profile for a static potential and flat rotation curve we impose on the gas. We assume the static potential includes a dark matter NFW profile (Navarro et al., 1997) with a scale radius of 12 kpc and virial mass of 1.8×10^{12} $M_\odot$ and a thin stellar disk profile with scale radius of 3.2 kpc and total surface density of 536 $M_\odot$ pc^2 (Binney & Tremaine, 2008). These assumptions do not account for the triaxiality of the Milky Way's dark matter distribution (Loebman et al., 2014) and the vertical structure of the stellar disk, but

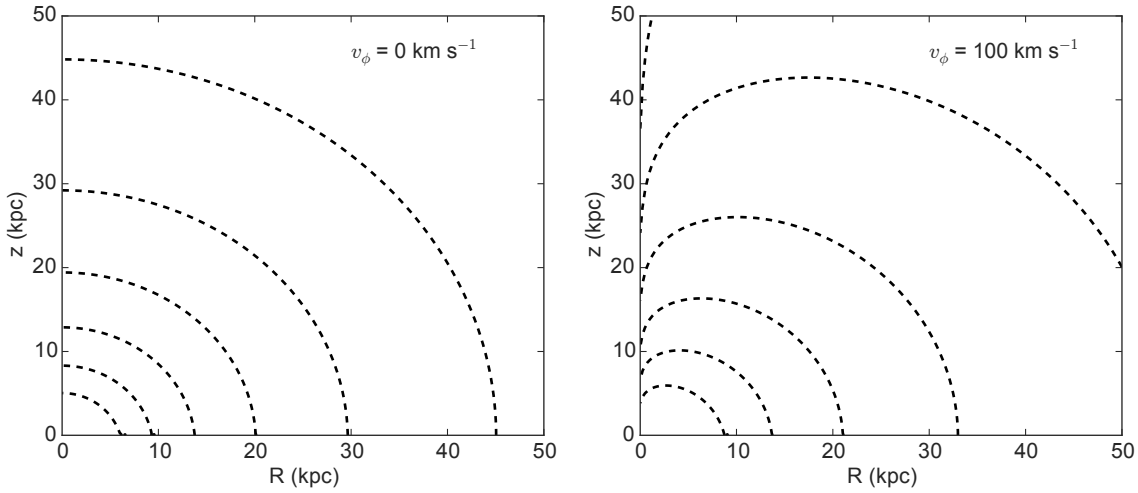

Figure 4.6: Isodensity contours for stationary hot gas distribution (left) and a distribution with a flat 100 km s^{-1} rotation curve (right). The contours are normalized to the maximum density values, and are log-spaced with a 0.5 interval between -3 through -5.5. Including rotation leads to a characteristic flattened morphology.

these calculations are meant to show the characteristic effect that rotation has on the hot gas. We also point out that the baryonic components contribute very little to the potential for $r \gtrsim 5$ kpc, implying the details of their assumed profile do not significantly affect our calculations. The results of these calculations for a stationary halo and a modest flat rotation curve of $v_\phi = 100$ km s^{-1} are seen in Figure 4.6. One sees that the isodensity contours are constant with r for the stationary halo, but become flattened with the inclusion of rotation. We also point out that these calculations and general results are consistent with those found by Marinacci et al. (2011), who estimated these same effects of coronal rotation on the underlying morphology.

In contrast with these model predictions, several observation-based lines of evidence suggest the Milky Way's hot gas distribution is not significantly flattened. As discussed in Section 4.4.1, analyses on large samples of line strength measurements, pulsar dispersion measures, and X-ray surface brightness measurements suggest a spherical morphology can better reproduce these observables than a disk-like mor-

phology. In particular, the models considered in Miller & Bregman (2013, 2015) included a flattened, extended distribution. However, the model fitting results for this flattened model (with an additional parameter and thus one less degree of freedom) were not a significant improvement in fitting the data compared to a spherical model. The analysis showed that a flattened halo was not required to fit the line strength measurements. Also, observations of hot gas in other galaxies do not indicate rotation significantly impacts their morphologies. The examples discussed in Section 4.4.1 found that the extended X-ray halos around both early- and late-type galaxies are typically fit well with spherical β models. Additional analyses on higher-resolution X-ray images of early-type galaxies indicate any X-ray observed ellipticity does not correlate with the galaxies' rotation velocities, implying rotation does not drive their morphologies (Diehl & Statler, 2007). Thus, the balance of observational evidence suggests the extended hot gas distributions around the Milky Way and other galaxies is approximately spherical.

The observed line centroids from Hodges-Kluck et al. (2016) combined with the models outlined in Section 4.4.2 lead to the robust result that there is global kinematic structure in the hot gas, regardless of the assumed density profile. This appears to be a valuable first step in this type of analysis, especially since there is little observational or theoretical background for the expected kinematic structure of this gas phase. The line profiles presented here are designed to highlight how we can learn about the Milky Way's hot gas kinematics, and show how the hot gas kinematics can potentially impact the inferred hot gas structure.

One example of how these line profile calculations can improve constraints on the hot gas structure is with a more accurate conversion between measured equivalent width and the column density. The velocity calculations presented in Section 4.4.3 imply that velocity flows modify the curve of growth analysis depending on the observed direction. Thus, one needs to account for bulk velocity flows to infer an

accurate column density from a measured equivalent width. These effects have not been considered in previous analyses of the Milky Way's hot gas, and impact inferred hot gas properties.

As an example application of the improved equivalent width-column density conversion, we examine the hot gas metallicity based on the observed O VII equivalent width toward the LMC direction and the hot gas dispersion measure in this direction. We convert the observed O VII equivalent width for the LMC X-3 X-ray binary into O VII column densities for different b values with and without velocity effects. These column densities are then converted to dispersion measures, which depend on the gas metallicity, and compared to the observed residual hot gas dispersion measure toward the LMC direction. The dispersion measure is the integral of free electrons along the line of sight, $\int_0^s n(s)ds$, which relates to the O VII column density (N_{OVII}) as follows:

$$\begin{aligned} \mathrm{DM} &= 1.2\frac{N_{OVII}}{f_{OVII}A_O Z} \\ &= 14.2\left(\frac{N_{OVII}}{10^{16}\mathrm{cm}^{-2}}\right)\left(\frac{f_{OVII}}{0.5}\right)^{-1}\left(\frac{A_O}{5.49\times10^{-4}}\right)^{-1}\left(\frac{Z}{Z_\odot}\right)^{-1}\mathrm{cm}^{-3}\mathrm{pc}, \end{aligned} \tag{4.17}$$

where f_{OVII} is the O VII ion fraction, A_O is the fixed solar oxygen abundance relative to hydrogen (Holweger, 2001), and Z is the gas metallicity. Thus, we infer an average hot gas metallicity by equating the inferred dispersion measure from the O VII measurement to the independently observed value.

The inferred metallicity depends on an accurate conversion between the observed O VII equivalent width and true column density, which we calculate above, and the residual dispersion measure due to hot gas. For the latter, analyses on LMC pulsars suggest the Milky Way's hot gas contributes 23 cm^{-3} pc to the total observed dispersion measures (Anderson & Bregman, 2010; Fang et al., 2013). Independent analyses report a consistent O VII equivalent width for the LMC X-3 spectrum, with

Wang et al. (2005) suggesting a value of 20 ± 6 mÅ and Bregman & Lloyd-Davies (2007) suggesting a value of 21 ± 5 mÅ (90% confidence regions). Here, we use a more current measurement with improved calibration from the Hodges-Kluck et al. (2016) analysis, 22^{+6}_{-4} mÅ. We also assume all of the absorption arises from the Milky Way's hot gas distribution, as opposed to a distribution associated with the LMC or intrinsic to the LMC X-3 X-ray binary. This appears to be a valid assumption since the O VII centroid is inconsistent with the LMC systemic velocity ($\sim$300 km s^{-1}) or the X-ray binary escape velocity ($\sim 10^3$ km s^{-1}) (Wang et al., 2005; Yao et al., 2009b). We convert this equivalent width to a column density using our curves of growth for the LMC direction, a range of plausible b values, and assuming either a stationary or corotating halo. We then use Equation 4.17 to convert these to dispersion measures for different metallicities. Figure 4.7 shows the lines where the calculated dispersion measure equals 23 cm^{-3} pc.

There are several key results to note from the calculations represented in Figure 4.7. Increasing the b value decreases the O VII column density required to match the observed equivalent width. Therefore, increasing the b value requires a decrease in metallicity in order to match the observed dispersion measure. For a stationary halo, the transition between solar and sub-solar metallicity occurs at $b = 130$ km s^{-1}. Including velocity effects broadens the line profile in this direction, which further reduces the O VII column density required to match the observed equivalent width. The transition between solar and sub-solar metallicity is at 100 km s^{-1} in this case. For both the stationary and corotating cases, the metallicity approaches a limit of $\approx 0.6 Z_\odot$ as b increases beyond 200 km s^{-1}. These results imply that the gas metallicity should be $\gtrsim 0.6 Z_\odot$ if b is less than the sound speed, but also that $b \gtrsim 100$ km s^{-1} if the gas metallicity is not greater than solar. This analysis provides important constraints on the average hot gas metallicity along the LMC sight line, however it also illustrates how the halo gas kinematics can impact inferred hot gas properties.

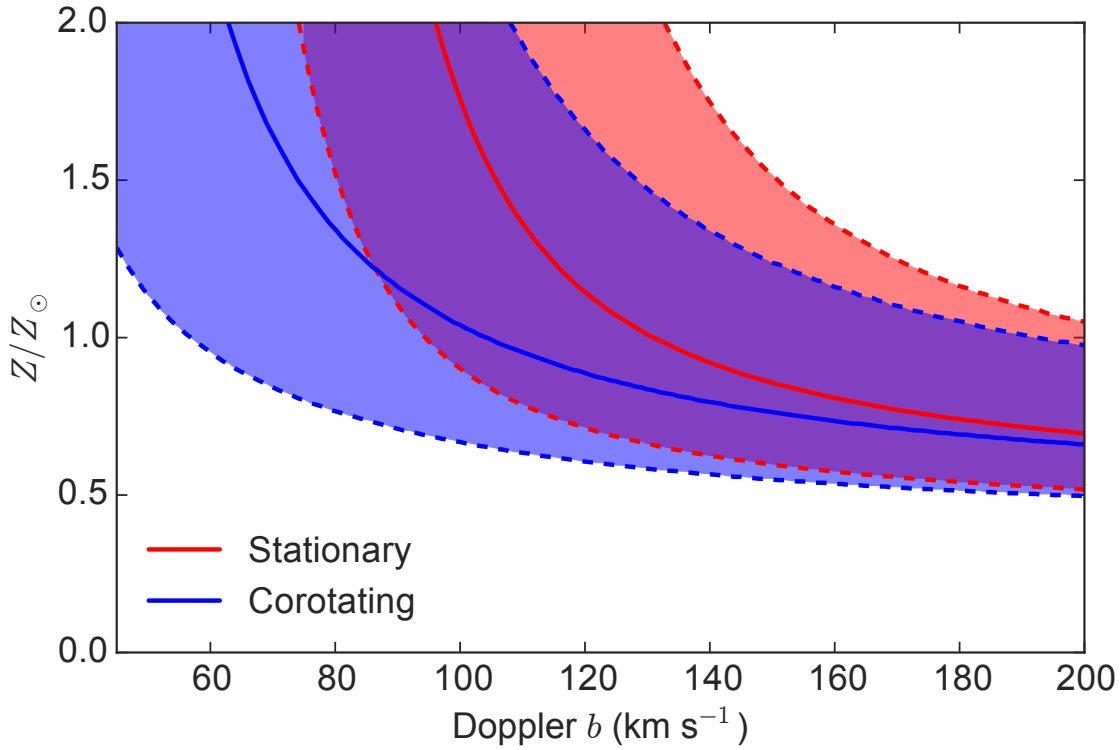

Figure 4.7: The hot gas metallicity and Doppler b values required for the observed LMC X-3 O VII equivalent width to equal a dispersion measure of 23 cm^{-3} pc (solid lines). The dashed lines incorporate the 90% uncertainty on the measured equivalent width. The red shaded region assumes a stationary halo for the column density conversion (or a standard curve of growth) while the blue shaded region assumes a corotating velocity profile.

4.5.2 Future Applications

These velocity considerations have important applications for future analyses on the Milky Way's hot gas structure. We have discussed several problems and initial attempts to solve them, such as the Milky Way's hot gas kinematic structure, the relation between the hot gas kinematics and density structure, and how to accurately interpret current hot gas observables. Here, we discuss strategies to solve these issues in the future, and highlight how our velocity calculations will be useful.

We can better constrain the Milky Way's hot gas kinematic structure by targeting sight lines that predict the largest differences between model line centroid values.

These regions provide the most leverage when validating or excluding different types of velocity flows. As an example, the upper-right panel in Figure 4.5 shows the absolute difference between the predicted line centroids for a stationary and corotating halo. Clearly, the regions near $l = 90^\circ$ and 270° show the largest differences of $\gtrsim$100 km s^{-1}, while regions near the Galactic pole and anticenter have differences of $\approx$0 km s^{-1}. Although we do not show a map with a v_r or v_z flow, the Galactic pole and anticenter are ideal locations to probe those effects since rotation produces a negligible shift in these regions. We also point out that a rotating gas profile predicts a distinctive line centroid feature near the Galactic center, in that the centroid switches sign for $|l| \lesssim 30^\circ$. It is possible that this effect could be observed, although the Galactic center is a complex region with other kinematic features due to the Fermi bubbles (Su et al., 2010; Fox et al., 2015). Regardless of these complications, these models should be used to motivate the most informative observations.

Interpreting current and future absorption line observations requires a better estimate for the plasma optical depth, or b value. Figure 4.4 indicates optical depth effects and line of sight kinematics introduce significant corrections to the equivalent width-column density conversion. The plasma b value is usually determined by the O VII Kβ to Kα ratio, but weak Kβ detections introduce systematic uncertainties in the inferred hot gas structural parameters (Williams et al., 2005; Gupta et al., 2012; Fang et al., 2015). One way to progress through this issue in the near future is with more sophisticated radiative transfer models. Monte Carlo radiative transfer methods (Whitney, 2011) are a promising avenue for these improvements since the codes predict both emission and absorption line strengths for an assumed plasma density profile and b value. Typical radiative transfer codes are not designed for analyses on the Milky Way's hot gas distribution, specifically with its extended geometry and our proximity embedded inside the distribution. We are currently developing a special radiative transfer code accounting for these geometric effects and the gas kinematic

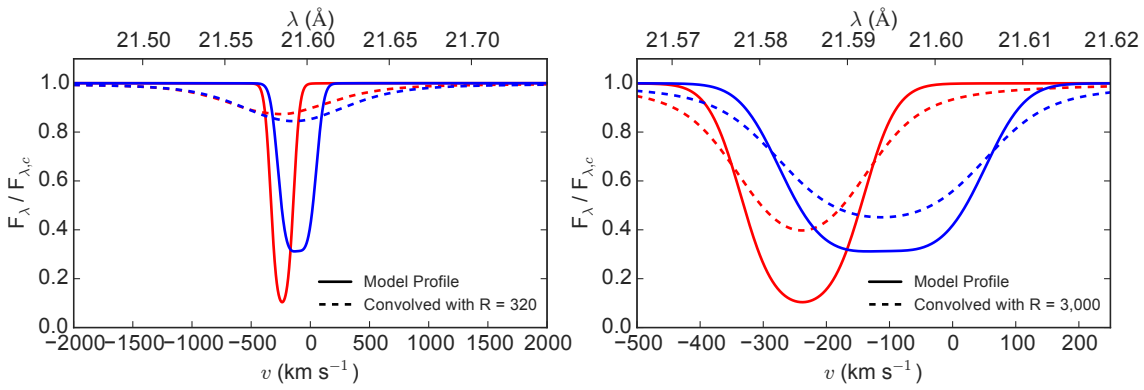

Figure 4.8: Same model absorption line profiles as Figure 4.2 (solid lines), but including convolutions with current and future instrumental line spread functions (dashed lines). The *left* panel shows the model lines convolved with an *XMM-Newton* RGS line spread function (approximately a Lorentzian with $R \approx 320$), while the *right* panel shows convolutions with an $R = 3000$ Lorenztian profile. The comparatively low resolution of current spectrographs only allows the equivalent widths and line centroids to be measured, but future high-resolution spectrographs will begin to resolve the line shapes and broadening due to velocity effects.

structure to model the plasma radiation field and resultant line strengths. Future projects with this code involve joint fits of the line strengths and shapes, resulting in improved estimates on the hot gas optical depth, structure, and kinematics. These techniques allow us to maximize the information we have from current X-ray observations, but we can gain significantly more information from future X-ray telescopes.

An X-ray spectrograph with higher spectral resolution than current X-ray spectrographs will yield significantly improved constraints on the Milky Way's hot gas structure. The *XMM-Newton* RGS and future missions, such as *Athena* and *Astro-H*, cannot resolve the absorption lines with spectral resolutions of $E/\Delta E \approx 300$–400 near 0.6 keV (den Herder et al., 2003, 2012). The intrinsic line widths and deviations from Gaussian line shapes are sensitive to how v_ϕ, v_r, and v_z depend on R, r, z, implying these spectrographs cannot probe these signatures. The left panel of Figure 4.8 shows the stationary and corotating line profiles from Figure 4.2 convolved

with a model RGS line spread function ($R \approx 320$), where any line asymmetry or velocity broadening due to kinematic effects is lost due to the low resolution (the difference in line widths is only $\approx$20 km s^{-1} in this case). Alternatively, technology exists for X-ray grating spectrographs with $R \approx$3000 in the soft X-ray band (Smith et al., 2014b). At this spectral resolution, kinematic signatures, such as the velocity broadening and line centroid, are much clearer and easier to detect compared to current absorption line observations. The right panel of Figure 4.8 illustrates this improvement, where we convolve the same intrinsic line profiles discussed above with an $R = 3000$ Lorentzian line spread function (the RGS line spread function is close to, but not a perfect Lorentzian). Thus, an improved X-ray spectrograph will provide significantly more information on the hot gas kinematics than current instruments.

Given these improved observations and tools to interpret them, we will continue to develop more sophisticated velocity models motivated by galaxy formation predictions. Galaxy formation simulations of Milky Way-like galaxies predict a diverse range of hot gas kinematic structures depending on the assumed formation mechanism. The supernova-driven outflow scenario predicts hot gas rotational velocities comparable to the disk and $v_{r,z} \gtrsim$100 km s^{-1} (e.g., Joung & Mac Low, 2006). On the other hand, the shock-heated coronal gas scenario predicts a largely hydrostatic halo, but with significant rotational velocities ($\gtrsim$100 km s^{-1}) near the disk (e.g., Nuza et al., 2014). Additional complexities include the assumed stellar feedback prescription, the impact of galaxy-galaxy interactions, and the inferred coupling between the hot gas and cooler gas phases. For example, Marinacci et al. (2011) explored the mixing and angular momentum transfer between $\sim 10^4$ K galactic fountain gas ejected from the disk and an initially static $\sim 10^6$ K corona. They found the cooler galactic fountain gas can accelerate the hotter coronal gas to velocities 80-120 km s^{-1} slower than the disk, broadly consistent with the results from Hodges-Kluck et al. (2016). Regardless of this consistency, there still exists many different velocity models that produce

distinct absorption line signatures. Future progress involves an iterative approach where velocity models become more complex to reflect a more realistic scenario, but the improved observations continue to validate or exclude different velocity models predicted in simulations. In this way, theory and observations provide additional information about how and when the hot gas obtains its kinematic structure.

4.5.3 Concluding Remarks

The model absorption line results presented here have numerous important applications regarding the Milky Way's hot gas structure. Many of the calculations were simple ideas, but were never applied to the Milky Way's extended hot gas distribution. We applied simple kinematic models to absorption line calculations to show what can be observed now, how the gas kinematics can alter our interpretation of current observables, what can be observed in the future, and future strategies for exploring these effects. Here, we summarize these results:

1. The model line centroid calculations presented here combined with the observed line centroids from Hodges-Kluck et al. (2016) indicate the Milky Way's hot gas distribution is likely not stationary. A model velocity profile with significant rotation velocity ($\approx$180 km s^{-1}) is most consistent with the data.

2. Ordered velocity flows of this magnitude can impact constraints on the hot gas density structure. Line of sight velocity effects alter the conversion between the equivalent width and column density. The corrections from an optically thin column can range between a factor of $\approx$2 to $\approx$5 depending on the underlying kinematic structure.

3. These flows can alter the underlying density profile into a flattened or "bow-tie" morphology as discussed in Marinacci et al. (2011). Current observational evidence suggests the Milky Way's hot gas is approximately spherical, although

the data cannot conclusively rule out a flattened morphology.

4. Future observational strategies should focus on the regions with the largest difference between predicted model centroid values. For probing the rotation curve, this is near the $l = 90^\circ$ and 270° directions. For probing accretion or outflows, this is near the Galactic pole or anticenter.

5. Current kinematic constraints are limited by the resolution of X-ray spectrographs. We show that an X-ray spectrograph with resolving power of $R \gtrsim 3000$ would begin to resolve the intrinsic line profiles, resulting in significantly better constraints on the hot gas kinematics.

6. Future model line profile calculations should incorporate more detailed kinematic structure derived from galaxy formation simulations, and account for optical depth effects in the plasma with radiative transfer codes. Both of these factors play significant roles in the absorption and emission line strength interpretations.

The work presented here can be considered an initial step toward understanding how these extended hot halos around late-type galaxies dynamically evolve with their host galaxies.

CHAPTER V

The Rotation of the Hot Gas Around the Milky Way

5.1 Preface

This chapter is adapted from work of the same title appearing in the Astrophysical Journal, Volume 822, 21 (Hodges-Kluck et al., 2016). Edmund J. Hodges-Kluck was the primary author of this work, while myself and Joel N. Bregman were coauthors. My contributions here include the absorption line centroid models discussed in Chapter IV and much of the discussion in Section 5.7.

5.2 Abstract

The hot gaseous halos of galaxies likely contain a large amount of mass and are an integral part of galaxy formation and evolution. The Milky Way has a 2×10^6 K halo that is detected in emission and by absorption in the O VII resonance line against bright background AGNs, and for which the best current model is an extended spherical distribution. Using XMM-Newton RGS data, we measure the Doppler shifts of the O VII absorption-line centroids toward an ensemble of AGNs. These Doppler shifts constrain the dynamics of the hot halo, ruling out a stationary halo at about 3σ and a co-rotating halo at 2σ, and leading to a best-fit rotational velocity $v_\phi = 183 \pm 41\,\mathrm{km\,s^{-1}}$

for an extended halo model. These results suggest that the hot gas rotates and that it contains an amount of angular momentum comparable to that in the stellar disk. We examined the possibility of a model with a kinematically distinct disk and spherical halo. To be consistent with the emission-line X-ray data the disk must contribute less than 10% of the column density, implying that the Doppler shifts probe motion in the extended hot halo.

5.3 Introduction

A basic prediction of ΛCDM galaxy-formation models is the existence of a hot ($10^6 - 10^7$ K) halo of gas accreted from the intergalactic medium around Milky Way-sized galaxies (extending to the virial radius), which forms as infalling gas is heated to the virial temperature at an accretion shock (e.g., White & Frenk, 1991). These halos may provide most of the fuel for long-term star formation in these galaxies (Crain et al., 2010; Joung et al., 2012), but their predicted properties are sensitive to the input physics, which can be constrained by the measurable properties of the gas.

Based on work over the past several years, we know that these extended halos exist, including around the Milky Way (Anderson & Bregman, 2011; Anderson et al., 2013; Miller & Bregman, 2015). The extent and luminosity of the hot gas implies that it has a similar mass to the stellar disk, and therefore could play an important role in galaxy evolution. Thus, it is important to measure the properties of the hot gas beyond mass and temperature (such as metallicity and density or velocity structure). However, hot halos are faint and the measurable X-ray luminosity can be dominated by stellar feedback ejecta near the disk (Li & Wang, 2013b), which makes these measurements difficult.

Only in the Milky Way can one measure the structure, temperature, metallicity, and kinematics of the hot gas through emission and absorption lines (Nicastro et al., 2002; Paerels & Kahn, 2003; McKernan et al., 2004; Yao & Wang, 2005; Williams

et al., 2005; Fang et al., 2006; Williams et al., 2006, 2007; Yao et al., 2009b; Henley & Shelton, 2012; Gupta et al., 2012), but kinematic constraints from prior studies (Bregman & Lloyd-Davies, 2007; Fang et al., 2015) are weak. Recent developments in the calibration of the X-ray grating spectrometers and the accumulation of multiple high quality data sets for individual objects have made it possible to determine line centroids to an accuracy of tens of $\mathrm{km\,s^{-1}}$, which enables us to improve the constraints on the kinematics of the gas by measuring Doppler shifts in lines that trace the hot gas. The λ21.602Å resonance O VII absorption line (Drake, 1988) is the best candidate, since it is sensitive to temperatures of $10^{5.5} - 10^{6.3}\,\mathrm{K}$ (which includes much of the Galactic coronal gas) and it is detected at zero redshift towards a large number of background continuum sources (e.g., Fang et al., 2015). The *emission* lines produced by the same species are useful for determining the structure and temperature of the hot gas (Henley & Shelton, 2012; Miller & Bregman, 2015), but they are too faint for high resolution spectroscopy. In this chapter we constrain, for the first time, the radial and azimuthal velocity of the hot gas by measuring the Doppler shifts in O VII lines detected towards bright sources outside the disk of the Milky Way.

5.4 Observations and Data Analysis

5.4.1 Sample and Reduction

To measure the global velocity of the million-degree gas around the Galaxy, one needs to measure Doppler shifts towards a range of sources across the sky in lines sensitive to this temperature. This gas is detected in X-ray emission and absorption, but the emission lines are far too faint for a focused grating observation. X-ray imaging CCDs measure the energies of incoming photons and are thus also low resolution spectrometers, but their spectral resolution is far too low to measure Doppler shifts of tens of $\mathrm{km\,s^{-1}}$. The only instruments capable of this accuracy are the *Chan-*

dra Low/High-Energy Transmission Grating (LETG/HETG) Spectrometers and the *XMM-Newton* Reflection Grating Spectrometer (RGS), and the 21.602Å O VII line is the only line that probes the relevant temperatures and is detected at $z = 0$ towards many background continuum sources. The OVIII line at 18.96Å probes slightly hotter gas and is only detected towards a few objects.

Our initial sample included all archival LETG and RGS data sets where the line has been detected in the literature. The LETG has modestly better spectral resolution at 21.6Å ($R = 400$) than the RGS ($R = 325$), but it only has a third of the effective area at this wavelength ($15\,\mathrm{cm}^2$ for the LETG, $45\,\mathrm{cm}^2$ for the RGS). In addition, unlike the LETG the RGS is always on (it has a dedicated telescope, whereas the gratings must be moved into the focal plane on *Chandra*), and thus has accumulated many more spectra. These factors lead to many more detected O VII lines in the RGS, so we only use the LETG data towards several calibration sources as a check on the wavelength solution (see below).

Our analysis sample includes 37 known O VII absorbers at $z = 0$ with RGS data (Nicastro et al., 2002; Fang et al., 2002; McKernan et al., 2004; Williams et al., 2005; Yao & Wang, 2005; Fang et al., 2006; Williams et al., 2006, 2007; Yao et al., 2009b; Gupta et al., 2012; Fang et al., 2015) (Table 5.1). These include AGNs as well as several X-ray binaries in the Milky Way's halo and Magellanic Clouds. We tried to include all sources known to be outside the disk with reported absorption lines, but we excluded three sources: NGC 3783, PKS $2005-489$, and Swift J1753.5 $-$ 0127. NGC 3783 has an intrinsic oxygen line with a P Cygni profile where we cannot disentangle the Galactic line, PKS $2005-489$ has a broad line that suggests blending or a non-Galactic origin, and the line in Swift J1753.5 $-$ 0127 is only detected in two of four high S/N exposures. We include NGC 5408 X-1 (which is an X-ray binary, not an AGN) and NGC 4051, but these systems have redshifts smaller than $1000\,\mathrm{km\,s^{-1}}$ so the lines may be intrinsic. NGC 4051 and MCG-6-30-15 also have known outflows;

as they have O VII lines attributed to the Galaxy in some prior studies (e.g., Fang et al., 2015) we include them here, but we show below that excluding them does not strongly change our results.

The data for each target were reprocessed using standard methods in the *XMM-Newton* Science Analysis Software (SAS v14.0.0) with the appropriate calibration files. This excluded hot, cold, and "cool" pixels, and data from periods when the background count rate exceeds 3σ from the mean. We applied the (default) empirical correction for the Sun angle of the spacecraft and its heliocentric motion (de Vries et al., 2015). We used the highest precision coordinates available rather than the proposal coordinates, which improves the accuracy of the wavelength scale. For each object, we merged the first-order RGS1 spectra and response matrices into a "stacked" spectrum. Standard processing resamples the data from native bins (about 0.011Å at 21.6Å) into a user-specified bin size. We binned the data to 0.02Å (one resolution element is about 0.055Å). This resampling causes small but stochastic changes in the bin assignment for some events, leading to variation under the same protocols, which we quantify by processing each object ten times in the same way.

Table 5.1. Oxygen Absorption Line Centroid Sample

Name	Gal Long. (deg)	Gal Lat. (deg)	z	$\sin(l)\cos(b)$	v_0 (km s^{-1})	$v_0 - v_{0,\mathrm{nc}}$ (km s^{-1})	Corotating (km s^{-1})	Stationary (km s^{-1})	Eq. Width (mÅ)	Cont. S/N
Mkn 421	179.832	65.031	0.0300	0.0013	-65^{+21}_{-21}	−29	0	0	13.1±0.5	232
3C 273	289.951	64.360	0.1580	−0.4069	33^{+45}_{-45}	−27	21	98	24.6±1.6	55
PKS 2155-304	17.730	−52.245	0.1160	0.1865	-39^{+38}_{-38}	−36	24	−45	15.4±0.9	95
Mkn 509	35.971	−29.855	0.0340	0.5094	-45^{+53}_{-50}	−41	0	−122	30.2±2.4	48
NGC 4051	148.883	70.085	0.0023	0.1761	110^{+46}_{-41}	8	−16	−42	40.4±3.6	33
MCG -06-30-15	313.292	27.680	0.0077	−0.6448	53^{+51}_{-54}	−1	26	154	35.1±3.2	38
Ark 564	92.138	−25.337	0.0247	0.9032	-57^{+93}_{-97}	21	−98	−217	12.3±1.9	50
ESO 141-55	338.183	−26.711	0.0371	−0.3323	-154^{+242}_{-264}	102	−35	80	21.2±5.1	18
H1426+428	77.487	64.899	0.1290	0.4142	83^{+153}_{-145}	−7	−25	−99	16.0±3.9	25
1H 0707-495	260.169	−17.672	0.0405	−0.9388	45^{+124}_{-121}	−21	109	225	24.3±6.1	22
PKS 0558-504	257.962	−28.569	0.1370	−0.8589	7^{+110}_{-104}	8	98	206	16.6±4.2	32
NGC 4593	297.483	57.403	0.0090	−0.4781	-63^{+153}_{-137}	11	24	115	27.1±7.1	13
Mrk 335	108.763	−41.424	0.0258	0.7100	-161^{+158}_{-206}	−40	−79	−170	19.3±5.3	22
PG 1211+143	267.552	74.315	0.0809	−0.2702	69^{+188}_{-195}	−57	14	65	40.3±11.	7
PG 1244+026	300.041	65.214	0.0482	−0.3631	130^{+286}_{-127}	−188	12	87	40.8±11.	10
Mkn 501	64.600	38.860	0.0337	0.7034	41^{+155}_{-173}	−68	−51	−169	25.2±10.	22
1ES 1028+511	161.439	54.439	0.3600	0.1853	40^{+180}_{-196}	81	−21	−44	36.4±11.	12
ESO 198-24	271.639	−57.948	0.0455	−0.5305	-652^{+231}_{-219}	−393	42	127	62.2±19.	7
NGC 2617	229.300	20.939	0.0142	−0.7079	58^{+124}_{-128}	−95	91	170	30.1±9.5	10
PG 1553+113	21.909	43.964	0.3600	0.2686	-149^{+162}_{-175}	45	25	−64	27.6±8.7	13

Table 5.1 (cont'd)

Name	Gal Long. (deg)	Gal Lat. (deg)	z	$\sin(l)\cos(b)$	v_0 (km s^{-1})	$v_0 - v_{0,\mathrm{nc}}$ (km s^{-1})	Corotating (km s^{-1})	Stationary (km s^{-1})	Eq. Width (mÅ)	Cont. S/N
H1101-232	273.190	33.079	0.1860	−0.8367	358^{+141}_{-152}	2	85	201	45.5±17.	8
3C 390.3	111.438	27.074	0.0561	0.8289	130^{+242}_{-515}	−21	−99	−199	25.0±10.	10
1H 0419-577	266.963	−42.006	0.1040	−0.7421	783^{+273}_{-255}	17	74	178	39.9±16.	6
Fairall 9	295.073	−57.826	0.0470	−0.4825	-18^{+291}_{-333}	−226	26	116	37.2±15.	6
IRAS 13224-3809	310.189	23.979	0.0660	−0.6982	63^{+201}_{-198}	31	35	167	45.1±19.	7
NGC 5408 X-1	317.149	19.496	0.0017	−0.6414	-19^{+216}_{-174}	−98	19	154	30.4±14.	7
PDS 456	10.392	11.164	0.1840	0.1770	57^{+267}_{-261}	47	76	−42	60.0±29.	7
Mrk 279	115.042	46.865	0.0305	0.6195	58^{+278}_{-229}	−29	−68	−149	14.2±7.0	15
E1821+643	94.003	27.417	0.2970	0.8855	85^{+241}_{-262}	−28	−97	−212	35.7±18.	7
IC 4329A	317.496	30.920	0.0160	−0.5799	-93^{+367}_{-229}	−73	15	139	38.3±20.	7
PG 0804+761	138.279	31.033	0.1000	0.5704	57^{+219}_{-236}	98	−73	−137	28.5±15.	6
NGC 5548	31.960	70.496	0.0172	0.1768	-46^{+183}_{-185}	−51	7	−42	18.0±10.	13
Mrk 766	190.681	82.270	0.0129	−0.0249	191^{+240}_{-365}	93	0	6	6.0±4.2	27
Local Group and Halo Sources										
LMC X-3	273.576	−32.082	-	−0.8457	35^{+69}_{-66}	7	63	203	23.1±3.0	36
4U 1957+11	51.308	−9.330	-	0.7702	-264^{+145}_{-152}	−124	32	−185	20.6±4.1	22
MAXI J0556-032	238.939	−25.183	-	−0.7751	137^{+85}_{-82}	84	39	186	16.0±3.3	33
SMC X-1	300.414	−43.560	-	−0.6251	117^{+127}_{-122}	−3	17	150	21.0±4.9	13

Note. — The quantity $v_0 - v_{0,\mathrm{nc}}$ is the difference between measurements with and without the heliocentric/sun-angle corrections. The corotating and stationary columns refer to model velocities. The equivalent width is for a Lorentzian line of fixed width (0.028Å), and the continuum S/N is per resolution element (∼0.055Å).

5.4.2 Velocity Measurements

To measure the Doppler shifts, we fit a model consisting of a power law and an absorption line to the spectrum in the 21-22Å bandpass using XSPEC v12.9.0 (Arnaud, 1996). We exclude an instrumental artifact between 21.75–21.85Å in each spectrum, and in several spectra there are one or more bad channels in the bandpass that we also exclude[1]. The parameters of the absorption-line model include the line centroid, the line width, and the line strength, but we fix the line width at the instrumental line-profile width because we do not expect detectable line broadening, an assumption we validated in the brightest sources. The best-fit centroid is converted to a velocity using the best-fit line energy from a stacked spectrum of Capella as a reference, corrected for the radial velocity of the star (described below). We measured the velocity for each of the ten stacked spectra per object, and we report the mean value with its 1σ uncertainty in Table 5.1, including the resampling uncertainty.

5.4.3 Wavelength Scale Accuracy

The systematic uncertainty in the wavelength scale limits the accuracy of our measurements, and recent improvements in the calibration of the wavelength scale (de Vries et al., 2015) and multiple high S/N spectra for the objects in our sample are largely what enable this study. Here we show the accuracy of the wavelength solution for the protocols we adopt and briefly describe the sources of uncertainty and their magnitudes.

We created spectra for the active stars Capella and HR 1099 following the protocols above, then measured the (emission) line centroids for strong, mostly unblended lines, and compared them to their laboratory rest wavelengths (Figure 5.1). We accounted for the radial velocity of each star ($+29.2\,\mathrm{km\,s^{-1}}$ for Capella and $-15.3\,\mathrm{km\,s^{-1}}$ for HR 1099; Karataş et al., 2004). We find no systematic offset in the 5-30 Å bandpass

[1] see http://xmm.esac.esa.int/external/xmm_user_support/documentation/uhb/rgsmultipoint.html

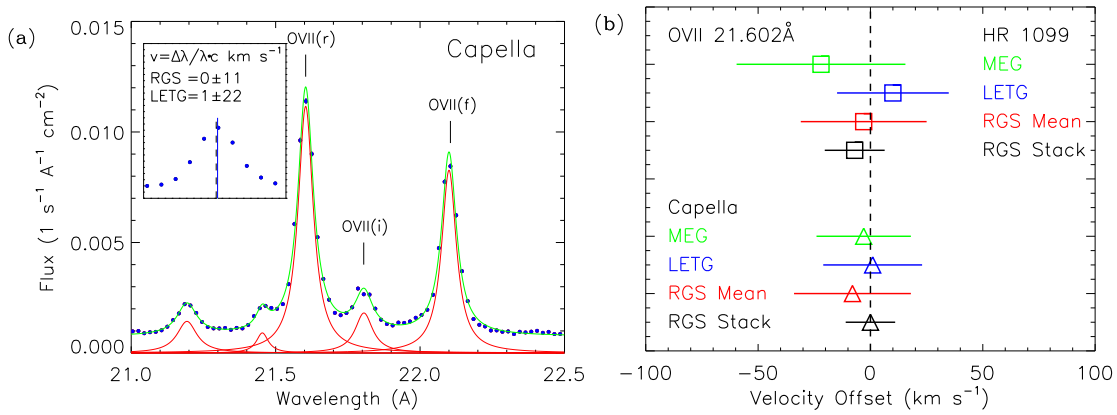

Figure 5.1: (a) The stacked RGS spectrum for Capella shows that the reduction protocols achieve an accurate wavelength solution (inset), and that averaging multiple data sets substantially reduces the systematic scatter in the wavelength grid. (b) Our measurements of the O VII emission line centroid relative to the 21.602Å rest wavelength in three instruments and two stars show that there are no serious cross-instrument issues with the wavelength grid. In each case, we accounted for the radial velocity of the stars.

or change over time. The wavelength offsets in O VII λ21.602Å for stacked spectra are $\Delta\lambda = 0.0 \pm 0.8$ mÅ (Capella) and 0.7 ± 1.6 mÅ (HR 1099). These correspond to $v = 0 \pm 11$ and $-7 \pm 22\,\mathrm{km\,s^{-1}}$. To verify that stacking does not introduce artificial offsets, we also measured centroids in each individual exposure (16 for Capella and 14 for HR 1099) and computed the weighted mean. The offsets are consistent with the stacked spectrum: $v = -8 \pm 26$ and $-3 \pm 28\,\mathrm{km\,s^{-1}}$ for Capella and HR 1099.

We also checked the wavelength solution against the LETG and HETG data for these stars. We reduced the data using the Chandra Interactive Analysis of Observations software (CIAO v4.7), and we found good agreement with spectra from the reduced data available through the TGCat project (Huenemoerder et al., 2011). We co-added the ±first-order spectra and stacked all observations. The LETG offsets are $v = 1 \pm 22\,\mathrm{km\,s^{-1}}$ (Capella) and $v = 10 \pm 26\,\mathrm{km\,s^{-1}}$ (HR 1099), whereas the HETG Medium Energy Grating offsets are $v = -3 \pm 21\,\mathrm{km\,s^{-1}}$ (Capella) and $v = -22 \pm 38\,\mathrm{km\,s^{-1}}$ (HR 1099). These results agree with the RGS and the labo-

ratory wavelength (Figure 5.1). We also compared velocity measurements between the RGS and LETG in the four brightest quasars (Rasmussen et al., 2003; Williams et al., 2005; Bregman & Lloyd-Davies, 2007; Rasmussen et al., 2007; Hagihara et al., 2010; Fang et al., 2015). The LETG and RGS centroids agree to within the 1σ error bar.

These results show that the wavelength scale is sufficiently accurate for our measurement, but it is important to note that there is a substantial systematic scatter that makes *individual* observations unreliable, and also that there will be systematic differences between our measurements and those reported for the same data using an earlier version of SAS or using incorrect source coordinates.

Different observations of the same object have a systematic scatter of $\sim$5 mÅ in the wavelength solution around the true mean value. This corresponds to $70\,\mathrm{km\,s^{-1}}$ at 21.602Å, and leads to the standard quoted systematic uncertainty[2] of $100\,\mathrm{km\,s^{-1}}$. The reason for this scatter is not clear, but about 3 mÅ could be explained by limits in the pointing accuracy of the telescope (de Vries et al., 2015). In any case, the scatter is normally distributed (based on measurements from many exposures of calibration stars such as Capella), and can thus be strongly mitigated with multiple observations of the same source. To reduce the scatter to within $20\,\mathrm{km\,s^{-1}}$ requires 15-20 independent spectra (assuming equal S/N and a $\sigma = 5$ mÅ). The sources in our sample have between 2-60 observations, and at the low end the reported 1σ statistical errors ($200\,\mathrm{km\,s^{-1}}$ or more) are much larger than a $70\,\mathrm{km\,s^{-1}}$ systematic error. For the bright quasars with many observations, we estimate a typical systematic error due to this scatter of $10 - 15\,\mathrm{km\,s^{-1}}$.

In addition to the scatter, there are systematic offsets produced by the Sun angle of the telescope and its projected heliocentric motion (possibly an inaccuracy in the star-tracker) that were measured and corrected by de Vries et al. (2015); we refer

[2]see the *XMM-Newton* Users' Handbook at https://heasarc.gsfc.nasa.gov/docs/xmm/uhb/rgs.html

the reader to their paper for a detailed description. The earliest version of SAS that contained these corrections was v13.0.0, and it was not enabled by default until v14.0.0; all prior absorption-line halo studies using the RGS used an earlier version or did not mention the correction. We measured line centroids with and without these corrections, and found centroid shifts in our sample with magnitudes between $0 - 100\,\mathrm{km\,s^{-1}}$ (higher for weak lines). To show the effect of not including them, we show the measured centroids without these corrections in Table 5.1. Finally, if we used the default (proposal) coordinates instead of the SIMBAD coordinates, we measured offsets of $\pm 10\,\mathrm{km\,s^{-1}}$.

Thus, we would expect our measured centroids to be correlated with prior results but perhaps significantly different relative to the statistical errors. For example, there is a systematic offset of about $60\,\mathrm{km\,s^{-1}}$ between our measurements and Fang et al. (2015) for the several systems where it can be measured. This offset cannot be entirely explained by the Sun angle and heliocentric motion corrections, but it is consistent with shifts seen relative to prior versions of SAS (de Vries et al., 2015). They do not report the line centroids for active stars, as they only need to measure the centroids to sufficient accuracy to identify halo absorbers. Thus, we do not regard the apparent inconsistency as reflecting an inherent uncertainty in line centroid measurements.

5.4.4 Other Systematics

In addition to the wavelength grid, there are a few sources of systematic uncertainty and some fitting choices that affect our final results but where we believe there is a correct choice. We briefly describe these here.

***Cool Pixels*:** There are several "cool" pixels in the vicinity of 21.6Å that have a lower than expected signal (by about 20%). By default, these pixels are included in the spectrum. We exclude them because they can affect weak absorption features.

The typical velocity shift between keeping and excluding them is $\Delta v = 10\,\mathrm{km\,s^{-1}}$ in bright sources.

***Binning and Resampling*:** The native RGS binning is about 11 mÅ at 21.6Å, but the default processing resamples the events onto a user-specified grid, with a default value of 10 mÅ. This resampling is probabilistic with a random element (normally distributed), which means that running the same protocol on a given data set multiple times will result in slightly different spectra. The magnitude of the velocity shift is strongly dependent on the line strength and the continuum S/N, so we reprocessed each data set ten times per reduction protocol set. We then added the standard deviation in the measured velocities in quadrature to the statistical error, since it behaves in essentially the same way. The bin sizes also affect the measured velocities, with a mean line centroid shift of $\Delta v = 7\,\mathrm{km\,s^{-1}}$ between bins of 10 mÅ and 20 mÅ in bright systems (we use the latter).

***Stacking*:** Temporal changes in the instrumental response or changes in the spectral shape of the source can bias the results of stacked spectra. On the other hand, jointly fitting several low-S/N spectra with the continuum shape as a free parameter leads to poorer constraints on the velocity of a line based on spectral bins far from the absorption line. We stack the spectra to improve the continuum S/N, but to determine if this provides systematic bias we measured the line shift between joint fits and stacked spectra in our brightest sources and the calibration sources. We find a typical $\Delta v = 5\,\mathrm{km\,s^{-1}}$ because the instrumental response in these regions does not appear to have temporal changes.

***Line Profile and Fixed Line Width*:** For lines with Doppler $b < 200\,\mathrm{km\,s^{-1}}$, we do not expect to measure reliable line widths (however, see the Doppler b measurements in some of the same lines in Fang et al., 2015). Since the RGS line-spread

function is best described as a Lorentzian near the core, we fit our spectra using a Lorentzian profile with the width fixed at the instrumental line width. If we use a Gaussian line profile instead but keep the width fixed, the line shift is consistent with zero in most cases but can be up to $\Delta v = 30\,\mathrm{km\,s^{-1}}$ in weak lines (statistical errors greater than $200\,\mathrm{km\,s^{-1}}$). When the line width is a free parameter, we find shifts in the Lorentzian centroids of $\Delta v = 0 - 15\,\mathrm{km\,s^{-1}}$ (the shift magnitude is negatively correlated with S/N) and $\Delta v = 20 - 50\,\mathrm{km\,s^{-1}}$ in the Gaussian case. However, for the Gaussian lines the best-fit line widths tend to be $1.5 - 2$ times the instrumental resolution, and the statistical error also increases. These fits are usually not significantly better than with a fixed line width, so in our view a non-zero line width is not required by the data, and these line widths reflect some small curvature in the continuum.

***Bandpass*:** The fitting bandpass is important because the continuum model needs to fit well even if the result is unphysical. Typically, one fits the local continuum, but in the literature for the O VII line this can vary from a fitting interval less than 1 Å wide to about 5Å wide. Our choice of fitting bandpass (21-22Å) is motivated by strong instrumental features below 21Å and above 22Å, but if we ignore these features and expand our bandpass by ±1Å, the typical velocity shift is $\Delta v = 3\,\mathrm{km\,s^{-1}}$.

***Bad Columns near 21.6Å*:** There is asymmetry in the line-spread function (LSF), which is the instrumental response to a δ-function, near the O VII line. This is not the same as the well known asymmetry in the LSF at the 1% level in the line wings (which is not important), but rather due to bad columns that are not included in the cool pixel list (Figure 5.2). For an arbitrarily strong δ-function line, the offset in the measured centroid from this defect can range from $\Delta v = 0 - 100\,\mathrm{km\,s^{-1}}$ depending on where the true line centroid is. However, if the line is unresolved but has some physical width (so that incident photons would be dispersed over multiple

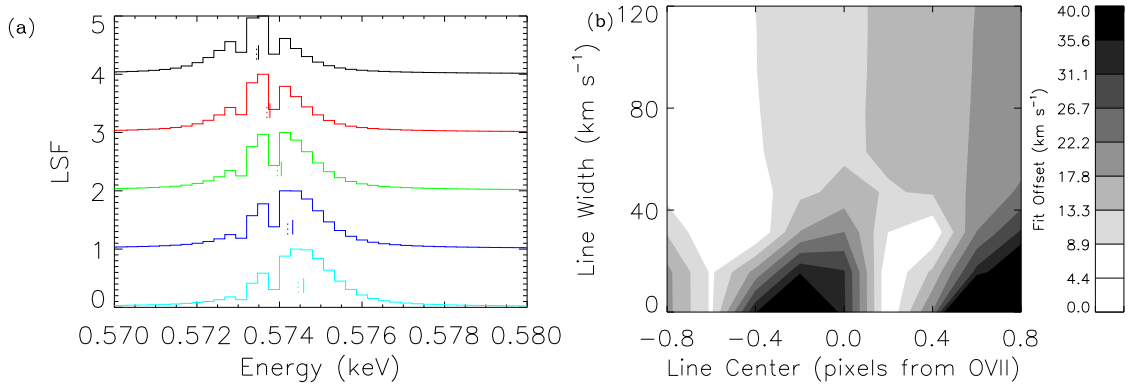

Figure 5.2: Bad columns near the O VII line can cause a systematic error in the centroid. (a) The difference between the nominal line center (dashed vertical tick) and the measured centroid (solid vertical tick) is a function of the true centroid. (b) The magnitude of this offset is plotted as a function of intrinsic line width and the nominal line centroid for *Xspec* simulations. For lines with an intrinsic width of 40 km s^{-1} or more, the typical error is about 15 km s^{-1}.

bins even before the LSF spreads them out), the error is strongly mitigated. We used XSPEC simulations to determine the error as a function of Doppler b parameter, and for $b > 40\,\mathrm{km\,s^{-1}}$ (about the thermal width even without turbulence), the typical error is reduced to $15\,\mathrm{km\,s^{-1}}$ (Figure 5.2). We expect the Galactic halo lines to be in this regime. Alternatively, one can ignore the columns, but because of their proximity to the region of interest, this will also bias the results.

Overall, the systematic error should allow measurements to better than $30\,\mathrm{km\,s^{-1}}$ accuracy with sufficient S/N. For the high S/N lines we estimate a typical systematic error of 15-20 km s^{-1}, and for lines weaker than about 4σ, the systematic error is dominated by the statistical error.

5.5 Halo Model

We used a simple halo model for comparison to the data. We adopted an extended density profile (Miller & Bregman, 2015) in which:

$$n(r) = n_0(1 + (r/r_c)^2)^{-3\beta/2}\ \mathrm{cm}^{-3}, \tag{5.1}$$

where $n_0 r_c^{3\beta} = 1.35 \pm 0.24\,\mathrm{cm}^{-3}\,\mathrm{kpc}^{3\beta}$ and $\beta = 0.50 \pm 0.03$, computed on a grid with 0.05 kpc cells. This model describes an all-sky sample of 649 O VIII emission lines (Henley & Shelton, 2012) well. We then imposed global bulk radial (v_r) or azimuthal (v_ϕ) velocities, assuming that these are constant with radius. These are the free parameters in the model. We likewise assume a constant metallicity of 0.3 $Z_\odot$ and a Doppler b parameter of $85\,\mathrm{km\,s}^{-1}$ due to turbulent motion in each cell, based on hydrodynamic simulations (Cen, 2012). We also account for intrinsic scatter (resulting from hydrodynamic flows) about any model by adding a velocity dispersion to the centroids when comparing to the models. This dispersion is not the same as line *broadening*, but refers to the typical value for a distribution of centroid shifts.

We obtain model velocities for each object by integrating from the position of the Sun outward along each line of sight, computing the line-of-sight velocity component and broadening for each cell and summing the resultant Voigt profiles (a more detailed description is given in Miller et al., 2016). We convolve the result with the LSF, compute the centroid, and add the solar reflex motion for comparison to the observations in the Local Standard of Rest frame. For this model, at least 50% of the total absorption comes from beyond 7 kpc from the Sun, and 90% from within 50 kpc. In the simplest case of a stationary halo, the Galactic rotation of the Local Standard of Rest ($v_{\mathrm{LSR}} = 240 \pm 8\,\mathrm{km\,s}^{-1}$; Reid et al., 2014) is reflected in the measured Doppler shifts: $v_{\mathrm{obs}} = -240\sin(l)\cos(b)$, where l is the Galactic longitude and b the Galactic latitude. The product $\sin(l)\cos(b) = \pm 1$ corresponds to the Sun moving directly towards or away from that direction, resulting in a Doppler shift of $\mp 240\,\mathrm{km\,s}^{-1}$. Another simple case is a corotating halo ($v_\phi = v_{\mathrm{LSR}}$), in which case the Doppler shifts will be closer to zero. Figure 5.3 shows the measured velocities with the stationary and corotating models.

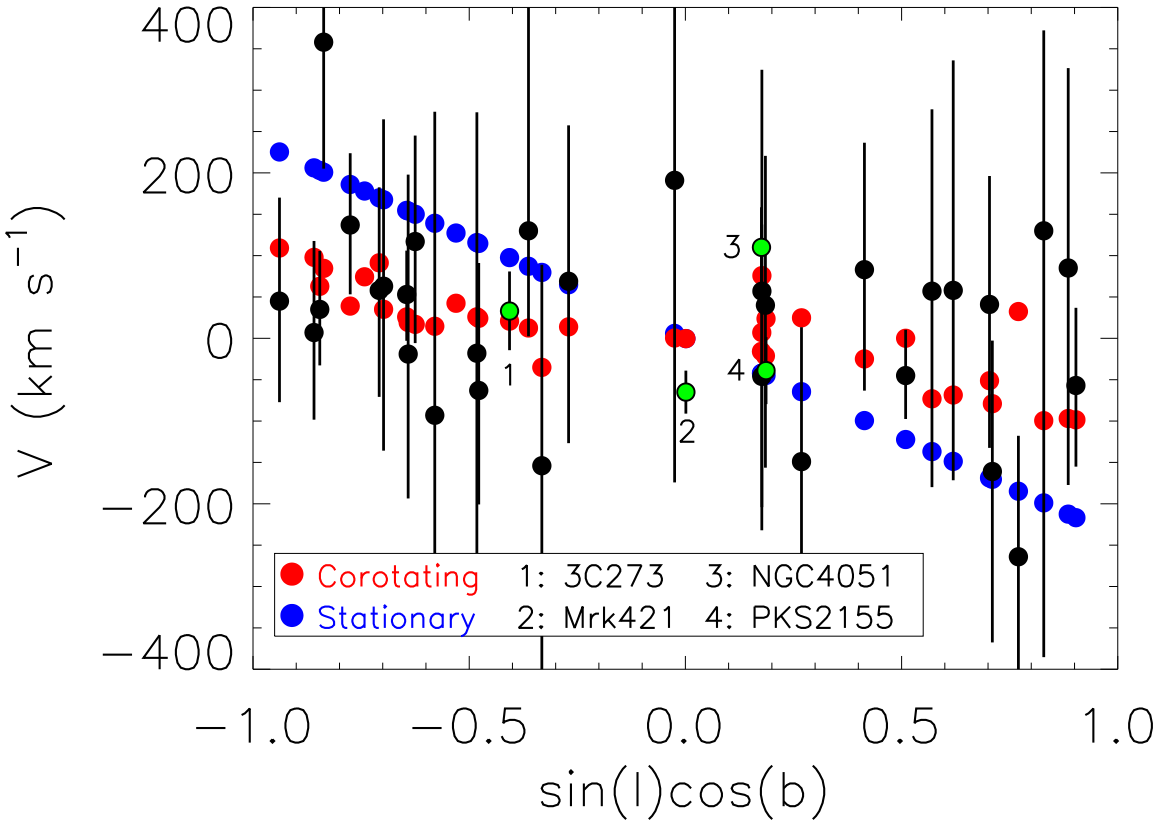

Figure 5.3: RGS measurements of O VII velocity offsets as a function of $\sin(l)\cos(b)$. Two models are shown for comparison with the data (black points): a stationary model (blue points) and a corotating model (red points). Error bars are 1σ (standard deviation). The four objects with the smallest error bars are labeled 1-4. The velocities of the lines towards Mrk 421 and NGC 4051 (labeled '2' and '3') suggest some intrinsic scatter.

5.6 Results

The best-fit v_r and v_ϕ values were obtained from a Markov-chain Monte Carlo (MCMC) approach, using the χ^2 statistic as a goodness-of-fit parameter. For zero dispersion, the best model has a prograde rotation velocity of $v_\phi = 183 \pm 41\,\mathrm{km\,s^{-1}}$ and a global inflow of $v_r = -15 \pm 20\,\mathrm{km\,s^{-1}}$, corresponding to a net accretion rate of $\dot{M} = 1 \pm 2 M_\odot\,\mathrm{yr}^{-1}$ (Figure 5.4). This is a formally acceptable fit, whereas the stationary halo is rejected with 99.95% probability and the corotating halo is marginally rejected with 95% probability. The velocity dispersion for which the reduced χ^2 is closest to

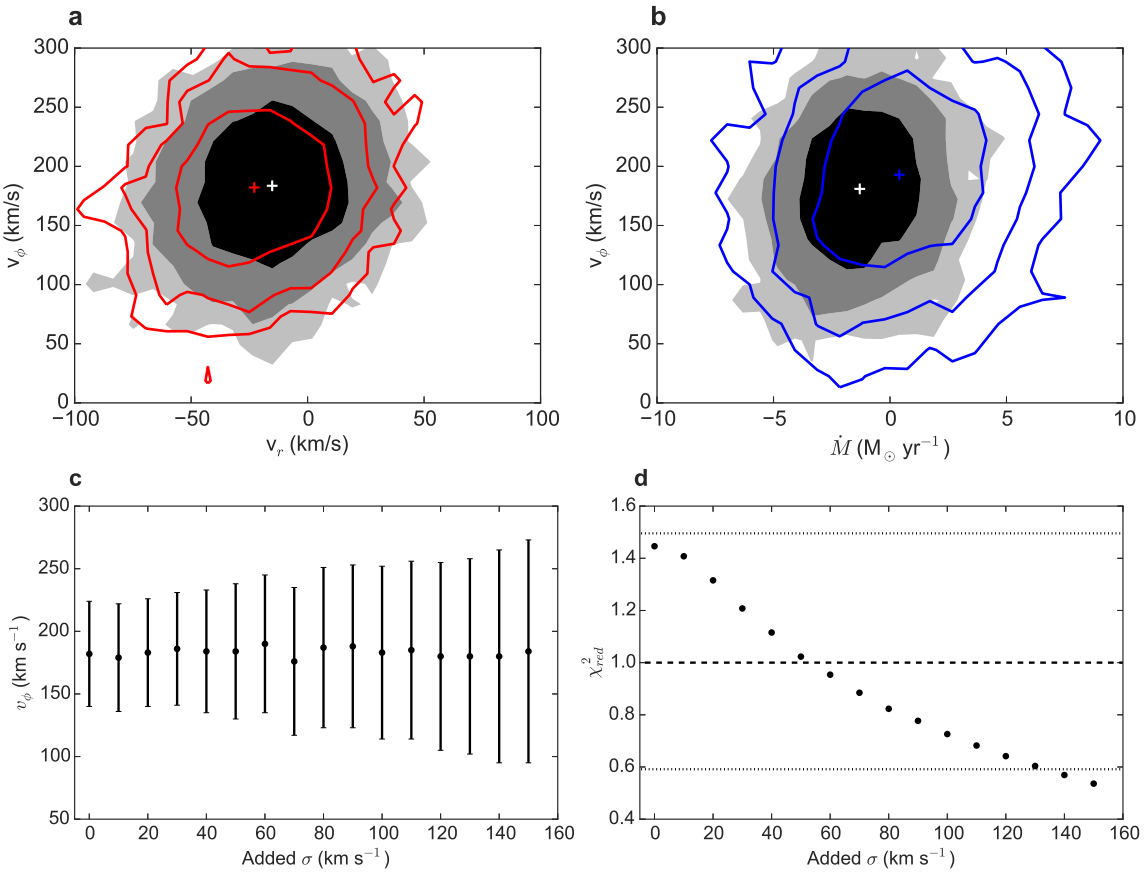

Figure 5.4: (a) Contours show the 1, 2, and 3σ deviations from the best-fit parameters for the whole sample (shaded) and lines with measurement errors less than 250 km s^{-1} (lines). (b) The radial velocity can be converted to an accretion or outflow rate, which is consistent with zero. (c) When the possibility of intrinsic scatter is included in the model, v_ϕ becomes less certain, but even with 150 km s^{-1} of added scatter, some rotation is necessary. (d) The added scatter value that brings the reduced χ^2 closest to 1.0 is near 50 km s^{-1}, with values above 140 km s^{-1} ruled out with 90% confidence (dotted lines).

1.0 is about 50 km s^{-1} (Figure 5.4); substantially more than this produces a χ^2 that is too small for the observed line centroids. The apparent inflow is not statistically significant, and the suggestion of inflow primarily results from Mrk 421 (Figure 5.3), which has a small uncertainty and is near $\sin(l)\cos(b) = 0$. Taking these results at face value, the large v_ϕ and extent of the halo imply that the total angular momentum

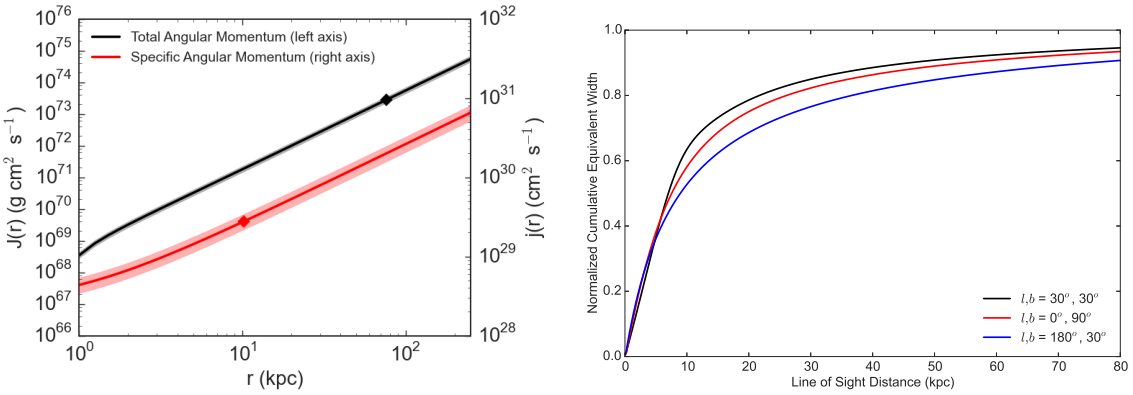

Figure 5.5: (a) The black (red) line shows the total (specific) angular momentum of the hot gas as a function of radius in our density model. Both assume $v_\phi = 183 \pm 41\,\mathrm{km\,s^{-1}}$. The diamonds show the values for the sum of stellar and HI values in the disk of the Milky Way. (b) The cumulative equivalent width for three sight lines shows that, while different sight lines are sensitive to gas at different distances, in all cases more than 70% of the equivalent width comes from beyond 5 kpc from the Sun.

of the hot gas within 50 kpc is comparable to that in the stars and gas in the disk of the Galaxy (Figure 5.5; Mo et al., 2010) The spread in recent measurements of $v_{\mathrm{LSR}} = 200 - 250\,\mathrm{km\,s^{-1}}$ (Brunthaler et al., 2011; Bovy et al., 2009; Reid et al., 2014) leads to $v_\phi = 130 - 180\,\mathrm{km\,s^{-1}}$, which does not change the picture of a lagging halo with prograde rotation.

In addition to parameter fitting, we used nonparametric statistical tests to test the hypothesis that some rotation is necessary. We tested the stationary and corotating models using the sign test and the Kolmogorov-Smirnov (KS) test, which compare distributions and are less sensitive to scatter. The sign test asks whether the medians of the measured and model velocities are consistent with each other (assuming a binomial distribution and a 50% probability that the model velocity exceeds the measured velocity). The left panel of Figure 5.6 shows the residuals from subtracting the data from the stationary model values, and the strong asymmetry rules out the stationary model with 99.87% probability. The KS test compares the cumulative distributions of the measured and model velocities, and this test rules out the stationary halo with

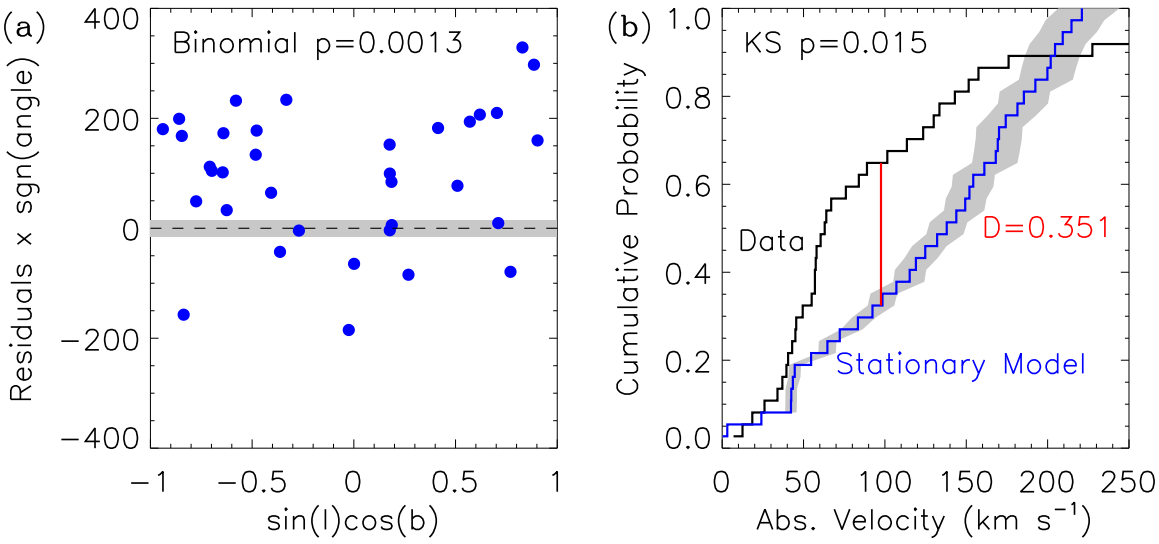

Figure 5.6: **(a).** The residual distribution around the stationary model shows that too many sight lines have velocities less than the model predictions. At each angle, a positive residual indicates that the model has a higher velocity magnitude than the measured offset. **(b).** The cumulative distributions of the model and measured velocity magnitudes (right panel) also rule out a stationary model by the KS test at the 98% level. The shaded grey regions in each panel represent $\pm 20\,\mathrm{km\,s^{-1}}$ from $v_{\mathrm{LSR}} = 240\,\mathrm{km\,s^{-1}}$.

98.5% probability. The corotating model is acceptable in the sign test (43% rejection probability) and not in the KS test (99.8% probability). The rejection of the stationary halo is model independent. If we exclude weak lines with $\sigma_{\mathrm{stat}} \geq 250\,\mathrm{km\,s^{-1}}$, a stationary model is still ruled out at more than 99.4% probability. If we exclude ambiguous lines (such as those towards NGC 5408 X-1, NGC 4051, and MCG-6-30-15), a stationary model is ruled out at about 98% probability in the KS test and 99.6% in the sign test. Excluding NGC 4051 (with its small error bars) increases the range of acceptable v_ϕ in the parametric fits, but the best-fit v_r does not change much as the error bars for Mrk 421 are even smaller.

We investigated the sensitivity of the best-fit parameters and the implied angular momentum to the model assumptions. First, the assumption of constant velocity must break down at some radius. An effort to measure the Galactic rotation curve to

200 kpc using disk and non-disk objects found (Bhattacharjee et al., 2014) that v_ϕ is flat to 80 kpc, while a measurement from disk stars in the Sloan Digital Sky Survey found (Xue et al., 2008) that v_ϕ in the disk declines by 15% from $v_{\rm LSR}$ at 10-20 kpc and remains constant from 20-55 kpc (the maximum probed). Thus, the assumption of a constant v_r or v_ϕ within $r < 80$ kpc appears to be reasonable, and more than 80% of the cumulative equivalent width comes from within this region (Figure 5.5). When we considered a model with a constant v_ϕ within 50 kpc and $v_\phi = 0\,{\rm km\,s^{-1}}$ beyond, the best-fit v_ϕ is nearly identical to the reported value. For a 10 kpc cutoff, the best-fit v_ϕ increases.

Second, there may be a metallicity gradient in the hot gas, in which case the cumulative equivalent width will be even more dominated by nearby gas. This would impact the inferred mass and total angular momentum of the halo gas. Constraints from OVII and OVIII and pulsar dispersion measures towards the Large Magellanic Cloud are consistent (Miller & Bregman, 2015) with a gradient of $Z(r) \propto r^{-0.2}$ with $Z = 0.39 Z_\odot$ at 1 kpc and $Z = 0.26 Z_\odot$ at 10 kpc. The uncertainty is large, but the gradient is shallow enough that gas beyond a few kpc contributes 50% or more of the equivalent width.

Finally, even a single-component hot halo is probably not isothermal and may also have flows arising from satellite galaxy motions or gaseous inflows and outflows. Since the combined emission- and absorption-line data favor an extended halo and its temperature is near the virial temperature, the gas is probably volume filling. Hydrodynamic flows in such a halo will primarily induce scatter of the type described above, which does not strongly affect our v_ϕ measurement (Figure 5.4). Thus, the measured halo rotation probably extends to tens of kpc and possibly to 100 kpc, and this gas will have a substantial angular momentum. However, the angular momentum values (Figure 5.5) are strongly model dependent, especially due to the assumption of constant $v_\phi(r)$.

5.7 Discussion

5.7.1 Halo and Disk Models

The interpretation of the measured Doppler shifts as a rotation signature depends on the validity of our single-component halo model. This depends on the following assumptions: (1) A volume-filling spherical halo is an approximately accurate representation of most of the hot gas around the Galaxy; (2) there is no strong local absorber that we have ignored; (3) The spherical halo has bulk global motion; (4) the assumption of $dv_\phi/dR = 0$ is reasonable within about 50 kpc; and (5) the Doppler shift measurements are accurate. The fourth and fifth assumptions were addressed above, so here we focus on the first three.

Two basic models are suggested in the literature for the structure of the hot halo: an extended, spherical distribution or an exponential disk with a scale height of a few kpc. When using individual sight lines or small samples (Yao et al., 2009a; Hagihara et al., 2010), the observed O VII and O VIII absorption and emission line strengths are consistent with an exponential disk model with a scale height of a few kpc. They are also consistent with a spherical model. However, larger samples of absorption lines (∼40 sight lines; Bregman & Lloyd-Davies, 2007; Gupta et al., 2012; Fang et al., 2015) and the all-sky emission-line intensities (≈1,000 sight lines Henley & Shelton, 2012; Miller & Bregman, 2013, 2015) favor a spherical model. Similar analyses on independent observables that also probe the hot gas, such as the pulsar dispersion measure towards the Large Magellanic Cloud and the ram-pressure stripping of Milky Way satellites favor an extended halo (Fang et al., 2013; Salem et al., 2015). Finally, a recent analysis of both Galactic and extragalactic sight lines for L_* galaxies finds that the O VII traces hot gas (Faerman et al., 2016). Thus, we adopted the spherical density profile of Miller & Bregman (2015).

However, these analyses are based on single-component models, and from basic

galaxy models we expect at least two X-ray absorbing components: infalling gas that is shock heated to the virial temperature ($T \approx 2\times10^6$ K for the Milky Way) and forms an extended halo (e.g., White & Frenk, 1991), and supernova-driven outflows from the disk (e.g., Shapiro & Field, 1976; Hill et al., 2012). In the latter case, we expect an exponential disk of hot gas with a scale height set (for a given Galactocentric radius) by the temperature at the midplane. It is worth noting that for $T = 2\times10^6$ K, the scale height at the Solar circle is larger than the Galactocentric distance, so the distribution of outflowing gas could also be spherical, if not very extended; the true shape depends on how widespread the outflows are in the disk, the actual midplane temperature, and the amount of radiative cooling. Within the galaxy disk itself, supernovae contribute to the hot interstellar medium, much of which is confined within the disk. Since X-ray absorption covers a wider temperature range than emission, we are also weakly sensitive to cooler gas (described in the following subsection).

These components may be kinematically distinct, as is seen in the warm gas by Nicastro et al. (2003); Savage et al. (2003), but at the relatively low resolution of the RGS, we expect them to be blended. This complicates the interpretation of the measured centroids, which are the weighted average of the offsets for each component along that line of sight. At a qualitative level, we expect the gas confined in the galaxy disk to rotate with it (although depending on the distances to the absorbers, there may not be any rotation signature) and the gas in supernova-driven outflows to rotate in the same direction but lagging the disk as it reaches larger heights or radii.

To constrain the column and thus the influence on the line centroids from a disk component, we extended the analysis of Miller & Bregman (2015) to fit a disk+halo model to the same data set they used: 648 O VIII emission lines from Henley & Shelton (2012), which are filtered for contamination from solar-wind charge exchange and ignore most of the Galactic plane. We refer the reader to Miller & Bregman (2015) for a more detailed explanation of the modeling procedure, but we summarize

our model components here.

The Sun exists in a region known as the Local Bubble, which emits soft X-rays (e.g., Cox & Reynolds, 1987; Snowden et al., 1997), and we adopt for the Bubble a temperature of 1.2×10^6 K, a variable path length between 100-300 pc, and a density $n_{\rm LB} = 4 \times 10^{-3}\,{\rm cm}^{-3}$. The nature of the Bubble and the density remain debatable because of the contribution from solar-wind charge exchange (e.g., Welsh & Shelton, 2009; Kuntz, 2009; Galeazzi et al., 2014; Snowden et al., 2015; Henley & Shelton, 2015). We have ignored hot interstellar gas confined within the galaxy disk other than the Local Bubble. Constraints from the intensity of the soft X-ray background imply that our sight lines will incur only a small column from this material, and the emission-line sample excludes the Galactic plane. For the extended halo component, we assume an isothermal (2×10^6 K) plasma with a density profile described by Equation 5.1. For the exponential disk component, we assume a form for the density of:

$$n = n_{0,{\rm disk}} e^{-z/h}\ {\rm cm}^{-3}, \tag{5.2}$$

where h is the scale height. The temperature declines in an analogous way, and we fix the midplane temperature and its scale height to 2.5×10^6 K and 5.6 kpc, respectively (Hagihara et al., 2010) because we do not model the line ratios as a temperature diagnostic. The free parameters are the normalizations, β, and h, which we constrain using the same MCMC method as Miller & Bregman (2015).

We assume that each component is optically thin and compute its contribution to the intensity along each line-of-sight s:

$$I = \frac{1}{4\pi} \int n(s)^2 \epsilon(T(s)) ds, \tag{5.3}$$

where $\epsilon(T)$ is the volumetric line emissivity from the APEC thermal plasma code

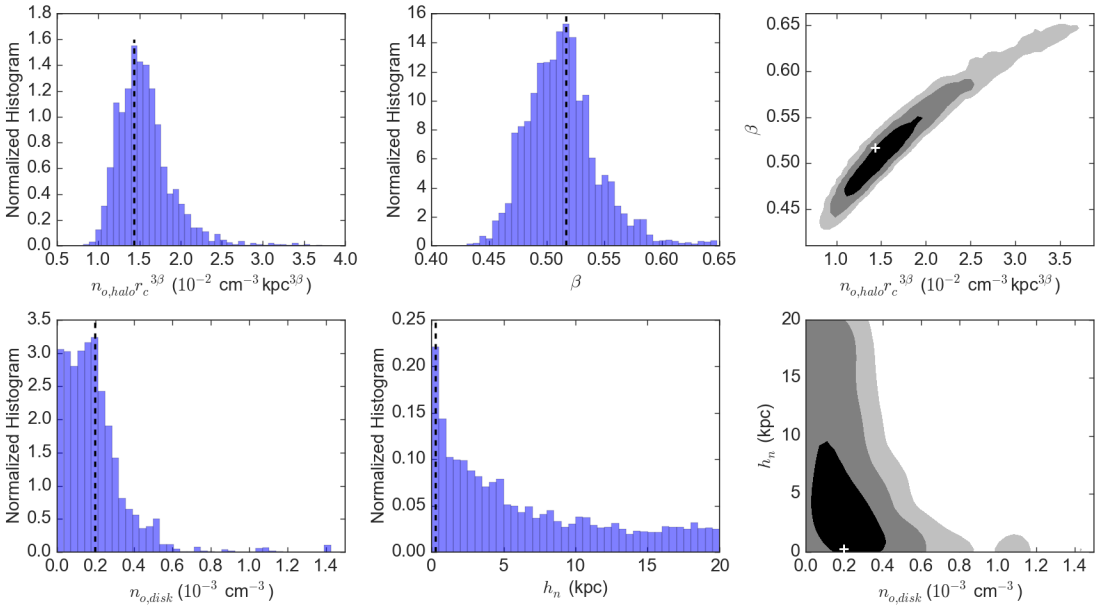

Figure 5.7: Our MCMC fitting results as marginalized posterior probability distributions (left and center columns) and contour plots for the model parameters (right column). The vertical dashed lines (distribution plots) and white crosses (contour plots) represent the best-fit model values. The halo parameter distributions (top left and top center panels) are almost identical to the results from Miller & Bregman (2015). The disk midplane density distribution (bottom left panel) implies densities significantly lower than previous estimates ($\approx 10^{-3}$ cm^{-3}).

(Foster et al., 2012). Finally, the line intensities from Henley & Shelton (2012) do not account for absorption due to Galactic HI, so to compare our model intensities to theirs we apply photoelectric absorption using the neutral hydrogen column from Kalberla et al. (2007) to the halo and disk components:

$$I(s) = I_{\rm LB}(s) + (I_{\rm halo}(s) + I_{\rm disk}(s))e^{-\sigma N_{\rm H}}, \tag{5.4}$$

where σ is the absorption cross-section and $I_{\rm LB}$ is the intensity from the Local Bubble.

Figure 5.7 shows the results from the MCMC analysis as marginalized posterior probability distributions for each of the free parameters. The model is not a signif-

icant improvement on the pure halo model, and the best-fit parameters for the halo ($n_{0,\mathrm{halo}} r_c^{3\beta} = 1.43 \pm 0.25 \times 10^{-2}\,\mathrm{cm^{-3}\,kpc^{3\beta}}$, $\beta = 0.52 \pm 0.03$) are consistent with the results in Miller & Bregman (2015). The disk parameters are poorly constrained and indicate that *the exponential disk contributes at most 10% of the total O* VII *column density.* This corroborates the Miller & Bregman (2015) result. In contrast, the Hagihara et al. (2010) disk model (which assumes the halo gas can be described entirely by a disk and is based on one sight line) finds $n_{0,\mathrm{disk}} = 1.4 \times 10^{-3}$ and $h = 2.3\,\mathrm{kpc}$. Yao & Wang (2005), who include some sight lines near the Galactic plane and some outside the plane, find that the O VII column is consistent with $n_{0,\mathrm{disk}} = 6.4 \times 10^{-3}\,\mathrm{cm^{-3}}$ and a scale height of $h = 1.2\,\mathrm{kpc}$, but the authors acknowledge that mixing results from sight lines towards nearby X-ray binaries at low latitudes and those at high latitudes can lead to a strong bias; the hot material confined to the galaxy disk is not part of the exponential disk structure that we have modeled, but it can contribute at low latitudes.

Thus, the impact of the disk component on the measured centroids must be small, since 80-90% of the column density will come from the spherical component. Assuming that the two components are kinematically distinct, for the latter to be stationary and consistent with the measured centroids requires a disk speed much faster than co-rotation. We verified this by modeling a rotating disk and a stationary halo where the disk contributes 10% of the column. Since this is inconsistent with models where the gas originates in the galaxy disk, the data probe motion in the spherical component. For reference, if the Hagihara et al. (2010) disk model is adopted instead of the Miller & Bregman (2015) model or our disk+halo model, the best-fit azimuthal and radial velocities are $v_\phi = 151 \pm 32\,\mathrm{km\,s^{-1}}$ and $v_r = -15 \pm 18\,\mathrm{km\,s^{-1}}$.

We have assumed that, to first order, the spherical component moves as a solid body with some v_ϕ and v_r. There may be second-order effects such as the internal flows mentioned above (perhaps due to satellite motions or infalling clouds) or

modes in the fluid, which would add scatter to the velocity measurements. However, if the halo is volume filling and in steady state, then large scale disturbances will tend to dissipate in a sound-crossing time (which could be a long time if the halo is very extended), and the gas (if stationary) will tend towards hydrostatic equilibrium. Multiple major kinematic components are therefore not expected, although we would expect differential rotation. In this case, the measured rotation velocity is some average but still provides useful information. Also, if the material is fresh infall from the cosmic web then it likely accretes along filaments, which lead to a preferential orbital angular momentum axis. Finally, gas ejected from the disk (either cold or hot) could spin up the halo (Marinacci et al., 2011), although perhaps not to the velocity that we infer.

It is possible that there is a layer of warm-hot gas near the Galactic plane (in addition to the Local Bubble) that affects every sight line out of the Galaxy, but to which our models are not sensitive because we ignore data close to the Galactic plane (where dust, supernova remnants, and other features make modeling very difficult). Characterizing the structure and filling factor of the hot interstellar medium has been a major effort by itself (e.g., Yao & Wang, 2005; Nicastro et al., 2016; Hagihara et al., 2011) and is beyond the scope of this chapter, but if there is such a layer (possibly a disk with a scale height of a few hundred pc) with a high density, the rotation signature in the RGS data could be misattributed to the halo. On the other hand, for plausible path lengths, oxygen column densities, and foreground absorption column densities this layer should also produce emission in excess of the Local Bubble contribution to the soft X-ray background.

To summarize, the halo models that are based on many data points as opposed to a few sight lines favor a spherical halo (especially in emission) as the dominant component. Any contribution to the column density from a kinematically distinct (thick) exponential disk is small in this scenario, so the Doppler shifts support a

non-stationary extended halo. Reinterpreting these shifts will be necessary if future data or analyses rule out a spherical halo (or at least a volume-filling one) or a high resolution X-ray spectrometer resolves the lines into components inconsistent with rotation. Also, we reiterate that the parametric fit strongly depends on the few AGNs with the highest S/N, but the nonparametric tests indicate rotation at some level.

5.7.2 Potential Bias from Cooler Gas

The O VII ion fraction is high between $3 - 20 \times 10^5$ K, so the cooler (non-coronal) gas seen in and around the Galaxy in O VI with *FUSE* (Nicastro et al., 2003; Savage et al., 2003; Wakker et al., 2003; Wang et al., 2005; Yao & Wang, 2007; Shelton et al., 2007; Bowen et al., 2008) will also absorb O VII . The O VI lines towards background objects reveal Galactic and high-velocity absorbers (Nicastro et al., 2003; Savage et al., 2003; Sembach et al., 2003). The Galactic absorbers (also seen towards stars) are consistent with an exponential disk of scale height 1-4 kpc (Savage et al., 2003; Bowen et al., 2008), whereas the high-velocity absorbers may come from the halo or outside the Galaxy. If the column densities of these O VI absorbers are high, then their O VII lines could bias our results. Since the disk component will rotate, we are most concerned about contamination from this gas.

Bowen et al. (2008) measured O VI column densities for about 150 sight lines around the Galaxy and found a typical column density of $N_{\rm OVI} \sin(b) \sim 1.6 \times 10^{14}\,{\rm cm}^{-2}$. For the sight lines in our sample, we expect $N_{\rm OVI} = 1 - 4 \times 10^{14}\,{\rm cm}^{-2}$. If the O VI absorbers are at $T = 3 \times 10^5$ K and in collisional ionization equilibrium, the OVII/O VI ratio is 1.7, which leads to an expected contribution of $N_{\rm OVII} = 2 - 7 \times 10^{14}\,{\rm cm}^{-2}$. In contrast, the typical O VII column (assuming an optically thin plasma) is $N_{\rm OVII} \sim 4 - 5 \times 10^{15}\,{\rm cm}^{-2}$ (Miller & Bregman, 2013). Hence, the contribution directly from O VI absorbers in the Galaxy is at most 15%. It is likely lower,

since Gupta et al. (2012) and Miller & Bregman (2015) argue that the O VII lines are not optically thin. The bias from the O VI absorbers also declines at higher latitude, since the O VII column declines more slowly than the O VI column with increasing b (corroborated in *emission* by Henley & Shelton, 2013). For most of our sight lines we estimate that the local and disk contribution to the O VII column is less than 10%.

Even a 10% contribution is important for measuring the true halo velocity, but compared to the uncertainty in our best-fit velocity parameters, it is small. More importantly, as with the hot disk considered above, it cannot by itself account for the measured velocities if we assume that the million-degree halo is stationary.

5.7.3 Summary and Conclusions

We have measured a signature of rotation in the O VII line around the Milky Way using 37 sight lines towards background AGNs and archival RGS data. The parametric fit strongly depends on the brightest AGNs, but nonparametric tests indicate that the O VII absorbers are not stationary, even when removing suspect lines. From larger samples of emission and absorption lines, we believe that an extended halo is more consistent with the data than an exponential (thick) disk, and in this case this halo rotates at some velocity smaller than $v_{\rm LSR}$. Taken at face value, this implies that the million-degree gas has a comparable angular momentum to the galaxy disk. It is possible that both components exist, in which case the RGS lines are blends of kinematically distinct components. We use a large sample of emission lines to constrain the contribution of each component to the column density, and find that an exponential disk accounts for no more than 10% of the O VII column density. Thus, the measured Doppler shifts are dominated by the motion of the gas in the extended halo, which is consistent with prograde rotation. Even if a disk were to dominate (which, for our data, produces an unacceptable χ^2 value), the best-fit azimuthal velocities imply that it is rotating at nearly the same speed and with a comparable amount of

angular momentum to the spherical model.

This conclusion depends on assumptions about the underlying model. Measuring the true velocity and separating the X-ray absorbers into their various components requires a high-resolution X-ray instrument with a large effective area (e.g. *ARCUS*, Smith et al., 2014b), which would also give important information on their line shapes that could constrain the optical depth and Doppler b parameters (Miller et al., 2016), as well as reveal the contribution to the total column from the disk and the coronal halo gas seen in X-ray emission.

The recent work on calibrating the conversion of dispersion angle to a wavelength grid for the RGS (de Vries et al., 2015) and stacking multiple observations of the same object enables a wavelength accuracy of tens of $\mathrm{km\,s^{-1}}$ for the first time (Figure 5.1). After investigating a variety of systematic issues, we find that the statistical uncertainty (due to the low S/N in many spectra and the relatively small sample) remains the major source of error. The inferred halo velocity and angular momentum are strongly model dependent (and the uncertainties that we report are large), but the basic conclusion that the hot gas distribution rotates is less so.

Several scenarios could produce a rotating halo that lags behind the disk, depending on the geometry. These include a galactic fountain of cool gas that spins up hot gas (Marinacci et al., 2011), a hot galactic fountain of superbubble ejecta that produces an exponential disk before cooling, or infall from the cosmic web with some preferential direction. Our measurements cannot, by themselves, distinguish between these models (which may not be mutually exclusive), but they are an important kinematic constraint for future halo and galaxy formation models.

CHAPTER VI

The Interaction of the Fermi Bubbles with the Milky Way's Hot Gas Halo

6.1 Preface

This chapter is submitted and currently under review for publication in the Astrophysical Journal, and is coauthored by Joel N. Bregman. Similar to the work in Chapter III, much of the emission line data comes from the work by Henley & Shelton (2012). My contributions include the production of a complementary dataset and all subsequent data modeling and analysis.

6.2 Abstract

The Fermi bubbles are two lobes filled with non-thermal particles that emit gamma-rays, extend ≈10 kpc vertically from the Galactic center, and formed from either nuclear star formation or Sgr A* accretion activity. Simulations predict a range of shock strengths as the bubbles expand into the surrounding hot gas halo distribution ($T_{halo} \approx 2 \times 10^6$ K), but with significant uncertainties in the energetics, age, and thermal gas structure. The bubbles should contain thermal gas with temperatures between 10^6–10^8 K, with potential X-ray signatures. In this work, we constrain the bubbles' thermal gas structure by modeling O VII and O VIII emission line strengths

from archival *XMM-Newton* and *Suzaku* data. Our emission model includes a hot thermal volume-filled bubble component cospatial with the gamma-ray region, and a shell of compressed material. We find that a bubble/shell model with $n \approx 1 \times 10^{-3}$ cm^{-3} and with $\log(T) \approx 6.60$-6.70 is consistent with the observed line intensities. In the framework of a continuous Galactic outflow, we infer a bubble expansion rate, age, and energy injection rate of 490^{+230}_{-77} km s^{-1}, $4.3^{+0.8}_{-1.4}$ Myr, and $2.3^{+5.1}_{-0.9} \times 10^{42}$ erg s^{-1}. These estimates are consistent with the bubbles forming from a Sgr A* accretion event rather than from nuclear star formation.

6.3 Introduction

The Fermi bubbles are important Galactic structures that were recently discovered by the *Fermi Gamma-ray Space Telescope* (Su et al., 2010). The bubbles are two diffuse lobes of material extending $\sim$50° above and below the Galactic plane ($\approx$10 kpc at the Galactic center). Their surface brightness shows little variation on the sky, their gamma-ray spectrum follows a power law with $dN/dE \propto E^{-2}$ between $\approx$1–200 GeV, and they have a counterpart in microwaves, known as the *Wilkinson Microwave Anisotropy Probe* (*WMAP*) haze (Dobler & Finkbeiner, 2008; Dobler et al., 2010; Su et al., 2010; Ackermann et al., 2014). It is still unclear what produces the gamma-rays, but all plausible mechanisms imply energetic cosmic ray particles exist within the bubbles. This inference combined with the bubbles' size and location on the sky suggest they are affiliated with a massive energy injection event near the Galactic center.

The bubbles' morphology is similar to wind-blown bubbles observed in other galaxies, indicating they formed from either a period of enhanced nuclear star formation or a Sgr A* outburst event (see Veilleux et al. (2005) for a review). Star formation can drive outflows through a combination of stellar winds from young stars and multiple type II supernova explosions (e.g., Leitherer et al., 1999), while black hole accretion

episodes can produce energetic jets or winds that inflate a cavity with thermal and non-thermal particles (e.g., McNamara & Nulsen, 2007; Yuan & Narayan, 2014). Both of these scenarios are critical events in galaxy evolution, as they both can deposit significant amounts of energy into the rest of the galaxy on $\gtrsim$10 kpc scales (see McNamara & Nulsen (2007) for a review). However, the details of these "feedback" effects (mass displacement, energy transport, etc.) are poorly understood since we observe them in external galaxies. The Fermi bubbles are a unique laboratory for understanding these processes since we can spatially resolve the bubbles across multiple wavebands.

A popular strategy to probe these effects and bubble origins has been the use of magnetohydrodynamic (MHD) simulations to reproduce the global bubbles' morphology and non-thermal properties. Simulations produce cosmic rays from either a black hole accretion event (Zubovas et al., 2011; Zubovas & Nayakshin, 2012; Guo & Mathews, 2012; Guo et al., 2012; Yang et al., 2012, 2013; Mou et al., 2014, 2015), nuclear star formation activity (Crocker, 2012; Crocker et al., 2014, 2015; Sarkar et al., 2015; Ruszkowski et al., 2016), or in-situ as the bubbles evolve (Mertsch & Sarkar, 2011; Cheng et al., 2011; Fujita et al., 2014; Lacki, 2014; Cheng et al., 2015; Sasaki et al., 2015), and compare the non-thermal emission to the bubbles' gamma-ray emission. All of these origin scenarios can reproduce the bubble morphology, but they imply significantly different input energetics and timescales required to inflate the bubbles ($\dot{E} \gtrsim 10^{41}$ erg s^{-1}, $t \lesssim 5$ Myr for black hole accretion compared to $\dot{E} \lesssim 5 \times 10^{40}$ erg s^{-1}, $t \gtrsim 50$ Myr for star formation). This variation in the feedback rate is a significant uncertainty in how the bubbles impact the Galaxy, but there are additional factors that can constrain the characteristic bubble energetics.

Constraining the bubbles' thermal gas distribution is a promising avenue to solve this problem, since the characteristic densities and temperatures should be significantly different depending on the bubble energetics. In the framework of expanding

galactic outflows and shocks (e.g., Veilleux et al., 2005), a higher energy input rate leads to a higher plasma temperature and a larger expansion rate for a fixed bubble size and ambient density. Thus, the plasma temperature at the interface between the bubbles and surrounding medium encodes information on the bubbles' shock strength, expansion properties, and overall energy input rate. A generic prediction from simulations and observations of galactic outflows is that the bubbles are over-pressurized and hotter compared to the surrounding medium ($\gtrsim 2 \times 10^6$ K), implying the bubbles' thermal gas should have signatures at soft X-ray energies. Indeed, the bubbles appear to be bounded by X-ray emission seen in the *ROSAT* 1.5 keV band (Bland-Hawthorn & Cohen, 2003; Su et al., 2010), however these observations do not constrain the intrinsic bubble thermal gas structure since the broad-band images are a weak temperature diagnostic. Spectral observations with current X-ray telescopes are a much better temperature diagnostic for this type of environment.

Initial efforts to observe the bubbles in soft X-rays with *Suzaku* and *Swift* and constrain their temperature and shock strength were carried out by several groups (Kataoka et al., 2013, 2015; Tahara et al., 2015). Kataoka et al. (2015) extracted soft X-ray background (SXRB) spectra in the 0.5–2.0 keV band for 97 sight lines that pass through the Fermi bubbles, and fit the spectra with thermal plasma models. They consistently measure plasma temperatures of $kT = 0.3$ keV for these sight lines, which is systematically higher than the characteristic temperature measured in sight lines away from the Galactic center ($kT \approx 0.2$ keV; Henley & Shelton, 2013). From this temperature ratio, they infer a shock Mach number of $\mathcal{M} \approx 0.3$ keV / 0.2 keV = 1.5, and corresponding expansion rate of ≈ 300 km s^{-1}. This is a valuable attempt to constrain these quantities, however the results likely underestimate the thermal gas temperature because the authors assume the measured plasma temperature of 0.3 keV is a direct probe of the Fermi bubbles' thermal gas. In practice, there are other known emission sources that contribute to the spectra.

A significant limitation to the aforementioned analyses is their treatment of the surrounding hot gas plasma known to emit in soft X-rays. The Milky Way hosts a hot gas distribution with $T \approx 2 \times 10^6$ K extending on scales $\gtrsim$10 kpc based on shadowing experiments from *ROSAT* all-sky data (Snowden et al., 1997; Kuntz & Snowden, 2000). This plasma is believed to dominate any SXRB spectrum, with O VII and O VIII being the characteristic observed line transitions (e.g., McCammon et al., 2002; Yoshino et al., 2009; Henley & Shelton, 2012). The structure of this extended plasma distribution has been debated in the literature, but numerous studies on both absorption and emission line strengths indicate the plasma is spherical and extended to at least $r \sim 50$ kpc (Fang et al., 2006; Bregman & Lloyd-Davies, 2007; Gupta et al., 2012; Fang et al., 2013; Miller & Bregman, 2013, 2015). In particular, Miller & Bregman (2015) (defined as MB15 henceforth) modeled a set of 648 O VIII emission line intensities from Henley & Shelton (2012) (defined as HS12 henceforth), and found a hot gas density profile with $n \propto r^{-3/2}$ extending to the virial radius reproduces the observed emission line intensities. These modeling studies have placed useful constraints on the Galactic-scale hot gas distribution, but also highlight the fact that this extended plasma is likely the dominant emission source in all 0.5–2.0 keV band spectra.

In this study, we improve the Kataoka et al. (2015) (defined as K15 henceforth) analysis by modeling the combined Fermi bubble and hot gas halo emission present in O VIII emission line measurements. We expand the Galactic-scale hot gas models from MB15 to include a Fermi bubble geometry, density, and temperature structure. Given a set of model parameters, we predict the emission contribution from the Fermi bubbles and hot gas halo along any sight line. Thus, we accurately infer the Fermi bubbles' density and temperature structure from our emission model.

The O VIII observations used in our analysis consist of published *XMM-Newton* measurements from HS12, and a new *Suzaku* data set produced for this work. The

XMM-Newton data are mostly the same measurements used in MB15, however we now include data near the Fermi bubbles. We supplement these data with archival *Suzaku* SXRB spectra measurements, which more than doubles the number of emission line measurements projected near the bubbles. These data are processed in a similar way to the *XMM-Newton* data reduction outlined in HS12, resulting in a uniformly processed data set of emission line intensities from the SXRB.

Following the methodology from MB15, we constrain the Fermi bubbles' density and temperature structure by finding the parametric model that is most consistent with the observed emission line intensities. We infer the characteristic bubble temperature from analyzing the distribution of observed O VIII/O VII line ratios near the bubbles, and the characteristic bubble density from explicitly modeling the O VIII emission line intensities. From these constraints, we infer a more accurate bubble shock strength, expansion velocity, energy input rate, and age. We also discuss these constraints within the context of galactic outflows and the possible bubble formation mechanisms discussed above.

The rest of the chapter is outlined as follows. Section 6.4 discusses how we compiled our emission line sample, including an overview of the *XMM-Newton* data set, and the *Suzaku* sample data processing. Section 6.5 defines our parametric density and temperature model, and discusses our line intensity calculation. Section 6.6 discusses our model fitting routine and results. Section 6.7 discusses our Fermi bubble constraints in the context of galactic outflows, previous X-ray studies, and simulations. Section 6.8 summarizes our results.

6.4 Emission Line Data

Our dataset includes O VII (He-like triplet at $E \approx 0.56$ keV) and O VIII (Lyα transition at $E \approx 0.65$ keV) emission lines, which are the dominant ions for thermal plasmas with temperatures between $T \sim 10^{5.5}$–10^{7} K (Sutherland & Dopita, 1993).

For an optically thin plasma in collisional ionization equilibrium, the emission line intensity depends on the plasma density and temperature as $I \propto n^2\epsilon(T)$, where $\epsilon(T)$ is the volumetric line emissivity. This implies the line strength ratio is a temperature diagnostic and the individual ion line strengths can be used to estimate the plasma density. Large, all-sky samples of emission line measurements in particular have been instrumental in constraining the Milky Way's global $\sim 10^6$ K gas density distribution (MB15).

The full dataset used in our modeling analysis is a combination of published *XMM-Newton* emission line measurements from HS12 and a complimentary sample of *Suzaku* measurements compiled specifically for this project. The *XMM-Newton* sample from HS12 contains ∼1000 emission line measurements distributed across the sky, making it a valuable starting point for our modeling work. While *XMM-Newton* has more collecting power than *Suzaku* near the emission lines (collecting area × field of view ≈140,000 cm^2 arcmin^2 for the MOS1 camera compared to ≈70,000 cm^2 arcmin^2 for the XIS1 detector), we include a supplemental *Suzaku* dataset for two reasons. *Suzaku's* low-Earth orbit results in a lower and more-stable particle background compared to *XMM-Newton's*, often resulting in higher signal-to-noise measurements at soft X-ray energies. Also, there are many valuable archival *Suzaku* observations projected near the Fermi bubbles, including 14 observations dedicated to observing the bubbles' edge. In practice, *Suzaku* data should have a comparable signal-to-noise to the *XMM-Newton* data, while probing the crucial region in and near the Fermi bubbles.

Our goal is to create a clean sample of uniformly processed emission line measurements by reducing the *Suzaku* data in a similar way to how HS12 reduced the *XMM-Newton* data. The main steps include: the removal of bright point sources, light curve filtering, spectral fitting, and filtering for solar wind charge-exchange (SWCX) emission. The following sections summarize how the *XMM-Newton* data were pro-

duced, and detail our *Suzaku* data reduction steps. After applying all these data reduction methods, our final sample includes 683 useful *XMM-Newton* measurements and 58 useful *Suzaku* measurements.

6.4.1 *XMM-Newton* Observations

We summarize the *XMM-Newton* emission line sample compilation here, but we refer the reader to HS12 for a more detailed description of their data reduction methods. Their initial sample included 5698 observations that had any EPIC-MOS exposure time. They reduced the data using the *XMM-Newton* Extended Source Analysis Software [1] (*XMM*-ESAS; Kuntz & Snowden, 2008; Snowden & Kuntz, 2011), which includes 2.5–12 keV band count rate screening for soft-proton flares. They also removed point sources from the spectral extraction regions using data from the Second *XMM-Newton* Serendipitous Source Catalog [2] (2XMM; Watson et al., 2009), as well as visual inspection for bright sources in the images. The authors attempted to reduce geocoronal SWCX emission by excluding observing periods with high solar wind proton flux measurements (see Section 6.4.3 for the details of this procedure), which they called their "flux-filtered" sample. These reduction methods resulted in 1868 total observations and 1003 flux-filtered observations with $\geq$5 ks of good observing time. Each of these observations includes an O VII and O VIII emission line intensity measurement, which have been used to analyze the known emission sources (i.e., Local Bubble, extended hot halo, SWCX).

This sample has been used before to successfully model the Milky Way's global hot gas structure, thus motivating its use to model the Fermi bubbles. MB15 compiled a subset of the HS12 flux-filtered sample with additional spatial screening criteria to reduce any residual emission from sources other than the Local Bubble (LB) and Galactic hot halo. To achieve this, they removed observations within 0.5° of potential

[1] `http://heasarc.gsfc.nasa.gov/docs/xmm/xmmhp_xmmesas.html`
[2] `http://xmmssc-www.star.le.ac.uk/Catalogue/2XMMi-DR3/`

bright X-ray sources (see Table 1 in MB15 for the types of sources), within 10° of the Galactic plane, and sight lines near the Fermi bubbles ($|l| \leq 22°$, $|b| \leq 55°$). This resulted in a subsample of 649 observations from the HS12 flux-filtered sample.

The *XMM-Newton* data used in this study is the same as the one used in MB15, but including the sight lines near the Fermi bubbles. We start with the HS12 flux-filtered sample, and still exclude sight lines near bright X-ray sources and within 10° of the Galactic plane. These screening criteria result in 683 total *XMM-Newton* measurements distributed across the sky, with 34 measurements passing near or through the bubbles' gamma-ray edge.

6.4.2 *Suzaku* Observations and Data Reduction

We compiled an initial *Suzaku* target list of all observations that were publicly available as of January 2015 and near the Fermi bubbles. This included any observations with Galactic coordinates $|l| \leq 25°$ and $10° \leq |b| \leq 55°$. There were 143 observations in this region of the sky which we inspected for usable spectra.

Each observation includes data from the three active X-ray Imaging Spectrometer (XIS) detectors on board *Suzaku* (Koyama et al., 2007). The detectors each have an $18' \times 18'$ field of view and a point spread function of $\approx 2'$. We only considered data from the back-illuminated XIS1 detector since it has a larger collecting area below 1 keV than the remaining detectors.

We processed all XIS1 data using HEAsoft version 6.17 and calibration database (CALDB) files from January 2015. We followed the standard data reduction procedure described in *"The Suzaku Data Reduction Guide* [3]. This includes recalibrating the raw data files, screening for flickering or bad pixels, energy scale reprocessing, and building good time interval (GTI) files. Fortunately, the FTOOL script `aepipeline` performs all these tasks for standard *Suzaku* observations. We used `aepipeline` ver-

[3] `https://heasarc.gsfc.nasa.gov/docs/suzaku/analysis/abc/`

sion 1.1.0 to generate reprocessed images, light curves, and spectra for our analysis.

We extracted all data products using `xselect` version 2.4. Each observation dataset included combined data from 3×3 and 5×5 editing modes where applicable. We did not impose any non-standard criteria to the data extraction steps with the exception of the cut-off rigidity (COR) of the Earth's magnetic field. This parameter varies throughout *Suzaku's* low-Earth orbit, and larger COR constraints result in less particle background counts. A higher cutoff than the standard COR > 4 GV has been used in previous SXRB spectral fits, and typically results in higher signal-to-noise between 0.5–2.0 keV (Smith et al., 2007; Kataoka et al., 2015). Here, we follow the suggested value from Smith et al. (2007) and use a COR > 8 GV constraint.

Since the observational goal of this study is to measure O VII and O VIII intensities from SXRB spectra, we removed point sources from each observation before we extracted spectra. We inspected each XIS1 image for point sources to remove with self-defined region files. Observations of exceptionally bright sources (i.e., where there was clear emission extending greater than $\approx 5'$), extended sources (galaxy clusters, star clusters, etc.), or other anomalous features were rejected from the dataset. We also rejected any observations not taken in the standard observing window mode due to the reduction in field of view collecting area. For any remaining visible point sources, we defined circular exclusion regions between $1'$–$4'$ in radius centered on each source. We then re-extracted the data products for each observation with the point source region excluded.

The next step in our data cleaning process was light curve inspection and filtering. We extracted 0.4–10.0 keV light curves and constructed count rate histograms for each observation. Our default screening criteria was to remove observing periods that were $> 2\sigma$ from the mean observation count rate. This led to a small reduction in observing time since most count-rate histograms followed an approximate Gaussian distribution. We flagged observations that did not have an approximate Gaussian

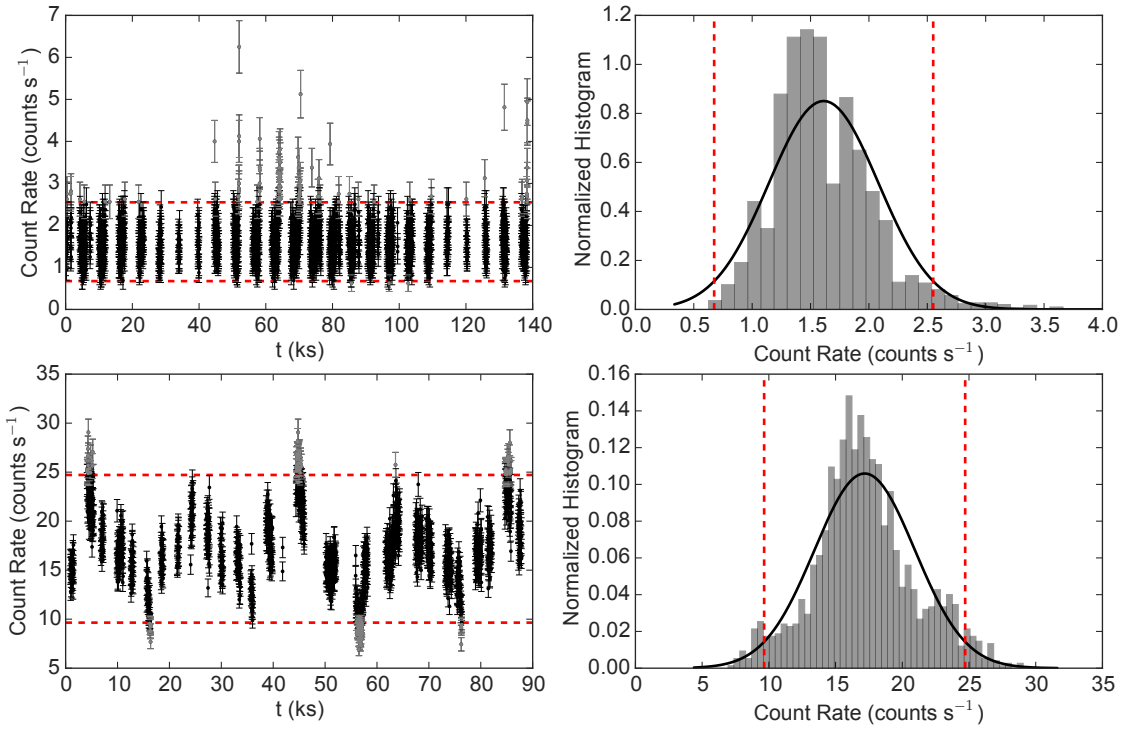

Figure 6.1: Example 0.4–10.0 keV light curves (*left* panels) and count rate histograms (*right* panels) with fitted Gaussian distributions for two observations in our initial sample. Observing periods within the 2σ limits (red dashed lines) were kept while periods outside of these limits were excluded (gray points in the *left* panels). The *top* panels show a Galactic bulge observation (Obs. ID 100011010) with a well-behaved, Gaussian light curve that we retained in our final sample. The *bottom* panels show an observation toward the X-ray binary 4U1822-37 (Obs. ID 401051010), but excluding the point source from the extraction region. We excluded this observation from the sample because the light curve shows clear episodic variations due to residual X-ray binary emission.

count rate distribution, which is indicative of additional soft proton flares or residual point source emission that may have been variable throughout the observation. Example light curves with the various filtering tasks can be seen in Figure 6.1. We also expanded on this analysis step in Section 6.4.3 where we excluded observing periods with high solar wind proton flux measurements. This light curve filtering created new GTI files, which we used to compile our initial data products.

The point source exclusion and light curve filtering procedures outlined above were the primary stages in our initial sample catalog. To summarize the main screening criteria, we excluded observations that showed anomalous features in either their images or light curves or that had exceptionally bright point sources, and we filtered the images for removable point sources. After these screening criteria, we kept observations with $\geq$5 ks of good observing time. This resulted in 112 observations out of the original 143.

6.4.3 Solar Wind Charge-Exchange Filtering

Solar wind charge-exchange emission can occur in any X-ray observation, however it is difficult to predict or attribute the amount of SWCX emission in individual SXRB observations (e.g., Carter & Sembay, 2008; Carter et al., 2011; Galeazzi et al., 2014; Henley & Shelton, 2015). The emission can occur either at the interface between the solar system and ISM (heliospheric emission) or as solar wind ions pass near the Earth's neutral atmosphere (geocoronal emission). Heliospheric emission is thought to vary with the overall solar cycle, the observed direction relative to the Sun's orbit and ecliptic plane, and the neutral ISM hydrogen and helium density (Cravens et al., 2001; Robertson & Cravens, 2003a; Koutroumpa et al., 2006, 2007, 2011; Galeazzi et al., 2014; Henley & Shelton, 2015). Geocoronal emission is thought to depend on the solar wind proton flux and the observed direction relative to the magnetosheath (Snowden et al., 2004; Wargelin et al., 2004; Fujimoto et al., 2007; Carter & Sembay, 2008; Carter et al., 2010, 2011; Ezoe et al., 2010, 2011; Ishikawa et al., 2013; Henley & Shelton, 2015). It is still unclear what the typical amount of SWCX emission is in a given X-ray observation, and models predict a wide range of O VII and O VIII intensities depending on the parameters listed above (Robertson & Cravens, 2003b; Robertson et al., 2006; Koutroumpa et al., 2006, 2007, 2011). For the purpose of this project, SWCX emission is considered to be contamination, and our goal is to reduce

the amount of potential emission as possible.

Following the work of HS12, we filter the observations for periods of high solar wind proton flux in an effort to reduce geocoronal SWCX. For each observation, we gathered solar wind data from the OMNIWeb databse [4], which includes data from the *Advanced Composition Explorer* and *Wind* satellites. The database includes solar wind densities and velocities, which we convert to fluxes. We cross-correlated each solar wind proton flux light curve with the X-ray light curves. Periods with solar wind flux values $> 2 \times 10^8$ cm^{-2} s^{-1} were flagged and considered to potentially include SWCX emission. We illustrate how this screening works for several example spectra in Figure 6.2. We made new GTI files incorporating these filtering periods and the $> 2\sigma$ count rate periods discussed above. These GTI files were used for the final spectral extraction used in the fitting analysis.

We point out that this filtering procedure is designed to reduce geocoronal SWCX emission, not heliospheric SWCX emission. The models suggesting heliospheric SWCX varies with ecliptic latitude imply that applying an ecliptic latitude cut to an observing sample may help reduce that emission. Indeed, Henley & Shelton (2013) discuss this effect and employ this screening criterion for their study on fitting SXRB spectra. However, the analysis in MB15 argues there does not appear to be a significant enhancement of O VII or O VIII line emission within 10° of the ecliptic plane, part of which passes through the Fermi bubbles. Therefore, heliospheric SWCX is likely present at softer X-ray energies, but it does not appear to be a significant emission source for the oxygen lines of interest.

This additional screening procedure can only reduce the good exposure time in a given observation. Some observations occurred entirely during a period of high solar wind proton flux, in which case the observation was removed from the sample. Other observations occurred entirely during a period of low solar wind proton flux,

[4] `http://omniweb.gsfc.nasa.gov/`

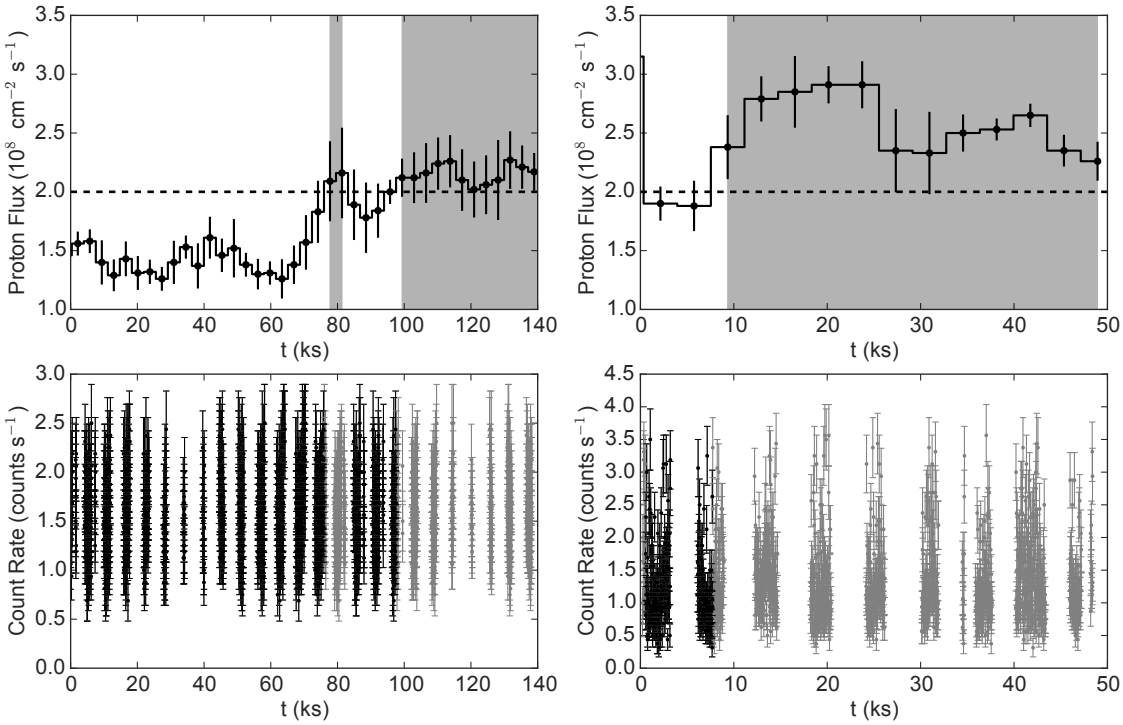

Figure 6.2: Example solar wind proton flux (*top* panels) and 0.4-10.0 keV (*bottom* panels) light curves for two observations in our initial sample. Observing periods when the solar wind proton flux exceeded 2×10^8 cm^{-2} s^{-1} (black dashed lines in the *top* panels) were excluded. We represent these periods with a gray background in the *top* panels and gray points in the *bottom* panels. The *left* panels show the same Galactic bulge observation from Figure 6.1 (Obs. ID 100011010), which had some observing time removed, but was retained in the sample because it had $\geq$5 ks of good observing time. The *right* panels show an observation from the Kataoka et al. (2013) analysis (FERMI_BUBBLE_N2; Obs. ID 507002010). We rejected this observation from the sample since most of the observation occurred during a period of high solar wind proton flux.

in which case the observation was unaffected. The rest of the observations were partially contaminated, leading to a reduction of observing time. We enforced the same good exposure time requirement noted above of >5 ks to keep observations in the sample. After the default screening outlined in Section 6.4.2 and this additional SWCX filtering, our sample includes 58 of the original 143 observations.

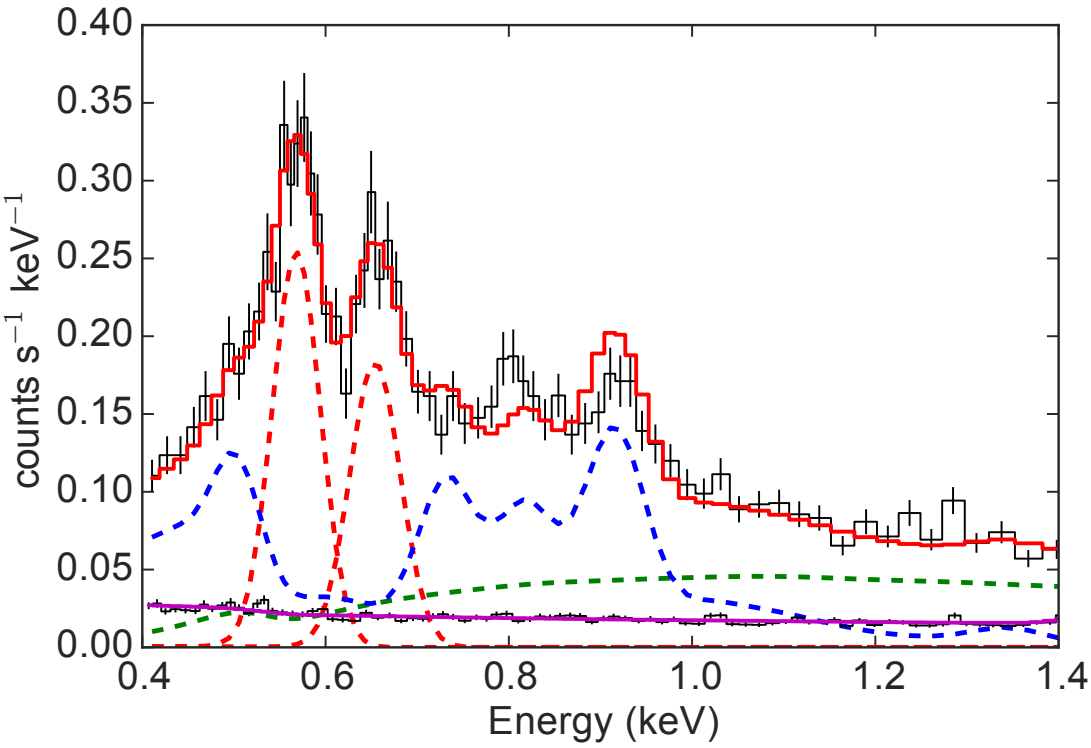

Figure 6.3: Binned SXRB spectrum showing our spectral model components (Obs. ID 702028010). The solid magenta line represents our NXB model, the green dashed line is the absorbed CXB power law, the blue dashed line is the absorbed hot gas continuum without the oxygen lines, the red dashed lines show the O VII and O VIII lines as Gaussian components, and the solid red line represents the total model spectrum. The oxygen lines dominate the spectrum between 0.5–0.7 keV.

6.4.4 Spectral Modeling

This section outlines our spectral fitting procedure, including the response files used, our spectral model, and resultant data products. We extracted spectra in the 0.4–5.0 keV band, which is broad enough to model the known SXRB emission sources. Each observation had its own particle, or non X-ray background (NXB), spectrum and response files. We used `Xspec` version 12.9.0 for all spectral fitting, where we used the Cash statistic as our fit statistic (Cash, 1979). Figure 6.3 shows an example observed spectrum and best-fit multi-component model. Our final result includes O VII and O VIII line intensities for each observation.

We generated response matrices and auxiliary response files using standard *Suzaku* scripts. The script `xisrmfgen` was used to generate response matrices (RMF files) for each observation. We used the ray-tracing program `xissimarfgen` to generate ancillary response files (ARFs) assuming a uniform-emitting source and a $20'$ radius circle for a simulated source region. The size of the source region acts as a normalization in our spectral fit values.

Each observation has a NXB spectrum collected by *Suzaku* observations of the Earth at night. We generated NXB spectra using the script `xisnxbgen` (Tawa et al., 2008). This creates an NXB spectrum using a weighted-sum of *Suzaku* night-Earth observations based on the observation exposure times. The only unique parameter we supplied to the script is the same COR >8 GV constraint we applied to the initial data extraction. Different SXRB studies have multiple approaches with how to treat these NXB spectra, with groups either subtracting the NXB counts from the observed spectrum (e.g., K15), or including the NXB spectrum as additional data and simultaneously modeling its contribution to the full spectrum (e.g., Smith et al., 2007). We follow the latter methodology, meaning we fit both our observed spectrum and the NXB spectrum as one process.

Our spectral model includes the following components: NXB spectrum, an absorbed cosmic X-ray background (CXB) or extragalactic power law, an absorbed hot gas continuum component with no oxygen emission lines, and the O VII and O VIII lines of interest. The absorbed components were attenuated using the `phabs` model in Xspec (Balucinska-Church & McCammon, 1992; Yan et al., 1998), and had column densities fixed to vales from the LAB survey (Kalberla et al., 2005). We also assume Asplund et al. (2009) metal abundance relative to hydrogen unless otherwise stated. The rest of the section details the spectral model assumed for each source.

The NXB model includes a contribution from particles hitting the XIS detectors that are not focused by the telescope and three instrumental lines. For the particle

spectrum, we include a power law where both the normalization and slope can vary. The instrumental lines include an Al K line at 1.49 keV, a Si K line at 1.74 keV, and an Au M line at 2.12 keV [5]. We model each of these lines as Gaussians with widths and normalizations left to vary as free parameters and the centroids fixed. This model component is only folded through the RMF response (as opposed to both the RMF and ARF), and contributes to both the observed and NXB spectra.

The CXB spectrum is typically modeled as an absorbed power law or multiple broken power laws, and is thought to be due to unresolved active galactic nuclei (AGNs). The differences between these spectral shapes have minimal effects on the measured oxygen line intensities, since the CXB contributes $\lesssim 10\%$ to the total SXRB flux below $\approx$1 keV. Therefore, we adopt the spectral shape used by HS12, which is a power law with fixed spectral index of 1.46 (Chen et al., 1997). These authors discuss the uncertainty in the CXB power law normalization, but argue for a nominal value of 7.9 photons cm^{-2} s^{-1} sr^{-1} keV^{-1} at 1 keV after accounting for CXB sources with $F_X < 5 \times 10^{-14}$ erg cm^{-2} s^{-1} in the 0.5–2.0 keV band (Moretti et al., 2003). We allow the CXB normalization to be a free parameter in our spectral model, but place $\pm$30% hard boundaries on the parameter to allow for field-to-field variation.

Although the oxygen lines are the measurement of interest, we still account for $\sim 10^6$ K gas continuum emission in our model. We model this component as an absorbed thermal APEC plasma (Smith et al., 2001) with fixed solar metallicty and without the oxygen lines. We achieve the latter by setting the oxygen line emissivities to zero in the standard Xspec APEC files (Lei et al., 2009; Henley & Shelton, 2012). The normalization and temperature were left as free parameters in the model. We expected the fitted plasma temperatures to be between 0.1–0.3 keV, however these temperatures are typically most sensitive to the oxygen lines which we disabled. Therefore, we let the plasma temperature vary outside this range, but with

[5] `https://heasarc.gsfc.nasa.gov/docs/suzaku/prop_tools/suzaku_td/`

hard boundaries between 0.05–5 keV.

Our final spectral model components are the O VII and O VIII emission lines. We model each of these components as Gaussian features with the widths fixed to the instrumental resolution. We fixed the O VIII centroid to its laboratory value of 0.6536 keV, but let the O VII centroid vary since the line is an unresolved blend of the resonance, forbidden, and intercombination lines. The Gaussian normalizations were also free parameters, as these represent the line strength measurements. We point out that this spectral fitting method measures the *total* emission line strengths from all emission sources (residual SWCX, LB, absorbed hot gas halo or Fermi bubble) for each sight line. This is why our astrophysical model line intensity calculation in Section 6.5.5 includes all emission sources when comparing to the total observed line intensities.

6.4.5 Data Summary

The final *Suzaku* sample with spectral fitting results can be seen in Table 6.1. We include the observation ID, the sight line in Galactic coordinates, the good XIS exposure time, and the oxygen line strengths with their 1σ uncertainties in Line Units (L.U.). The emission line measurements presented here are designed to have as little SWCX as possible, while only containing emission from astrophysical sources of interest (i.e., Galactic hot gas halo and Femri bubbles). We also outlined a data reduction, extraction, and cleaning procedure as similar as possible to the work by HS12, such that this sample and the *XMM-Newton* are processed in a uniform way.

Our total data sample used in our astrophysical modeling combines the *XMM-Newton* and *Suzaku* measurements. There are 683 *XMM-Newton* measurements in total distributed across the sky, with 34 projected near the Fermi bubbles. The *Suzaku* data are exclusively projected near the Fermi bubbles, and there are 58 measurements included here. Figure 6.4 show all-sky maps of the oxygen emission line strengths.

Table 6.1. *Suzaku* Data

Obs. ID	l (°)	b (°)	t_{exp}[a] (ks)	N_H[b] (10^{20} cm^{-2})	I_{OVII} (L.U.)[c]	I_{OVIII} (L.U.)[c]
100011010	341.0	18.0	28.7	6.47	31.37 ± 0.84	20.93 ± 0.57
100041020	358.6	-17.2	20.0	6.57	17.05 ± 1.10	9.12 ± 0.65
101009010	358.6	-17.2	9.3	6.57	18.17 ± 1.95	10.54 ± 1.13
102015010	358.6	-17.2	20.1	6.57	20.35 ± 1.59	9.95 ± 0.87
103006010	358.6	-17.2	18.2	6.57	18.76 ± 1.79	9.14 ± 0.93
104022010	358.6	-17.2	5.6	6.57	22.13 ± 3.70	11.92 ± 1.97
104022020	358.7	-17.1	22.0	6.57	20.67 ± 1.77	9.91 ± 0.93
104022030	358.6	-17.2	19.7	6.57	20.78 ± 2.05	11.19 ± 1.03
105008010	358.6	-17.2	27.4	6.57	21.57 ± 1.76	12.08 ± 0.92
106009010	358.6	-17.2	23.5	6.57	37.77 ± 4.63	12.39 ± 1.39
107007010	358.6	-17.2	29.6	6.57	19.43 ± 1.58	11.54 ± 0.92
107007020	358.6	-17.2	29.0	6.57	39.46 ± 2.29	11.56 ± 0.85
108007010	358.6	-17.2	29.7	6.57	23.77 ± 1.64	11.64 ± 0.89
108007020	358.6	-17.2	27.5	6.57	22.71 ± 1.70	11.04 ± 0.89
109008010	358.6	-17.2	26.8	6.57	23.60 ± 1.74	11.86 ± 0.93
401001010	344.0	35.7	26.9	7.36	14.15 ± 0.79	8.52 ± 0.48
401041010	348.1	15.9	7.1	12.90	9.03 ± 1.60	8.30 ± 1.16
402002010	5.0	-14.3	25.4	8.72	23.17 ± 1.47	14.19 ± 0.87
402038010	6.3	23.6	55.7	12.10	6.79 ± 0.64	4.28 ± 0.38
403024010	349.2	15.6	24.3	13.90	0.82 ± 0.82	1.50 ± 0.56

Table 6.1 (cont'd)

Obs. ID	l (°)	b (°)	t_{exp}[a] (ks)	N_H[b] (10^{20} cm^{-2})	I_{OVII} (L.U.)[c]	I_{OVIII} (L.U.)[c]
403026010	17.9	15.0	22.9	16.20	6.03 ± 1.27	7.18 ± 0.82
403034020	351.5	12.8	7.6	16.70	10.91 ± 2.16	7.64 ± 1.43
403034060	351.5	12.8	9.4	16.70	7.22 ± 1.79	5.29 ± 1.19
405032010	2.6	15.5	15.5	12.30	17.23 ± 2.00	11.38 ± 1.07
406033010	19.8	10.4	36.5	19.90	10.49 ± 0.95	4.22 ± 0.54
406042010	15.9	-12.7	6.0	9.18	17.41 ± 3.48	10.22 ± 2.08
503082010	17.2	-51.9	22.4	1.48	6.26 ± 0.95	1.50 ± 0.43
503083010	18.2	-52.6	19.5	1.56	6.86 ± 1.10	2.84 ± 0.49
507011010	351.5	-49.8	7.7	1.51	14.31 ± 2.52	4.05 ± 1.09
507012010	351.2	-52.3	6.8	1.03	17.14 ± 3.09	2.31 ± 1.03
507013010	351.0	-53.1	5.9	1.10	13.30 ± 3.19	0.43 ± 1.00
701029010	349.6	-52.6	75.4	1.06	7.01 ± 0.56	3.07 ± 0.31
701056010	10.4	11.2	41.5	19.60	5.61 ± 0.68	5.79 ± 0.43
701094010	351.3	40.1	84.8	6.90	9.13 ± 0.47	3.92 ± 0.27
702028010	20.7	-14.5	17.4	7.35	16.49 ± 1.33	6.49 ± 0.66
702118010	335.9	-21.3	49.6	6.45	15.82 ± 0.95	9.84 ± 0.56
703005010	351.3	40.1	28.2	6.89	8.93 ± 1.08	4.26 ± 0.58
703015010	335.8	-32.8	24.8	3.16	8.55 ± 1.26	4.52 ± 0.62
703030010	15.1	-53.1	64.1	1.95	5.70 ± 0.65	1.59 ± 0.33
704010010	340.1	-38.7	29.3	6.07	8.64 ± 1.06	2.70 ± 0.53

Table 6.1 (cont'd)

Obs. ID	l (°)	b (°)	t_{exp}[a] (ks)	N_H[b] (10^{20} cm^{-2})	I_{OVII} (L.U.)[c]	I_{OVIII} (L.U.)[c]
705014010	345.6	-22.4	34.5	4.87	17.44 ± 1.32	10.65 ± 0.69
705026010	358.2	42.5	7.7	7.39	9.59 ± 4.07	7.48 ± 1.27
705028010	341.2	-37.1	17.8	5.52	7.59 ± 1.30	3.57 ± 0.70
705041010	10.4	11.2	102.7	19.60	6.49 ± 0.60	5.91 ± 0.36
706010010	341.6	30.8	40.4	8.33	19.27 ± 1.27	7.64 ± 0.69
706044010	348.8	13.3	6.2	13.60	21.48 ± 3.89	9.98 ± 1.67
707035010	10.4	11.2	33.7	19.60	9.52 ± 1.03	5.19 ± 0.64
707035020	10.4	11.2	52.9	19.60	10.31 ± 0.90	5.87 ± 0.50
801001010	2.7	39.3	15.6	8.41	7.13 ± 1.22	2.87 ± 0.65
801002010	2.9	39.3	12.0	8.34	6.69 ± 1.40	3.23 ± 0.74
801003010	2.9	39.1	14.2	8.34	4.33 ± 1.09	3.39 ± 0.74
801004010	2.7	39.1	12.6	8.40	8.81 ± 1.44	3.39 ± 0.77
801094010	341.4	-33.1	5.2	4.60	18.43 ± 2.41	5.22 ± 1.03
803022010	6.9	30.5	22.5	10.90	0.57 ± 1.04	1.70 ± 0.80
803071010	6.6	30.5	94.0	10.80	6.65 ± 0.57	3.00 ± 0.31
805036010	340.6	-33.6	22.5	4.33	14.19 ± 1.79	5.50 ± 0.95
807048010	10.0	-53.5	51.2	1.27	23.45 ± 1.80	2.97 ± 0.38
807062010	349.3	54.4	5.2	2.90	10.37 ± 2.73	4.13 ± 1.41

Note. — Table summarizing our *Suzaku* emission line sample. The columns represent the observation ID, the observation Galactic coordinates, the good XIS1 exposure time, the Galactic hydrogen column density, and the oxygen emission lines of interest. The emission line uncertainties are the 1σ statistical uncertainties from `Xspec`.

[a]The total good XIS1 exposure time after our default light curve filtering and additional flux-filtering to remove geocoronal SWCX emission.

[b]We use hydrogen column densities from the LAB survey (Kalberla et al., 2005). These columns are used in our spectral fitting to absorb hot plasma continuum emission and in our model line emission calculation to attenuate hot gas halo and Fermi bubble/shell emission.

[c]1 L.U. = 1 Line Unit = 1 photons s^{-1} cm^{-2} sr^{-1}

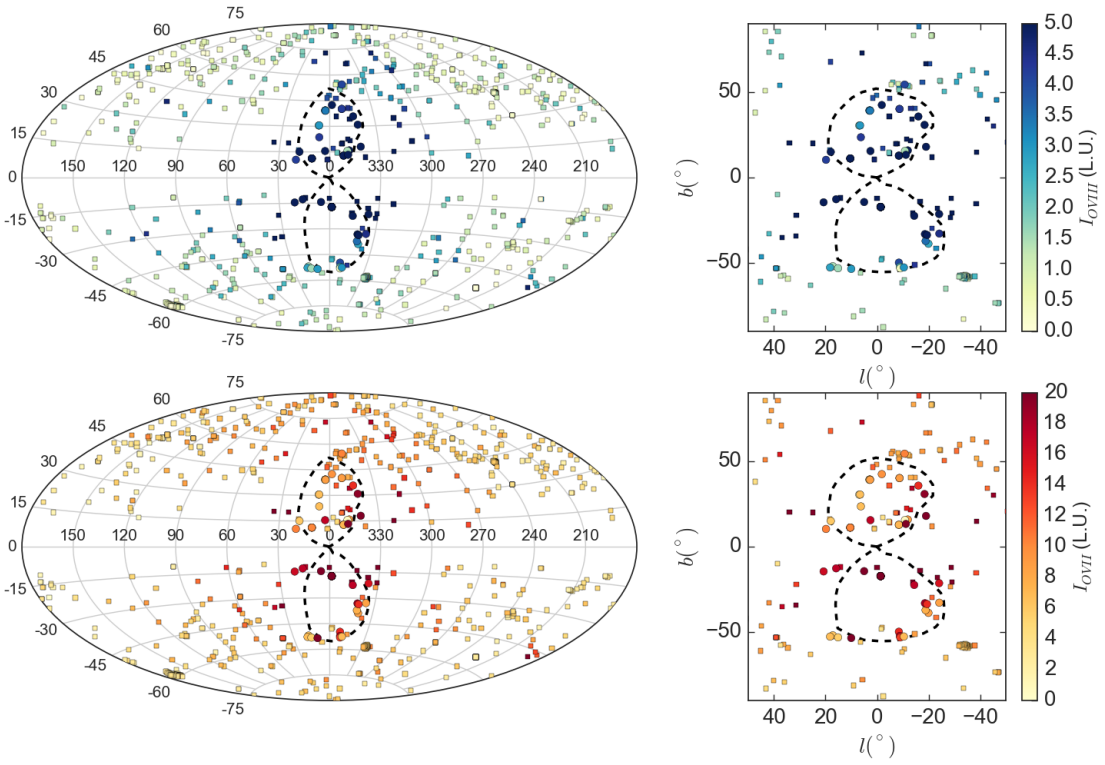

Figure 6.4: All-sky Aitoff projections (*left* panels) and a projection near the Fermi bubbles (*right* panels) of our O VIII and O VII emission line samples (*top* and *bottom* panels respectively). The squares represent measurements from *XMM-Newton* (HS12), the circles represent our new *Suzaku* measurements, and the dashed lines represent the Fermi bubbles' gamma-ray edge. We use the O VIII data in our model fitting process.

6.5 Model Overview

In this section, we define our parametric astrophysical models and assumptions. The SXRB is known to have at least two plasma sources, a "local" source within ≈300 pc from the Sun, and a "distant" source at $\gtrsim$5 kpc from the Sun. These sources have all been modeled in different ways, resulting in different inferences on their underlying emission properties. The Fermi bubbles have not been considered in most SXRB modeling studies, with the exception of recent studies by K15. Here, we identify all emission sources in our model, and justify our choices for the underlying

source distributions.

We point out that this work is an advancement over the modeling work presented in MB15, who used the same *XMM-Newton* data discussed in Section 6.4.1 to constrain the Milky Way's hot gas halo structure. The model used in that study is identical to the model outlined below, with the exception of the Fermi bubble emission source. We summarize these models in Section 6.5.1 and Section 6.5.2, but we refer the reader to MB15 for additional explanation for the model choice.

6.5.1 Local Bubble / Residual SWCX Model

The "local" emission source has been argued to include emission from both the LB and SWCX based on numerous shadowing experiments (Smith et al., 2007; Galeazzi et al., 2007; Koutroumpa et al., 2007, 2011) and studies of the *ROSAT* 1/4 keV band (Kuntz & Snowden, 2000; Galeazzi et al., 2014). As discussed in Section 6.4.3, SWCX emission is difficult to predict or quantify, however the flux-filtering techniques are designed to reduce its contribution to our measured line strengths. The physical properties of the LB have also been debated, with some studies arguing the LB is volume-filled with $\sim 10^6$ K gas (Smith et al., 2007), and others arguing the emission primarily comes from the bubble edges about 100–300 pc away (Lallement et al., 2003; Welsh & Shelton, 2009). Regardless of these differences, our goal is to choose a parametrization that characterizes the emission from this source.

We parametrize the LB as a volume-filled plasma with a constant density and temperature and size varying between 100–300 pc. This follows interpretation from Smith et al. (2007), who conducted SXRB modeling with *Suzaku* on the nearby molecular cloud MBM12. Under the assumption of a volume-filled plasma, these authors concluded the LB has a temperature of 1.2×10^6 K and a density between $1\text{–}4\times10^{-3}$ cm^{-3}. In our model, we fix the plasma temperature to this value and let the density, n_{LB}, be a free parameter.

While we include a Local Bubble emission source in our model for completeness, it is unlikely to have a significant impact on our results. The "local" plasma source is known to contribute more to the *ROSAT* 1/4 keV band as opposed to *ROSAT* 3/4 keV band (e.g., Snowden et al., 1997; Kuntz & Snowden, 2000). This implies the "local" emission source should produce more O VII than O VIII in a given observation. Shadowing spectroscopic observations verify this, and show there is minimal ($\lesssim$0.5 L.U.) O VIII due to "local" sources (Smith et al., 2007; Koutroumpa et al., 2007, 2011). Furthermore, MB15 showed that this LB model effectively has no contribution to the O VIII emission lines from the *XMM-Newton* sample discussed in Section 6.4.1. Our modeling work below focuses on O VIII emission lines, so we do not believe this LB parametrization will affect our results.

6.5.2 Hot Halo Model

We assume the Milky Way's "extended" hot gas plasma structure is dominated by a spherical, volume-filling halo of material extending to the virial radius, as opposed to the alternative assumption of an exponential disk morphology with scale height between 5–10 kpc. The latter structure is believed to form from supernovae in the disk (e.g., Norman & Ikeuchi, 1989; Joung & Mac Low, 2006; Hill et al., 2012), and can reproduce X-ray absorption and emission line strengths in several individual sight lines (Yao & Wang, 2005, 2007; Yao et al., 2009b; Hagihara et al., 2010). However, numerous studies have shown that a spherical, extended morphology due to shock-heated gas from the Milky Way's formation reproduces a multitude of observations (e.g., White & Frenk, 1991; Cen & Ostriker, 2006; Fukugita & Peebles, 2006). These include ram-pressure stripping of dwarf galaxies (Blitz & Robishaw, 2000; Grcevich & Putman, 2009; Gatto et al., 2013), the pulsar dispersion measure toward the Large Magellanic Cloud (Anderson & Bregman, 2010; Fang et al., 2013), and the aggregate properties of oxygen absorption and emission lines distributed in multiple sight lines

across the sky (Bregman & Lloyd-Davies, 2007; Gupta et al., 2012; Miller & Bregman, 2013, 2015; Faerman et al., 2016). This distribution has been proven to reproduce most of the O VIII emission line intensities from the *XMM-Newton* portion of the sample, thus justifying its use in this modeling work.

Our parametrized density distribution follows a spherical β-model, which assumes the hot gas is approximately in hydrostatic equilibrium with the Milky Way's dark matter potential well. The β-model has also been used to fit X-ray surface brightness profiles around early-type galaxies (e.g., O'Sullivan et al., 2003) and massive late-type galaxies (Anderson & Bregman, 2011; Dai et al., 2012; Bogdán et al., 2013a,b; Anderson et al., 2016). The model is defined as:

$$n(r) = n_o(1 + (r/r_c)^2)^{-3\beta/2}, \tag{6.1}$$

where r is the galactocentric radius, $n_\circ$ is the central density, r_c is the core radius ($\lesssim$5 kpc), and β defines the slope (typically between 0.4–1.0). The previous modeling by MB15 was limited to using an approximate form of this model in the limit where $r \gg r_c$, since they specifically did not include observations near the expected r_c. This resulted in constraints on a power law density distribution:

$$n(r) \approx \frac{n_o r_c^{3\beta}}{r^{3\beta}}. \tag{6.2}$$

The emission line sample in this study includes 33 sight lines that pass within 20° of the Galactic center, so we present model results assuming both types of distributions. The net effect of this will be for the power law model to produce more halo emission for sight lines near the Galactic center than the usual β-model since the density continues to increase at small r instead of approach n_o for $r \lesssim r_c$.

We assume the halo gas is isothermal with a temperature of $\log(T_{halo}) = 6.30$, or $T_{halo} = 2 \times 10^6$ K. This temperature is characteristic of the Milky Way's virial tem-

perature, thus consistent with the picture that the "extended" plasma is spherical and extended to r_{vir}. This temperature is also constrained by observations. Henley & Shelton (2013) provide the strongest observational constraints on the plasma temperature, as they fit SXRB spectra for 110 high latitude ($|b| > 30°$) sight lines from the HS12 sample. They fit the spectra with thermal APEC plasma models, and found a narrow plasma temperature range (median and interquartile range of $2.22 \pm 0.63 \times 10^6$ K). These results suggest the plasma is nearly isothermal, thus validating our assumption.

6.5.3 Fermi Bubble Geometry

Our Fermi bubble structure includes two components: a volume-filled component designed to represent the gamma-ray-emitting region, and a shell of shocked or compressed circumgalactic medium (CGM) material. Observations indicate the bubbles have a flat gamma-ray intensity distribution on the sky with no strong limb brightening effect, suggesting the presence of a quasi-spherical volume-filled component. Hard X-ray emission also bounds the bubbles at low Galactic latitudes, suggesting the presence of hotter, compressed material near the bubble edges (Bland-Hawthorn & Cohen, 2003; Su et al., 2010). These components are designed to parametrize the outer regions of galactic outflows, including hot, shocked wind material and a shell of shocked ISM/CGM material (see Section 6.7.2.1 for an overview of galactic wind morphology). We define the bubble volume as a three-dimensional ellipsoid designed to match the bubbles' projected gamma-ray edge on the sky. Each bubble (positive and negative Galactic latitudes) is centered at $|z| = 5$ kpc away from the Galactic plane, has a semi-major axis of 5 kpc, and has both minor axes set to 3 kpc. We also tilt each bubble 5° toward the negative longitude direction to match the slight asymmetry observed in the bubble shape. Figure 6.5 shows this bubble volume in physical and projected coordinates.

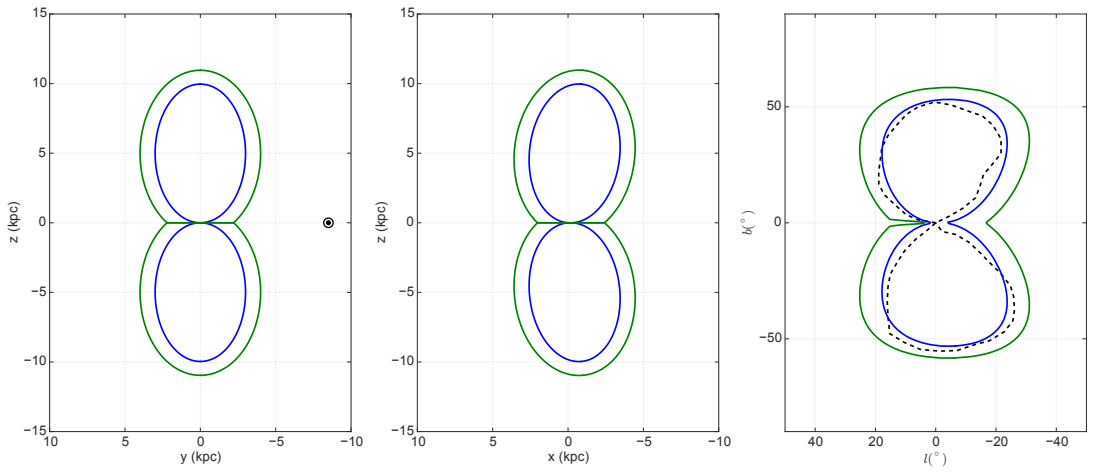

Figure 6.5: Outlines of our volume-filled (blue lines) and shell (green lines) model distributions in physical galactocentric coordinates (*left* and *center*) and projected Galactic coordinates (*right*). The *left* panel shows a side-view of the structure in the $l = 0°$ plane (the $\odot$ symbol represents the Sun), while the *center* panel shows a face-on view at the Galactic center. The *right* panel indicates our volume-filled distribution creates a projection consistent with the bubbles' observed gamma-ray outline (black dashed line).

The shell volume is defined in the same way as the bubble volume, but with a thickness of ≈1 kpc away from the bubble surface. This implies the shell ellipsoids are also centered at $|z| = 5$ kpc from the Galactic plane, have semi-major axes of 6 kpc, and minor axes of 4 kpc. The region inside this surface, but outside the bubble surface is considered to be the shell region. We note this parametrization is different from the modeling work presented by K15, who considered Fermi bubble emission from only two angled shells (one for each bubble) with inner and outer radii of 3 kpc and 5 kpc. However, Figure 6.5 indicates our bubble volume is consistent with the projected bubble outline, and the expected galactic wind morphology suggests there should be at least two distinct outflow regions we can observe (the shocked wind and shocked ISM/CGM). Therefore, we feel our choice of bubble volume is reasonable given the observational constraints available at this time.

6.5.4 Fermi Bubble Density and Temperature

We assume the bubble and shell components each have constant electron densities, defined as n_{FB} and n_{shell}. This parametrization is useful since it is simple, yet still allows us to constrain the average thermal gas densities. Simulations suggest the bubbles have some thermal gas substructure (e.g., Yang et al., 2012), and we did explore more sophisticated models with density gradients away from the Galactic plane or from the bubble edges. However, the data did not provide statistically significant constraints with these profiles (any gradient parameter was consistent with a constant-density profile within the 1σ uncertainties). These constant-density models should be considered a valuable first step when analyzing the bubbles' thermal gas structure.

The bubble and shell temperatures are likely hotter than the surrounding medium, so we assume each component has a characteristic temperature $\geq 2 \times 10^6$ K. Like the bubble and shell densities, each component has a constant temperature (T_{FB} and T_{shell}). However, these temperatures are each initially fixed to 3×10^6 K during the model fitting process. The temperatures are not free parameters in our models because the calculated line intensity scales with density and temperature as $I \propto n^2\epsilon(T)$, where ϵ has a temperature dependence. Since we explicitly model a sample of O VIII emission line intensities, the density and temperature parameters would be degenerate with each other. Section 6.6 discusses how we constrain the bubble and shell temperatures by looking at the distribution of O VIII/O VII line ratios for different assumed temperatures.

6.5.5 Line Intensity Calculation

Calculating model line intensities depends on the density and temperature profile along each line of sight. For any given Galactic coordinate (l, b), we divide the line of sight into cells extending to the virial radius ($r_{vir} = 250$ kpc). Each cell position along

the line of sight (s) is converted to Galactic coordinates (R, z, r) by the standard equations:

$$R^2 = R_\odot^2 + s^2 \cos(b)^2 - 2sR_\odot \cos(b)\cos(l) \tag{6.3}$$

$$z^2 = s^2 \sin(b)^2 \tag{6.4}$$

$$r^2 = R^2 + z^2, \tag{6.5}$$

where $R_\odot = 8.5$ kpc is the Sun's distance from the Galactic center. We assign a density and temperature to each cell based on its set of Galactic coordinates and the assumed model parameters. The hot halo profile described in Section 6.5.2 sets the density and temperature for cells outside the shell volume. The parameters n_{shell} and T_{shell} set the density and temperature for cells within the shell volume, while n_{FB} and T_{FB} set the density and temperature for cells within the bubble volume. Therefore, sight lines not passing through the bubbles only include halo emission, while sight lines passing through the bubbles include hot gas halo, bubble, and shell emission.

We assume an optically thin plasma in collisional ionization equilibrium to calculate all line intensities. Given a line of sight density and temperature profile, the model line intensity is defined as:

$$I(l,b) = \frac{1}{4\pi} \int n_e(s)^2 \epsilon(T(s)) ds, \tag{6.6}$$

where $n_e(s)$ is the line of sight electron density, $T(s)$ is the line of sight temperature profile, and $\epsilon(T)$ is the volumetric line emissivity for a thermal APEC plasma. We use AtomDB version 2.0.2 for all line emissivities (Foster et al., 2012), and characteristic values for O VIII (in photons cm^3 s^{-1}) are $\epsilon(T_{halo}) = 1.45 \times 10^{-15}$ and $\epsilon(3 \times 10^6 \text{ K}) = 3.84 \times 10^{-15}$. Although believed to be minimal, the intensity contribution from the LB is defined as:

$$I_{LB}(l,b) = \frac{n_{LB}^2 L(l,b)\epsilon(T_{LB})}{4\pi}, \tag{6.7}$$

where $L(l,b)$ defines the LB path length (≈100–300 pc; see Lallement et al. (2003) and MB15). The total line intensity is thus defined as:

$$I_{total}(l,b) = I_{LB} + e^{-\sigma N_{HI}}(I_{halo} + I_{FB} + I_{shell}), \tag{6.8}$$

where the exponential term accounts for attenuation due to neutral hydrogen in the disk, N_{HI} is the same neutral hydrogen column assumed for each sight line in in the spectral fitting procedure, and σ is the H I absorption cross section (Balucinska-Church & McCammon, 1992; Yan et al., 1998). Thus, our model line intensities are comparable to the total observed line intensities.

6.6 Results

Our results include a discussion of the O VII and O VIII line intensity distributions along with a parametric modeling analysis. Section 6.6.1 presents the combined *XMM-Newton* and *Suzaku* line strength and ratio distributions on the sky. The latter provides model-independent evidence that the bubbles contain gas at higher temperatures than the surrounding medium ($> 2\times10^6$ K). Section 6.6.2 builds on this evidence and the modeling work from MB15 to constrain the characteristic thermal gas densities and temperatures associated with the bubbles.

6.6.1 Emission Line Ratios

The observed O VIII/O VII ratios in our sample can be used as crude temperature diagnostics. If the observed emission lines come from a single, cospatial plasma source, Equation 6.6 indicates the O VIII/O VII ratio is a direct temperature diagnostic because $I_{OVIII}/I_{OVII} \propto n^2\epsilon_{OVIII}(T)/n^2\epsilon_{OVII}(T) = \epsilon_{OVIII}(T)/\epsilon_{OVII}(T)$. The

observations from SXRB spectra are more complicated since we know multiple plasma sources exist along each line of sight. This implies the total observed O VIII/O VII line ratio probes the emission measure-weighted temperature due to the various plasma sources. However, we discussed in Section 6.5 how the LB is believed to produce little O VIII emission with a variable amount of O VII emission, and the hot halo plasma is believed to be nearly isothermal at $\approx 2 \times 10^6$ K. The expected O VIII/O VII line ratio for a thermal plasma at this temperature is ≈ 0.25, so the observed line ratios in our sample would be $\lesssim 0.25$ if they only included emission from the LB and hot halo.

We explore this idea by examining the O VIII/O VII distribution on the sky from our total observation sample. Figure 6.6 shows our line intensity ratio distribution on the sky. Inspecting the sky projection alone suggests the line intensity ratios are systematically higher for sight lines that pass through or near the Fermi bubbles ($\approx$0.5) than those farther away from the Galactic center ($\approx$0.2). To quantify this, we bin the sight lines on the sky and calculate the median and interquartile range for the line ratios in each bin. The bin edges are defined as ellipses in l, b space, where the first bin includes sight lines that pass though the Fermi bubbles and subsequent bins include sight lines extending farther into the halo (see dotted lines in Figure 6.6). Figure 6.6 shows the line ratio median and interquartile range for observations in each bin. These results clearly show the line ratios are systematically higher for sight lines in the first bin, and are also higher than the characteristic ratio expected if the observations included just LB and hot gas halo emission (gray shaded band in Figure 6.6).

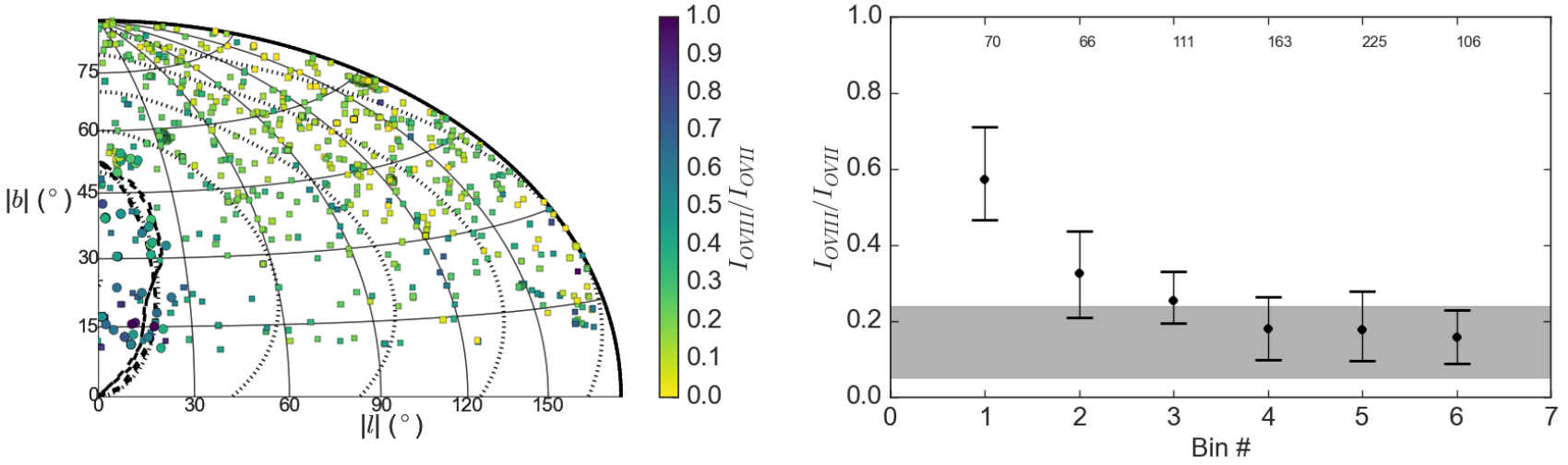

Figure 6.6: *Left:* Measured O VIII/O VII ratio distribution folded into one quadrant of an Aitoff projection with the circles and squares representing *Suzaku* and *XMM-Newton* observations respectively. The black dashed lines represent the observed Fermi bubble outline while the black dotted lines represent edges used to bin the data. The line ratios are systematically larger for sight lines passing near the Fermi bubbles compared to sight lines near the Galactic pole or anti-center. *Right:* Median and interquartile ranges for binned line ratio distributions on the sky. The bin edges are the black dotted lines in the *left* panel, with the first bin including all observations within the Fermi bubbles. The top of the gray band represents the line ratio expected for a plasma with $T = 2 \times 10^6$ K, and the bottom includes a contribution from a cooler LB plasma source or SWCX. The observations in the first bin have significantly larger line ratios than the expected range in the gray band, indicating the presence of a plasma at $> 2 \times 10^6$ K.

These systematically larger line ratios near the Galactic center indicate the presence of hotter gas than the ambient 2×10^6 K plasma. This interpretation is model-independent and builds upon the fact that we know the Fermi bubbles occupy a significant volume above and below the Galactic center. While this is a useful result that only relies on observations, the observed line ratios do not encode the bubbles' detailed temperature structure due to additional emission from the LB and hot gas halo. Regardless, this result motivates the modeling work below and validates the assumption that the bubbles contain gas hotter than 2×10^6 K.

6.6.2 Comparing Models with Data

As a preliminary test, we explore an emission model including only contributions from the LB and hot gas halo. This model assumes that the bubble and shell volumes contribute no line emission, or equivalently that $n_{FB} = n_{shell} = 0$. For the other emission components, we assume a parametric model distribution from MB15. This includes a LB density of $n_{LB} = 4 \times 10^{-3}$ cm^{-3} and a hot gas density profile described by Equation 6.2 with $n_o r_c^{3\beta} = 1.35 \times 10^{-2}$ cm^{-3} kpc$^{3\beta}$ and $\beta = 0.5$. This model likely *over-estimates* any halo emission since it assumes a power law all the way to the Galactic center, as opposed to having a flat core density. We calculate model O VIII emission line intensities for this limiting case and compute the residual emission defined as $(I_{observed} - I_{model})/I_{error}$. Figure 6.7 shows how the residual emission varies on the sky, with a particular emphasis on the strong ($\gtrsim 3\sigma$) positive residuals near the Fermi bubbles. We interpret these residuals as missing emission due to the Fermi bubbles, which motivates the modeling procedure outlined below.

The goal of our modeling procedure is to find a density model that is most consistent with our observed data set, including contributions from the Fermi bubble and shell components. We quantify this consistency with the model χ^2 or likelihood ($\mathcal{L} \propto \exp(-\chi^2/2)$). We use the publicly available Markov Chain Monte-Carlo (MCMC)

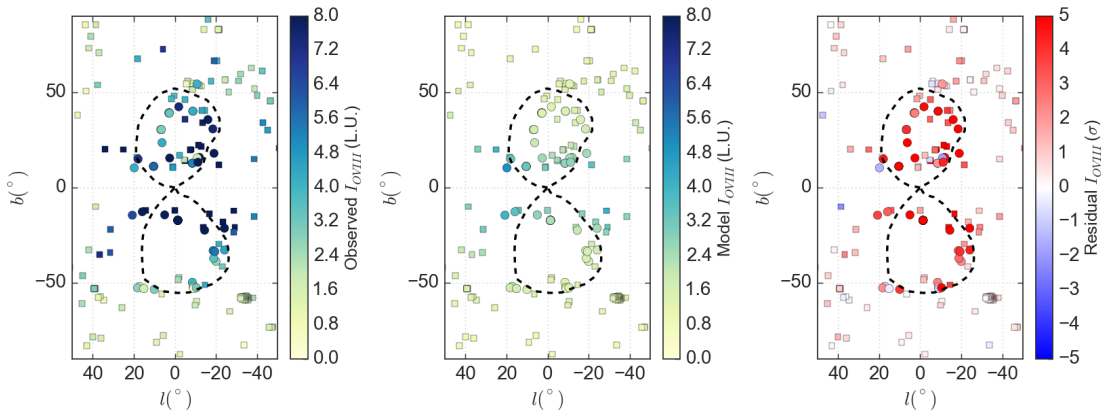

Figure 6.7: Observed emission line intensities (*left* panel), model emission line intensities (*center* panel), and residuals (*right* panel) for a model without a bubble or shell emission component. The hot gas halo dominates the model O VIII emission in this case. Sight lines passing through the bubbles have significant ($\gtrsim 3\sigma$) positive residual O VIII emission, which we attribute to the bubbles and their interaction with the ambient hot halo medium.

Python package `emcee` (Foreman-Mackey et al., 2013) to explore our model parameter space and find the parameters that minimize the model χ^2, or maximize the model $\ln(\mathcal{L})$. The output chains for each model parameter are treated as marginalized posterior probability distributions. We define "best-fit" parameters as the median values for each binned chain distribution, which yields identical results to the Gaussian-fitting procedure outlined by MB15, assuming the distributions are approximately Gaussian. Thus, these best-fit parameters maximize the model likelihood, given the data.

We considered several different model parametrizations in our model fitting process. These included hot gas halo density models described by either a power law (Equation 6.2) with two free parameters (the normalization and β) or a full β-model (Equation 6.1) with r_c and β left to vary. We did not let n_o vary independently in this model since the previous modeling work from MB15 effectively constrained the halo normalization parameter $n_o r_c^{3\beta}$. Our modeling procedure keeps this quantity

fixed to $n_o r_c^{3\beta} = 1.35 \times 10^{-2}$ cm^{-3} kpc$^{3\beta}$, while letting the core radius vary as the free parameter. We also experimented with fixing the hot gas halo profile with the fit values from MB15 or with $r_c = 3$ kpc, however we found this made little difference in the best-fit parameters for either the halo density profile or bubble/shell densities.

Table 6.2 summarizes our best-fit model parameters, including 1σ uncertainties encompassing the 68% probability ranges from the posterior probability distributions. There are several trends to note from these results. The LB density parameter is consistent with zero, validating the assumption that the LB contributes little emission to the O VIII data. The halo density profile results are consistent with those reported in MB15 when considering the same power law density parametrization ($n_o r_c^{3\beta} = 1.35 \times 10^{-2}$ cm^{-3} kpc$^{3\beta}$, $\beta = 0.5$). This implies the hot gas density profile constraints are not biased due to observations near the Fermi bubbles. We also find characteristic best-fit core radii between 2–3 kpc, which is expected. The parameters of interest, n_{FB} and n_{shell}, have characteristic best-fit densities between 5–8$\times 10^{-4}$ cm^{-3} assuming a temperature of $\log(T) = 6.50$. The inferred densities are lower if we assume a power law halo gas density model compared to if we assume a β-model. We expect to see this trend since the power law model produces more halo emission near the Galactic center than a β-model with a core radius/density, thus resulting in less Fermi bubble/shell emission required to produce the observed emission. After weighing these effects, we define our fiducial model to be one with a β-model and r_c fixed to 3 kpc. This results in best-fit parameters of $n_{FB} = 7.2 \pm 0.2 \times 10^{-4}$ cm^{-3}, and $n_{shell} = 7.7 \pm 0.2 \times 10^{-4}$ cm^{-3}. Figure 6.8 shows the marginalized posterior probability distributions and contour plots from our MCMC analysis assuming this parametric model (generated using the Python code `corner.py`; Foreman-Mackey et al., 2016).

We also explored a model with no shell distribution to determine its significance in our model fitting procedure. This is equivalent to setting the shell thickness to 0 kpc in our geometric model, and not including n_{shell} as a parameter in our emission

Table 6.2. Fermi Bubble Fitting Results

n_{LB} [a] (10^{-3} cm^{-3})	$n_o r_c^{3\beta}$ (10^{-2} cm^{-3} kpc$^{3\beta}$)	n_o (10^{-3} cm^{-3})	r_c (kpc)	β	n_{FB} [b] (10^{-4} cm^{-3})	n_{shell} [b] (10^{-4} cm^{-3})	χ^2 (dof)
< 5.81	1.01 ± 0.06	–	–	0.45 ± 0.01	6.70 ± 0.19	6.25 ± 0.30	2683 (736)
< 5.42	1.35 (fixed)	4.47	2.12 ± 0.22	0.49 ± 0.01	6.67 ± 0.19	6.20 ± 0.29	2669 (736)
3.83 (fixed)	1.35 (fixed)	–	–	0.50 (fixed)	6.61 ± 0.18	6.01 ± 0.27	2716 (739)
3.83 (fixed)	1.35 (fixed)	2.60 (fixed)	3 (fixed)	0.50 (fixed)	7.17 ± 0.17	7.48 ± 0.22	2783 (739)

Note. — Unless noted otherwise, all best-fit values are defined as the most likely parameter values from the MCMC marginalized posterior probability distributions. The uncertainties encompass the 68% probability region relative to the maximum likelihood value for each parameter.

[a]The Local Bubble (LB) produces minimal O VIII emission in our model. With this in mind, we either report the fixed value for n_{LB} or the 2σ upper limit from our MCMC analysis.

[b]These best-fit densities assume each component has a temperature of $\log(T_{FB,\ shell}) = 6.50$ when calculating line intensities. See Table 6.3 for densities with hotter assumed temperatures.

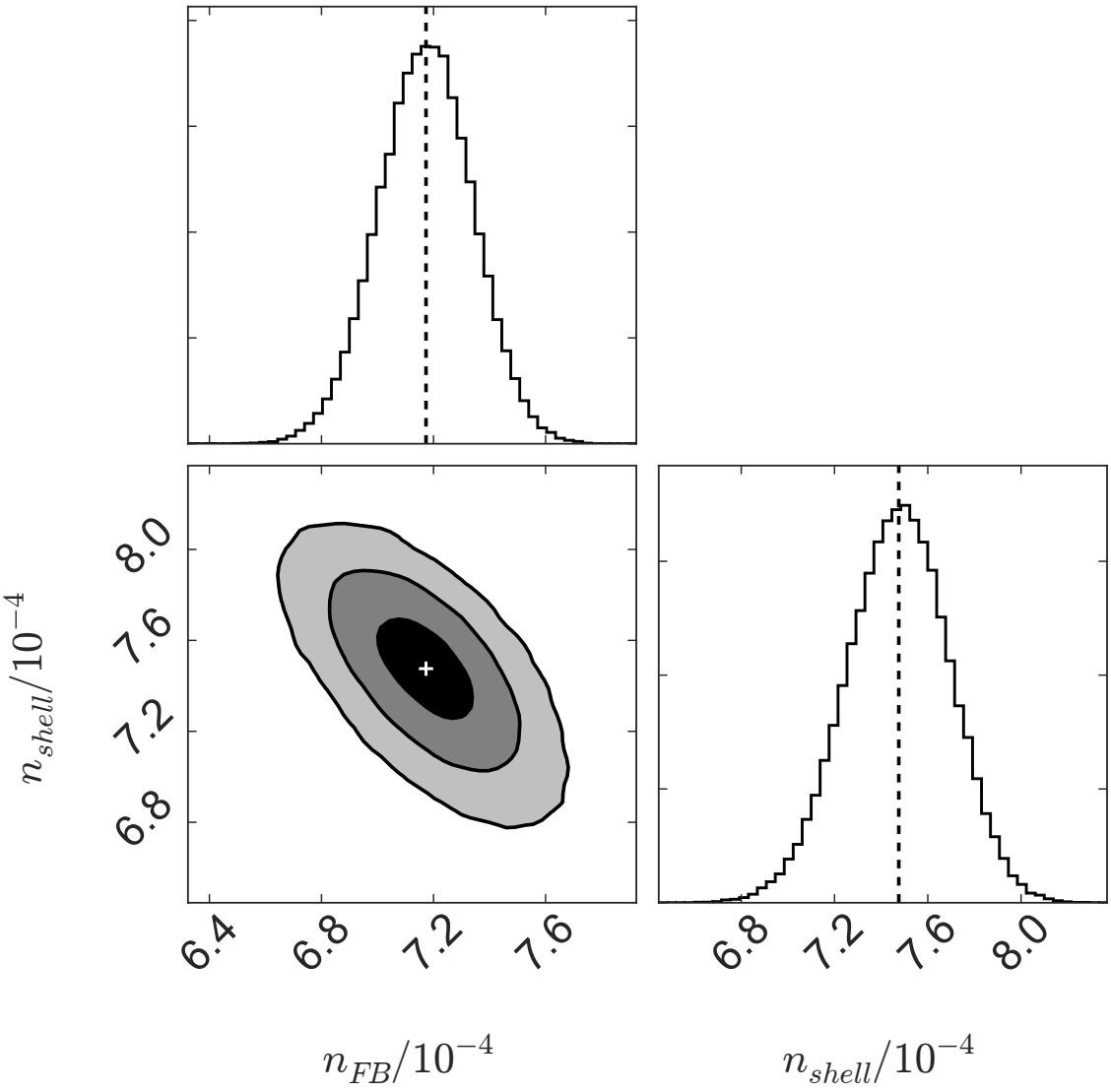

Figure 6.8: Our model fitting results for the Fermi bubble volume-filled and shell components represented as marginalized posterior probability distributions and a two-dimensional contour plot. The dashed lines and white cross represent the best-fit model values and the contour ranges include 1, 2, and 3σ. This model assumes the bubble and shell components have a temperature of $\log(T) = 6.50$.

model. When we re-fit the data with this model (r_c fixed to 3 kpc), we find the Fermi bubble density parameter increases from 7.2×10^{-4} cm^{-3} to 7.7×10^{-4} cm^{-3} in order to compensate for the lack of model shell emission. This leads to a marginal improvement in the overall fit quality ($\chi^2_{r,\ with\ shell}$ (dof) = 2783 (739) to $\chi^2_{r,\ no\ shell}$ (dof) = 2741 (740)), implying the shell structure is not required to fit the data. However, the difference in χ^2_r is relatively small compared to the degrees of freedom, and expanding wind models physically require at least two distinct outflow regions. Therefore, while our best-fit model does not require a shell structure, we assume the bubble and shell structures are each present in our discussion and temperature analysis.

In order to constrain the bubble and shell temperatures, we compare best-fit model line ratios for different temperature distributions with the observed O VIII/O VII line ratio distribution near the Fermi bubbles. To do this, we change the bubble and shell temperatures while keeping the product $n^2\epsilon_{OVIII}(T)$ fixed from the best-fit model results. This fixes the O VIII emission coming from the bubble and shell, but changes the model O VII emission because $\epsilon_{OVII}(T)$ decreases faster than $\epsilon_{OVIII}(T)$ with increasing temperature. Thus, increasing the assumed temperature leads to an increase in the model line ratios, an increase in the inferred best-fit densities (ϵ_{OVIII} decreases for $T > 3 \times 10^6$ K), and a constant O VIII emission contribution.

A model temperature distribution with $\log(T_{FB}) = 6.60$ and $\log(T_{shell}) = 6.70$ leads to a model line ratio distribution most consistent with the observed line ratios near the Fermi bubbles. This changes the inferred best-fit densities to $n_{FB} = 8.2 \times 10^{-4}$ cm^{-3} and $n_{shell} = 1.0 \times 10^{-3}$ cm^{-3} in order to keep the product $n^2\epsilon_{OVIII}(T)$ fixed for each component. Figure 6.9 shows the observed and new best-fit model line ratio histograms for sight lines that pass within $\approx 5^\circ$ of the projected bubble edge ($\sim$100 sight lines). These densities and temperatures produce a O VIII/O VII ratio distribution median and interquartile range of 0.52 (0.41–0.60), consistent with the

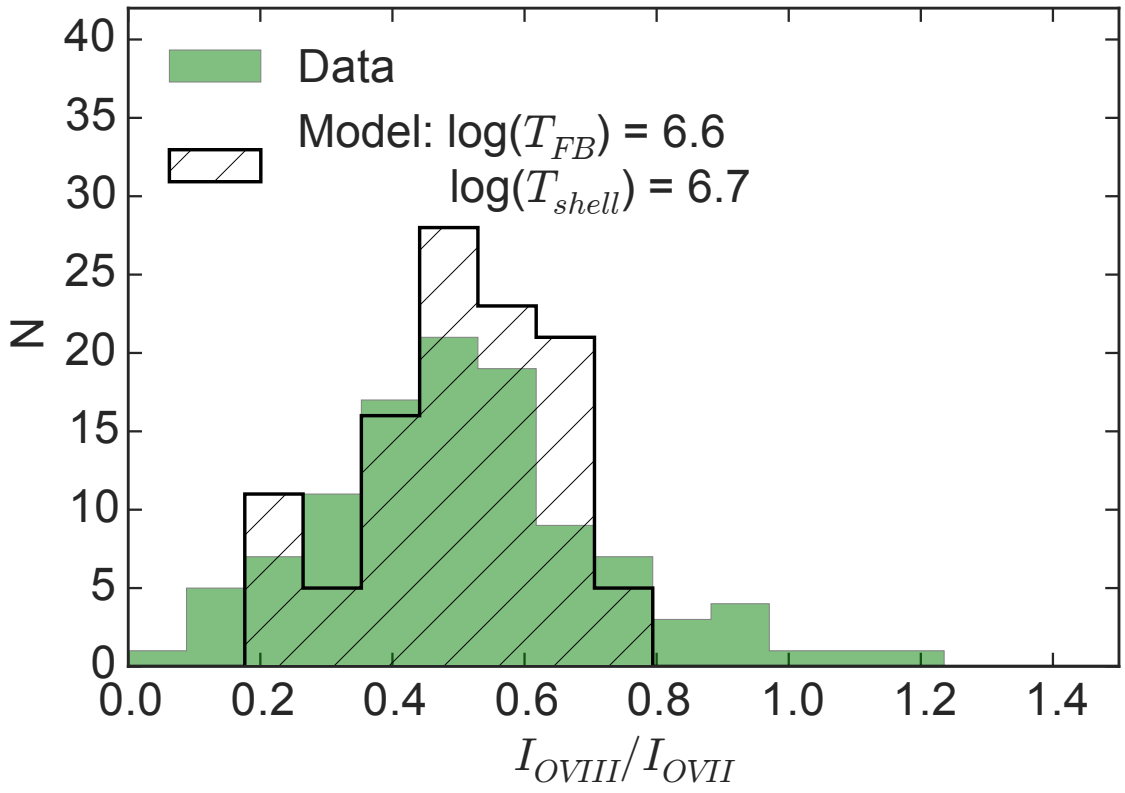

Figure 6.9: Observed (shaded green areas) and model (black hatched areas) O VIII/O VII line ratio histograms for sight lines passing through the Fermi bubbles. The model assumes $\log(T_{FB}) = 6.60$ and $\log(T_{shell}) = 6.70$, which produces line ratios that are most consistent with the observations.

observed median and interquartile range of 0.49 (0.38–0.62). We treat these densities and temperatures as the characteristic physical properties for the bubble and shell components in our subsequent analysis.

6.7 Discussion

In this section, we discuss how our constraints fit in with our current picture for the Fermi bubbles and Milky Way. This includes an overview of the constrained thermal gas structure, and how this compares to the surrounding hot medium. We extend these constraints to infer the bubbles' characteristic shock strength, current

expansion velocity, energy input rate, age, and likely formation scenario. We also discuss how our constraints compare with previous Fermi bubble analyses.

Table 6.3 summarizes our most important inferred quantities discussed below for the best-fit densities and temperatures discussed above. The density uncertainties follow directly from our MCMC results summarized in Table 6.2. We use less strict criteria for the temperature uncertainties since we did not directly fit the O VIII/O VII line ratios. The temperature limits represent where the differences between the observed and model line ratio medians are less than 1σ of the corresponding sample median uncertainties. Uncertainties on all subsequent calculated quantities (masses, expansion rates, ages, etc.) use the density and temperature uncertainties listed in Table 6.3.

6.7.1 Inferred Bubble Structure

We discuss our inferred bubble densities and temperatures in this section, and compare them to the assumed ambient structure. Overall, our constraints indicate the bubbles are hotter and over-pressurized compared to the surrounding medium, consistent with previous bubble observations (Su et al., 2010; Kataoka et al., 2015). Figure 6.10 shows our best-fit model as two-dimensional density, temperature, and pressure maps projected at the Galactic center. This visualizes the comparison with the surrounding medium we discuss in the rest of the section.

The bubble and shell densities have characteristic values of $\sim 10^{-3}$ cm^{-3}, which are comparable to the surrounding medium at low z. Including a hot gas halo core radius of 3 kpc in our fiducial model implies a core density of 2.6×10^{-3} cm^{-3}, assuming a fixed power law normalization of $n_o r_c^{3\beta} = 1.35 \times 10^{-2}$ cm^{-3} kpc$^{3\beta}$. This suggests $n_{shell} \sim n_{halo}$ within $|z| \lesssim 5$ kpc. The hot gas halo density decreases by about a factor of 6 between r =1–10 kpc, meaning our bubble and shell densities are larger than the surrounding medium farther away from the Galactic plane. We also note that

Table 6.3. Bubble Properties

Quantity	Value	Uncertainty/Range	Unit
n_{FB}	8.2	± 0.2	10^{-4} cm^{-3}
$\log(T_{FB})$	6.60	6.60–6.65	log(K)
P_{FB}	4.5	4.5–5.5	10^{-13} dyne cm^{-2}
M_{FB}	4.6	4.6–5.0	10^6 $M_\odot$
n_{shell}	10.0	± 0.3	10^{-4} cm^{-3}
$\log(T_{shell})$	6.70	6.60–6.95	log(K)
P_{shell}	6.9	4.7–19.7	10^{-13} dyne cm^{-2}
M_{shell}	6.1	5.2–9.8	10^6 $M_\odot$
$\mathcal{M}$	2.3	1.9–3.4	–
v_{exp}	490	413–720	km s^{-1}
$t_{dyn,\ h}$[a]	20.0	13.6–23.7	Myr
$t_{dyn,\ w}$[a]	6.0	4.1–7.11	Myr
t_{age}[b]	4.3	2.9–5.1	Myr
$2 \times \xi \times \dot{E}$[c]	2.3	1.4–7.4	10^{42} erg s^{-1}

Note. — Summary of our inferred bubble properties discussed in Section 6.7. The densities have uncertainties from the MCMC analysis, while the temperatures (and all other derived quantities) have 1σ uncertainties based on the line ratio median difference between the observations and models.

[a] $t_{dyn} = d/v_{exp}$, where $t_{dyn,\ h}$ is for the full bubble height and $t_{dyn,\ w}$ is for half the bubble width.

[b] t_{age} is the bubble age defined in Equation 6.9.

[c] $\xi \dot{E}$ is the energy injection rate defined in Equation 6.10.

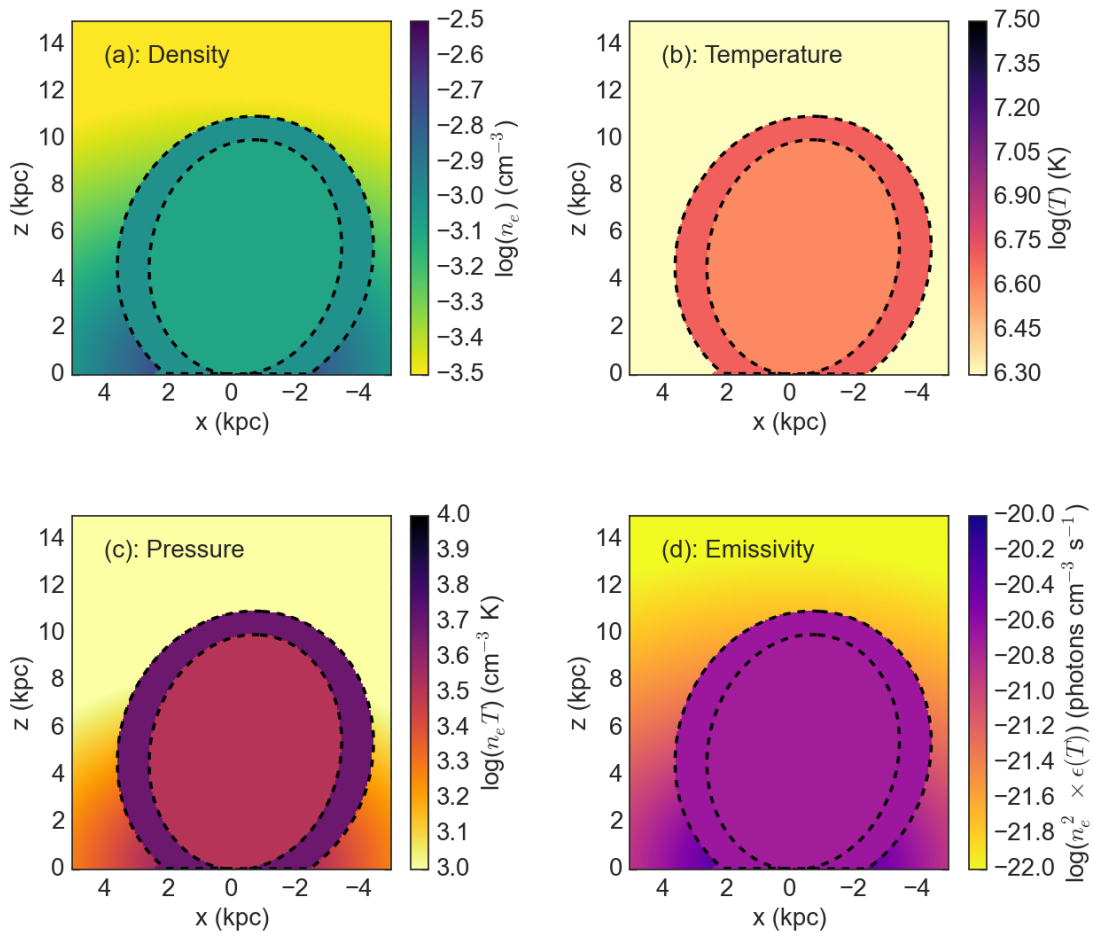

Figure 6.10: Our best-fit Fermi bubble model compared to the surrounding hot gas halo profile as two-dimensional slices at the Galactic center. The dashed lines represent the boundaries between the bubble and shell surfaces. The panels represent: density (a), temperature (b), pressure (c), and O VIII emissivity defined as $n_e^2 \times \epsilon(T)$ (d). There is variation with height away from the Galactic plane, but the bubbles are hotter and over-pressurized compared to the surrounding halo medium.

$n_{FB} \approx n_{shell}$ from our model fitting results, making it difficult to distinguish between volume-filling emission compared to limb-brightened emission. This might be due to our choice to parametrize the structures with constant densities and temperatures, but our constraints still probe the average densities associated with the bubbles.

Our inferred bubble and shell temperatures of $\log(T_{FB,\ shell}) = 6.60$–$6.70$ are hotter

than the surrounding medium ($\log(T_{halo}) = 6.30$). This is broadly consistent with the bubbles injecting enough energy to shock-heat the surrounding medium, although simulations predict a wide range of shock strengths and bubble temperatures as high as $\sim 10^8$ K (e.g., Guo & Mathews, 2012; Yang et al., 2012). It is possible the bubbles contain gas at these high temperature, however this temperature plasma would not produce observable O VIII emission. Our modeling results indicate the average bubble and shell temperatures are hotter than the surrounding medium, but still at low enough temperatures to produce observable signatures in the data.

Combining the density and temperature constraints indicates the bubbles' are over-pressurized compared to the surrounding medium. Our best-fit bubble and shell parameters indicate thermal gas pressures of $P_{FB} = 4.5 \times 10^{-13}$ dyne cm^{-2}, $P_{shell} = 6.9 \times 10^{-13}$ dyne cm^{-2}, or P/k ≈3000–5000 cm^{-3} K. The surrounding thermal gas pressure varies with r and z due to the decreasing density profile, with characteristic values of ≈5000 cm^{-3} K near the Galactic center and ≈1000 cm^{-3} K at $r = 10$ kpc. In this picture, the bubbles are in approximate pressure equilibrium at lower z, but become over-pressurized with increasing height away from the Galactic plane. These estimates are also a lower limit to how over-pressurized the bubbles actually are, because they do not account for non-thermal or magnetic pressure contributions. Regardless, these constraints indicate the bubbles are generally over-pressurized, and thus expanding into the surrounding medium.

We use these quantities to infer a characteristic shock strength and instantaneous expansion velocity associated with the bubbles. The classic treatment of shocks propagating through the ISM yield specific pre- and post-shock jump conditions for the gas density, temperature, and pressure given a shock expansion velocity (e.g., Shull & Draine, 1987). The Fermi bubbles expansion is more complex than this traditional treatment since they do not appear to be spherical, and they are presumably expanding into a medium with varying density. For example, the ratio between n_{shell}

(treated as post-shocked material) and the ambient halo gas density along the shell edge (treated as pre-shock material) ranges between ≈0.5 near the Galactic center to ≈3 at the maximum bubble height. On the other hand, our choice to parametrize the hot gas halo and shell with constant temperatures allows us to use the temperature ratio as a shock strength diagnostic similar to K15. Assuming a monotonic gas (γ=5/3), an ambient gas sound speed of c_s= 212 km s^{-1}, $T_{shell} = 5 \times 10^6$ K, and $T_{halo} = 2 \times 10^6$ K, our temperature ratio implies a fiducial mach number and corresponding expansion velocity of $\mathcal{M} = 2.3$ and $v_{exp} = 490$ km s^{-1}. The uncertainty in T_{shell} expands these constraints to $\mathcal{M}$ =1.9–3.4 and v_{exp} = 413–720 km s^{-1}. These shock parameters are broadly consistent with the range of density and pressure ratios we estimate, indicating these constraints probe the bubbles' current expansion rate into the surrounding medium.

6.7.2 Bubble Energetics and Origin Scenarios

6.7.2.1 The Bubbles as a Confined Galactic Wind

We treat the bubbles in the framework of a continuous galactic outflow/superbubble with self-similar Sedov-Taylor solutions (e.g., Castor et al., 1975; Weaver et al., 1977; Mac Low & McCray, 1988; Veilleux et al., 2005). The outflow morphology consists of five zones (from closer to farther from the outflow origin): the energy injection zone, a free-flowing outflow, shocked wind material, a shell of shocked ISM/CGM material, and the ambient ISM/CGM. Our model constraints probe the last three zones since we do not model observations in the inner ≈1 kpc from the Galactic center. The Sedov-Taylor solutions for this type of outflow relate the ambient density, bubble age, bubble size, expansion velocity, and average energy injection relate to each other. Assuming the outflow is still in the energy-conserving phase (cooling time greater than the bubble age), the relations between these quantities are as follows:

$$t_{age} = \ 11.8\ Myr\ \left(\frac{r}{10\ \mathrm{kpc}}\right)\left(\frac{v}{500\ \mathrm{km\ s^{-1}}}\right)^{-1}, \tag{6.9}$$

$$\xi\dot{E} = \ 3.7\times10^{42}\ \mathrm{erg\ s^{-1}}\ \left(\frac{n_o}{10^{-3}\ \mathrm{cm^{-3}}}\right)\left(\frac{r}{10\ \mathrm{kpc}}\right)^{2}\left(\frac{v_{exp}}{500\ \mathrm{km\ s^{-1}}}\right)^{3}, \tag{6.10}$$

where n_o is the ambient density in cm^{-3}, r is the bubble radius in kpc, v_{exp} is the expansion velocity in km s^{-1}, t_{age} is the bubble age in Myr, $\dot{E}$ is the energy injection rate in erg s^{-1}, and ξ is the thermalization efficiency of the mechanical energy. This thermalization efficiency is believed to vary with environment, but is estimated to be $\gtrsim$10% in average galaxies with a typical assumed value of 0.3 (e.g., Larson, 1974; Wada & Norman, 2001; Melioli & de Gouveia Dal Pino, 2004).

Our modeling results constrain three of the five variables in these equations. As discussed above, a hot gas halo model with $r_c = 3$ kpc and fixed power law normalization of 1.35×10^{-2} cm^{-3} kpc$^{3\beta}$ results in an ambient core density of $n_o = 2.6\times10^{-3}$ cm^{-3}. The bubble/shell temperature constraints suggest an outflow velocity of 490 km s^{-1}. The bubble size is not trivial to estimate in this framework, where the outflow is typically treated as a spherical shell with radius r centered on the injection source. The bubbles' shape is more complex than this since two lobes exist on each side of the Galactic plane. We use a characteristic bubble size defined as the geometric mean of the three ellipsoidal axes, resulting in $r = 3.6$ kpc.

Given these constrained values, we estimate the bubbles' age and average mechanical energy injection rate. The bubbles' dynamical timescale, $t_{dyn} = d/v_{exp}$, is a crude age estimate that does not incorporate the bubble environment or energy source. For $v_{exp} = 490$ km s^{-1}, the dynamical timescale for the full bubble height is $t_{dyn,\ h} = 10$ kpc / 490 km s^{-1} = 20.0 Myr, and the dynamical timescale for half the bubble width is $t_{dyn,\ w} = 3$ kpc / 490 km s^{-1} = 6.0 Myr. The superbubble model

calculation (Equation 6.9) is a refined bubble age estimate, where we find $t_{age} = 4.3$ Myr for r defined as the geometric mean above and $v_{exp} = 490$ km s^{-1}. We also infer a combined energy injection for both bubbles ($2 \times \xi \times \dot{E}$) of 2.3×10^{42} erg s^{-1} using Equation 6.10. Accounting for the uncertainty in v_{exp} leads to a characteristic age range between ≈3–5 Myr and energy injection rate between ≈1–7×10^{42} erg s^{-1}. We compare this characteristic age and energy injection rate with possible bubble formation mechanisms.

6.7.2.2 Sgr A* Accretion Origin

One suggested bubble formation mechanism has been a past accretion event onto Sgr A*, resulting in an AGN episode in the Milky Way. Sgr A* has an estimated mass of 4×10^6 $M_\odot$ (Schödel et al., 2002; Ghez et al., 2003, 2008; Gillessen et al., 2009a,b; Meyer et al., 2012), which is capable of producing significant amounts of energy during an accretion episode. We also know that accretion onto super-massive black holes can produce galactic outflows with significant energy injection rates and morphologies similar to the observed Fermi bubbles (e.g., McNamara & Nulsen, 2007; Yuan & Narayan, 2014). Here, we consider observations of Sgr A*, its possible accretion history, and compare the expected energetics with our modeling constraints.

Sgr A* is currently in a quiescent state with a bolometric luminosity of $L_{bol} \sim 10^{36}$ erg s^{-1} $\sim$ 2×10^{-9} L_{Edd} (e.g., Yuan & Narayan, 2014). Our proximity to Sgr A* allows for a combination of techniques to estimate current mass accretion rates. *Chandra's* resolution is comparable to the Sgr A* Bondi radius, and has constrained the Bondi accretion rate to be $\sim 10^{-5}$ $M_\odot$ yr^{-1} (Baganoff et al., 2003). Polarized radio emission constrains the accretion rate near the event horizon, with limits being between $> 2 \times 10^{-9}$ $M_\odot$ yr^{-1} and $< 2 \times 10^{-7}$ $M_\odot$ yr^{-1} depending on the magnetic field orientation (e.g., Marrone et al., 2007). While this is a significant uncertainty in the current mass accretion rate, the consensus is that Sgr A* is accreting well below

its Eddington rate, and has been a well-modeled source for radiatively inefficient accretion flows (RIAFs).

There are a number of observational indications that Sgr A* has been more active in the past (Totani, 2006). Mou et al. (2014) summarizes these lines of evidence, which include: a higher Sgr A* luminosity is required to produce fluorescent iron emission and reflection nebula seen in several nearby molecular clouds (Koyama et al., 1996; Murakami et al., 2000, 2001a,b), there exists an ionized halo of material surrounding Sgr A* (Maeda et al., 2002), there are dynamic features indicating an outflow near the Galactic center in the form of the Galctic Center Lobe (Bland-Hawthorn & Cohen, 2003) and the Expanding Molecular Ring (Kaifu et al., 1972; Scoville, 1972), excess Hα emission seen in the Magellanic Stream (Bland-Hawthorn et al., 2013), and possibly the Fermi bubbles themselves. The RIAF modeling from Totani (2006) argues that Sgr A* should have had an accretion rate $\sim 10^3$–10^4 times larger than its current accretion rate over the past $\sim$10 Myr to reproduce these observations. This introduces additional scatter in the inferred past Sgr A* accretion rate, but motivates the assumption that Sgr A* has injected energy into the surrounding medium through an accretion event.

We estimate an energy injection rate due to past Sgr A* accretion and compare with our constrained energy input rate. The mechanical energy injection rate from black hole accretion is tied to the accretion power by the following relation:

$$\dot{E}_{BH} = \epsilon \dot{M}_{acc} c^2 = 5.7 \times 10^{45} \text{ erg s}^{-1} \left(\frac{\epsilon}{0.1}\right) \left(\frac{\dot{M}_{acc}}{M_\odot \text{ yr}^{-1}}\right), \tag{6.11}$$

where $\dot{E}_{BH}$ is the mechanical energy injection rate, $\dot{M}_{acc}$ is the accretion rate near the event horizon in $M_\odot$ yr^{-1}, and ϵ is the mechanical energy rate efficiency. If we assume a past accretion rate of 10^{-3} $M_\odot$ yr^{-1} (near the high end of the values discussed above), we find that $\dot{E}_{BH}$ equals our inferred vale of 2.3×10^{42} erg s^{-1} for $\epsilon \approx 0.05$. This efficiency is larger than the typical values inferred from simulations

(10^{-4}–10^{-3}; Yuan et al., 2015), however this mechanical efficiency is often treated as a free parameter in simulations. We also point out that the required efficiency is less than one, indicating that this analysis does not violate energy conservation constraints. *Thus, it is plausible that a past accretion episode onto Sgr A* could have produced enough energy required to match our energy injection rate constraints.*

The bubble age indicates this Sgr A* accretion episode had a shorter active period compared to the typical AGN duty cycle. Studies constrain the AGN duty cycle by either comparing black hole mass functions (inferred from the M_{BH}–σ relation) to AGN luminosity functions at different redshifts (e.g., Yu & Tremaine, 2002; Shankar et al., 2004; Hao et al., 2005; Schawinski et al., 2010), or through analytic black hole accretion models (e.g., Hopkins & Hernquist, 2006; Shankar et al., 2009). These techniques suggest black holes with masses of $\sim 10^6$ $M_\odot$ should have active periods of $\sim 10^8$ yr at $z = 0$, or ∼1% of a Hubble time. Our Fermi bubble age estimate is an upper limit to the active Sgr A* accretion time, and our constraint of 4.3 Myr is much smaller than the inferred duty cycle from AGN populations. One possible explanation for this discrepancy is that the Fermi bubble outburst was one of several past accretion events in the Galactic center. Our constraints imply the Fermi bubbles are due to a relatively weak AGN event, and it is possible that multiple Sgr A* accretion events of comparable or less energy have occurred over the past $\sim 10^8$ yr. Our results are also consistent with the overall decrease in AGN activity since $z \sim 2$ (e.g., Hopkins et al., 2007), as opposed to a prolonged Sgr A* accretion/growth phase.

6.7.2.3 Nuclear Star Formation Origin

Numerous studies also suggest that the Fermi bubbles formed from a period of enhanced star formation activity near the Galactic center. The Galactic center hosts several young stellar clusters with ages ranging between 5–20 Myr and accounting for $\sim 5 \times 10^5$ $M_\odot$ of material. The massive stars in these clusters could have generated

a galactic-scale outflow due to stellar winds and type II supernova explosions (e.g., Leitherer et al., 1999). Here, we compare the expected energy output from past star formation near the Galactic center to our energy injection rate constraints.

The Galactic center star formation history is complex and difficult to measure, but several studies argue for an average star formation rate (SFR) of $\approx$ 0.05 $M_\odot$ yr^{-1} over the past $\sim$10 Myr. Crocker (2012) reviews these studies, most of which utilize *Spitzer* observations of young stellar objects within the inner $\sim$500 pc from the Galactic center. For example, Yusef-Zadeh et al. (2009) conducted a census of these objects using the Infrared Array Camera and Multiband Imaging Photometer on board *Spitzer*, and concluded the average SFR has been between 0.04–0.08 $M_\odot$ yr^{-1} over longer timescales ($\sim$10 Gyr). Immer et al. (2012) performed a similar analysis using *Spitzer* Infrared Spectrogaph data, and argue for an average SFR of $\approx$ 0.08 $M_\odot$ yr^{-1} over the past $\sim$Myr. Others estimate the SFR to be $\approx$0.01–0.02 $M_\odot$ yr^{-1} by counting the mass in young star clusters and dividing that by estimates for the period of star formation (Figer et al., 2004; Mauerhan et al., 2010). Thus, it appears a characteristic SFR of $\approx$ 0.05 $M_\odot$ yr^{-1} over the past $\sim$10 Myr is a reasonable assumption.

Similar to our black hole accretion energy argument above, we estimate the energy injection rate due to star formation in the Galactic center to compare with our constrained energy input rate. Assuming a Kroupa initial mass function (Kroupa, 2001), and 10^{51} ergs of mechanical energy input from a type II supernova, the mechanical energy input rate from type II supernova relates to the star formation rate as:

$$\dot{E}_{nsf} = 1.1 \ \times 10^{40} \text{ erg s}^{-1} \ \left(\frac{\epsilon}{0.3}\right)\left(\frac{SFR}{.1 \ M_\odot \text{ yr}^{-1}}\right), \tag{6.12}$$

where $\dot{E}_{nsf}$ is the mechanical energy input rate due to nuclear star formation, SFR is the star formation rate in $M_\odot$ yr^{-1}, and ϵ is an efficiency factor typically assumed to be $\approx$0.3 (see Crocker et al. (2015) or Sarkar et al. (2015) for equivalent relations).

This implies that an average star formation rate of 0.05 $M_\odot$ yr^{-1} over the past ∼10 Myr produces an energy injection rate of $\approx 6 \times 10^{39}$ erg s^{-1}. This estimate falls ≈400 times lower than our estimated energy input rate of 2.3×10^{42} erg s^{-1}. It is possible that the star formation rate has been more variable over the past ∼10 Myr, however the upper limits are only ≈3 times higher than the average value (Yusef-Zadeh et al., 2009). *Thus, star formation in the Galactic center does not produce enough energy to inflate the bubbles based on our energy injection rate constraints.*

6.7.3 Thermal Gas Masses

We use our density constraints to estimate the amount of thermal gas mass within the bubble and shell structures. This is a straightforward calculation since we assume each component has a constant density and fixed volume. Thus, the mass in each component is defined as $M = \mu m_H \times n \times V$, where $\mu = 0.61$ is the average weight per particle, m_H is the mass of hydrogen, n is the inferred density, and V is the volume. Our geometric models imply a bubble volume of $V_{FB} = 2 \times 4/3 \times \pi \times 5 \times 3^2 = 377$ kpc^3 (the factor of two is for two ellipsoidal bubbles), and a combined shell volume of $V_{shell} = 411$ kpc^3. The densities in Table 6.3 imply bubble and shell thermal gas masses of $M_{FB} = 4.6 \times 10^6$ $M_\odot$ and $M_{shell} = 6.1 \times 10^6$ $M_\odot$, with a characteristic range between 5–10$\times 10^6$ $M_\odot$ given the density uncertainties. These masses represent material that has been shock-heated by the bubbles or injected into the bubbles by the energy source.

We first explore whether the bubble and shell plasmas are predominantly shocked hot halo material by comparing the masses derived above to the inferred hot gas halo mass that would exist within the bubble and shell volumes. If the Fermi bubbles did not exist and the total bubble+shell volume was instead occupied by our hot gas halo density model with $r_c = 3$ kpc, the halo mass in the volume would be 1.11×10^7 $M_\odot$. The calculations above indicate the combined thermal gas mass

within the bubble+shell volumes is $M_{FB} + M_{shell} = 1.07 \times 10^7\ M_\odot$. The consistency between these values suggests that most of the thermal gas associated with the bubbles is shock-heated ambient material, as opposed to injected material from the energy source.

As a consistency check, we estimate the amount of injected material from the energy source, either AGN or star formation, to compare with the above masses. The mass-loss rate due to nuclear star formation activity (or mass injection rate) is believed to be $\dot{M}_{inj,\ nsf} \approx 0.3(SFR/M_\odot yr^{-1})$ (Leitherer et al., 1999). Mass-loss rates from black hole accretion events (either from jets or winds) are more uncertain, but accretion wind simulations of radiatively inefficient accretion flows suggest values ranging between 2–20% of $\dot{M}_{Edd} = 10L_{Edd}/c^2$ (Yuan et al., 2012, 2015). Assuming a nuclear SFR of 0.05 $M_\odot$ yr^{-1}, $\dot{M}_{Edd} \sim 10^{-1}\ M_\odot$ yr^{-1} for Sgr A*, and a bubble active period of 4.3 Myr, we find characteristic injected mass estimates of $\dot{M}_{inj} \lesssim 10^5\ M_\odot$ for both origin scenarios. This is significantly less than our constrained mass estimate of $\sim 10^7\ M_\odot$, thus validating our claim that the bubbles contain predominantly shocked halo gas.

6.7.4 Comparing with Previous Work

6.7.4.1 Analyses at Soft X-ray Energies

The most direct comparison to our analysis are the previous soft X-ray spectral analyses (Kataoka et al., 2013, 2015; Tahara et al., 2015). These studies follow a similar methodology and find similar results, with K15 being the most current and comprehensive work of the three. These authors compiled a sample of 29 *Suzaku* observations and 68 *Swift* observations distributed across the Fermi bubbles. They fit the *Suzaku* XIS data and *Swift* X-ray Telescope spectra with a multi-component thermal plasma model, where one component is typically fixed at $kT = 0.1$ keV to represent LB and residual SWCX emission, and the other represents the combined

halo and Fermi bubble emission. They systematically find a hot gas halo/Fermi bubble plasma temperature of $kT = 0.3$ keV, which is hotter than the characteristic value found for sight lines away from the bubbles ($kT = 0.2$ keV; Henley & Shelton, 2013). From this temperature, they infer a relatively weak shock strength and expansion velocity of $\mathcal{M} = 0.3$ keV / 0.2 keV = 1.5 and $v_{exp} = 300$ km s^{-1}. They also find emission measures that vary by over an order of magnitude, which they claim is due to a combination of Galactic halo and Fermi bubble emission. The authors model the emission measures in the northern Galactic hemisphere with a hot gas halo density model from Miller & Bregman (2013) and a Fermi bubble shell distribution with an inner radius of 3 kpc, an outer radius of 5 kpc, and a density of 3.4×10^{-3} cm^{-3}.

Our approach is similar to these studies, but there are several differences that can explain the discrepancy between their inferred shock properties and ours. The data sets are different since we consider fitted emission line intensities as opposed to APEC plasma emission measures and temperatures. In principle, these are more useful quantities to model, since our emission line intensities deal with the inherit degeneracy between density and temperature. In practice, fitting a full 0.5–2.0 keV SXRB spectrum with a thermal plasma model requires more counts than fitting only the oxygen emission lines, implying our sample is larger and has better sky coverage than the K15 sample. However, this should make a minor difference in the inferred bubble properties since the fitted plasma temperature is most sensitive to the O VIII/O VII ratio for plasma temperatures between ≈0.1–0.3 keV. The bigger discrepancy involves the interpretation of the fitted emission measures and temperatures.

The primary difference between our work and those discussed above is the treatment of combined X-ray emission from the hot gas halo and Fermi bubbles. The fitted plasma temperature of 0.3 keV is the emission measure-weighted temperature from all plasma sources along the sight lines of interest, which includes at least a hot gas halo and Fermi bubble component. However, K15 uses the temperature ratio 0.3 keV

/ 0.2 keV to infer the shock strength and expansion velocity. This assumption that the Fermi bubble plasma has a temperature of 0.3 keV effectively ignores the hot gas halo contribution to the spectrum. The fitted temperature of 0.3 keV includes a contribution from a 0.2 keV hot halo plasma and a Fermi bubble plasma likely >0.3 keV. Our emission line ratio modeling correctly accounts for these plasmas, which is why we infer a hotter Fermi bubble plasma temperature than these studies ($kT_{FB,\ shell} \approx$ 0.4–0.5 keV).

A similar interpretation difference likely explains the emission measure analysis from K15, who claim bubble densities 3–4 times higher than our constraints. Their Fermi bubble geometric distribution includes only a shell component that is 2 kpc thick, while ours includes both a volume-filled and shell component. This implies our bubble+shell emission model has a longer path length along most sight lines near the bubbles compared to their model. The emission measure scales with density and path length as $EM \propto n^2 L$, so a longer inferred path length would lead to a lower inferred density than we suggest. We also point out their hot gas halo density model only extends to $r = 20$ kpc. While the hot halo emission is likely dominated by gas within $r \lesssim 25$ kpc, failing to account for emission at further radii can decrease the amount of modeled halo emission. This would lead to an over-estimated Fermi bubble emission contribution, and thus density, in order to match the total observed emission. Therefore, our inferred densities are more accurate than those in K15 since our models account for all possible emission sources.

6.7.4.2 Kinematic Estimates from UV Absorption Lines

A different approach to constrain the Fermi bubble kinematics involve UV absorption line analysis near background quasars. Fox et al. (2015) observed the quasar PDS 456 ($l, b = 10.4°, 11.2°$) with the Cosmic Origins Spectrograph on board the *Hubble Space Telescope*. The 1133–1778 Å spectrum covers several ionic species in-

dicative of gas with $T \sim 10^4$–10^5 K, including Si II , Si III , Si IV , C II , C IV , and N V . They detect multiple absorption components for each species, however they argue the near symmetric components at v_{LSR} = -235 km s^{-1} and +250 km s^{-1} are unlikely to come from absorbers in the disk or farther in the halo. If these absorbers represent material entrained gas near the bubble edges, their velocities can be used to constrain the bubble kinematics. Indeed, the authors apply a Galactic wind model from Bordoloi et al. (2014) to simulate v_{LSR} absorbers and find an intrinsic outflow velocity of $\geq$900 km s^{-1} is required to reproduce the observed absorption features.

There is tension between these results and our lower inferred expansion rate of $\approx$500 km s^{-1}. Although we infer a higher expansion rate than Kataoka et al. (2015), they discuss this discrepancy as well. The outflow model used by Fox et al. (2015) has two important parameters, the outflow velocity and the opening angle. They assume an opening angle of 110° to match the hard X-ray arcs seen by Bland-Hawthorn & Cohen (2003). However, this geometry produces a significant correction between the intrinsic outflow velocity and v_{LSR} at low latitudes. Their model implies that most of the bubble velocity at $l, b \approx 10°, 10°$ is tangential to the line of sight, which may not be the case. If instead the bubbles have a rounder surface at lower z or a stronger outflow velocity vector away from the Galaxy's polar axis, a lower intrinsic velocity could reproduce the observed absorption. Thus, the unknown intrinsic bubble geometry plausibly accounts for the different expansion velocities inferred from these two methodologies.

6.7.4.3 Comparing with Simulations

The Fermi bubble have motivated numerous simulations of Galactic outflows since their discovery. Typically, these studies primarily focus on the gamma-ray source, which is tied to the underlying cosmic ray composition (leptonic or hadronic) and where the cosmic rays are produced (injected from the central source, accelerated in-

situ, etc.). All of these simulations predict various distributions for the non-thermal and thermal gas within the bubbles, but information on the latter is often not discussed in detail. This limits our comparison to characteristic densities, velocities, and energetics, although our results are initial steps toward constraining these properties.

Simulations are also generally segregated by the assumed energy source, either a black hole accretion event or nuclear star formation. There is much variation with the assumed outflow parameters, but black hole accretion simulations tend to be more energetic on shorter time scales than star formation simulations. For example, simulations producing the bubbles with AGN jets have characteristic total energy injection rates and ages of $\gtrsim 10^{44}$ erg s^{-1} and $\approx$1-3 Myr (e.g., Guo & Mathews, 2012; Guo et al., 2012; Yang et al., 2012, 2013), whereas simulations producing the bubbles from weaker AGN winds suggest values between 10^{41}–10^{42} erg s^{-1} and 5–10 Myr (e.g., Mou et al., 2014, 2015). Alternatively, nuclear star formation simulations can reproduce the bubble morphology with energy injection rates between $\approx$1–5$\times10^{40}$ erg s^{-1} over $\gtrsim$50 Myr timescales (e.g., Crocker et al., 2014, 2015; Sarkar et al., 2015). The AGN simulations also tend to predict stronger outflow velocities than star formation simulations ($\gtrsim$1000 km s^{-1} compared to $\lesssim$500 km s^{-1}).

Our inferred energy injection rate, bubble age, and expansion velocity are most consistent with the weaker black hole accretion simulations, where the bubbles are inflated by an AGN wind (Mou et al., 2014, 2015). AGN jet simulations predict higher energy input rates than our results, while star formation simulations are typically weaker and over a much longer timescale than our constraints. It is difficult to make stronger claims at this point since these simulations are subject to a number of uncertainties. For example, the energy injection rate required to match the bubble morphology is degenerate with the surrounding medium density since it opposes the ram pressure from the galactic wind. Most simulations assume an ambient density comparable to our core density ($\sim 10^{-3}$ cm^{-3}), but this is a well-documented degen-

eracy in the simulations. Regardless of these limitations, our constraints should be used to motivate future simulations designed to analyze the bubbles.

Our thermal pressure constraints also address the bubbles' cosmic ray composition and whether thermal or non-thermal pressure drives the bubbles' expansion. Simulations can produce the bubbles' gamma-ray and microwave emission by accelerating either leptonic or hadronic cosmic rays, leading to uncertainties in the inferred non-thermal pressure (cosmic rays and magnetic fields). For example, the leptonic AGN jet simulations from Yang et al. (2013) predict a total pressure inside the bubbles of $\sim 10^{-10}$ dyne cm^{-2} and a cosmic ray pressure of $\sim 10^{-12}$ dyne cm^{-2}. This implies that the bubbles are either dominated by a thermal gas pressure much larger than our estimates (magnetic pressure is negligible), or an additional hadronic cosmic ray source could contribute most of the pressure. The former scenario is consistent with nuclear star formation simulations that accelerate cosmic ray leptons (Sarkar et al., 2015) or hadrons (Crocker et al., 2015). Alternatively, limits from hard X-ray spectra near the bubbles imply a cosmic ray electron and magnetic pressure of $\approx 2 \times 10^{-12}$ dyne cm^{-2} (Kataoka et al., 2013), which is approximately equal to the (K15) thermal pressure estimate. Our constrained thermal gas pressure range of 5–20$\times 10^{-13}$ dyne cm^{-2} should be used in future modeling work to build a more accurate census of the bubbles' energy and pressure budget.

6.8 Conclusions

This work is a comprehensive observational analysis of the Fermi bubbles at soft X-ray energies. The O VII and O VIII emission line sample includes data from *XMM-Newton* and *Suzaku*, with 741 sight lines in total and $\sim$ 100 sight lines projected near the Fermi bubbles. The new *Suzaku* measurements were processed in a similar way to the *XMM-Newton* measurements, making this the largest emission line sample designed to probe Galactic-scale hot gas distributions.

We used this sample to model the Fermi bubbles' thermal gas emission, resulting in significantly improved constraints on the bubbles' physical properties and their role in the Milky Way's evolution. Our modeling procedure is similar to previous studies at soft X-ray energies (Kataoka et al., 2013, 2015; Tahara et al., 2015), but we find systematic differences in the inferred gas temperature and expansion rate. This is likely due to different interpretations of how the other known X-ray emission sources, specifically the hot halo, contribute to the observed spectra. Our hot gas halo and Fermi bubble models correctly account for all the soft X-ray emission expected to exist in current observations. Thus, these are the most accurate constraints on the Fermi bubbles' thermal gas distribution given the data currently available.

We summarize our primary conclusions and inferred bubble properties:

1. The observed O VIII/O VII ratios are systematically larger for sight lines near the bubbles, suggesting the presence of a plasma with $T > 2 \times 10^6$ K.

2. Our best-fit parametric model implies $n_{FB} = 8.2 \pm 0.2 \times 10^{-4}$ cm^{-3}, $n_{shell} = 10.0 \pm 0.3 \times 10^{-4}$ cm^{-3}, $\log(T_{FB}) = 6.60$–6.65, and $\log(T_{shell}) = 6.60$–6.95 with an optimal value of 6.70. This involves explicitly fitting the O VIII line intensities and analyzing the O VIII/O VII ratio distribution near the bubbles.

3. These densities imply thermal gas masses within the bubble and shell volumes of $M_{FB} = 4.6$–5.0×10^6 $M_\odot$ and $M_{shell} = 5.2$–9.8×10^6 $M_\odot$. We interpret this as predominantly shock-heated hot gas halo material.

4. The inferred bubble/shell temperature (5×10^6 K) compared to ambient halo gas temperature (2×10^6 K) suggests a shock Mach number and expansion rate of $\mathcal{M} = 2.3^{+1.1}_{-0.4}$ and $v_{exp} = 490^{+230}_{-77}$ km s^{-1}. These are larger than the values suggested from other soft X-ray modeling analyses (K15), and smaller than the value suggested by the UV absorption line analysis by (Fox et al., 2015). The

differences are likely explained by geometric assumptions for the latter, and modeling the hot gas halo emission for the former.

5. Treating the bubbles as a galactic outflow with Sedov-Taylor expansion solutions leads to an inferred energy injection rate and age of $2.3^{+5.1}_{-0.9} \times 10^{42}$ erg s^{-1} and $4.3^{+0.8}_{-1.4}$ Myr. These energetics and timescales suggest the bubbles likely formed from a Sgr A* accretion episode, as opposed to sustained nuclear star formation activity.

6. Our results are broadly consistent with predictions from MHD simulations of galactic outflows. The constrained energy injection rate and age are most consistent with simulations that generate the bubbles from a relatively weak AGN wind (Mou et al., 2014, 2015).

This analysis is an initial effort to constrain the Fermi bubbles' thermal gas structure using soft X-ray observations, but it should also motivate future observational and theoretical studies. Future analyses using additional spectral data or all-sky maps from MAXI or eROSITA will help probe the bubbles' structure and interaction with the surrounding medium. The results should also motivate future simulations that predict characteristic bubble densities, temperatures, pressures, and expansion rates.

CHAPTER VII

Concluding Remarks

7.1 Discussion of Results

The results from this dissertation have significantly improved our understanding of the Milky Way's hot gas structure. This includes the first comprehensive analysis on all-sky samples of oxygen absorption and emission lines that directly trace million degree gas in the Milky Way. Modeling the all-sky line strength distributions, as opposed to individual sight lines, leads to reliable inferences regarding the global hot gas distribution. The results include significantly improved constraints on the Milky Way's hot gas density and kinematic structure, as well as the relationship between the Fermi bubbles and this medium. The most important results are discussed below.

7.1.1 Galactic Hot Gas Structure

The collective works in this dissertation are a significant improvement over previous studies on the Milky Way's hot gas structure due to the observation samples and modeling methodology. Prior to this work, studies on hot gas in the Milky Way typically focused on an individual sight line or $\lesssim$20 sight lines in either emission or absorption, but not both. This led to uncertainties in the hot gas structure, since measurements in these small samples could not rule out models with significantly different functional forms. Data mining projects on archival *Chandra*, *XMM-Newton*,

and *Suzaku* observations have since extracted line strength measurements covering the entire sky. The ≈30 O VII absorption line measurements (Bregman & Lloyd-Davies, 2007) and ≈1000 O VII and O VIII emission line measurements (Henley & Shelton, 2012) are powerful datasets because different types of models predict distinct line strength variations on the sky. Thus, modeling these all-sky distributions constrains the Milky Way's *global* hot gas distribution with much more certainty than models from individual sight lines.

A self-consistent density model for both the absorption and emission lines is also an important aspect of this dissertation, since it provides a reliable comparison for the absorption and emission line observations. The absorption and emission lines are presumably produced by the same plasma sources, but previous studies often made different assumptions for the plasma optical depth, metallicity, and intrinsic structure depending on whether absorption or emission line strengths were the primary observable. These different approaches led to systematic biases in the inferred hot gas properties. The models in this work incorporate the same assumptions to predict the absorption and emission expected from a given density profile, so the absorption and emission model fitting results are directly comparable.

The absorption line modeling from Miller & Bregman (2013) and emission line modeling from Miller & Bregman (2015) independently find that a low density, spherical hot gas profile extending to r_{vir} best matches the observed line strengths. These results are critical for two reasons. First, a single hot gas model, regardless of the functional form, explains both the O VII absorption and O VIII emission line observations. Thus, the observed line strengths are consistent with each other. Second, both datasets independently verify the type of hot gas distribution is a spherical, extended corona that formed during the Milky Way's formation. This spherical, extended distribution dominates the hot gas absorption and emission, and rules out a disk-like morphology for the dominant hot gas component. This opposes several pre-

vious works that successfully modeled line strengths in *individual* sight lines with a flatter, disk-like hot gas morphology (Yao & Wang, 2005; Yao et al., 2009b; Hagihara et al., 2010), however the all-sky samples and consistent modeling approach produce reliable constraints on the Milky Way's *global* hot gas distribution.

The O VIII emission line observations provide the best constraints on the hot gas density distribution beyond the Local Bubble, and the modeling in Miller & Bregman (2015) results in a best-fit model with $n \propto r^{-3\beta}$ and $\beta = 0.50 \pm 0.03$. The inferred β value is interesting for several reasons. This density slope is consistent with measured hot halo X-ray surface brightness profiles around massive spiral galaxies (Anderson & Bregman, 2011; Dai et al., 2012; Bogdán et al., 2013b,a; Anderson et al., 2016), as well as predicted hot halo profiles from galaxy formation simulations (e.g., Nuza et al., 2014). The inferred hot halo entropy profile ($S = kTn_e^{2/3}$) is also consistent with entropy profiles observed in galaxy groups and clusters (e.g., Walker et al., 2012; Panagoulia et al., 2014), as opposed to a constant entropy profile with more hot gas mass (Maller & Bullock, 2004; Fang et al., 2013). Finally, a spherical hot gas density profile with β exactly equal to 0.5 is expected if the gas is in hydrostatic equilibrium with the dark matter potential well. These results strengthen our current picture of hot gas halo formation in $L \gtrsim L^*$ galaxies, assuming the Milky Way is a typical galaxy, and produce meaningful constraints on additional hot gas quantities.

Extrapolating the hot gas density profile to the Milky Way's virial radius (250 kpc) results in a characteristic hot gas mass between 2–5$\times10^{10}$ $M_\odot$. Prior to this work, the Milky Way's hot gas mass estimates ranged between 10^8–10^{11} $M_\odot$ depending on the inferred structure (e.g., Fang et al., 2013). This uncertainty was important since the Milky Way is missing $\approx2\times10^{11}$ $M_\odot$ of baryonic mass compared to the cosmological baryon fraction, so it was unclear whether hot gas in the Galaxy could account for the missing mass. The results here indicate the hot gas mass is comparable to the Milky Way's stellar and neutral gas mass (6–7$\times10^{10}$ $M_\odot$), but it does not account

for all of the Milky Way's missing baryons. The hot gas profile would need to extend to 3–5r_{vir} to account for the missing baryon mass, and there is evidence for extended hot halos from a *Planck* Sunyaev-Zeldovich stacking analysis (Planck Collaboration et al., 2013).

Several lines of evidence indicate the gas metallicity is sub-solar, with a lower limit of $0.3Z_{\odot}$. The residual hot gas pulsar dispersion (DM) measure between the Sun and the LMC is 23 cm^{-23} pc (Anderson & Bregman, 2010; Fang et al., 2013). The dispersion measure and metallicty are related as DM $\propto Z^{-1}$, and model profile constraints indicate that the hot gas metallicity must be $\geq 0.3Z_{\odot}$ to be consistent with the observed dispersion measure. A metallicity of $0.3Z_{\odot}$ results in a model 0.5–2.0 keV band luminosity between 1–5$\times10^{39}$ erg s^{-1}, which is consistent with models for the *ROSAT* 3/4 keV band emission (Snowden et al., 1997; Wang, 1998). This sub-solar metallicity is also broadly consistent with simulations of hot halos around L^{*} galaxies (Toft et al., 2002; Cen & Ostriker, 2006; Cen, 2012).

This dissertation also includes one of the first studies on the Milky Way's hot gas kinematic structure and observational signatures. The kinematic absorption line modeling in Miller et al. (2016) is analogous to previous studies on neutral H I and UV absorption line kinematics (Westerhout, 1957; Savage et al., 2003), but the observational signatures of velocity flows in an extended hot gas halo have not been considered until now. Potential bulk motions include rotation similar to the Milky Way's disk, accretion/inflow of cooling halo gas, or hot gas outflows from the disk. The intrinsic line structures and centroids encode information on these kinematic motions, the plasma optical depth, and amount of turbulent motions present in the gas. The line structures are not resolved with current X-ray telescopes, but line centroid deviations from $v_{LSR} = 0$ km s^{-1} are measured in high signal-to-noise observations.

The kinematic absorption line modeling in Miller et al. (2016) combined with the observed O VII absorption line centroid distribution from Hodges-Kluck et al.

(2016) indicate there are bulk velocity flows present in the Milky Way's hot gas distribution. The latter study measured O VII absorption line centroids in 37 sight lines, and determined that the line centroid variation on the sky is inconsistent with a stationary hot gas distribution relative to the Galactic Standard of Rest. Using the models described in Miller et al. (2016), the best fit is a rotating hot gas model with a flat rotation curve of $v_\phi = 183 \pm 41$ km s^{-1}. This indicates that the hot gas lags behind the baryons in the disk (v_ϕ between 220–240 km s^{-1}), and also contains comparable angular momentum to the stellar disk. This is an important result for galaxy formation simulations since there are few observational studies of $\sim 10^6$ K gas kinematics in galaxies similar to the Milky Way (Marinacci et al., 2011). The combined efforts in Miller et al. (2016) and Hodges-Kluck et al. (2016) should be considered an original analysis in this field with implications for hot gas dynamics in galaxy formation.

7.1.2 The Fermi Bubbles

The Fermi bubble analysis is the most comprehensive work on the bubbles in soft X-rays, and provides the most accurate constraints on bubbles' thermal gas distribution. The emission line sample contains 683 archival *XMM-Newton* observations across the sky from Henley & Shelton (2012), along with 58 archival *Suzaku* observations projected through the bubbles that were specifically analyzed for this study. The overall methodology presented in this analysis is similar to previous works modeling X-ray spectra near the bubbles (Kataoka et al., 2013, 2015; Tahara et al., 2015), but these do not account for hot gas halo emission in their spectral fitting procedure. This leads to an underestimated Fermi bubble thermal gas temperature and overestimated thermal gas density. We expand on the hot gas halo models from Miller & Bregman (2015) to account for all the known soft X-ray emission sources present in the observations, including the hot gas halo, a volume-filled bubble component, and

a shell of compressed material surrounding the bubbles.

The best-fit model results include characteristic bubble thermal gas densities and temperatures of $n \approx 1 \times 10^{-3}$ cm^{-3} and $\log(T) = 6.60$–6.70. The densities imply a total thermal gas mass between 5–10$\times 10^6$ $M_\odot$ inside the bubbles, which is consistent with the inferred hot CGM mass that would exist in that volume if the bubbles did not exist. The bubble temperature compared to the surrounding hot halo temperature ($\log(T_{halo}) = 6.30$) indicates that the bubbles' expansion is supersonic with a Mach number between 1.9–3.4 and $v_{exp} = 490^{+230}_{-77}$ km s^{-1}. This is higher than the inferred shock strength from the Kataoka et al. (2015) analysis ($v_{exp} \approx$300 km s^{-1}), although their emission model likely underestimates the true bubble temperature. The densities, temperatures, and shock properties presented here are a significant improvement over previous estimates.

Treating the bubbles as a continuous galactic wind yields independent bubble age and energy input rate estimates. Given constraints on the ambient medium density, bubble geometry, and expansion rate discussed above, the Sedov-Taylor self-similar solutions for expanding bubbles provide estimates for the bubbles' energy input rate and age (e.g., Veilleux et al., 2005). In this framework, the modeling results yield a bubble age and energy input rate of $4.3^{+0.8}_{-1.4}$ Myr and $2.3^{+5.1}_{-0.9} \times 10^{42}$ erg s^{-1}. These estimates are important because Galactic outflow MHD simulations predict a wide range of bubble ages, energy input rates, and expansion rates, with nuclear starburst simulations typically being less energetic over a longer inflation time ($\dot{E} \approx$1–5$\times 10^{40}$ erg s^{-1}, $t_{age} \gtrsim$50 Myr), and AGN simulations being more energetic over a shorter inflation time ($\gtrsim 10^{41}$ erg s^{-1}, $t_{age} \lesssim$10 Myr) (e.g., Guo & Mathews, 2012; Yang et al., 2012; Mou et al., 2014; Crocker et al., 2015). The prior uncertainty in the bubble energetics permitted multiple possible origin scenarios, but these results rule out several outflow models.

The bubble age and energy input rates presented here combined with Galactic

center activity over the past ≈20 Myr provide a valuable constraint on the bubbles' origins. The average Galactic center star formation rate over the past 20 Myr has been $\approx 0.08\ M_{\odot}\ \mathrm{yr}^{-1}$ (e.g., Yusef-Zadeh et al., 2009). This implies an average mechanical energy input rate of $\approx 6 \times 10^{39}$ erg s^{-1}, which is significantly lower than the inferred energy input rate from the new thermal gas constraints. Alternatively, Sgr A* was likely more active in the past than its current quiescent state, with accretion rates possibly as high as $10^{-3}\ M_{\odot}\ \mathrm{yr}^{-1}$ (Totani, 2006). Converting this accretion rate into a mechanical luminosity indicates that an accretion event can match the measured energy input rate for a mechanical feedback efficiency of 5%. Thus, the energetic constraints from this work indicate that the bubbles likely formed as a result of a Sgr A* accretion event, as opposed to prolonged nuclear star formation activity.

7.2 Future Work

While this work has produced a clearer picture for the Milky Way's hot gas structure, there are several topics that can be explored with a combination of current telescope facilities, future missions, improved modeling techniques, or specialized simulations. These topics include: the observed variation in the O VII emission line data, optical depth effects in the hot gas plasma, the ongoing interaction between the Fermi bubbles and hot gas halo, and the detailed hot gas kinematic structure. I discuss potential strategies to probe these topics below.

7.2.1 Analyses with Current Data and Telescopes

The stochastic variation seen in O VII emission line observations is currently unexplained, but a combination of X-ray shadowing experiments, temporal analyses, and hot ISM simulations will help solve this problem. The model fitting results in Miller & Bregman (2015) show that a single smooth plasma model (spherical halo or disk-like morphology) does not produce an acceptable fit to the O VII emission line

observations. This suggests the presence of an additional emission mechanism that varies spatially on the sky or temporally throughout the lifetimes of current X-ray telescopes. Plausible sources that could produce more O VII than O VIII include time-varying solar wind charge exchange (SWCX) reactions or a combination of the Local Bubble (LB) and local hot ISM. Shadowing observations toward molecular clouds with known distances are the only direct probe for non-halo SXRB emission. The largest X-ray shadowing experiment sample consists of seven fields (Henley & Shelton, 2015), which is not large enough to provide robust constraints on the observed variation. Increasing this sample with more on-cloud and off-cloud observations would provide more stringent limits on the O VII emission from non-halo sources. Determining whether the emission line intensities in this sample vary with time (on hourly, daily, or yearly timescales) would reveal whether SWCX or the LB creates most of the emission. If the emission correlates with overall solar activity, solar wind proton flux, or observing direction relative to the magnetosheath, then SWCX is an important emission component. If SWCX does not dominate the O VII line emission, then the LB or local hot ISM is the most plausible explanation. Simulations of a hot, turbulent ISM driven by supernova explosions predict pockets of $\sim 10^6$ K gas $\sim$100 pc in size, which are similar to the LB morphology (e.g., de Avillez & Breitschwerdt, 2012). X-ray emission from the local ISM varies across the sky (e.g., Kuntz & Snowden, 2000), but it is unclear how this observed "patchiness" relates to the formation and energetics of the Milky Way's hot ISM. A systematic comparison between emission predicted from simulations and the observed O VII line emission (from either on-cloud observations or the large sample that currently exists) may explain the spatial emission variation.

The plasma optical depth is also still unknown due to the weakly constrained Doppler b parameter (Williams et al., 2005; Fang et al., 2015), but radiative transfer codes with joint absorption and emission line fitting can improve these constraints.

The Doppler b value is difficult to constrain with current X-ray observations because the absorption line profiles are not resolved and there are only three weak detections of the O VII $K\beta$ transition (18.63 Å) to compare with the dominant $K\alpha$ line. This leads to systematic uncertainties in the halo gas structure since the b value impacts the conversion between absorption line equivalent widths and column densities, as well as the emission line radiative transfer equation. A useful tool to solve this problem will be a Monte Carlo Radiative Transfer (MCRT) code designed for our location in the Milky Way and the extended gas geometry (e.g., Whitney, 2011). This type of radiative transfer code defines a source function for a gas density profile and Doppler b parameter, and would produce radiation field maps for a given set of parameters. The model column densities and radiation field could then be converted to equivalent widths and line intensities to compare with the observed line strengths. By jointly fitting the absorption and emission line samples with this type of code, one would obtain improved density profile constraints along with an average Doppler b value. This would be an improvement over the works presented in this dissertation, which either assume the plasma is optically thin or assume a Doppler b value to compare with the optically thin case.

There are also several theoretical and observational projects that will further constrain the Fermi bubbles' energy budget and kinematics. The results presented in this dissertation constrain the average bubble thermal gas density and temperature, but simulations predict different thermal gas structures depending on the origin scenario and injected energy. A rigorous comparison between the results here and the model predictions will provide a coherent picture for the bubbles' pressure content and origins. An independent analysis with a larger sample of UV absorption line systems projected through the bubbles will also constrain the bubbles' expansion and mechanical energy. The tension between the inferred expansion rates here and the UV absorption line results from Fox et al. (2015) is likely due to the assumed bubble

geometry, which includes a significant LSR velocity correction at low Galactic latitudes. Additional UV sight lines projected through different bubble locations will provide tighter constraints on the bubbles expansion into the surrounding medium.

7.2.2 Observations with Future X-ray Telescopes

The next generation of all-sky X-ray maps will provide additional insight on the Milky Way's hot gas distribution and Fermi bubbles, and be similar to *ROSAT's* impact. The Monitor of All-sky X-ray Image (MAXI; Tomida et al., 2000) satellite and eROSITA (Predehl et al., 2010) instrument are similar to *ROSAT* in many ways. Both are all-sky X-ray telescopes that will map the entire sky in the 0.5–2.0 keV band in addition to their other primary science objectives. eROSITA will be *ROSAT's* spiritual successor due to its improved spatial resolution and a 0.5–2.0 keV effective area $\sim$10 times greater than *ROSAT*. For example, angular emission variations in the softest energy bands are valuable constraints on the LB emission (Kuntz & Snowden, 2000). All-sky maps are also valuable tools for probing the Fermi bubbles' interaction with the hot halo. The northern Fermi bubble appears to be bounded by enhanced 1.7–4.0 keV band emission seen in MAXI data, suggesting there is a region of shocked-heated, compressed material at the northern cap. MAXI and eROSITA will be valuable resources that improve our picture of hot gas in the Milky Way, and will motivate future spectroscopic observations.

Progress with future X-ray spectrographs depends on improved spectral resolution and collecting area between 0.5–2.0 keV compared to current X-ray telescopes. The product of these factors determines how efficiently absorption lines can be detected. This improved total sensitivity will yield detections of weaker absorption lines, possibly associated with hot halos around external galaxies, while improved resolution will constrain the plasma optical depth and velocity structure. Unfortunately, the planned X-ray missions to succeed current telescopes will not have improved resolu-

tion or sensitivity below 2 keV compared to the LETG or the RGS. For example, *Athena's* microcalorimeter will have a comparable spectral resolution to the RGS near 0.6 keV ($\Delta v \approx 1000$ km s^{-1}; den Herder et al., 2012), which is much larger than the expected line widths ($\lesssim$300 km s^{-1}). Significant progress in this field requires an X-ray spectrograph with $R \approx 3000$ to begin resolving the line profiles and detecting extragalactic hot halos in absorption. Fortunately, technology exists for such a spectrograph (*ARCUS*; Smith et al., 2014b), and its eventual launch would provide significantly improved absorption line data compared to current observations.

7.3 Final Comments

This dissertation answers fundamental questions on the Milky Way's structure and about the bigger picture of how galaxies form. The original prediction of a long-lived, hot gaseous medium in the Milky Way from Spitzer (1956) is observationally difficult to verify. This is largely due to the technical challenges of X-ray observations and because of our location inside the Milky Way. There are now all-sky samples of O VII and O VIII absorption and emission line strengths from numerous archival data analysis projects (Bregman & Lloyd-Davies, 2007; Henley & Shelton, 2012; Fang et al., 2015). The work here models these observations in a way that accounts for our perspective in the disk to constrain the Milky Way's global hot gas distribution. The data indicate the Milky Way indeed hosts a spherical hot gas halo, which is consistent with theoretical predictions of galaxy formation.

I also want to emphasize that the vast majority of this work relied on publicly available archival data. Most of the data used in this dissertation were essentially byproducts of observations with other primary scientific objectives. Important questions have been answered as a result of these data products, which emphasizes the power contained in archival data.

BIBLIOGRAPHY

BIBLIOGRAPHY

Ackermann, M., Albert, A., Atwood, W. B., et al. 2014, ApJ, 793, 64

Anders, E., & Grevesse, N. 1989, Geochim. Cosmochim. Acta, 53, 197

Anderson, M. E., & Bregman, J. N. 2010, ApJ, 714, 320

—. 2011, ApJ, 737, 22

Anderson, M. E., Bregman, J. N., & Dai, X. 2013, ApJ, 762, 106

Anderson, M. E., Churazov, E., & Bregman, J. N. 2016, MNRAS, 455, 227

Arnaud, K. A. 1996, in Astronomical Society of the Pacific Conference Series, Vol. 101, Astronomical Data Analysis Software and Systems V, ed. G. H. Jacoby & J. Barnes, 17

Asplund, M., Grevesse, N., & Sauval, A. J. 2005, in Astronomical Society of the Pacific Conference Series, Vol. 336, Cosmic Abundances as Records of Stellar Evolution and Nucleosynthesis, ed. T. G. Barnes, III & F. N. Bash, 25

Asplund, M., Grevesse, N., Sauval, A. J., & Scott, P. 2009, ARA&A, 47, 481

Baganoff, F. K., Maeda, Y., Morris, M., et al. 2003, ApJ, 591, 891

Bailin, J., & Steinmetz, M. 2005, ApJ, 627, 647

Balucinska-Church, M., & McCammon, D. 1992, ApJ, 400, 699

Barnabè, M., Ciotti, L., Fraternali, F., & Sancisi, R. 2006, A&A, 446, 61

Begelman, M. C., & Fabian, A. C. 1990, MNRAS, 244, 26P

Bernardi, M., Sheth, R. K., Nichol, R. C., Schneider, D. P., & Brinkmann, J. 2005, AJ, 129, 61

Bhattacharjee, P., Chaudhury, S., & Kundu, S. 2014, ApJ, 785, 63

Binney, J., & Tremaine, S. 2008, Galactic Dynamics: Second Edition (Princeton University Press)

Bland-Hawthorn, J., & Cohen, M. 2003, ApJ, 582, 246

Bland-Hawthorn, J., Maloney, P. R., Sutherland, R. S., & Madsen, G. J. 2013, ApJ, 778, 58

Blitz, L., & Robishaw, T. 2000, ApJ, 541, 675

Bogdán, Á., Forman, W. R., Kraft, R. P., & Jones, C. 2013a, ApJ, 772, 98

Bogdán, Á., Forman, W. R., Vogelsberger, M., et al. 2013b, ApJ, 772, 97

Bogdán, Á., Vogelsberger, M., Kraft, R. P., et al. 2015, ApJ, 804, 72

Borch, A., Meisenheimer, K., Bell, E. F., et al. 2006, A&A, 453, 869

Bordoloi, R., Lilly, S. J., Kacprzak, G. G., & Churchill, C. W. 2014, ApJ, 784, 108

Bovy, J., Hogg, D. W., & Rix, H.-W. 2009, ApJ, 704, 1704

Bovy, J., & Rix, H.-W. 2013, ApJ, 779, 115

Bowen, D. V., Jenkins, E. B., Tripp, T. M., et al. 2008, ApJS, 176, 59

Boylan-Kolchin, M., Bullock, J. S., Sohn, S. T., Besla, G., & van der Marel, R. P. 2013, ApJ, 768, 140

Bregman, J. N. 1980, ApJ, 237, 681

Bregman, J. N., Alves, G. C., Miller, M. J., & Hodges-Kluck, E. 2015, Journal of Astronomical Telescopes, Instruments, and Systems, 1, 045003

Bregman, J. N., & Houck, J. C. 1997, ApJ, 485, 159

Bregman, J. N., & Lloyd-Davies, E. J. 2007, ApJ, 669, 990

Brinkmann, W., Yuan, W., & Siebert, J. 1997, A&A, 319, 413

Brunthaler, A., Reid, M. J., Menten, K. M., et al. 2011, Astronomische Nachrichten, 332, 461

Burton, W. B. 1976, ARA&A, 14, 275

Carter, J. A., & Sembay, S. 2008, A&A, 489, 837

Carter, J. A., Sembay, S., & Read, A. M. 2010, MNRAS, 402, 867

—. 2011, A&A, 527, A115

Cash, W. 1979, ApJ, 228, 939

Castor, J., McCray, R., & Weaver, R. 1975, ApJ, 200, L107

Cen, R. 2012, ApJ, 753, 17

Cen, R., & Ostriker, J. P. 2006, ApJ, 650, 560

Chen, L.-W., Fabian, A. C., & Gendreau, K. C. 1997, MNRAS, 285, 449

Cheng, K. S., Chernyshov, D. O., Dogiel, V. A., & Ko, C. M. 2015, ApJ, 804, 135

Cheng, K.-S., Chernyshov, D. O., Dogiel, V. A., Ko, C.-M., & Ip, W.-H. 2011, ApJ, 731, L17

Coil, A. L., Weiner, B. J., Holz, D. E., et al. 2011, ApJ, 743, 46

Costantini, E., Pinto, C., Kaastra, J. S., et al. 2012, A&A, 539, A32

Cox, D. P., & Reynolds, R. J. 1987, ARA&A, 25, 303

Cox, D. P., & Smith, B. W. 1974, ApJ, 189, L105

Crain, R. A., McCarthy, I. G., Frenk, C. S., Theuns, T., & Schaye, J. 2010, MNRAS, 407, 1403

Cravens, T. E., Robertson, I. P., & Snowden, S. L. 2001, J. Geophys. Res., 106, 24883

Crocker, R. M. 2012, MNRAS, 423, 3512

Crocker, R. M., Bicknell, G. V., Carretti, E., Hill, A. S., & Sutherland, R. S. 2014, ApJ, 791, L20

Crocker, R. M., Bicknell, G. V., Taylor, A. M., & Carretti, E. 2015, ApJ, 808, 107

Dai, X., Anderson, M. E., Bregman, J. N., & Miller, J. M. 2012, ApJ, 755, 107

de Avillez, M. A., & Breitschwerdt, D. 2012, ApJ, 761, L19

de Avillez, M. A., Breitschwerdt, D., Asgekar, A., & Spitoni, E. 2013, ArXiv e-prints, arXiv:1301.2890

de Avillez, M. A., & Mac Low, M.-M. 2001, ApJ, 551, L57

de Blok, W. J. G., Walter, F., Brinks, E., et al. 2008, AJ, 136, 2648

de Vries, C. P., den Herder, J. W., Gabriel, C., et al. 2015, A&A, 573, A128

den Herder, J. W., Bagnali, D., Bandler, S., et al. 2012, Proc. SPIE, 8443, 2

den Herder, J.-W. W., Brinkman, A. C., Kahn, S. M., et al. 2003, Proc. SPIE, 4851, 196

Diehl, S., & Statler, T. S. 2007, ApJ, 668, 150

Dobler, G., & Finkbeiner, D. P. 2008, ApJ, 680, 1222

Dobler, G., Finkbeiner, D. P., Cholis, I., Slatyer, T., & Weiner, N. 2010, ApJ, 717, 825

Drake, G. W. 1988, Canadian J. Phys., 66, 586

Dunkley, J., Komatsu, E., Nolta, M. R., et al. 2009, ApJS, 180, 306

Ezoe, Y., Ebisawa, K., Yamasaki, N. Y., et al. 2010, PASJ, 62, 981

Ezoe, Y., Miyoshi, Y., Yoshitake, H., et al. 2011, PASJ, 63, S691

Faerman, Y., Sternberg, A., & McKee, C. F. 2016, ArXiv e-prints, arXiv:1602.00689

Fang, T., Bullock, J., & Boylan-Kolchin, M. 2013, ApJ, 762, 20

Fang, T., Buote, D., Bullock, J., & Ma, R. 2015, ApJS, 217, 21

Fang, T., & Jiang, X. 2014, ApJ, 785, L24

Fang, T., Marshall, H. L., Lee, J. C., Davis, D. S., & Canizares, C. R. 2002, ApJ, 572, L127

Fang, T., Mckee, C. F., Canizares, C. R., & Wolfire, M. 2006, ApJ, 644, 174

Feldmann, R., Hooper, D., & Gnedin, N. Y. 2013, ApJ, 763, 21

Figer, D. F., Rich, R. M., Kim, S. S., Morris, M., & Serabyn, E. 2004, ApJ, 601, 319

Finoguenov, A., Ponman, T. J., Osmond, J. P. F., & Zimer, M. 2007, MNRAS, 374, 737

Foreman-Mackey, D., Hogg, D. W., Lang, D., & Goodman, J. 2013, PASP, 125, 306

Foreman-Mackey, D., Vousden, W., Price-Whelan, A., et al. 2016, corner.py: corner.py v1.0.2, doi:10.5281/zenodo.45906

Forman, W., Jones, C., & Tucker, W. 1985, ApJ, 293, 102

Foster, A. R., Ji, L., Smith, R. K., & Brickhouse, N. S. 2012, ApJ, 756, 128

Fox, A. J., Savage, B. D., Wakker, B. P., et al. 2004, ApJ, 602, 738

Fox, A. J., Wakker, B. P., Savage, B. D., et al. 2005, ApJ, 630, 332

Fox, A. J., Bordoloi, R., Savage, B. D., et al. 2015, ApJ, 799, L7

Fraternali, F., & Binney, J. J. 2008, MNRAS, 386, 935

Fujimoto, R., Mitsuda, K., Mccammon, D., et al. 2007, PASJ, 59, 133

Fujita, Y., Ohira, Y., & Yamazaki, R. 2014, ApJ, 789, 67

Fukugita, M., & Peebles, P. J. E. 2006, ApJ, 639, 590

Gaensler, B. M., Madsen, G. J., Chatterjee, S., & Mao, S. A. 2008, PASA, 25, 184

Galeazzi, M., Gupta, A., Covey, K., & Ursino, E. 2007, ApJ, 658, 1081

Galeazzi, M., Chiao, M., Collier, M. R., et al. 2014, Nature, 512, 171

Gatto, A., Fraternali, F., Read, J. I., et al. 2013, MNRAS, 433, 2749

Ghez, A. M., Duchêne, G., Matthews, K., et al. 2003, ApJ, 586, L127

Ghez, A. M., Salim, S., Weinberg, N. N., et al. 2008, ApJ, 689, 1044

Gibson, B. K., Giroux, M. L., Penton, S. V., et al. 2000, AJ, 120, 1830

Gillessen, S., Eisenhauer, F., Fritz, T. K., et al. 2009a, ApJ, 707, L114

Gillessen, S., Eisenhauer, F., Trippe, S., et al. 2009b, ApJ, 692, 1075

Gnat, O., & Sternberg, A. 2007, ApJS, 168, 213

Goodman, J., & Weare, J. 2010, Comm. App. Math. Comp. Sci., 5, 65

Gould, A., Bahcall, J. N., & Flynn, C. 1996, ApJ, 465, 759

Grcevich, J., & Putman, M. E. 2009, ApJ, 696, 385

Guo, F., & Mathews, W. G. 2012, ApJ, 756, 181

Guo, F., Mathews, W. G., Dobler, G., & Oh, S. P. 2012, ApJ, 756, 182

Gupta, A., Mathur, S., Galeazzi, M., & Krongold, Y. 2014, Ap&SS, 352, 775

Gupta, A., Mathur, S., Krongold, Y., Nicastro, F., & Galeazzi, M. 2012, ApJ, 756, L8

Hagihara, T., Yamasaki, N. Y., Mitsuda, K., et al. 2011, PASJ, 63, 889

Hagihara, T., Yao, Y., Yamasaki, N. Y., et al. 2010, PASJ, 62, 723

Hao, L., Strauss, M. A., Fan, X., et al. 2005, AJ, 129, 1795

Haslam, C. G. T., Salter, C. J., Stoffel, H., & Wilson, W. E. 1982, A&AS, 47, 1

Henley, D. B., & Shelton, R. L. 2010, ApJS, 187, 388

—. 2012, ApJS, 202, 14

—. 2013, ApJ, 773, 92

—. 2015, ApJ, 808, 22

Henley, D. B., Shelton, R. L., Kwak, K., Joung, M. R., & Mac Low, M.-M. 2010, ApJ, 723, 935

Hill, A. S., Joung, M. R., Mac Low, M.-M., et al. 2012, ApJ, 750, 104

Hodges-Kluck, E., & Bregman, J. N. 2014, ApJ, 789, 131

Hodges-Kluck, E. J., Miller, M. J., & Bregman, J. N. 2016, ApJ, 822, 21

Holweger, H. 2001, in American Institute of Physics Conference Series, Vol. 598, Joint SOHO/ACE workshop "Solar and Galactic Composition", ed. R. F. Wimmer-Schweingruber, 23–30

Hopkins, P. F., & Hernquist, L. 2006, ApJS, 166, 1

Hopkins, P. F., Richards, G. T., & Hernquist, L. 2007, ApJ, 654, 731

Huenemoerder, D. P., Mitschang, A., Dewey, D., et al. 2011, AJ, 141, 129

Immer, K., Schuller, F., Omont, A., & Menten, K. M. 2012, A&A, 537, A121

Ishikawa, K., Ezoe, Y., Miyoshi, Y., et al. 2013, PASJ, 65, doi:10.1093/pasj/65.3.63

Joung, M. K. R., & Mac Low, M.-M. 2006, ApJ, 653, 1266

Joung, M. R., Putman, M. E., Bryan, G. L., Fernández, X., & Peek, J. E. G. 2012, ApJ, 759, 137

Kacprzak, G. G., Churchill, C. W., & Nielsen, N. M. 2012, ApJ, 760, L7

Kaifu, N., Kato, T., & Iguchi, T. 1972, Nature Physical Science, 238, 105

Kalberla, P. M. W., Burton, W. B., Hartmann, D., et al. 2005, A&A, 440, 775

Kalberla, P. M. W., Dedes, L., Kerp, J., & Haud, U. 2007, A&A, 469, 511

Karataş, Y., Bilir, S., Eker, Z., & Demircan, O. 2004, MNRAS, 349, 1069

Kataoka, J., Tahara, M., Totani, T., et al. 2015, ApJ, 807, 77

—. 2013, ApJ, 779, 57

Kaufmann, T., Mayer, L., Wadsley, J., Stadel, J., & Moore, B. 2006, MNRAS, 370, 1612

Kent, S. M. 1987, AJ, 93, 816

Kereš, D., Katz, N., Fardal, M., Davé, R., & Weinberg, D. H. 2009, MNRAS, 395, 160

Keshet, U., Waxman, E., & Loeb, A. 2004, J. Cosmology Astropart. Phys., 4, 6

Klypin, A., Zhao, H., & Somerville, R. S. 2002, ApJ, 573, 597

Koutroumpa, D., Acero, F., Lallement, R., Ballet, J., & Kharchenko, V. 2007, A&A, 475, 901

Koutroumpa, D., Lallement, R., Kharchenko, V., et al. 2006, A&A, 460, 289

Koutroumpa, D., Smith, R. K., Edgar, R. J., et al. 2011, ApJ, 726, 91

Koyama, K., Maeda, Y., Sonobe, T., et al. 1996, PASJ, 48, 249

Koyama, K., Tsunemi, H., Dotani, T., et al. 2007, PASJ, 59, 23

Kroupa, P. 2001, MNRAS, 322, 231

Kuntz, K. D. 2009, in American Institute of Physics Conference Series, Vol. 1156, American Institute of Physics Conference Series, ed. R. K. Smith, S. L. Snowden, & K. D. Kuntz, 3–15

Kuntz, K. D., & Snowden, S. L. 2000, ApJ, 543, 195

—. 2008, A&A, 478, 575

Kwak, K., & Shelton, R. L. 2010, ApJ, 719, 523

Lacki, B. C. 2014, MNRAS, 444, L39

Lallement, R., Welsh, B. Y., Vergely, J. L., Crifo, F., & Sfeir, D. 2003, A&A, 411, 447

Larson, R. B. 1974, MNRAS, 169, 229

Lehner, N., Howk, J. C., Thom, C., et al. 2012, MNRAS, 424, 2896

Lei, S., Shelton, R. L., & Henley, D. B. 2009, ApJ, 699, 1891

Leitherer, C., Schaerer, D., Goldader, J. D., et al. 1999, ApJS, 123, 3

Leitner, S. N., & Kravtsov, A. V. 2011, ApJ, 734, 48

Li, J.-T., Li, Z., Wang, Q. D., Irwin, J. A., & Rossa, J. 2008, MNRAS, 390, 59

Li, J.-T., & Wang, Q. D. 2013a, MNRAS, 428, 2085

—. 2013b, MNRAS, 435, 3071

Loeb, A., Reid, M. J., Brunthaler, A., & Falcke, H. 2005, ApJ, 633, 894

Loebman, S. R., Ivezić, Ž., Quinn, T. R., et al. 2014, ApJ, 794, 151

Mac Low, M.-M., & McCray, R. 1988, ApJ, 324, 776

Mac Low, M.-M., McCray, R., & Norman, M. L. 1989, ApJ, 337, 141

Maeda, Y., Baganoff, F. K., Feigelson, E. D., et al. 2002, ApJ, 570, 671

Maller, A. H., & Bullock, J. S. 2004, MNRAS, 355, 694

Marinacci, F., Fraternali, F., Nipoti, C., et al. 2011, MNRAS, 415, 1534

Marinacci, F., Pakmor, R., Springel, V., & Simpson, C. M. 2014, MNRAS, 442, 3745

Marrone, D. P., Moran, J. M., Zhao, J.-H., & Rao, R. 2007, ApJ, 654, L57

Matković, A., & Guzmán, R. 2005, MNRAS, 362, 289

Mauerhan, J. C., Cotera, A., Dong, H., et al. 2010, ApJ, 725, 188

McCammon, D., Almy, R., Apodaca, E., et al. 2002, ApJ, 576, 188

McKee, C. F., & Ostriker, J. P. 1977, ApJ, 218, 148

McKernan, B., Yaqoob, T., & Reynolds, C. S. 2004, ApJ, 617, 232

McNamara, B. R., & Nulsen, P. E. J. 2007, ARA&A, 45, 117

Meiring, J. D., Tripp, T. M., Werk, J. K., et al. 2013, ApJ, 767, 49

Melioli, C., & de Gouveia Dal Pino, E. M. 2004, A&A, 424, 817

Ménard, B., Scranton, R., Fukugita, M., & Richards, G. 2010, MNRAS, 405, 1025

Mertsch, P., & Sarkar, S. 2011, Mem. Soc. Astron. Italiana, 82, 876

Mewe, R., Kaastra, J. S., & Liedahl, D. A. 1995, Legacy, 6, 16

Meyer, L., Ghez, A. M., Schödel, R., et al. 2012, Science, 338, 84

Miller, E. D., Tsunemi Hiroshi, Bautz, M. W., et al. 2008, PASJ, 60, 95

Miller, M. J., & Bregman, J. N. 2013, ApJ, 770, 118

—. 2015, ApJ, 800, 14

Miller, M. J., Hodges-Kluck, E. J., & Bregman, J. N. 2016, ApJ, 818, 112

Mo, H., van den Bosch, F. C., & White, S. 2010, Galaxy Formation and Evolution

Moretti, A., Campana, S., Lazzati, D., & Tagliaferri, G. 2003, ApJ, 588, 696

Mou, G., Yuan, F., Bu, D., Sun, M., & Su, M. 2014, ApJ, 790, 109

Mou, G., Yuan, F., Gan, Z., & Sun, M. 2015, ApJ, 811, 37

Murakami, H., Koyama, K., & Maeda, Y. 2001a, ApJ, 558, 687

Murakami, H., Koyama, K., Sakano, M., Tsujimoto, M., & Maeda, Y. 2000, ApJ, 534, 283

Murakami, H., Koyama, K., Tsujimoto, M., Maeda, Y., & Sakano, M. 2001b, ApJ, 550, 297

Navarro, J. F., Frenk, C. S., & White, S. D. M. 1997, ApJ, 490, 493

Nicastro, F., Senatore, F., Gupta, A., et al. 2016, MNRAS, 457, 676

Nicastro, F., Zezas, A., Drake, J., et al. 2002, ApJ, 573, 157

Nicastro, F., Zezas, A., Elvis, M., et al. 2003, Nature, 421, 719

Norman, C. A., & Ikeuchi, S. 1989, ApJ, 345, 372

Nuza, S. E., Parisi, F., Scannapieco, C., et al. 2014, MNRAS, 441, 2593

Okabe, N., Umetsu, K., Tamura, T., et al. 2014, PASJ, 66, 99

Oort, J. H. 1932, Bull. Astron. Inst. Netherlands, 6, 249

O'Sullivan, E., Ponman, T. J., & Collins, R. S. 2003, MNRAS, 340, 1375

Paerels, F. B. S., & Kahn, S. M. 2003, ARA&A, 41, 291

Panagoulia, E. K., Fabian, A. C., & Sanders, J. S. 2014, MNRAS, 438, 2341

Paturel, G., Petit, C., Prugniel, P., et al. 2003, A&A, 412, 45

Piffaretti, R., Arnaud, M., Pratt, G. W., Pointecouteau, E., & Melin, J.-B. 2011, A&A, 534, A109

Planck Collaboration, Ade, P. A. R., Aghanim, N., et al. 2013, A&A, 557, A52

Predehl, P., Andritschke, R., Böhringer, H., et al. 2010, in Proc. SPIE, Vol. 7732, Space Telescopes and Instrumentation 2010: Ultraviolet to Gamma Ray, 77320U

Putman, M. E., Peek, J. E. G., & Joung, M. R. 2012, ARA&A, 50, 491

Rasmussen, A., Kahn, S. M., & Paerels, F. 2003, in Astrophysics and Space Science Library, Vol. 281, The IGM/Galaxy Connection. The Distribution of Baryons at z=0, ed. J. L. Rosenberg & M. E. Putman (Dordrecht: Kluwer), 109

Rasmussen, A. P., Kahn, S. M., Paerels, F., et al. 2007, ApJ, 656, 129

Rasmussen, J., Sommer-Larsen, J., Pedersen, K., et al. 2009, ApJ, 697, 79

Raymond, J. C., & Smith, B. W. 1977, ApJS, 35, 419

Reid, M. J., Menten, K. M., Brunthaler, A., et al. 2014, ApJ, 783, 130

Robertson, I. P., Collier, M. R., Cravens, T. E., & Fok, M.-C. 2006, Journal of Geophysical Research (Space Physics), 111, 12105

Robertson, I. P., & Cravens, T. E. 2003a, Journal of Geophysical Research (Space Physics), 108, 8031

—. 2003b, Geophys. Res. Lett., 30, 1439

Robitaille, T. P., & Whitney, B. A. 2010, ApJ, 710, L11

Ruszkowski, M., Yang, H.-Y. K., & Zweibel, E. 2016, ArXiv e-prints, arXiv:1602.04856

Salem, M., Besla, G., Bryan, G., et al. 2015, ApJ, 815, 77

Sarkar, K. C., Nath, B. B., & Sharma, P. 2015, MNRAS, 453, 3827

Sasaki, K., Asano, K., & Terasawa, T. 2015, ApJ, 814, 93

Savage, B. D., & Sembach, K. R. 1991, ApJ, 379, 245

Savage, B. D., Sembach, K. R., & Lu, L. 1997, AJ, 113, 2158

Savage, B. D., Sembach, K. R., Wakker, B. P., et al. 2003, ApJS, 146, 125

Schawinski, K., Urry, C. M., Virani, S., et al. 2010, ApJ, 711, 284

Schechter, P. 1976, ApJ, 203, 297

Schödel, R., Ott, T., Genzel, R., et al. 2002, Nature, 419, 694

Scoville, N. Z. 1972, ApJ, 175, L127

Sembach, K. R., Wakker, B. P., Savage, B. D., et al. 2003, ApJS, 146, 165

Sembay, S., Abbey, A., Altieri, B., et al. 2004, Proc. SPIE, 5488, 264

Shankar, F., Salucci, P., Granato, G. L., De Zotti, G., & Danese, L. 2004, MNRAS, 354, 1020

Shankar, F., Weinberg, D. H., & Miralda-Escudé, J. 2009, ApJ, 690, 20

Shapiro, P. R., & Field, G. B. 1976, ApJ, 205, 762

Shattow, G., & Loeb, A. 2009, MNRAS, 392, L21

Shelton, R. L., Sallmen, S. M., & Jenkins, E. B. 2007, ApJ, 659, 365

Shull, J. M., & Draine, B. T. 1987, in Astrophysics and Space Science Library, Vol. 134, Interstellar Processes, ed. D. J. Hollenbach & H. A. Thronson, Jr., 283–319

Sivakoff, G. R., Sarazin, C. L., & Carlin, J. L. 2004, ApJ, 617, 262

Smith, R. K., Brickhouse, N. S., Liedahl, D. A., & Raymond, J. C. 2001, ApJ, 556, L91

Smith, R. K., Foster, A. R., Edgar, R. J., & Brickhouse, N. S. 2014a, ApJ, 787, 77

Smith, R. K., Bautz, M. W., Edgar, R. J., et al. 2007, PASJ, 59, 141

Smith, R. K., Ackermann, M., Allured, R., et al. 2014b, Proc. SPIE, 9144, 4

Snowden, S. L., Collier, M. R., & Kuntz, K. D. 2004, ApJ, 610, 1182

Snowden, S. L., Cox, D. P., McCammon, D., & Sanders, W. T. 1990, ApJ, 354, 211

Snowden, S. L., Heiles, C., Koutroumpa, D., et al. 2015, ApJ, 806, 119

Snowden, S. L., & Kuntz, K. D. 2011, Cookbook for Analysis Procedures for XMM-Newton EPIC MOS Observations of Extended Objects and the Diffuse Background, version 4.3

Snowden, S. L., McCammon, D., & Verter, F. 1993, ApJ, 409, L21

Snowden, S. L., Egger, R., Freyberg, M. J., et al. 1997, ApJ, 485, 125

Sommer-Larsen, J. 2006, ApJ, 644, L1

Spitzer, Jr., L. 1956, ApJ, 124, 20

Stewart, K. R., Brooks, A. M., Bullock, J. S., et al. 2013, ApJ, 769, 74

Strickland, D. K., Heckman, T. M., Colbert, E. J. M., Hoopes, C. G., & Weaver, K. A. 2004, ApJS, 151, 193

Su, M., Slatyer, T. R., & Finkbeiner, D. P. 2010, ApJ, 724, 1044

Sutherland, R. S., & Dopita, M. A. 1993, ApJS, 88, 253

Tahara, M., Kataoka, J., Takeuchi, Y., et al. 2015, ApJ, 802, 91

Tawa, N., Hayashida, K., Nagai, M., et al. 2008, PASJ, 60, S11

Taylor, J. H., & Cordes, J. M. 1993, ApJ, 411, 674

Toft, S., Rasmussen, J., Sommer-Larsen, J., & Pedersen, K. 2002, MNRAS, 335, 799

Tomida, H., Matsuoka, M., Ueno, S., et al. 2000, in Proc. SPIE, Vol. 4012, X-Ray Optics, Instruments, and Missions III, ed. J. E. Truemper & B. Aschenbach, 178–185

Totani, T. 2006, PASJ, 58, 965

Tozzi, P., & Norman, C. 2001, ApJ, 546, 63

Tüllmann, R., Pietsch, W., Rossa, J., Breitschwerdt, D., & Dettmar, R.-J. 2006, A&A, 448, 43

van de Voort, F., Quataert, E., Hopkins, P. F., et al. 2016, ArXiv e-prints, arXiv:1604.01397

van Woerden, H., & Wakker, B. P. 2004, in Astrophysics and Space Science Library, Vol. 312, High Velocity Clouds, ed. H. van Woerden, B. P. Wakker, U. J. Schwarz, & K. S. de Boer, 195

Veilleux, S., Cecil, G., & Bland-Hawthorn, J. 2005, ARA&A, 43, 769

Voges, W., Aschenbach, B., Boller, T., et al. 1999, A&A, 349, 389

Voit, G. M., Kay, S. T., & Bryan, G. L. 2005, MNRAS, 364, 909

Wada, K., & Norman, C. A. 2001, ApJ, 547, 172

Wakker, B. P., & van Woerden, H. 1997, ARA&A, 35, 217

Wakker, B. P., Savage, B. D., Sembach, K. R., et al. 2003, ApJS, 146, 1

Walker, S. A., Fabian, A. C., Sanders, J. S., & George, M. R. 2012, MNRAS, 427, L45

Wang, Q. D. 1998, in Lecture Notes in Physics, Berlin Springer Verlag, Vol. 506, IAU Colloq. 166: The Local Bubble and Beyond, ed. D. Breitschwerdt, M. J. Freyberg, & J. Truemper, 503–512

Wang, Q. D., Yao, Y., Tripp, T. M., et al. 2005, ApJ, 635, 386

Wargelin, B. J., Markevitch, M., Juda, M., et al. 2004, ApJ, 607, 596

Watson, M. G., Schröder, A. C., Fyfe, D., et al. 2009, A&A, 493, 339

Weaver, R., McCray, R., Castor, J., Shapiro, P., & Moore, R. 1977, ApJ, 218, 377

Welsh, B. Y., & Shelton, R. L. 2009, Ap&SS, 323, 1

Westerhout, G. 1957, Bull. Astron. Inst. Netherlands, 13, 201

White, S. D. M., & Frenk, C. S. 1991, ApJ, 379, 52

White, S. D. M., & Rees, M. J. 1978, MNRAS, 183, 341

Whitney, B. A. 2011, BASI, 39, 101

Williams, R. J., Mathur, S., & Nicastro, F. 2006, ApJ, 645, 179

Williams, R. J., Mathur, S., Nicastro, F., & Elvis, M. 2007, ApJ, 665, 247

Williams, R. J., Mathur, S., Nicastro, F., et al. 2005, ApJ, 631, 856

Xue, X. X., Rix, H. W., Zhao, G., et al. 2008, ApJ, 684, 1143

Yan, M., Sadeghpour, H. R., & Dalgarno, A. 1998, ApJ, 496, 1044

Yang, H.-Y. K., Ruszkowski, M., Ricker, P. M., Zweibel, E., & Lee, D. 2012, ApJ, 761, 185

Yang, H.-Y. K., Ruszkowski, M., & Zweibel, E. 2013, MNRAS, 436, 2734

Yao, Y., Shull, J. M., Wang, Q. D., & Cash, W. 2012, ApJ, 746, 166

Yao, Y., Tripp, T. M., Wang, Q. D., et al. 2009a, ApJ, 697, 1784

Yao, Y., & Wang, Q. D. 2005, ApJ, 624, 751

—. 2007, ApJ, 658, 1088

Yao, Y., Wang, Q. D., Hagihara, T., et al. 2009b, ApJ, 690, 143

Yoshino, T., Mitsuda, K., Yamasaki, N. Y., et al. 2009, PASJ, 61, 805

Yu, Q., & Tremaine, S. 2002, MNRAS, 335, 965

Yuan, F., Bu, D., & Wu, M. 2012, ApJ, 761, 130

Yuan, F., Gan, Z., Narayan, R., et al. 2015, ApJ, 804, 101

Yuan, F., & Narayan, R. 2014, ARA&A, 52, 529

Yuan, W., Brinkmann, W., Siebert, J., & Voges, W. 1998, A&A, 330, 108

Yusef-Zadeh, F., Hewitt, J. W., Arendt, R. G., et al. 2009, ApJ, 702, 178

Zubovas, K., King, A. R., & Nayakshin, S. 2011, MNRAS, 415, L21

Zubovas, K., & Nayakshin, S. 2012, MNRAS, 424, 666